THE UNIVERSITY OF CHICAGO

SELF-ASSEMBLY AND ION TRANSPORT BEHAVIOR OF POLYMER ELECTROLYTE THIN FILMS

A DISSERTATION SUBMITTED TO
THE FACULTY OF THE PRITZKER SCHOOL OF MOLECULAR ENGINEERING
IN CANDIDACY FOR THE DEGREE OF
DOCTOR OF PHILOSOPHY

BY
PETER BENNINGTON

CHICAGO, ILLINOIS
MARCH 2022

TABLE OF CONTENTS

LIST OF FIGURES

LIST OF TABLES

LIST OF SCHEMES

NOMENCLATURE

Abbreviations

AC	alternating current
AFM	atomic force microscopy
AIBN	azobisisobutyronitrile
ALD	atomic layer deposition
ATR	attenuated total reflection
BCC	body-centered cubic sphere phase
BCE	block copolymer electrolyte
BCP	block copolymer
BVAF	bond vector autocorrelation function
CNC	cellulose nanocrystal
CPBD	2-cyano-2propyl benzodithioate
CPDTC	2-cyano-2-propyl dodecyltrithiocarbonate
CPE	constant phase element
CTA	chain transfer agent
DC	direct current
DIS	disordered phase
DMC	dimethyl carbonate
DMF	dimethylformamide
DMSO-d_6	deuterated dimethyl sulfoxide
DSA	directed self-assembly
DSC	differential scanning calorimetry
EC	ethylene carbonate
EIS	electrochemical impedance spectroscopy
EO	ethylene oxide repeat unit
FTIR	Fourier transform infrared spectroscopy
GISAXS	grazing-incidence small-angle X-ray scattering
GMA	glycidyl methacrylate
GYR	gyroid phase
^{1}H-NMR	proton nuclear magnetic resonance
HEX	hexagonally packed cylinder phase
HMDS	hexamethyldisilazane
IDE	interdigitated electrode
IL	ionic liquid
LAM	lamellar phase
LIB	lithium-ion battery
LiTf	lithium triflate
LiTFSI	lithium bis(trifluoromethanesulfonyl)imide
LLTO	lithium lanthanum titanate
LMB	lithium metal battery
MD	molecular dynamics
MeOH	methanol
MFT	mean-field theory
MMA	methyl methacrylate
mP2VP	iodomethane-functionalized poly(2-vinylpyridine)
MSD	mean squared displacement

MW	molecular weight
NMP	n-methyl-2-pyrrolidone
OEM	oligo(ethylene oxide) methyl ether methacrylate
OEM-GC	POEM-*ran*-PGCMA
PEO	poly(ethylene oxide)
PGCMA	poly(glycerol carbonate methacrylate)
PGMA	poly(glycidyl methacrylate)
PIL	poly(ionic liquid)
PMMA	poly(methyl methacrylate)
PNF	Pritzker Nanofabrication Facility
POEA	poly[oligo(ethylene oxide) methyl ether acrylate]
POEM	poly[oligo(ethylene oxide) methyl ether methacrylate]
POEM$_x$	POEM with x EO units in the side-chain
PS-P2VP	polystyrene-*block*-poly(2-vinylpyridine)
PSCF	Polymer Self-Consistent Field code developed by David Morse and coworkers
PSS-PMB	poly(styrene sulfonate)-*block*-poly(methyl butylene)
RAFT	reversible addition-fragmentation chain transfer polymerization
SAXS	small-angle X-ray scattering
SCFT	self-consistent field theory
SEC	size-exclusion chromatography
SEM	scanning electron microscopy
SEO	polystyrene-*block*-poly(ethylene oxide)
SHE	standard hydrogen electrode
SPE	solid polymer electrolyte
SST	strong segregation theory
THF	tetrahydrofuran
VTF	Vogel-Tammann-Fulcher
WAXS	wide-angle X-ray scattering
WCA	water contact angle
x-PS	crosslinked polystyrene
XPS	X-ray photoelectron spectroscopy

Greek Letters

δ	(a) diffusion layer thickness; (b) distance from center of SEO interface where PEO remains nonconductive; (c) chemical shift in NMR spectrum
δ_s	symmetric deformation mode
Δ	interfacial width
Δd	additional effective electrode spacing for IDEs coated by thin films
η	electrode metal fraction, $w/(d+w)$
ε_0	vacuum permittivity
ε_R	relative permittivity
θ	X-ray scattering angle

κ	(a) cell constant; (b) solvation site edge density
λ	X-ray wavelength
ν_{s}	symmetric stretching mode
ρ_{A}	mass density of species A
σ	ionic conductivity
σ_{BCE}	conductivity of BCE
σ_{c}	conductivity of the conductive phase of BCE
σ_{n}	block copolymer conductivity normalized by conductive phase volume fraction and equivalent homopolymer conductivity
σ_{nr}	normalized, temperature-reduced conductivity
σ_{PEO}	PEO homopolymer conductivity
σ_{SEO}	SEO conductivity
τ	mean relaxation time from fitting of BVAF
ϕ	phase shift
ϕ_{A}	volume fraction of A block in a block copolymer
$\phi_{\mathrm{A}}(z)$	concentration of A monomers at distance z from center of BCP interface
ϕ_{active}	active volume fraction of PEO within SEO BCE
ϕ_{c}	volume fraction of the conductive phase of BCE
ϕ_{inactive}	inactive volume fraction of PEO within SEO BCE
φ	electric potential
φ_0	potential perturbation amplitude
χ	Flory-Huggins interaction parameter
χ_{eff}	effective χ
ω	angular frequency

Symbols

A	(a) electrode surface area; (b) VTF prefactor
a	constant phase element exponent
b	statistical segment length
C	capacitance
D	diffusion coefficient
Đ	molecular weight dispersity
d	(a) interelectrode spacing; (b) real-space distance
$\vec{E}$	applied electric field
E_{a}	VTF equation psuedo-activation energy
[EO]	molar concentration of EO units
f	frequency
f_{τ}	BCE conductivity tortuosity factor
h	thin film height
I	current
I_0	current response amplitude
j	imaginary unit, $\sqrt{-1}$
$\overrightarrow{k}$	incident X-ray wavevector

$\overrightarrow{k'}$	scattered X-ray wavevector
L	inductance
L_0	block copolymer domain spacing
$[\mathrm{Li}^+]$	molar concentration of Li^+
l	IDE electrode overlap length
M_A	molar mass of species A
M_n	number average molecular weight
N	(a) number of IDE electrodes; (b) degree of polymerization
n	some positive integer
Q	(a) apparent capacitance of constant phase element; (b) total surface charge on a capacitor
q	reciprocal space distance
$\overrightarrow{q}$	scattering vector
q^*	primary scattering peak location
q_y	in-plane scattering direction
q_z	through-plane scattering direction
R	resistance
r	molar ratio of Li^+ to EO units
T	temperature
T_0	Vogel temperature
T_g	glass transition temperature
t	time
v	molar volume
w	IDE electrode width
w_eff	effective IDE electrode width in the case of thin films
x_EO	ether oxygen mole fraction
x_O	molar ratio of ether oxygen plus carbonate units to the total number of atoms in the repeat unit
Z	impedance
Z'	real component of impedance
Z''	imaginary component of impedance
Z_0, $\lvert Z\rvert$	impedance magnitude
z	distance from the center of BCP interface

ACKNOWLEDGMENTS

I would first and foremost like to thank my family for their love and support throughout my life in whatever I have chosen to pursue. Graduate school would have been far more difficult without their encouragement.

I would also like to thank my advisors, Paul Nealey and Shrayesh Patel. Thank you for your guidance and patience with me over the years. Thank you for allowing me the freedom to pursue projects which I found the most engaging.

I would not have had the success in graduate school that I did without the mentorship and assistance of a number of older graduate students and postdocs across the Nealey and Patel Groups. To Dr. Moshe Dolejsi, I am so grateful for your constant willingness to teach me everything you knew about polymers, fab, SEM, and anything else I came to bother you about. I was always impressed by the depth of your knowledge in so many areas, and even more impressed with your curiosity and ability to make thoughtful suggestions for people working on very different projects than your own. To Dr. Yu Kambe, I am grateful for all you taught me about electrochemistry and for blazing a trail for me to follow. Without your work, my own project could not have happened. I am also very thankful for Dr. Ban Dong, Dr. James Dolan, and Prof. Xiao Li, each of whom was very helpful in my early years as a graduate student and who set great examples of how to be successful researchers. I am also very thankful to Garrett Grocke, a fellow graduate student who enabled the work of the entire Patel group and much of the Nealey group over the past five years. He hand built the experimental setups that enabled all of my work (and that of many others), and I am deeply thankful to have had the privilege of working in the group at the same time as him.

Perhaps no one has taught me as much as Prof. Daniel Sharon. For the first four years of graduate school, Daniel was my mentor and partner on every project I engaged with. He taught me so much of what I know, and I can honestly say I would not be at this point right now without him. I am very aware of how unique our relationship was and how few graduate

students are given the type of hands-on guidance, day in and day out, that I got from Daniel. Perhaps even more unique was his willingness to share credit and projects with me and to treat me as a coequal partner. Daniel, I cannot thank you enough for your mentorship and friendship.

In the latter half of my PhD work, when I began to explore synthesizing my own polymers, a number of people were critical to making this a success. Dr. James Lettow was the first to stand up and gladly offer his help, as he so often was. He was incredibly helpful as I took my first baby steps into polymer synthesis, and much of what I know today is thanks to his patience in explaining these new ideas to me. Similarly, Dr. Hongbo Feng was very helpful and always gracious in allowing me to use his space and equipment as I started out in this direction, and I am very thankful to both of you. More recently, I have had the pleasure of working alongside Dr. Regina Sánchez. Regina's expertise in polymer synthesis has greatly elevated the work we had been doing and has opened the doors to ideas that would simply not have been possible without her. I am grateful for all that I have learned from you, and for having you as someone to work with for the past few years. To all of the other members of the Nealey and Patel groups, past and present, thank you for your help and camaraderie over the years. I have learned something from each you, and I am very grateful to have had the privilege of working with such a bright and engaging group of people.

I have been fortunate to work with a number of excellent collaborators throughout my time as a PhD student. The first of these collaborations was with Dr. Preston Sutton and Dr. Ilja Gunkel from AMI in Friborg, Switzerland. Working with the two of you taught me a lot about polymer electrolytes and block copolymers, as well as many general lessons about how to conduct research and ask the right questions. More recently, I had the pleasure of working with Dr. Qiujie Zhao and Prof. Christopher Evans from UIUC. Our work together was a very rewarding and interesting component of my research experience, and I am very thankful to have had the opportunity to work with the both of you. For several years now, ongoing collaboration with the de Pablo group here at the PME has been a critical component of my work. To Prof. de Pablo and Prof. Michael Webb, I am very grateful for your guidance and mentorship on these projects. I am especially thankful to Chuting Deng, my graduate student counterpart in the de Pablo group. Chuting is a true expert in the modeling of polymer electrolytes, and our work and discussions together have truly enriched my experience here. You have taught me so much, and I am truly thankful to have had you as a colleague and partner.

The work presented in this dissertation relied on a number of user facilities and shared pieces of equipment. I am fortunate to have been given the chance to use these world-class facilities and to have had the chance to learn from the managers of these facilities. In particular, Peter Duda (Technical Director of the Pritzker Nanofabrication Facility) and Dr. Phil Griffin (Director of the Soft Matter Characterization Facility) have been tremendous resources and teachers during my time here. Peter has time and again been able to quickly tell me what is wrong with my fabrication process and point me in the right direction (and he cooks a mean tri tip). Phil has similarly been an incredible teacher about all things polymers characterization, and I am very grateful to have had the chance to learn from him.

Finally, I am very thankful for the many great friends who have made my time in Chicago so enjoyable. When I think back on my time in graduate school, my best memories will be of time spent with friends. After work trips to Jimmy's, softball on Friday afternoons, training for the triathlon at the lake, and countless apartment-based hangs over the past five years will be cherished memories for many years to come. In particular, I am extremely grateful to Chris Conner, Elena Glen, and Amy Butcher. These past couple years have not been easy for anyone, but our little family on Harper Ave. has made it much easier. Thank you for all the support and the happy memories.

ABSTRACT

The increasing demand for portable electronics and electric vehicles has necessitated improved electrochemical energy storage devices, and lithium-based batteries will be a critical component of this growing energy storage market. More energy dense batteries could be made possible by the use of Li metal anodes, though solid electrolytes are likely necessary to inhibit dendrite growth and enable safe battery cycling. Solid polymer electrolytes (SPEs), and microphase separating block copolymer electrolytes (BCEs) in particular, are one interesting set of candidate materials for this application. Developing SPEs that meet the stringent material property requirements for use in a Li battery, however, requires further improvement to their ionic conductivity, among other properties. Greater understanding of the ion transport behavior of these materials is necessary to make these improvements.

Developing molecular-level structure-function relationships for nanostructured BCEs has been limited by the inability to precisely control or quantify the ion transport pathways through the material. This remains a challenge due to fundamental limitations of the experimental approach taken to studying these materials that results in hierarchical assembly of randomly ordered grains with tortuous, defect-filled transport pathways. In this dissertation, a different approach consisting of coplanar interdigitated electrodes (IDEs) and polymer electrolyte thin films is developed. In Chapter 3, the microfabrication procedure and a derivation of the cell constant for these devices are presented. In Chapter 4, this theoretical cell constant is validated experimentally, and a robust framework for the use of IDEs for electrochemical impedance spectroscopy (EIS) measurements of thin SPE films is developed. In Chapter 5, thin BCE films are assembled into single-grain structures on top of IDEs in order to probe the intrinsic ion transport behavior of the material. In Chapter 6, thin films of cylinder-forming materials are self-assembled on the IDEs, and complexities related to different wetting-behaviors are discussed. The results from these studies clarify the importance of monomeric mixing and dilution of the ion solvation site network at the

BCE domain interface.

In the final section of the dissertation, the role of solvation site formation and connectivity is explored for a series of side-chain SPEs synthesized by controlled radical polymerization. In Chapter 7, the role of side-chain length in determining ion solvation and transport behavior is elucidated through a combined experimental and computational study. In contrast to linear polymer electrolytes, the ionic conductivity is poorly predicted by differences in glass transition temperature. Instead, conductivity is determined by the local relaxation rate of specific solvation sites. In Chapter 8, these side-chain materials are copolymerized with a highly polar cyclic carbonate monomer to explore the role of polarity in ion solvation and transport. Surprisingly, lithium ions are solvated exclusively by the low polarity polyether segments, and ionic conductivity was adversely affected by the addition of the high polarity component. These findings are in contrast with analogous small molecule electrolyte systems. In Chapter 9, these results are summarized, and some interesting future research directions are discussed.

Chapter 1

Introduction

The demand for cheaper, safer, and more efficient electrochemical energy storage devices has grown substantially in recent years, and that growth is expected to continue to accelerate. Secondary (rechargeable) batteries are of particular interest for three key areas: portable electronics, hybrid and electric vehicles, and grid-scale storage of renewable energy such as wind and solar. Lithium-ion batteries (LIB), which have dominated the portable electronics market, are increasingly being used for automotive and renewables storage purposes as the price has plummeted over the last decade.[1,2] Improvements to the energy density and materials costs of these devices is still required, however, if LIBs are to reach the price point of $100/kWh that is necessary to truly supplant internal combustion engines for automotive applications.[3]

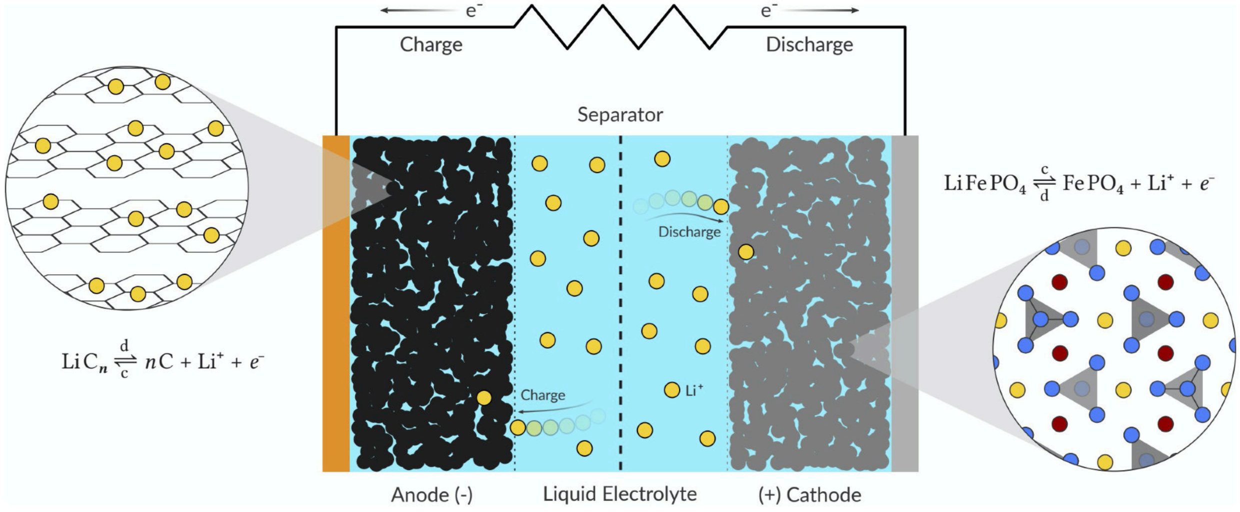

Figure 1.1 – Illustration of a conventional lithium-ion battery consisting of a graphite anode, $\mathrm{LiFePO_4}$ cathode, and an organic solvent electrolyte.

An illustration of a conventional LIB is shown in Figure 1.1. The device consists of a graphite anode and transition metal-based cathode (*e.g.* $LiCoO_2$, $LiFePO_4$) with a porous separator between the two electrodes.[4,5] The plastic separator is filled with an organic electrolyte solution, typically consisting of a lithium salt dissolved in a mixture of ethylene carbonate (EC) and dimethyl carbonate (DMC) or similar solvents.[6] In such a device, Li^+ is shuttled back and forth between the anode and cathode during charge and discharge and can be inserted between the planes of the layered electrode materials in a process known as intercalation. Although the energy density of these so-called "rocking chair" type LIBs has been improved to nearly the theoretical limits, they are still not energy dense enough to meet the stringent demands of electric vehicle consumers.[7]

1.1 Solid Polymer Electrolytes

A significant increase in the energy density of lithium-based batteries could be realized by replacing the graphite anode with metallic lithium. Lithium metal batteries (LMBs) have not been commercialized yet due to intractable problems with the use of lithium metal.[8–10] Chief among these problems is the tendency for nonuniform deposition of lithium metal on the anode, resulting in dendrite nucleation.[11–13] These dendrites can then grow uncontrollably, resulting in short circuit of the battery and catastrophic failure.[14] Suppressing the formation and growth of dendrites is therefore imperative if LMBs are to be realized. One approach to dendrite suppression that has received significant attention is to replace the liquid organic electrolyte with a solid-state electrolyte.[15–17] Solid electrolytes can be inorganic ceramics, polymers, or ceramic-polymer composites. Solid polymer electrolytes (SPEs) have a number of attractive properties, including low cost, solution processability, and good interfacial contact with solid electrode surfaces.[18]

1.1.1 Ion transport mechanisms in SPEs

SPEs are comprised of a lithium salt and a polymer that can dissolve and conduct ions. The first such system was demonstrated by Wright and coworkers in 1973 when they showed that poly(ethylene oxide) (PEO) was capable of dissociating and conducting alkali metal ions.[19] Since then, PEO has remained by far the most widely studied polymer electrolyte system, and a great deal of understanding about how this system works has been developed. PEO dissolves salt by strong coordination of the metal cation with the electron lone pairs on the ether oxygens. The most favorable configurations for PEO-lithium salt systems involve Li^+ being coordinated by five or six ether oxygens.[20–22] These ether oxygens typically come from either contiguous ethylene oxide (EO) repeat units along a single polymer backbone, or from at most two adjacent chains. Coordination of a lithium ion in one of these so-called "solvation sites" is shown in Figure 1.2a. Ion transport in PEO and similar materials is understood to occur by short-range hopping of ions between adjacent solvation sites (either inter- or intra-chain), with longer range transport being facilitated by segmental motion of the polymer chains (Figure 1.2b).[23–25] Fast segmental dynamics in polymers is typically associated with a low glass transition temperature (T_{g}), and much of the work on improving SPE ionic conductivity has focused on lowering T_{g}. This transport mechanism lies somewhere between the behavior of liquid electrolytes, where the solvent host relaxes at a similar rate to the ionic motion,[26] and solid inorganic materials, where ions hop between vacancies in a static solvation environment.[27]

Much of the mechanistic understanding of ion transport in SPEs has come from molecular dynamics (MD) simulations. MD simulations consist of generating a model based on the size, shape, and other properties (*e.g.* charge) of the particles in the system and calculating trajectories of each particle based on Newtonian equations of motion and model-specific force-fields and interaction potentials.[28] MD models can range from low detail, such as considering each monomer on a polymer chain to be an identical spherical bead (coarse-grained), to

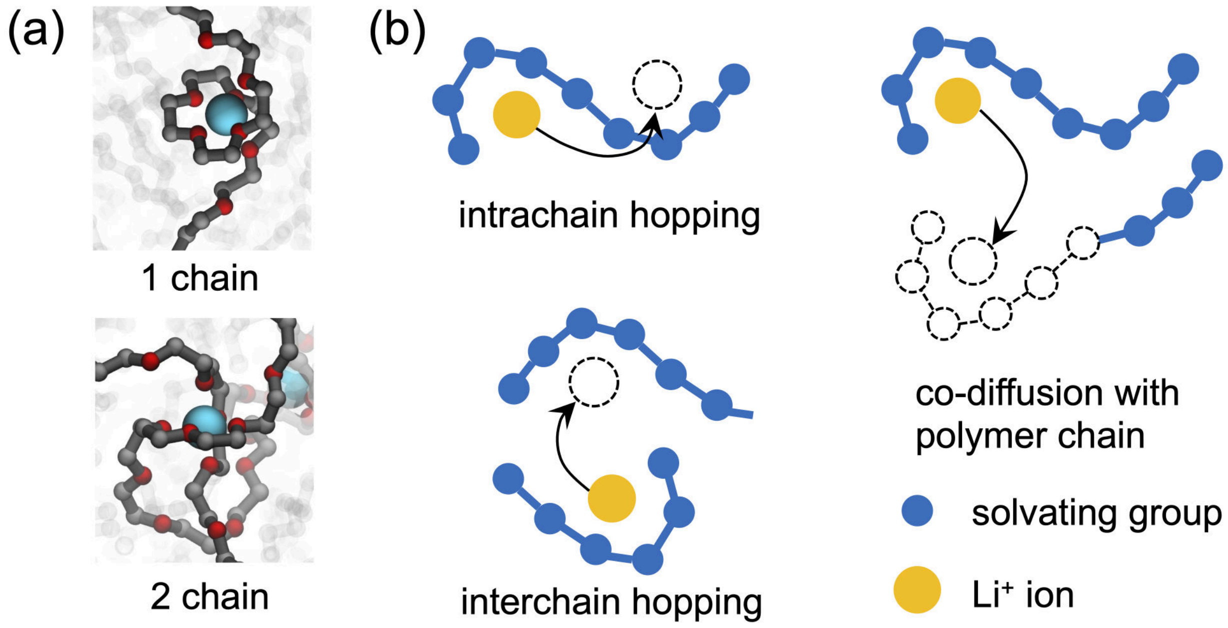

Figure 1.2 – (a) MD simulation snapshot showing the solvation of Li^+ by either one or two polyether chains, adapted from *ref.* [22] (red atoms are ether oxygens, blue are Li^+) and (b) illustrations of ion transport mechanisms in SPEs

highly detailed where each individual atom with a given partial charge is considered. Because MD simulations calculate particle position at very small timesteps (often 1 fs resolution), they can provide detailed information about how individual ions move in an SPE. With any simulation, however, there is a clear trade-off between resolution and computational power. Highly detailed models simulated for long times can be prohibitively expensive for the computational resources available, and choices must be made as to which elements of the system can be modeled coarsely and still produce physically meaningful results. In this regard, polymers can be challenging to model accurately, as large numbers of molecules are needed to capture the polymer physics of entangled chains, and the time needed for these systems to achieve thermodynamic equilibrium can be long.

In a seminal work by Borodin and Smith, the authors used MD simulations of a PEO-based SPE to provide detailed insight into the different ion transport mechanisms and their individual contributions to the overall conductivity of the electrolyte.[20] They confirmed previous experimental work that showed PEO forms Li^+ solvation sites by wrapping around the ion in a helical-like shape, with ions coordinated by typically five or six ether oxygens from either one or two polymer chains, as shown in Figure 1.2a. The authors also determined that fast ion transport relies on a combined transport mechanism involving subdiffusive movement of ions along a PEO backbone (intrachain hopping) and diffusive movement of ions with the polymer backbone and hopping between different polymer chains (interchain hopping), illustrated in Figure 1.2b. Similar studies have been applied to a wide range of materials chemistries, and MD simulation studies continue to be an important part of the polymer electrolyte literature.[29–36]

Solvation site connectivity in SPEs

In a recent series of combined computational and experimental studies, Webb and coworkers demonstrated another critical material property for enabling high ionic conductivity in SPEs that they termed "solvation site connectivity".[37–39] The solvation site connectivity model posits that, in addition to the ability to solvate Li^+ ions and fast segmental dynamics, the material should exhibit a well-connected or percolated network of Li^+ solvation sites. In a study of a series of linear polyethers, all of the materials had similar ability to solvate Li and all had low T_{g}.[39] Even after correcting for differences in T_{g} and molar salt concentration, there was a systematic decrease in the ionic conductivity as the prevalence of ether oxygens in the system was decreased. This trend was attributed to a lower density of solvation sites and a less well-connected solvation site network in materials with lower EO fraction. Solvation site connectivity can be directly visualized and calculated from atomistic MD simulations, such as those performed by Webb and coworkers, and when coupled with experimental measurements can yield deep insights into the ionic transport behavior of SPEs. This model has been applied with great success to a limited number of materials; understanding the implications of solvation site networks more generally, however, remains an open challenge for the field. Applying this idea to the study of more diverse materials chemistries is critical to fully understanding the behavior of polymer electrolytes and realizing improved ion transport properties. The most powerful impactful studies in this regard will be those that can use MD simulations to relate the molecular-level motion of particles to the macroscopic behavior of the material system that can be measured by experiment.[40]

1.1.2 Effect of salt concentration on ionic conductivity in SPEs

A key metric for determining the conductivity of any electrolyte system is the salt concentration. In SPEs, the salt concentration produces a number of effects that impact the conductivity. A higher salt concentration corresponds to a greater number of potential charge carriers, which generally corresponds to higher ionic conductivity. This increase in the number of mobile charge carriers is limited, however, by the ability of the material to fully solvate and dissociate the salt. For PEO-based SPEs, the optimal configuration of five or six EO units per solvation site can only be achieved up to a salt concentration of roughly $r = 0.2$, where $r = [\mathrm{Li}^+]/[\mathrm{EO}]$.[41] Additionally, the presence of ions in the material affects the polymer segmental dynamics, as can be observed by changes in T_g. In particular, Li^+ that is coordinated by two PEO chains acts a physical cross-linking site, and T_g generally increases with increasing salt concentration.[42] The conductivity of an SPE consisting of PEO and a common lithium salt, lithium bis(trifluoromethansulfonyl)imide (LiTFSI) at different salt concentrations is shown in Figure 1.3. The competing effects of greater number of charge carriers and higher T_g results in a conductivity maximum around $r = 0.085$. Similar conductivity-concentration relationships are observed for many, though not all, polymer electrolyte systems.

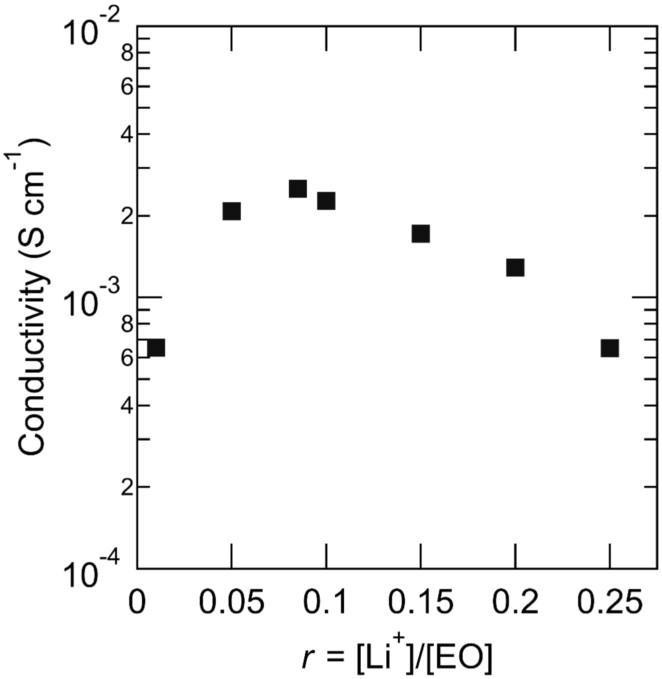

Figure 1.3 – Conductivity of PEO-LiTFSI as a function of salt concentration at 100 °C

1.1.3 Shortcomings of PEO as an electrolyte

Despite the early promise of SPEs, they still fall short of a number of key material property criteria. A major drawback of PEO as an electrolyte material is the fact that it is semicrystalline with a melting temperature of around 50 °C. Below this melting point, the ionic conductivity is well below the benchmark value of 10^{-4} S cm^{-1} thought to be necessary to enable its use in a functional LMB.[43] Above the melting point, however, the mechanical properties of PEO diminish greatly as the material enters the melt state. This inherent tradeoff between mechanical modulus and ionic conductivity is a feature of any material that relies on fast segmental mobility for ion transport. As high mechanical modulus is the primary way in which solid electrolytes are thought to be able to inhibit dendrite growth, addressing this tradeoff of properties is paramount for the eventual utilization of SPEs in a commercial battery.[16,44,45] Moreover, PEO appears unsuitable to meet the stringent chemical and electrochemical stability requirements of an LMB. In particular, the electrochemical stability window of PEO is limited to around 3.8 V *vs.* Li/Li$^+$.[46] While this electrochemical stability makes PEO compatible with current generation $LiFePO_4$ cathodes, it is well below the operating potential of next generation high voltage cathodes such as the lithium nickel manganese cobalt oxide materials currently being developed ($>$ 4.5 V).[47] On the anode side, PEO does appear to be stable at the low reducing potential of Li (-3.04 V *vs.* SHE.), but recent work has indicated that chemical reactivity may limit the lifetime of a PEO-based SPE in contact with Li metal.[48,49] These shortcomings are not trivial, and it seems clear that PEO on its own will not meet all of the requirements needed to enable LMBs.

Though PEO has been the most widely studied polymer electrolyte system, any material containing polar or Lewis basic groups capable of coordinating with lithium ions and dissociating them from the counterion may be considered as well. A wide range of polymers, including other polyethers, polyesters, polynitriles, and polycarbonates have been studied as electrolyte materials as well.[50–55] Among the potential materials chemistries for SPEs, polycarbonates are a particular interesting class of materials receiving significant attention. Linear polycarbonates (*i.e.* those with the carbonate group located in the backbone) such as poly(ethylene carbonate) have been shown to have reasonably high oxidative stability, even as high as 5.0 V vs Li/Li$^+$.[33,56] Tominaga and coworkers have also demonstrated that the conductivity-salt concentration relationships are very different in polycarbonates than in polyethers, and that highly concentrated ($>$ 180 mol% salt to polymer) electrolyte films can be prepared with these materials.[56–58] Although much less widely studied than their polyether counterparts, polycarbonates represent an interesting and potentially viable option for use in solid-state lithium batteries. Work remains, however, to understand more completely the ion conduction processes of these materials and how they interact with the other components in the battery system.

1.2 Block Copolymer Electrolytes

1.2.1 Block copolymer self-assembly

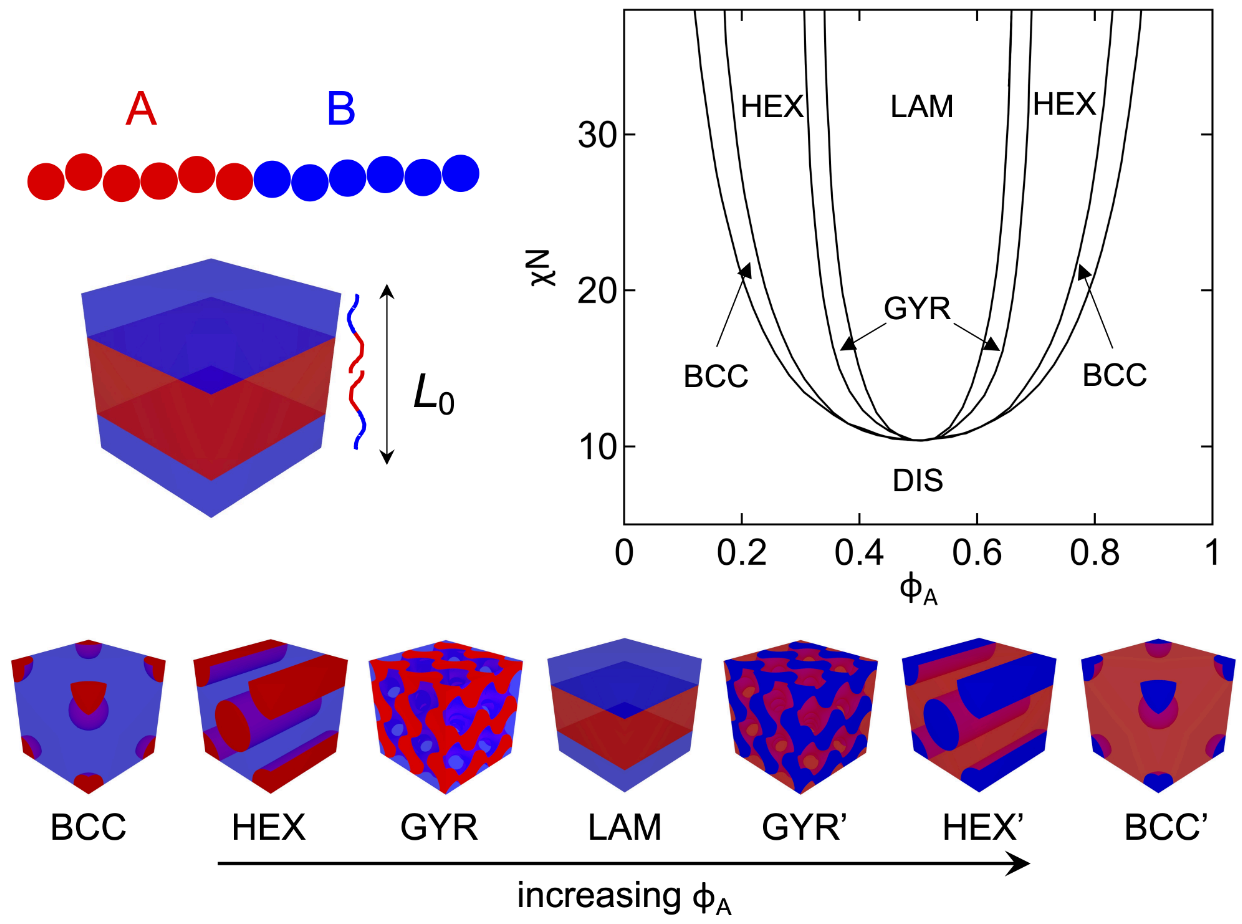

Figure 1.4 – Nanostructures exhibited by linear diblock copolymers. Phase diagram for linear diblock copolymer predicted by self-consistent mean field theory calculations, reproduced from *ref.* [59].

One approach to optimizing the seemingly orthogonal properties of mechanical modulus and conductivity is to use a nanostructured block copolymer electrolyte (BCE). Block copolymers (BCPs) consist of two chemically distinct polymer chains (comprised of A monomers and B monomers, respectively) connected at one end by a covalent bond, as illustrated in Figure 1.4. The two blocks will tend to phase separate due to unfavorable interaction between monomers of different type. The extent of this phase separation is limited, however, by the covalent bond between the two blocks. A balance between the enthalpic driving force for phase separation and the entropic penalty due to chain stretching results in so-called "microphase separation" of the material into periodic structures with characteristic lengths scales typically on the order of tens of nanometers.[60] A phase diagram for a linear diblock copolymer is shown in Figure 1.4.[59] The nanostructure formed is determined by the volume fraction of the A block, ϕ_{A}, and the strength of segregation, χN. Here χ refers to the Flory-Huggins interaction parameter, and N is the degree of polymerization compared to some reference volume. χ is a function of the chemistry of the different blocks and varies inversely with temperature according to Equation 1.1.[61,62]

$$\chi = A + \frac{B}{T} \tag{1.1}$$

The phase diagram in Figure 1.4, which was determined by solving self-consistent mean field theory equations (SCFT), shows that BCPs exhibit an upper critical solution temperature (UCST) behavior, with a disordered (DIS) phase occurring at higher temperatures (low χN).[63] This order-disorder transition for symmetric diblock copolymers is predicted to occur at $\chi N = 10.5$. The periodicity of the structure, or the BCP domain spacing, L_0, is also a function of χ and N, and is typically on the order of 10s or 100s of nanometers. Between the domains of the microphase separated structure there is a diffuse interface due to imperfect alignment of the block copolymer junctions and fluctations of the polymer chains. In the strong segregation limit ($\chi N \gg 1$), the monomer concentration across this interface varies like $\tanh(z)$, where z is the distance from the center of the interface. BCPs with higher χ exhibit a sharper domain interface.[64] The periodic structure formed by the material can be lamellar (LAM), hexagonally packed cylinders (HEX), gyroid (GYR), body-centered cubic spheres (BCC), or other more exotic phases. If one phase of this structure consists of an ionically conductive material, such as PEO, and the other is comprised of a mechanically robust material, such as polystyrene (PS), theoretically each of these properties could be tuned independently.

BCPs, like homopolymers, are rendered ionically conductive by blending with an appropriate salt. In BCPs, however, the effects of added salt are more complex and have therefore been the subject of extensive research activity. It is typically assumed that in an amphiphilic BCP such as PS-*block*-PEO (SEO), the salt will preferentially reside in the hydrophilic (or high polarity) domain. This preferentiality for one domain has the effect of exacerbating the chemically dissimilarity of the two blocks, and a higher effective χ (χ_{eff}) is observed. Epps *et al.* showed this with a study of polyisoprene-*block*-polystyrene-*block*-poly(ethylene oxide) where χ_{eff} was found to vary linearly with the salt concentration.[65] Work by several other groups has explored the phase behavior of a wide range of materials chemistry and blended salts.[66–71] Generally, the χ_{eff} tends to increase with the addition of salt, while the exact slope of the increase depends on the specific chemistry of the both the BCP and the salt.

The phase behavior of BCP-salt blends has been rich territory for computational researchers as well. Work by Olvera de la Cruz and others was able to predict the asymmetry introduced to BCP phase diagrams by the addition of ionic species using modified SCFT calculations.[72] Similar results were obtained in an MD simulation study SEO-lithium salt mixtures by Chu *et al.*[73] The addition of electrostatic interactions to the MD simulations significantly increases the computational power necessary, however, and great care must be taken in appropriately truncating the model to still be able to accurately capture the behavior of the material. This approach often involves coarse-graining the polymer repeat units such that all chemically specific character is lost.[74] Instead, monomers are often modeled as identical beads with differing dipole moments or dielectric constant. Nakamura and Wang demonstrated the importance of model choice on the phase behavior of BCEs by varying key model parameters such as the difference in dielectric constant of the two blocks or how they accounted for the interaction between PEO and the Li ions.[75] Hall and coworkers have successfully used a potential that varies as $1/r^4$ to describe some of the electrostatics of BCEs to replicate some of the experimentally observed phase behavior and ionic association for these systems.[76,77] It is important to note, however, that this potential has no physical meaning, and is instead introduced phenomenologically to simplify the calculations in a way that preserves the correct behavior of the system. Nevertheless, such coarse-grain modeling has been able to capture many of the important aspects of the phase behavior of BCEs.

1.2.2 Block copolymer electrolyte conductivity

Microphase separating BCEs have been extensively studied over the last decade, with SEO being the most widely used material for lithium battery applications. In an important early study of these materials, Balsara and coworkers demonstrated that the conductivity of phase-separating SEO-based BCEs increased with molecular weight (MW).[78] This result for BCEs is in contrast to homopolymer electrolytes, which tend to show a decrease in conductivity with increasing MW, up to the entanglement weight, due to increased free volume at the chain ends.[79] Balsara attributed the increased conductivity in high MW BCEs to the increase in domain spacing of the phase separated material. They hypothesized that ion dissociation, distribution, or diffusion might be adversely affected by the somewhat perturbed PEO chain conformations near the junction with the PS block, *i.e.* at the domain interface. At higher MW and larger domain spacings, the interfacial volume becomes less prevalent, and the domain interfaces become sharper. Direct physical explanation for differences in conductivity at the interface have yet to be elucidated, however.

Since publication of this work, a growing subset of the polymer electrolyte community has sought to elucidate the physical underpinnings of the reduced ion transport at domain interfaces and to optimize the conductivity of microphase-separated BCEs. Work in this area is confounded, though, by the hierarchical assembly exhibited by block copolymers in bulk samples. This hierarchical assembly exhibited in bulk BCE films is illustrated in Figure 1.5.

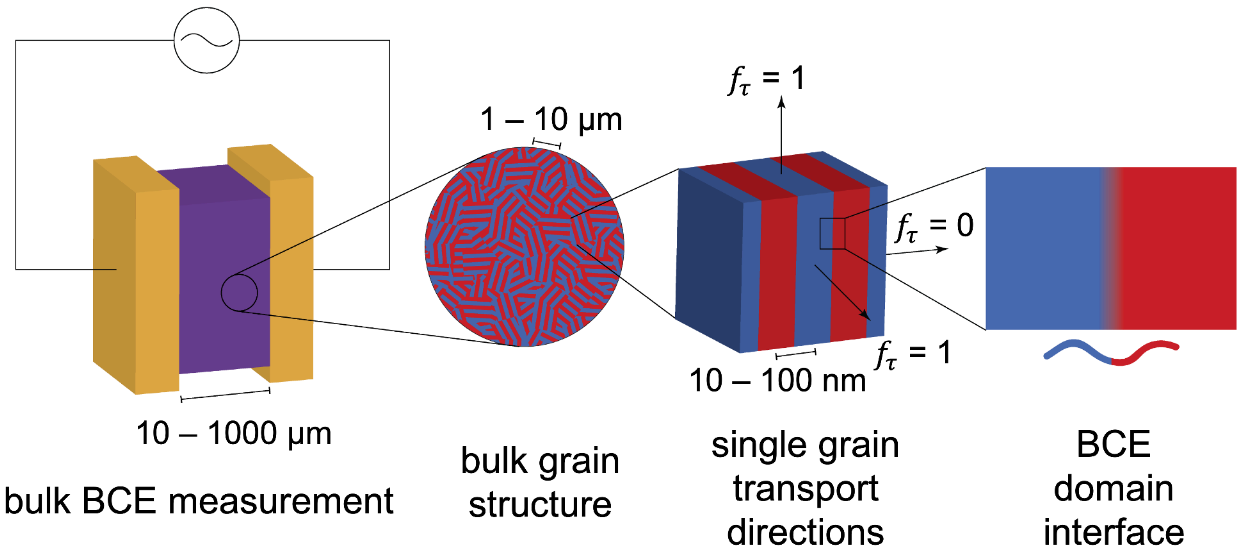

Figure 1.5 – Hierarchical assembly exhbited by bulk block copolymer electrolytes. Free standing electrolyte films (10s–1000s μm thick) consist of randomly oriented grains (each 1–10s μm in size). The grain structure is dependent on the thermal history and processing conditions of the film (extrinsic). Each grain of a single orientation consists of aligned domains of the micro-phase separated BCE with a thermodynamically determined domain spacing (10s–100s nm). Within each grain, polymer chains assemble to form the periodic structures, with diffuse interfacial regions where the block copolymer junctions are aligned.

As noted by Simone and Lodge, the ultimate conductivity of SEO electrolytes is limited by the randomly oriented microstructure of the BCE grains.[80] A commonly cited model for predicting the conductivity of BCEs assumes that the conductivity should be a function of the conductivity of the conductive phase (σ_c), which is often assumed to be equal to the conductivity of the equivalent homopolymer material, the volume fraction of the conductive phase (ϕ_c), and a factor related to the tortuosity of the conductive network between the electrodes (f_τ).[81,82] This tortuosity factor is often assumed to be a simple function of the dimensionality of the BCE nanostructure. In lamellae-forming BCEs, two of the three spatial dimensions of a given grain allow for ion transport, so the overall tortuosity factor for the film should be the average orientation of all of the grains with respect to the applied electric field, *i.e.* 2/3. Similar arguments can be made for other BCE morphologies. Under this model, any system where the conductive phase is continuous throughout the thickness of the film should have an $f_{\mathcal{T}}$ equal to unity. The equation for this effective-medium theory prediction is given below.

$$\sigma_{\mathrm{BCE}} = f_{\mathcal{T}} \phi_{\mathrm{c}} \sigma_{\mathrm{c}} \tag{1.2}$$

More recent work by Balsara and coworkers has demonstrated the outsized effect that average grain size can have on the macroscopic conductivity of a BCE.[83,84] They found that smaller grain size resulted in higher ionic conductivity, owing possibly to a greater number of connected conducting domains in samples with smaller grains. A clear reason for this effect was not given, however, and no predictive theory has emerged from this work. These grain boundaries and blocking defects can reduce the conductivity of the BCE by orders of magnitude from the predicted value from Equation 1.2. In systems where the conductive phase is continuous throughout the entire film, the conductivity of the BCE can approach this theoretical maximum for that material, as demonstrated in a study by Lodge *et al.* of a bicontinuous nanostructured BCE.[85] However, in a study of a gyroid-forming BCE also by Lodge, the conductivity was more than an order of magnitude lower than the predicted value, and no clear explanation was offered.[86] The issue of blocking defects is exacerbated in BCEs with a greater fraction of nonconducting material is present. If the material forms cylinders of conducting material, for example, the mechanical modulus can be quite high, but all of the grain boundaries in the system are blocking and the ionic conductivity suffers.[87] The conductivity of these systems again falls well short of the predictions from Equation 1.2. Though the importance of grain structure to the macroscopic conductivity has been made clear repeatedly, little has been shown experimentally about how transport within grains is impacted by the presence of the domain interfaces. These works have made clear, though, that little can be said about quantitative effects of the block copolymer nanostructure on the ionic conductivity in systems where the ionic pathways are not known and are not perfectly oriented with the electric field.

A number of methods have been employed to attempt to improve the alignment of ion conducting BCE domains or to more precisely characterize the tortuosity factor necessary to account for the effects of the bulk film microstructure. In one such study, Majewski *et al.* used high magnetic fields to align the cylindrical PEO channels of a liquid crystalline diblock copolymer.[88] They found that when the conducting cylinders were aligned with the electric field of the parallel plate electrodes, the measured conductivity was more than an order of magnitude higher than an unaligned sample. The conductivity of the aligned sample still fell well below the value expected from Equation 1.2, suggesting that the alignment was incomplete, and blocking defects remained throughout the film. Park and Balsara attempted a number of alignment methodologies to improve the conductivity of a proton conducting polystyrenesulfonate-*block*-polymethylbutylene BCE, including electric field and shear alignments.[89] Again, the authors were able to effect a higher conductivity in the aligned samples, but a significant number of defects remained, and tortuosity factors were high. It is important to note that in none of these works was the fundamental, molecular-level ion transport mechanism altered by the alignment of BCE domains. Instead, differences in conductivity upon different processing conditions represent changes only to the extrinsic conductivity of the film. These studies, therefore, provide no insight into the effects of block copolymer chemistry on the intrinsic material conductivity.

Rather than trying to eliminate defectivity and tortuosity, some researchers have attempted to more precisely quantify the structural factors that impact measured conductivity. If the defectivity and tortuosity of the film could be known precisely, one would be able to analyze effects of the block copolymer interface precisely. Bouchet *et al.* measured a series of PS-*block*-PEO-*block*-PEO triblock copolymers and analyzed the BCE conductivity using a more complex relationship between nanostructure and tortuosity than originally introduced by Balsara and coworkers.[90] By fitting their data to an empirical model based on assumptions about the size and shape of the BCE grains, the authors predicted that an "exclusion zone" of around 1.6 nm at the domain interface did not contribute to conduction. While this value appears sensible and is supported by previous studies of the extent to which crystallization is suppressed by BCP domain boundaries, the assumptions about the structure are impossible to verify.[91] Sharick *et al.* attempted to define the tortuosity factor more precisely by using 2D small angle X-ray scattering (SAXS) to quantify the anisotropy of the BCE domain alignment.[92] Although they were able to demonstrate evidence for the reduction in conductivity near domain interfaces by comparing samples with different molecular weight but similar structural factors, they were unable to provide any quantitative analysis of this interfacial effect.

Due to the complex and unpredictable effects of grain boundaries and microstructure orientation on ionic conductivity of BCEs, quantitative measure of interfacial effects is necessarily limited to systems where single BCE grains can be measured. To date, this kind of analysis has been limited to the domain of MD simulations, although these studies have provided meaningful insight into the problem. Ganesan *et al.* used coarse-grained MD simulations to model PEO and SEO electrolytes, and they observed the same qualitative trends in conductivity with MW that was found experimentally by Balsara and coworkers previously.[93] These simulations modeled only single grains of BCEs, so no effects of grain boundaries or tortuosity were present. This study lent credence to the hypothesis by Balsara that the MW-dependent conductivity of BCEs is an intrinsic property related to the relative thickness of an interfacial layer. Later, more detailed simulations suggested that there may be a heterogeneity in the spatial distribution of ions across the BCE interface, an idea which has some experimental support as well.[94–96] MD simulations alone, however, are often not sufficient to develop predictive models of the macroscopic transport behavior of BCEs. When coupled with experimental studies of the same materials, though, MD simulations can provide deep mechanistic insight into the trends observed by experiment. The work of Hall and Epps exemplifies this approach, where they have used a combination of simulation and experimentation to explore the mechanisms of ion transport in BCEs with gradient composition at the domain interface as well as the self-assembly of nonlinear BCEs.[40,97,98] Such studies would be most meaningful, however, if experimental measurements were made on single-grain structures, identical to those of the simulation environment, from which quantitative values can be taken.

1.2.3 Thin film block copolymer electrolyte measurements

Measurement of single-grain BCE samples has remained an intractable problem in the BCE community due to the inherent limitation in control of BCP microstructure orientation at the length scale of typical bulk samples. For most experiments, BCE films are cast to somewhere between 1 and 1000 µm and annealed before being placed between two parallel plate electrodes for electrochemical measurement. In this configuration, microphase separated grains will necessarily nucleate at multiple locations, leading to a random orientation of grains throughout the resulting film. Various post-annealing alignment methods may improve the degree of alignment, but the dynamics of the system are simply too slow to ever fully remove all of the blocking defects. This problem is intrinsic to the way that these electrochemical measurements are made, and single grain BCE measurements will likely never be made on a bulk sample.

Single grain, perfectly ordered BCPs can be created, however, if the material is cast as a thin film ($<$ 1 µm thick).[99,100] In thin films cast on supporting substrates (often Si wafers, possibly with some surface modification), additional driving forces for self-assembly are introduced. Looking at Equation 1.3 below, the total energy that should be minimized comes from a combination of the entropy of chain stretching (F_{elastic}) and A-B monomer interaction enthalpy ($F_{\text{poly-poly}}$) that are present in the bulk as well as two additional terms arising from the polymer-substrate ($F_{\text{interface}}$) and polymer-free surface interactions (F_{surface}).[101] These additional interface interactions are present in bulk films too, but the length scale over which they propagate into the film is much smaller than the size of a typical free-standing film. In thin films, however, these interfacial terms can large compared to the total energy.

$$F_{\text{total}} = F_{\text{poly-poly}} + F_{\text{elastic}} + F_{\text{interface}} + F_{\text{surface}} \tag{1.3}$$

The interfacial energy terms generally do not alter the morphology or domain spacing of the BCP, but rather they control the orientation of polymer domains. This orientational control for a symmetric, lamellae-forming BCP is illustrated in Figure 1.6. If the interaction energy between one of the blocks and the substrate is substantially lower than that of the other block and the substrate, the lower energy block will preferentially wet the substrate to minimize the total energy of the system.[102] A similar process will occur at the free surface. Preferential wetting at one or the other of the surfaces will induce the lamellar domains of the BCP to orient parallel to the substrate. If both blocks have equal surface energy with a given interface (so-called “nonpreferential wetting”), the lamellar domains will orient perpendicularly to the substrate. Without further orientational control, the perpendicular lamellae will form randomly oriented grains in the in-plane direction, and the top-down image of these structures exhibits a "fingerprint" structure. In the case of preferential wetting, the surface energies are strong driving forces for orientation of the domains, as evidenced by what happens at arbitrary film thicknesses. Only for very specific film thicknesses can equilibrium L_0 and morphology be maintained while ensuring that the lower energy block is in contact with each interface. If the film is not at a commensurate thickness, the free surface will stratify into “holes” or “islands”—topographical features that differ in height from the rest of the film by $1L_0$—to minimize the other energetic constraints of the system.[103,104] For materials that exhibit nonpreferential wetting, the domains can be further oriented by patterning the substrate with guiding stripes that are similar in size and preferential to one of the blocks.[105–107] This “directed self-assembly” (DSA) has been implemented by the Nealey group and others to produce perfectly ordered BCP domains over arbitrarily large surface areas.

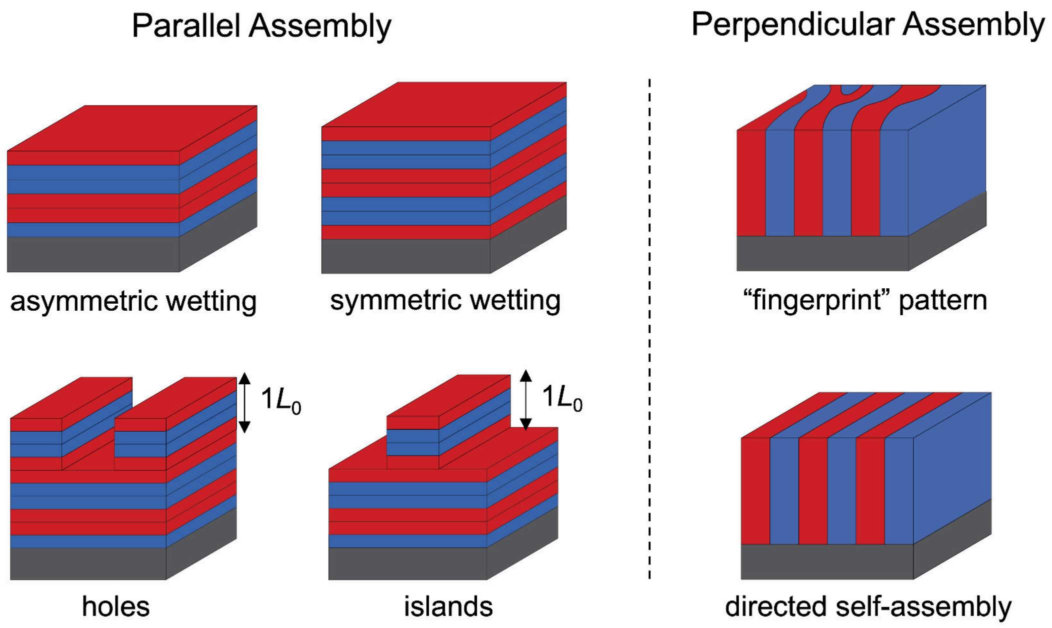

Figure 1.6 – Illustration of self-assembly of block copolymer thin films

Though DSA has been primarily implemented as a technique for lithographic patterning for integrated circuit fabrication, more recently the Nealey group has sought to introduce this technique to the study of BCEs. In a series of recent reports, Nealey and coworkers used interdigitated electrodes (IDEs), devices consisting of an array of electrodes deposited on Si wafers, as substrates for deposition of BCE thin films which could then be electrochemically analyzed.[108–110] Groundwork for this idea was laid by Diederichsen *et al.*, where researchers cast thin films of perpendicularly oriented lamellae on substrates and then selectively replaced one of the domains with Au nanowires.[111] Au contact pads were then added to perform measurements of the BCP-templated nanowire resistivity. By measuring thin films of perpendicularly oriented lamellae, the authors were able to use top-down scanning electron microscopy (SEM) to precisely image the defect structure and tortuosity of the ion conduction network. In doing so, they were able to demonstrate the outsized role that grain boundaries and defects play in reducing the measured conductivity. Arges *et al.* built on this work by instead using IDEs, which offer far higher sensitivity, to directly measure the conductivity of a BCE.[108] Many of the findings of Diederichsen *et al.* were confirmed by this work, but an important step towards measuring a single grain BCE structure had been made. Kambe *et al.* took the further step of implementing DSA techniques to create BCE structures perfectly aligned with the applied electric field.[110] By using patterned trenches (graphoepitaxy), polymer brushes on the substrate surface (chemoepitaxy), and solvent vapor annealing, the authors were able to create a film where the lamellar domains of an ion-functionalized polystyrene-*block*-poly(2-vinylpyridine) (PS-P2VP) were fully connected between the sensing electrodes. By comparing these ideal structures with the randomly oriented samples generated by undirected self-assembly of the BCE, they were able to precisely quantify the extent to which defects reduce measured conductivity. This work represents a fundamentally different approach to the measurement of BCEs, and it opens the door to establishing truly quantitative structure-function relationships.

1.3 Outstanding Challenges in the Field

Rational design of improved SPEs requires deeper insight into the fundamentals of ion solvation, transport, and self-assembly of these materials. New understanding of SPEs may be facilitated by new experimental techniques, such as the use of IDEs to probe polymer thin films, and through combined experimental and compuatational research. Though IDEs have been widely used for various sensing and electrochemical measurements, their application to measurements of SPE ionic conductivity is rather new. As such, there is little theoretical framework or thorough experimental guidelines for the use of IDEs in this application. Significant work remains to be done in the area of thin film BCE electrochemical measurements and in applying the findings of thin film measurements to the understanding of SPEs more generally. The use of IDEs for BCE measurements has also only just begun, and questions remain unanswered regarding ion transport in nanostructured materials. Though Kambe *et al.* were able to create a perfectly aligned BCE structure, the methods for doing so were complex and highly material specific. Only a select few polymers can be readily assembled into perpendicular structures, owing to the strict criteria of equal surface energy between each of the two chemically dissimilar blocks and the free surface. PS-P2VP, which was used by Kambe *et al.*, has been studied extensively for DSA purposes, and the solvent annealing procedures used were already well-established. If the use of IDEs for BCE conductivity measurements is to be generalized to a larger materials library, a different approach to domain alignment must be implemented.

Finally, the ultimate goal of such studies is to gain deeper understanding of ion transport phenomena at the nanoscale and to relate that observed function with the materials structure and chemistry. To date, much of the work in the field of SPEs has emphasized synthesis of new materials chemistries, while insufficient attention has been paid to developing a thorough framework for the physics underpinning the electrochemical performance of these materials. In particular, many of the SPEs investigated in recent years have involved incorporating multiple functional groups. Secondary functional group may consist of linkages between solvating chains, as in the case of bottle-brush or network polymer electrolytes, or they may impart additional desirable materials properties, as in the case of BCEs or single-ion-conducting SPEs. Understanding how charged species interact with each of the functionalities of such a material, and how those interactions affect solvation and transport of ions, becomes increasingly complex as more functionality is imparted to the material. More general understanding of the way materials chemistry affects SPE performance requires further fundamental study of these materials.

1.4 Outline of the Dissertation

This dissertation describes new insights into the study of polymer electrolyte thin films and the fundamental relationships between polymer chemistry, chain architecture, self-assembly, and ion transport. In Chapter 2, some of the important experimental techniques and their theoretical underpinnings are described. In Chapter 3, the microfabrication and theoretical basis for the use of IDEs for thin film EIS measurements are presented in detail. In Chapter 4, the use of IDEs for EIS measurements of thin polymer films is investigated experimentally. First, the relationship between the IDE geometry and the EIS response is explored, and key design parameters are determined. Then, several interesting phenomena related to the thin film geometry are observed and explained.

New insights into the structure-function relationships of BCEs are addressed in depth in the middle part of the dissertation. In Chapter 5, the IDE platform is coupled with parallel assembly of SEO lamellae to demonstrate a universal approach to the measurement of a single grain block copolymer electrolyte. This approach enables a quantitative description of how the ion transport is impacted by the block copolymer domain interface. In Chapter 6, this same BCE thin film platform is used to probe cylinder-forming SEO materials. Due to the asymmetry in the composition and the more complex thin film assembly of cylinder-forming materials, confounding effects of surface wetting and film thickness must be taken into account. This work generalizes some of the findings of previous chapters and describes ways in which this IDE platform may be useful in more practical electrode-electrolyte interface studies.

In the final third of this dissertation, focus is shifted to exploring how polymer chemistry affects the way in which polymers solvate and transport ions. These chapters emphasize using combined experiment and simulation, coupled with recent insight about the importance of solvation site networks, to explore the relationships between ion mobility and polymer architecture. This work is enabled by synthesis of new polymer electrolytes by controlled radical polymerization, as well as molecular dynamics simulations performed by collaborators. In Chapter 7, a series of side-chain polyethers are synthesized and characterized both experimentally and computationally. This work provides new insight into the way such materials form Li^+ solvation sites and how ions move between those sites. In Chapter 8, a family of polyether-polycarbonate copolymers are synthesized and characterized. New understanding of the importance of polymer polarity and chain configurations to the formation of Li^+ solvation sites was gained from this work. Finally, in Chapter 9 the results of this dissertation are summarized, and some outlook on the future of this field are discussed.

Chapter 2

Experimental Techniques

2.1 Electrochemical Impedance Spectroscopy

Electrochemical impedance spectroscopy (EIS) is a powerful and sensitive electroanalytical technique that is used to determine the response of a system to an oscillatory electric field as a function of frequency. This response can be related to the electrochemical properties and processes within the system. Such processes can include, but are not limited to, faradaic reactions, ionic conduction, double-layer charging, and dipole relaxation. By measuring across broad frequency ranges (approx. 1 Hz–1 MHz), different time- and rate-dependent processes can be distinguished. The impedance response of an electrochemical system is commonly analyzed by an equivalent circuit model. In this approach, physicochemical properties and processes are modeled as circuit elements depending on how those processes respond to an applied perturbation. Proper fitting and analysis of impedance data requires a clear understanding of all relevant processes in the system. This section describes the fundamentals of how impedance spectroscopy works as well as the basics of equivalent circuit fitting. Chapter 4 describes in great detail how this technique can be applied to the study of ion conducting polymers, and, in particular, how the analysis of impedance data may differ when polymer thin films are considered. EIS is then used throughout the remainder of this dissertation to determine the ionic conductivity of different materials.

2.1.1 EIS Theory

EIS can be performed by either applying a potential (φ) and measuring a current response (I) (potentiostatic) or applying a current and observing a potential response (galvanostatic). Impedance (Z) is the opposition to alternating current (AC), as given by Equation 2.1 and is analogous to the direct current (DC) expression for Ohm's Law ($R = \varphi/I$). Potentiostatic and galvanostatic EIS measurements should result in identical impedance spectra. Here we will consider the case of a potentiostatic measurement.

$$Z = \varphi(t)/I(t) \tag{2.1}$$

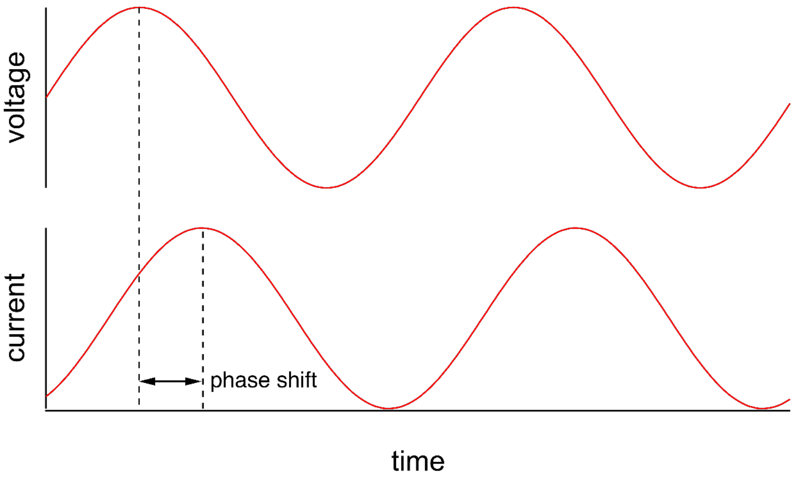

Figure 2.1 – Current response of a linear system to a sinusoidal potential

The response of a linear (or pseudo-linear) system is shown in Figure 2.1. In a linear system, the current response to an applied sinusoidal potential is a sinusoid with the same frequency with some phase shift. The idea of linearity will be discussed in greater detail in a later section. The excitation potential is of the form

$$\varphi(t) = \varphi_0 \sin(\omega t) \tag{2.2}$$

where φ_0 is the amplitude of the perturbation and ω is the angular frequency. The current response for a linear system will be given by

$$I(t) = I_0 \sin(\omega t - \phi) \tag{2.3}$$

where ϕ is the phase shift and I_0 is the amplitude of the current response. The impedance of such a system is then given by

$$Z(t) = \frac{\varphi_0 \sin(\omega t)}{I_0 \sin(\omega t - \phi)} = Z_0 \frac{\sin(\omega t)}{\sin(\omega t - \phi)} \tag{2.4}$$

where the impedance has some magnitude, Z_0, and phase shift.

It is convenient to express the impedance using complex numbers, rather than sinusoids. Because the system is linear, we can add inputs and multiply by constants to get an output that is equal to the sum of the outputs to each input. We can alternatively consider an input wave given by

$$\varphi(t) = \varphi_0[\cos(\omega t) + j \sin(\omega t)] \tag{2.5}$$

Here we use j to represent the imaginary number $\sqrt{-1}$ to avoid confusion with the current density, often represented by i. By expressing the potential input as a cosine wave added to a sine wave scaled by j, we can make use of Euler's formula

$$e^{j\theta} = \cos\theta + j \sin\theta \tag{2.6}$$

to express the impedance as an imaginary number.

$$Z(\omega) = \frac{\varphi_0 e^{j\omega t}}{I_0 e^{j(\omega t - \phi)}} = Z_0 e^{j\phi} = Z_0 \left(\cos\phi + j \sin\phi\right) \tag{2.7}$$

2.1.2 Circuit Elements and Equivalent Circuits

EIS data is typically analyzed by fitting to an equivalent circuit model. These equivalent circuits consist of common electrical circuit elements such as resistors, capacitors, and inductors, as well as some less familiar circuit elements such as the Warburg element. The circuit elements chosen for a model should be based on the physical and electrochemical processes of the system. The choice of an appropriate equivalent circuit for the study of polymer electrolyte thin films is discussed extensively in Chapter 4. In this section, some of the most relevant circuit elements and how they relate to electrochemical phenomena are discussed. The equations for th impedance of the circuit elements used in this work are shown in Figure 2.2.

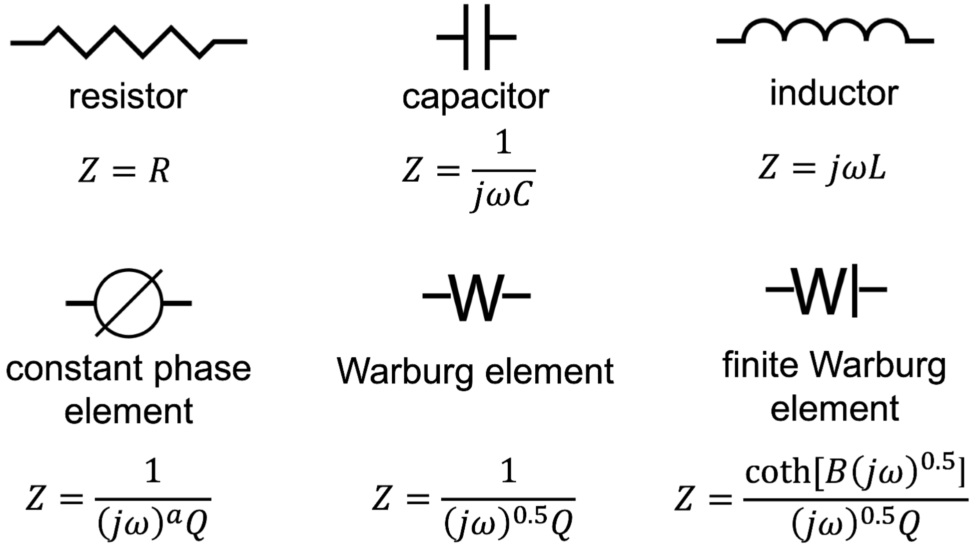

Figure 2.2 – Symbol and impedance for the circuit elements used in this work

Resistors

The impedance of a resistor is simply equal to the value of the resistance, R. Notably, the impedance of a resistor has no frequency, and the current response is in phase with the applied voltage. Resistors can be used describe any electrochemical process that responds in phase with the potential. Of greatest importance to this work is the electrolyte ionic conductivity, which manifests as a resistance in EIS data. Resistors are also commonly used to describe kinetically controlled electrochemically controlled reactions. Intrinsic resistances in the experimental system, such as at connections along the path between the electrodes and the measurement instrument often need to considered in the equivalent circuit model as well.

Capacitors, Inductors, and Constant Phase Elements

Capacitors produce a time dependent relationship between voltage and current governed by $I = Cd\varphi/dt$ where C is the capacitance. The impedance, therefore, has a frequency dependence, and the current is phase shifted by -90°. A capacitor can be used to describe electrochemical phenomena involving the accumulation of charged species in an analogous way to how charge builds up on the surface of a parallel plate capacitor over time as a voltage is applied. In a DC experiment, this charge buildup leads to a voltage drop building up in the opposite direction of the applied field, reducing the current through any resistors in that path. In an AC system, the direction of the electric field is constantly switched, and the charge on either face of a capacitor changes with it. The magnitude of the voltage drop caused by charge accumulation, and therefore the impedance to current flow, is a function of the frequency of the AC potential. Longer buildup time (lower frequency) allows for greater charge buildup, resulting in higher impedance. Capacitors can be used to model processes that explicitly resemble this surface charge accumulation, such as the charging of an electric double layer, or the high frequency reorientation of molecular dipoles.

Inductors have the opposite current-voltage relationship, $\varphi = LdI/dt$, where L is the inductance. When inductance is observed, the current is phase shifted by +90°. Not many electrochemical systems exhibit behavior that should be modeled as an inductor, though an inductance may be observed as a result of experimental setups.

Constant phase elements (CPE) are not conventional electronic circuit elements, but they are commonly employed to model electrochemical systems. They can be thought of as "imperfect" or "leaky" capacitors, where the exponent a in the impedance equation varies from 0 to 1 and describes the nonideality. The closer that a is to 1, the more like an ideal capacitor the CPE is. CPEs are often used to describe the formation of the electric double layer, with the nonideality potentially arising from roughness of the electrode surface. However, physical meaning should not be ascribed to the value of a, and it should instead be treated as a fitting parameter.

Warburg Elements

The Warburg element is a special case of a constant phase element with $a = 0.5$. This corresponds to a 45° phase angle, exactly between the behavior of a resistor and capacitor. This behavior arises from diffusion of charged species in the system. This general form of the Warburg element only applies to systems with an infinite (or semi-infinite) diffusion layer. More common is a system with a finite boundary layer diffusion which is modeled by a so-called finite Warburg element. Two cases of this finite, or bounded, Warburg can be considered, one where the boundary is transmissive and one where it is reflective. In all of the experiments discussed in this work, the electrodes are ion-blocking (*i.e.* there is no faradic charge transfer reaction and they are nonporous), and so the reflective boundary case is appropriate. This reflective finite Warburg is sometimes referred to as a T-element, and the additional $\coth\left[B(j\omega)^{0.5}\right]$ term accounts for the finite boundary layer. Here $B = \delta/D$ where δ is the diffusion layer thickness and D is the average diffusion coefficient of the diffusing species.

Equivalent circuits

Circuit elements can be combined into an equivalent circuit to describe the overall behavior of the electochemical system. As with the choice of the individual circuit elements, the way that circuits are put together must relate to the physcial processes underpinning the EIS response. Figure 2.3 shows a simple equivalent circuit with a resistor and capacitor in parallel. This circuit is a simplified form of the Randles circuit which can be used describe a number of electrochemical systems, such as uniform corrosion of a metal electrode. In such a system, double layer buildup (capacitance) is occuring simultaneously with the charge transfer corrosion reaction (resistance). This simple RC circuit is a common building block for many electrochemical systems.

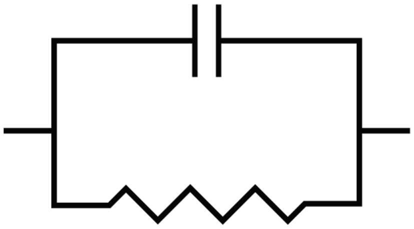

Figure 2.3 – Simple parallel RC circuit

Mathematically, the total impedance of an equivalent circuit can be determined based on the individual elements. Impedances add in the same way as resistors in a DC system, as described in Equation 2.8.

$$\begin{aligned} \text{series: } & Z = Z_1 + Z_2 + ... + Z_n \\ \text{parallel: } & \frac{1}{Z} = \frac{1}{Z_1} + \frac{1}{Z_2} + ... + \frac{1}{Z_n} \end{aligned} \tag{2.8}$$

Looking at the total impedance of an equivalent circuit can provide insight into how it will behave as frequency changes. Because frequency is often varied by six to eight orders of magnitude to obtain an impedance spectrum, capacitive impedance values similarly chage by many orders of magnitude. Resistance values on the other hand, are constant with frequency. Consider the equation for the simple parallel RC circuit shown in Figure 2.3:

$$\begin{aligned}\frac{1}{Z} &= \frac{1}{R} + j\omega C \\ Z &= \frac{1}{1/R + j\omega C} \\ Z &= \frac{R}{1 + j\omega RC}\end{aligned} \tag{2.9}$$

At very high frequencies, the imaginary term in the denominator will be much larger than 1, and the total impedance will approach the impedance of the capacitor alone and the current will be out of phase by -90°. This makes sense physically because at high frequency the charge buildup, and thus the impedance, on the capacitor will be small, and this will be the path of least resistance for any current through the system. At very low frequency, however, the imaginary term will be small (capacitances are typically on the order of nF to µF) relative to the real component. Here, the impedance will be determined entirely by the resistor, and the current will be entirely in phase. At an intermediate frequency, $\omega_\mathrm{c} = 1/RC$, the real and imaginary components are equal, and the current is -45° out of phase. The importance of this cutoff frequency (or its inverse, the RC circuit time constant) to interpretting EIS data is discussed at length in Chapter 4.

2.1.3 Data Visualization

From Equation 2.7, the impedance can be represented either by a magnitude and phase shift ($|Z| = Z_0$ and ϕ, respectively) or by its real and imaginary components (often denoted as Z' and Z'', respectively). Both forms of the impedance are mathematically identical, but different visual representation may be preferred for different purposes. Figure 2.4 shows the Nyquist plot of the parallel RC circuit discussed in the previous section. On a Nyquist plot, the x-axis is Z' (the real component) and the y-axis is $-Z''$ (the imaginary component). The impedance measured at each frequency can be plotted either as a single point or as a vector with magnitude $|Z|$ and angle above the horizontal ϕ. What is not shown, however, is the

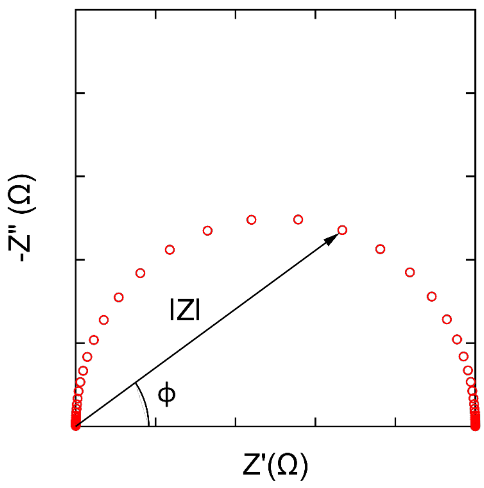

Figure 2.4 – Nyquist plot corresponding to the RC circuit in Figure 2.3

frequency of any of the data points. Typically higher frequency is on the right, and some Nyquist plots will include an arrow indicating the direction of increasing frequency. Some (particularly older) sources may also explicitly note the frequency of a handful of data points. The semicircle motif in the Nyquist plot is characteristic of an RC circuit with a single time constant, and the apex of the semicircle occurs when the angular frequency is equal to the inverse of this time constant. This resistive process could be a charge transfer reaction, ion conduction, or electron conduction, to name a few. Multiple resistive processes occurring in the same system will result in multiple time constants, and therefore multiple semicircle motifs. *Ref.* [112] provides a good understanding of how and why these multiple semicircles might appear in different conductive systems with potentially multiple charge conduction pathways, and this is a good resource for understanding the qualitative impedance spectrum we should expect for a given system.

The other common way of representing impedance spectroscopy data is by a Bode plot, as seen in Figure 2.5. The data shown here is identical to that in Figure 2.4. In the Bode plot (which actually consists of two plots), the magnitude and phase shift of the impedance is plotted as a function of frequency. This direct frequency dependence is the major difference between the Bode and Nyquist representations. In the Bode representation,

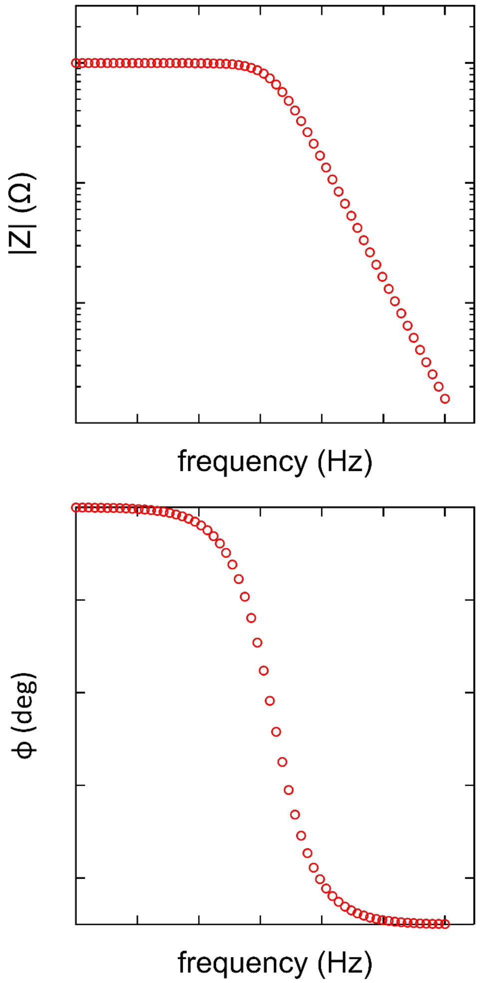

Figure 2.5 – Bode plot corresponding to the RC circuit in Figure 2.3

RC circuit time constants can be seen explicitly from the cutoff frequencies between regions of frequency-dependent and frequency-independent impedance. In the high frequency regime, the magnitude of the impedance decreases with increasing frequency (with a slope of -1 on the log $|Z|$ *vs.* log f), as is expected from a capacitive response. In the low frequency regime where the capacitive impedance is high, the circuit exhibits purely resistive behavior and frequency independent impedance. The point where the resistive and capacitive (real and imaginary) components are equal is evident from the phase plot where the phase shift is 45° and from the magnitude plot where $|Z|$ is equal to half the resistance. The use of either Bode or Nyquist plots to represent impedance data is largely situational and a matter of personal taste. Both depictions have upsides, and both will be used extensively in the rest of the text.

2.1.4 Linearity and Stability

Two critical assumptions made when interpretting EIS are (i) that the response to the input is linear (or pseudo-linear) and (ii) that the system is stable on the time scale of the measurement.

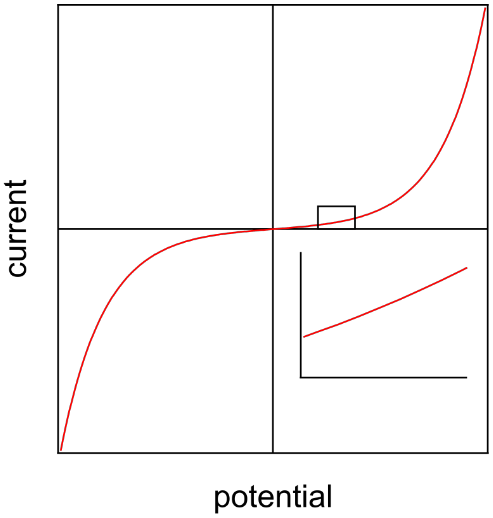

Figure 2.6 – Generic current-potential relationship of an electrochemical system

A linear system is defined by two properties: (a) if the input signal is scaled by a constant, the resulting output is scaled by the same constant; and (b) the output to a sum of input waves is equal to to the sum of the output to each individual input wave. In general, electrochemical systems are not linear in response to an applied potential. Figure 2.6 shows the current response of a generic system as a function of the applied overpotential. Over a wide potential range, the response is clearly nonlinear. Over a sufficiently small potential range, however, the system does appear linear. This is what is meant by pseudo-linearity. The inset to Figure 2.6 shows this idea. In order to analyze the resulting impedance using simple equivalent circuits, it is critical that the system can be accurately assumed to be linear. It is standard to use a very small perturbation (1–100 mV) potential when making impedance measurements. The impedance of a linear system will be independent of the applied perturbation potential. A simple way of confirming the linearity of a system is to measure the impedance at several different voltages and confirm that the resulting spectra are identical. Performing this type of validation test is good practice when beginning study of a new material system or a new cell geometry.

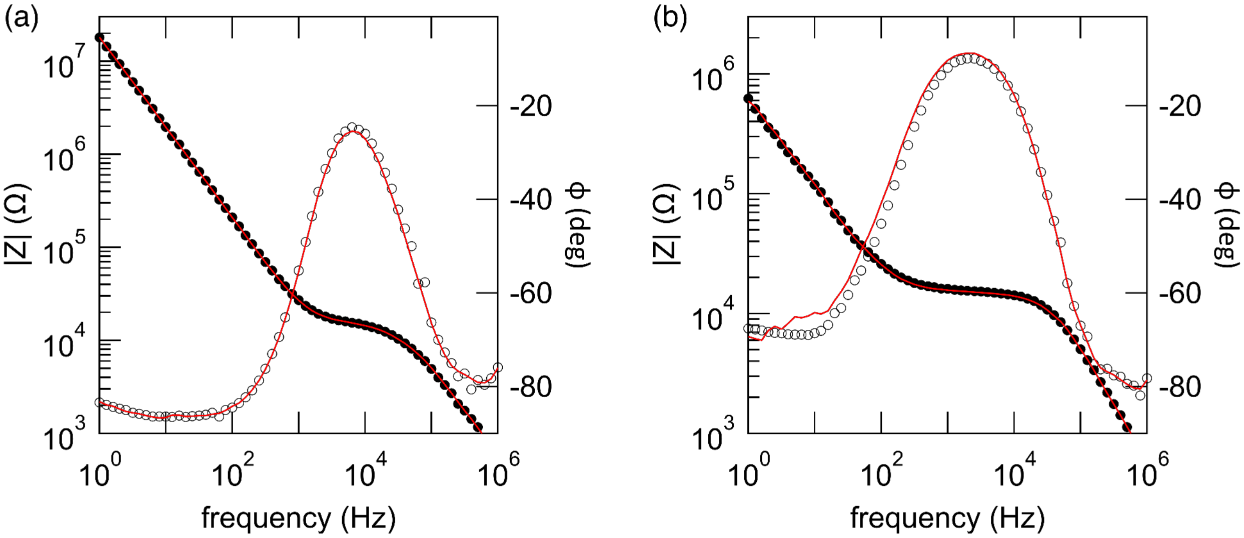

Figure 2.7 – Kramers-Kronig fitting to (a) a stable system and (b) an unstable system

The system under investigation must stable, *i.e.* at steady-state, throughout the time frame of the measurement. Instability can arise from a number of electrochemical or adsorption processes, or, as is most likely in the measurement of polymer electrolyte conductivity, thermal instability. If the temperature drifts or the system has not been properly equilibrated before the measurement begins, the resulting impedance will be inaccurate. There is a straightforward way to evaluate the stability of an impedance spectrum. Any impedance spectrum measured from a system that is stable and linear will follow the Kramers-Kronig relations. The Kramers-Kronig relations connect the real and imaginary components of any complex analytical function. This has application to a number of systems in physics, including complex refractive index and relative permittivity (and thus complex impedance). One can evaluate the stability of an impedance spectrum by performing the Kramers-Kronig transform to the real component of the spectrum and comparing to the measured value. Unfortunately, performing this analysis requires integrating from a frequency of zero to infinity. The Gamry Echem Analyst software provides a convenient way of applying this analysis in practice, though. By fitting to an arbitrary model that is Kramers-Kronig compliant, we can get a sense of how stable the measurement was. Figure 2.7 shows this fitting for a common polymer electrolyte system. In Figure 2.7a, the fit to the Kramers-Kronig model is good across the entire frequency range, and the spectrum appears stable and linear. In Figure 2.7b, however, the model fits poorly in the lower frequency range. Clearly, the system was not stable on the timescale of the measurement, and therefore equivalent circuit fitting of the data will not provide useful analysis. Performing this quick and simple test for stability on at least one dataset per sample is always good practice. Furthermore, stability should always be checked before any additional circuit elements are added to explain deviations from the expected impedance response. The idea is discussed further in Chapter 4.

2.2 Small-Angle X-ray Scattering

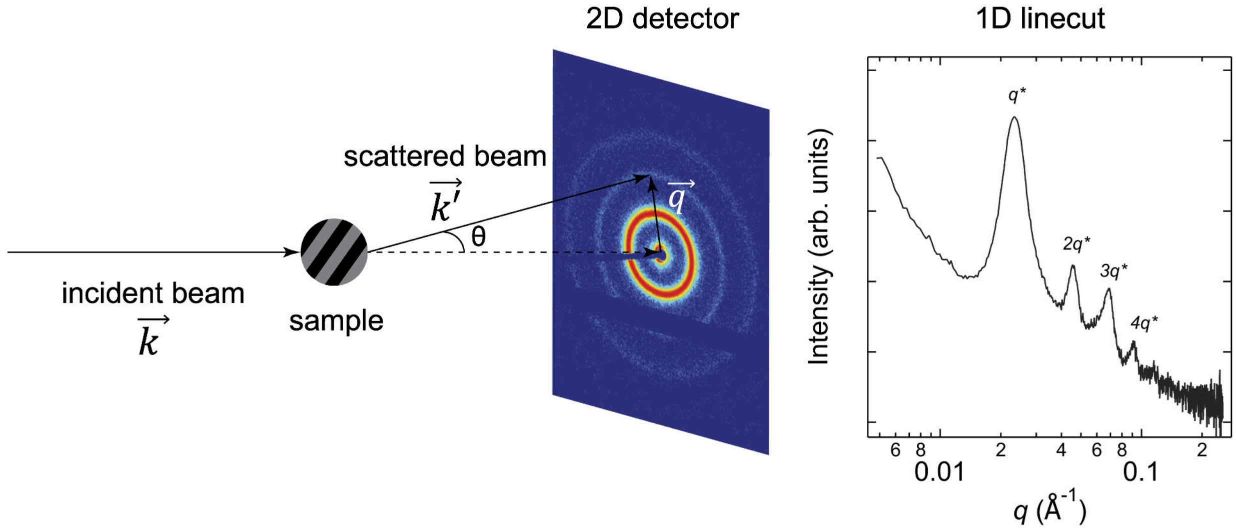

Figure 2.8 – Schematic of SAXS experiment. Incident photons with momentum $\overrightarrow{k}$ are elastically scattered by electrons in the sample. Outgoing photons with momentum $\overrightarrow{k'}$ are collected over a range of q values by a 2D detector. Scattering peaks are analyzed by converting to a 1D plot of scattered intensity *vs.* q.

Small-angle X-ray scattering (SAXS) is a common technique for probing the nanostructure of a material, and it is used extensively in the study of block copolymers (BCPs). Figure 2.8 shows a schematic of a SAXS measurement. An incident beam of X-rays with momentum $\overrightarrow{k}$ and some energy (or wavelength, λ) is targeted at a sample. Some of the incident X-rays are scattered by the sample by some angle (θ). The scattered light has some new momentum $\overrightarrow{k'}$. In the case of SAXS, scattering events are elastic, meaning that there is no transfer of energy between the incident photons and the sample.

The scattering vector, $\overrightarrow{q}$ is defined as the difference between the scattered and incident wave vectors.

$$\overrightarrow{q} = \overrightarrow{k'} - \overrightarrow{k} = \frac{4\pi \sin\theta}{\lambda} \tag{2.10}$$

The magnitude of $\overrightarrow{q}$ (q) is in units of inverse length as $\overrightarrow{q}$ is related to the reciprocal lattice of the sample. Real space (or d-space) distances are related to $\overrightarrow{q}$ by $d = 2\pi/q$. The range of q values accessible during a scattering experiment depends on the distance between the sample and the detector. In SAXS measurements, the detector is often around 1 m away from the sample, and only scattered photons with very low θ are detected (hence, small-angle scattering). These small-angle scattering vectors correspond to real space feature sizes on the order of 1-100 nm. The related technique of wide-angle scattering (WAXS) is performed the same way except with the detector much closer to the sample. With WAXS measurements, high q value scattering events are detected, and feature sizes on the order of 1 Å can be measured.

Generally, measurements detect scattered light over the full range of q values accessible to the 2D detector. In ordered systems, peaks in the intensity of the scattered beam arise at q values corresponding to the periodicity of the sample. This 2D image is then often converted to a 1D plot of intensity *vs.* q, as shown in Figure 2.8. In microphase separated block copolymer (BCP) systems, the primary scattering peak, q^* occurs at $2\pi/L_0$, where L_0 is the domain spacing of the BCP. The full-width half-maximum of the primary scattering peak corresponds to the average grain size of the sample, with narrower q^* peaks corresponding to larger grain size. Bragg reflections of the q^* peak appear at multiples of L_0 depending on the morphology exhibited by the BCP.[113] The scattering peaks present for different morphologies is summarized in Table 2.1. The 1D scattering profile shown in Figure 2.8 was taken from a lamellae-forming BCP sample. The morphology is evident from the Bragg reflections only at integer multiples of the primary peak.

Table 2.1 – Peak position of Bragg reflections for different BCP morphologies

Morphology	q/q^*
LAM	$1, 2, 3, 4, 5, \ldots$
HEX	$1, \sqrt{3}, \sqrt{4}, \sqrt{7}, \sqrt{9}, \sqrt{12}, \ldots$
GYR	$1, \sqrt{4/3}, \sqrt{7/3}, \sqrt{8/3}, \sqrt{10/3}, \sqrt{11/3}, \ldots$
BCC	$1, \sqrt{2}, \sqrt{3}, \sqrt{4}, \sqrt{5}, \sqrt{6} \ldots$

2.2.1 *Silicon nitride membranes*

The simplest way to make a SAXS measurement of a BCP is to use a solid chunk of the material. For much of the work in this dissertation, however, most SAXS measurements were made on block copolymer electrolytes (BCEs). BCEs were prepared by mixing a BCP solution and a salt solution. The resulting BCE solution could then be cast onto various substrates for different measurements. While large enough amounts of material could be cast to make a standard bulk SAXS sample, as the material is dried from the solution phase it is often much less manageable than the neat polymers recovered by precipitation (as described in the preceding section). Instead, it was more convenient to cast BCE films onto suspended silicon nitride windows, as depicted in Figure 2.9.

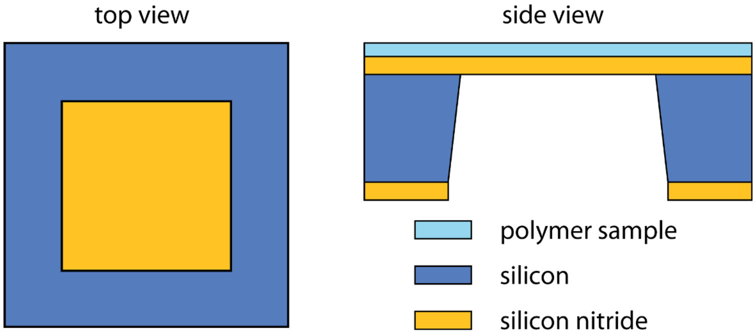

Figure 2.9 – Top-down and cross-section view of silicon nitride windows used for bulk SAXS measurements

These substrates consist of a 2.5 mm × 2.5 mm area of 100 nm thick amorphous silicon nitride suspended by a 5 mm × 5 mm silicon wafer support. The windows were fabricated in-house according to the procedure described by Ren *et al.*[114] Briefly, 535 µm thick silicon wafers coated with 100 nm silicon nitride on each side were oxygen plasma cleaned and coated on one side with a positive photoresist. The 2.5 × 2.5 mm^2 window area of a 10 × 10 array of windows was patterned using the Heidelberg MLA150 Direct Write Lithographer, along with guidelines for cleaving the wafer in the future. The patterned area was then etched through the silicon nitride by a fluorine plasma reactive ion etch to expose the silicon beneath. After removing the residual photoresist, the wafer was placed in a 85 °C bath of 30 wt % KOH in water. The KOH selectively etches the silicon while not affecting the silicon nitride. The wet etch is allowed to continue until reaching the silicon nitride on the backside, leaving a suspended silicon nitride window. These substrates were used for all of the SAXS measurements of BCEs described in Chapter 5, 6, and 8.

2.2.2 Grazing-incidence small-angle X-ray scattering

Grazing-incidence small-angle X-ray scattering (GISAXS) is an important subset of SAXS measurements for the study of nanostructured thin films. In GISAXS measurements, the incident beam strikes the sample, often a film on a silicon substrate, at an angle close to the critical angle for total reflection (around 0.18° for Si at 11 keV X-ray energy). The reflected and scattered beams are again detected by a 2D detector, but this time giving information about the orientational anisotropy of the sample within the film. Unlike in bulk SAXS measurements where scattering in all directions is detected and randomly oriented grains produces circular scattering peaks, GISAXS provides information about different nanostructure orientation in the in-plane and through-plane dimensions. Scattering intensity in the vertical direction (q_z) corresponds to ordering in the through-plane direction (such as parallel oriented lamellae), whereas scattering in the horizontal direction (q_y) corresponds to ordering in the in-plane direction (such as perpendicular lamellae). This technique is particularly useful for the study of block copolymer thin films, and GISAXS can be used to determine perpendicular *vs.* parallel assembly of the material. GISAXS is used in Chapter 6 to verify the orientation of a cylinder-forming block copolymer material.

2.3 RAFT Polymerization

A number of controlled chain growth polymerization techniques have been developed to synthesize polymers with narrow dispersity (Đ) and living chain ends to grow additional blocks. These techniques can be based on anionic, cationic, or radical reaction mechanisms. One of the most accessible and straightforward of these controlled growth reactions is reversible addition-fragmentation chain transfer (RAFT) polymerization.[115] RAFT is a form of controlled radical polymerization that has exploded in popularity since it was first introduced in the late 1990s.[116] This technique is highly versatile and can be used to polymerize styrenes, acrylates, methacrylates, acrylamides, and many other vinyl monomers.The reaction mixture consists of the monomer to be polymerized, a radical initiator, such as azobisisobutyronitrile (AIBN), and the RAFT agent (or chain-transfer agent, CTA). The RAFT agent is of the form Z−C(=S)S−R, where the choice of Z and R groups affect the compatibility with different monomers as well the rate of reaction and dispersity. The Z group affects the addition and fragmentation rates, while the R group primarily affects the rate of reinitiation. The Z group is often a phenyl ring (for dithiobenzoates CTA) or an alkyl thiol (for trithiocarbonates). The R group is chosen such that it can reversibly reinitiate the polymerization reaction. A common R group for CTA is one similar to the radical product of AIBN, making it a good homolytic leaving group and initiating species.

The general RAFT reaction scheme is shown in Scheme 2.1. First, radicals are formed by the initiator (I). These radicals react with the monomers in the system to form a growing polymer chain (II). These growing polymer chains can then react with the CTA to form dormant CTA-terminated polymer chains (III). This dormant species can in turn reversibly react to form a nonradical CTA terminated polymer chain and a radical R group, which can then initiate new chain growth (IV). These new chains enter an equilibrium between dormant and active species, where propagation occurs on the active chain ends (V). Importantly, the propagation reaction is slow relative to the addition-fragmentation equilibrium reaction, so

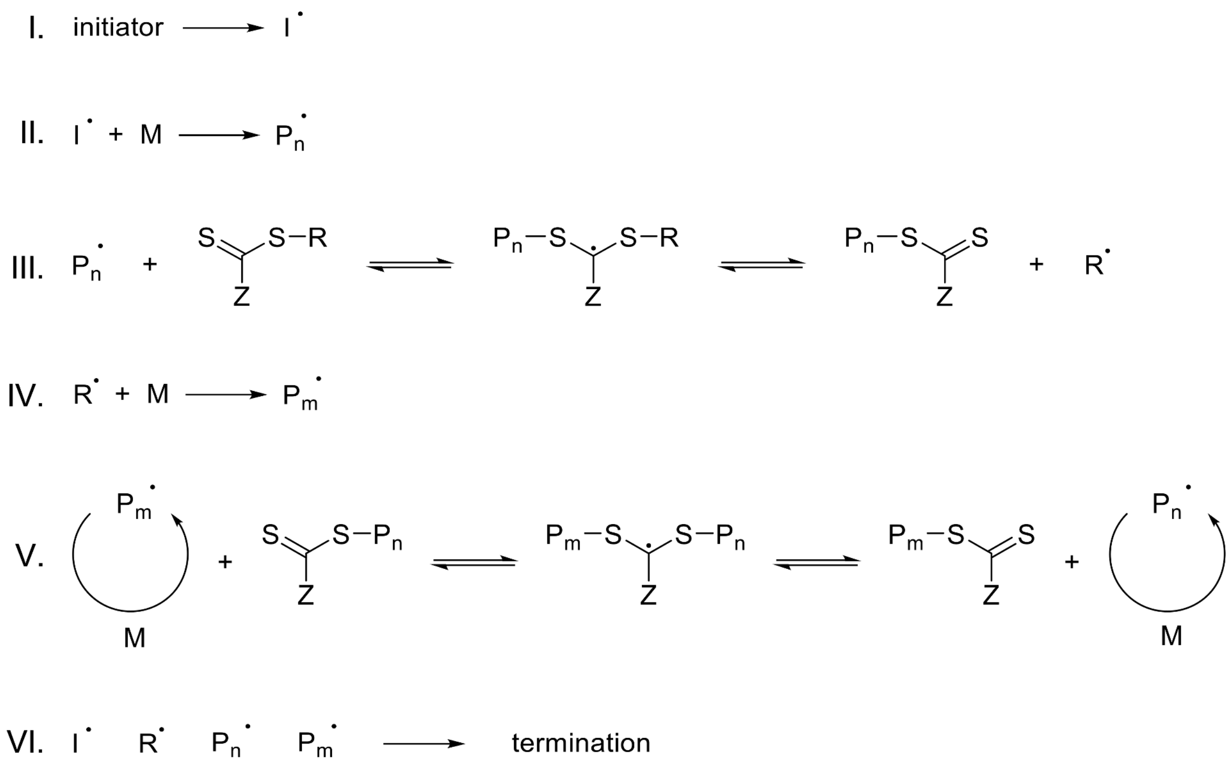

Scheme 2.1 – Generic RAFT reaction mechanism

chains grow at roughly the same rate. This fact is crucial to producing a low molecular weight dispersity. Finally, the radical chains can terminate by reaction with radical initiator products, other radical terminated polymers, or radical R groups (VI). The first two of these termination reactions results in so-called "dead" chains which cannot be reinitiated. Those chains terminated by R groups, however, are living, and they can be reinitiated. These chains are polymers where the CTA R and Z groups are the α and ω end groups. These chains can act as "macroCTA" for the reinitiation of a second block. The remaining chains are not able to reinitiate. By keeping the ratio of radical initiator to CTA low (typically 1:5 or 1:10), the fraction of living chains in the material is high. The number of polymer chain coupling termination events can be kept to a minimum by keeping the monomer conversion relatively low (50–70%).

There are a number of reaction conditions that can be considered for improving the control of the polymerization. The RAFT reaction can be done in bulk, though the use of solvent can often produce lower Đ by reducing the number of chain termination events.[116] A lower initiator:CTA ratio can also improve Đ by reducing the rate of chain termination by initiator. It is also critical to any radical polymerization that the system be oxygen free. This can be achieved by the common freeze-pump-thaw process, where the reaction vessel is degassed at cryogenic temperatures. In practice, this is often not necessary, and the less laborious practice of simply sparging the reaction mixture with dry nitrogen is sufficient. The freeze-pump-thaw method is much better at removing residual water in the system, which is imperative for anionic polymerization. For radical polymerization, however, this is not nearly as big of a concern, and no difference in the dispersity was noticed between these two methods. In this work, all polymerization reactions were prepared by sparging with nitrogen. Monomer, initiator, and CTA were dissolved in solvent at approximately 1 M monomer concentration. CTA and initiator concentration are chosen to target a particular molecular weight at 50–70% conversion. The solution is stirred to dissolve in a round bottom flask, topped with a rubber septum, and then a long needle is pushed through the septum and under the reaction solution and a smaller outlet needle was placed in the septum as well. Nitrogen is bubbled through the solution while stirring for 20 minutes before removing the outlet needle. The reaction can then proceed either with a constant overpressure of nitrogen, or more commonly, after removing the needle. The temperature of the reaction is also a key factor in controlling both the reaction rate and the dispersity. The temperature should be sufficiently high for the radical initiator to decompose quickly (often about the 10 hr half life of the initiator). However, slower propagation reaction at lower temperature can improve the livingness of the resulting polymer. For AIBN initiated reactions, 65 or 70 °C was often chosen as a balance between these two factors.

Another important reaction parameter is the choice of solvent, if any. Many reactions can be done neat, with the remaining monomer serving as the solvent for the growing polymer chains. For POEM, the reaction mixture can become highly viscous as the polymerization proceeds, so it is preferable to use a solvent. Introducing a solvent lowers the concentration of all species in the system, and therefore reduces the reaction rates. RAFT polymerization tends to follow first-order reaction kinetics, as shown in Figure 2.10 below. Lowering the monomer concentration will decrease the polymerization rate, but it can also help keep dispersity low by lowering the rate of chain termination reactions. The solvent chosen should be a good solvent for all monomers in the system as well as the resulting polymers. This can be challenging in the case of block copolymerization where each block may dissolve in very different solvents. Tetrahydrofuran (THF) and dimethylformamide (DMF) were commonly used for RAFT polymerization of various monomers.

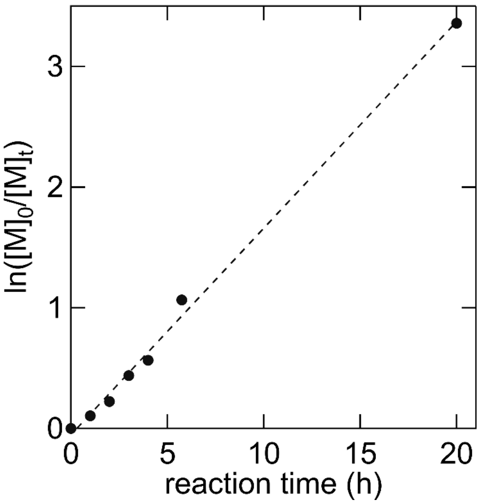

Figure 2.10 – Kinetics of RAFT polymerization of POEM. Remaining monomer concentration $[\mathrm{M}]_\mathrm{t}$ was determined by ^{1}H−NMR. Linear fit to this plot (dashed line, $R^2 = 0.993$) is indicative of first-order kinetics.

2.3.1 Polymer purification

Polymers are commonly purified from residual monomer by dissolving the crude reaction product in a small amount of solvent and then adding the crude solution to a large excess of another solvent. This excess solvent should be a good solvent for the monomer and any other remaining impurities, but it should be a nonsolvent for the polymer product. Importantly, the two solvents must be highly miscible. When the crude product solution is added to excess solvent, the polymer will precipitate out while the monomer and initial solvent stay in the liquid phase. This can then be poured off and a purified polymer can be recovered. This is typically repeated three times to achieve high purity of the polymer product. For polymerization of many common polymers (polystyrene, poly(methyl methacrylate), poly(glycidyl methacrylate)), the standard is to use THF as the solvent for the polymer mixture and methanol (MeOH) as the nonsolvent. For POEM, unfortunately, MeOH is a good solvent for the polymer as well. Moreover, many of the nonsolvents for the polymer (hexane, and other nonpolar solvents) were also nonsolvents for the polymer. One combination that does work reasonably well is using THF as the polymer solvent and precipitating from excess diethyl ether, or a mixture of diethyl ether and hexanes. However, the ether is not a perfect nonsolvent for the polymer, and some of the product tends to be lost during this process.

2.4 Fourier Transform Infrared Spectroscopy

Fourier transform infrared spectroscopy (FTIR) is a technique used to measure the absorption or transmission spectrum of a sample over the infrared frequency range. Each molecule or functional group has a characteristic IR spectrum based on its vibrational modes. Specifically, FTIR is sensitive to vibrational modes that result in changes in the moleuclar dipole moment, such as the asymmetric stretch of CO_2. This allows for fairly straightforward characterization of the chemical composition of unknown samples by this technique. This can also be used, as in this dissertation, to determine the extent of reaction or functionalization of a particular functional group. Additionally, absorption peaks can be shifted by small amounts if a given functional group interacts with another species in the system that changes the effective bond length, and therefore the vibrational frequency. This is of particular interest for analyzing which groups interact with ions in an electrolyte system, and this technique is used extensively in Chapters 7 and 8.

Most FTIR instruments work by shining a broad spectrum light source into a Michelson interferometer, directing the light onto the sample, and measuring how much light is absorbed at each frequency. This measurement is repeated with different sets of frequencies until a full spectrum is recorded. The data as a function of the Michelson interferometer mirror position (in cm) is converted to a function of wavenumber (cm^{-1}) by Fourier transform. The Shimadzu IRTracer-100 instrument used in this work functions in this way.

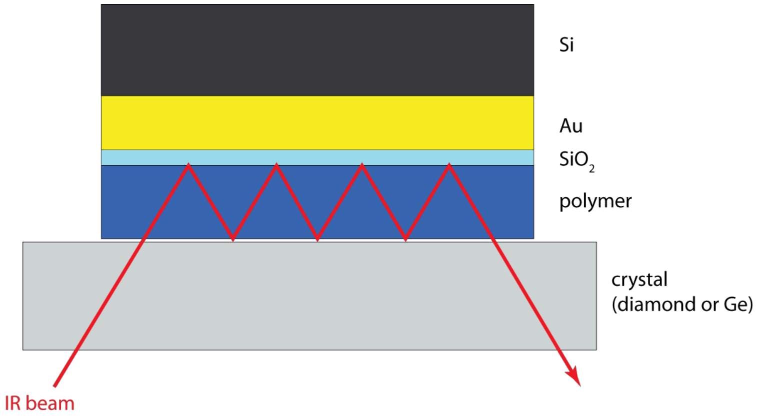

Figure 2.11 – Illustration of thin film ATR-FTIR measurement

FTIR can be performed by either measuring transmission of light through a bulk sample or by reflection of light using attenuated total reflection (ATR). In the ATR configuration, the sample is placed on top of a crystal and IR light is passed through the crystal and directed upwards at the sample. This produces an evanescent wave with a penetration depth of around 1 µm. After reflection off of the sample, the outgoing beam is attenuated at the frequencies where the material is IR absorbing. Importantly, the crystal should be of higher refractive index than the material being measured to achieve total internal reflection. In this work the crystal used was either diamond or germanium. While diamond produces high quality results for many IR wavelengths, it has a broad phonon band between 1900 and 2600 cm^{-1} that can produce noise in this range. The Ge crystal tends to produce higher quality results.

2.4.1 ATR-FTIR Sample Preparation

ATR-FTIR can be performed on bulk samples, powders, or thin films. In this work, thin film measurements were performed for all measurements. This technique allows for relatively small amounts of material to be used, and electrolyte solutions that were prepared for spin casting on IDEs can be used without alteration for preparation of FTIR samples. Common Si and SiO_2 substrates are not ideal for use with ATR-FTIR. Both materials are IR transparent across much of the frequency range of interest (400–4000 cm^{-1}), and the signal from the thin film coating would be negligible. Instead, it is recommended to use an IR reflective substrate, such as Ag or Au. For all of the work done in this dissertation, substrates were prepared by first depositing a 5 nm Ti adhesion layer on a Si wafer, then depositing 95 nm of Au as a reflective coating. Some of the materials studied do not wet a gold surface particularly well. In such cases, a roughly 1 nm layer of SiO_2 can be deposited by ALD to create a hydrophilic substrate. This small amount of silica does not meaningfully affect the data collected. A schematic of this sample configuration is shown in Figure 2.11. Before collecting the sample data, a background scan of the Au coated Si should be taken. The measurement of these thin films can produce relatively noisy and weak signal. This can be improved greatly by taken a larger number of scans. Taking between 64 and 128 scans has produced high quality data for polymer films of around 50 nm on these substrates.

2.5 Raman Microscopy

Raman spectroscopy is another technique used to probe the vibrational and rotational modes of the molecules in a system. Although it probes similar energy ranges to FTIR, it relies on fundamentally different principles. Unlike FTIR, which probes absorption of IR radiation by the sample, Raman spectroscopy measures inelastic scattering of photons (referred to as Raman scattering). This inelsatic scattering occurs when an incident photon is absorbed and excites a molecule and is then emitted at a higher or lower frequency than the incident photon. This effect is only present for vibrational modes where there is a change in the polarizability of the molecule, such as the symmetric stretch of CO_2. Modes that are Raman active are often, though not always, FTIR inactive, and vice versa. For this reason FTIR and Raman are complementary techniques and provide different information about the material in question.

Inelastic scattering events are relatively rare compared to elastic, or Rayleigh, scattering, and therefore the intensity of Raman signal tends to be very weak. To produce sufficiently high scattered photon counts to get a high quality spectrum, greater sample mass, higher laser intensity, and longer exposure time can be used. In this dissertation all Raman experiments were done using the same Au-coated Si substrates used for FTIR measurements. Si can also be used, but it exhibits a very strong Raman peak at 521 cm^{-1} which can overshadow the relatively weaker Raman scattering from the polymer film. SiO_2 or glass substrates could be used, but they also exhibits a number of peaks and broad bands in the regions of interest to polymer electrolyte study. Au exhibits little background signal in the relevant frequency ranges, and high quality spectra of many materials have been produced on these substrates. Raman samples are prepared by drop casting polymer solutions onto the gold substrates and heating on a hot plate to remove solvent. This produces films on the order of several microns thick which provides sufficient material to produce high Raman intensity.

Raman measurements are done using a monochromatic laser, often in the visible or near IR range. The laser should be chosen such that the material under investigation does not absorb or fluoresce at that wavelength. The Horiba LabRAM HR Evolution Confocal Raman Microscope used in this work is equipped with lasers at 473 nm, 532 nm, 633 nm, and 785 nm. The lower wavelength 473 nm and 532 nm lasers were found to produce a broad fluorescence background on many of the polymer samples studies. The 785 nm laser does not produce fluorescence, but the relatively lower power of this laser makes achieving sufficient Raman intensity difficult. The 633 nm laser was therefore used for all of the measurements presented in this work. A high laser power (50–100%) and long aquisition time (> 10 minutes) was necessary to produce high quality spectra. For some materials, this may cause the sample to burn or degrade, so care should be taken when using such high power and exposure times.

2.5.1 *Fitting Raman Data*

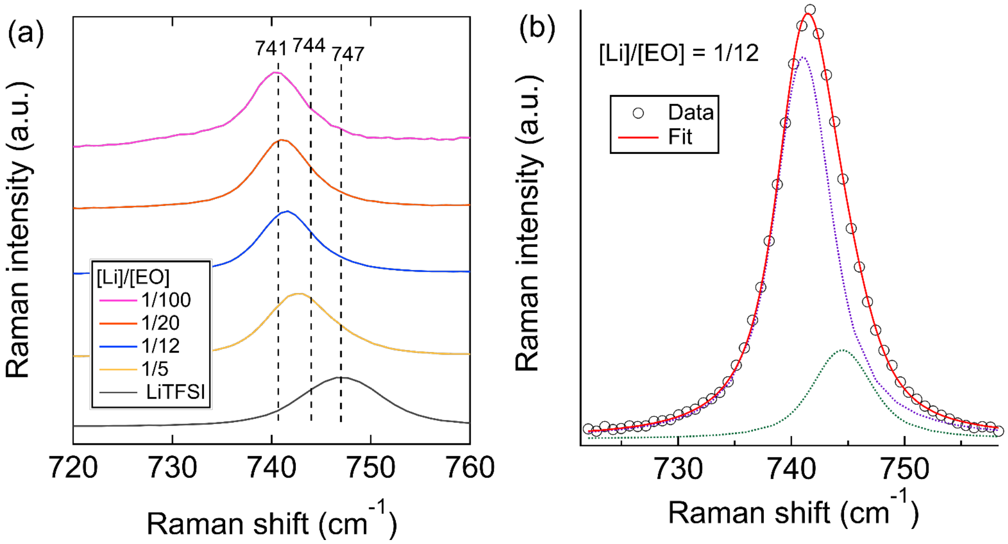

Figure 2.12 – (a) Raman spectra of PEO with various concentrations of LiTFSI salt and (b) fitting of "free" and "associated" TFSI ion peaks

As with FTIR data, Raman data can be interpreted qualitatively by the presence and location of various peaks. Figure 2.12a shows the shift of the Raman peak at 741 cm^{-1} to higher wavelength as the salt concentration of the PEO-LiTFSI electrolyte is increased. A peak around 741 cm^{-1} corresponds to a fully dissociated TFSI anion (a "free" ion), whereas a peak at 747 cm^{-1} corresponds to TFSI tightly coordinated with Li^{+}, as exemplified by the spectrum of LiTFSI salt at the bottom of Figure 2.12a. An intermediated state corresponding to partial solvation of Li^{+} by the polymer and weak association between Li^{+} and TFSI^{-} (contact ion pair) exhibits a peak around 744 cm^{-1}.[117] Samples with intermediate salt concentration exhibit a peak center somewhere between 741 and 744 cm^{-1}, suggesting a mixture of associated and dissociated ions.

Fitting or deconvoluting this peak into a free and associated peak, centered at 741 and 744 cm^{-1}, respectively, can provide a quantitative measure of the fraction of dissociated ions in the system. An example of this fitting is shown in Figure 2.12b. The free anion peak at 741 cm^{-1} and the contact ion peak at 744 cm^{-1} are each fit to Voigt peaks after subtracting a linear baseline. In theory, the transitions between different vibrational states of a molecule should occur at single, quantized energies (frequencies). In practice, however, all molecules in the system are surrounded by and interact with other molecules, resulting in a broadening of the vibrational transitions. This broadening can be modeled with either Gaussian or Lorentzian profiles, depending on specifics of the system. For solid systems, the molecules tend to vibrate coherently, and Gaussian fitting is most appropriate. For gas states, decoherence begins before most excited molecules relax to the ground state, and the peak shape is Lorentzian. Liquids systems lie somewhere between these two, and combined Gaussian and Lorentzian profiles are most appropriate. Additionally, Gaussian characteristic may arise from broadening by the instrumentation, such as the mirrors and detectors. Voigt profiles are a convolution of Gaussian and Lorentzian profiles that tend to fit polymer electrolyte systems well. As with all fitting, only peaks with physical meaning should be included in the fit. Here, only two peaks are necessary and make physical sense. The inclusion of additional peaks may reduce the overall error of the fit, but it would not provide a more accurate description of the system. Once the Raman spectrum has been fit to reasonable peaks, an estimate for the fraction of free ions in the system can be taken as the area of the free ion peak divided by the total area of the anion peak. This type of analysis is employed extensively in Chapters 7 and 8 to compare the solvation capability of different materials.

Chapter 3

Fabrication and Use of Interdigitated Electrodes for Thin Film Impedance Measurements

All of the electrochemical measurements made as part of this work were performed using interdigitated electrodes (IDEs) that were spin coated with thin ($>$ 200 nm) thin films. This chapter describes the experimental setup and the custom probe station designed for these measurements. A detailed description of the IDE microfabrication process is also given. Finally, the IDE cell constant, which is used to relate the measured resistance of a thin film to the material conductivity, is derived in detail.

3.1 The Experimental Setup

The IDEs used for electrochemical impedance spectroscopy (EIS) measurements were mounted on a custom-built heating stage inside of an argon or nitrogen glovebox (shown in Figure 3.1) and connected to a Gamry Reference 600+ potentiostat. The heating stage consists of an aluminum block with two heating rods and a thermocouple probe inserted into the side. The heating rods are connected to an external temperature controller. Two tungsten probe tips connected to the working and counter/ reference electrodes of the potentiostat, respectively, are used to contact the two large pads of the IDEs, each of which is electrically connected to one half of the interdigitated array of electrodes.

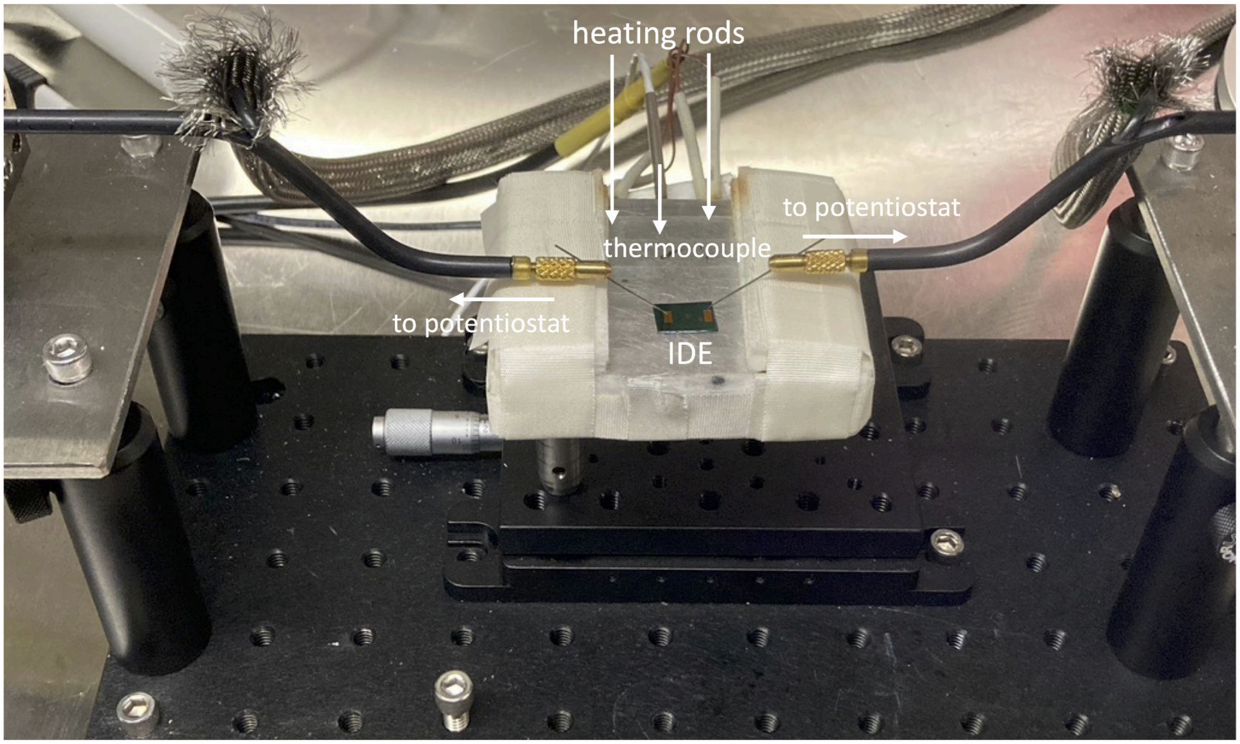

Figure 3.1 – Custom-built heating stage for connecting IDEs to potentiostat for electrochemical measurements

3.2 Interdigitated Electrode Fabrication

All of the IDEs used in this work were microfabricated in-house in the Pritzker Nanofabrication Facility (PNF). IDEs can be purchased commercially, but by fabricating our own we were able to control the geometry of the devices and the process conditions more precisely. IDEs can be fabricated on any insulating substrate, but for this work Si wafers with 1 µm thermal oxide were used exclusively. IDEs have also been successfully fabricated by the same process on quartz wafers for applications where an optically transparent substrate was desirable. Two generations of IDEs were used in this work. Initially, electrodes were created by first lithographically defining the electrode area, etching into the underlying oxide layer, and depositing the metal electrodes by electron beam (e-beam) evaporation. This process is briefly depicted in Figure 3.2.

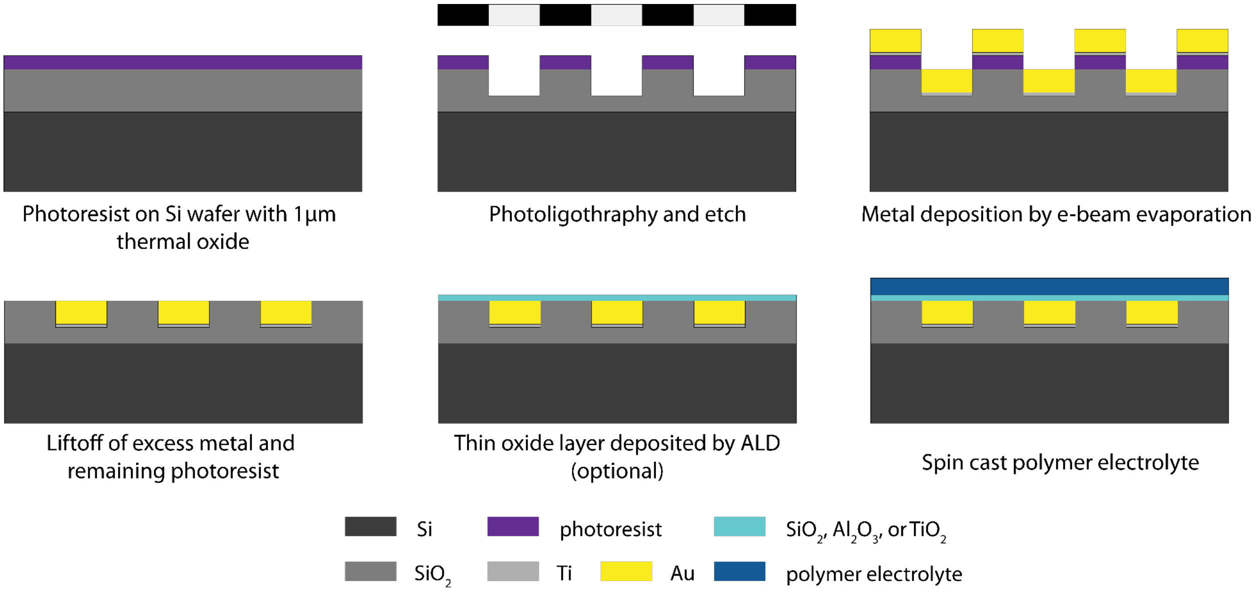
Photoresist on Si wafer with 1µm thermal oxide

Photoligothraphy and etch

Metal deposition by e-beam evaporation

Liftoff of excess metal and remaining photoresist

Thin oxide layer deposited by ALD (optional)

Spin cast polymer electrolyte

Figure 3.2 – Process flow diagram for fabrication of IDEs using positive photoresist

The process shown in Figure 3.2 was performed using the positive resist AZ 703. With positive resist the area exposed to UV light—here, the 405 nm laser using the Heidelberg MLA150 direct write lithography tool—is degraded and made soluble in developer (AZ MIF 300, a dilute solution of tetramethylammonium hydroxide). After development the sidewall structure tends to be vertical. This pattern is then transfered into the substrate by etching 100 nm deep using a reactive ion etch using fluorine chemistry. Next, metal was deposited by e-beam lithography. First, a 5 nm adhesion layer of Ti was deposited, followed by 95 nm of Au. Finally the remaining resist and excess metal were removed by liftoff in a 80 °C *n*-methyl-2-pyrrolidone (NMP). IDEs can then be optionally coated with a thin oxide (SiO_2, Al_2O_3, or TiO_2 were used) before spin casting a polymer electrolyte film.

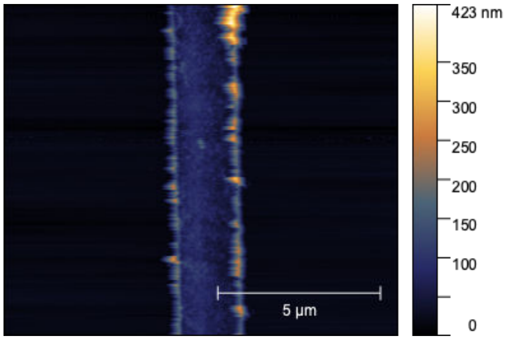

Figure 3.3 – AFM height map of an electrode produced by etching and backfilling with metal by e-beam evaporation

This process produces high quality devices, and all of the data reported in Chapter 3 of this dissertation were taking using devices made in this way. The problem with this approach, however, comes from the use of positive resist and an etching step. In order to ensure that metal is deposited uniformly inside of the trenches, the substrate is rotated during the deposition step. This results in conformal coating of the trench and resist sidewalls. During the liftoff process, the connection between the metal in the trench and the metal on the resist sidewall is torn, resulting in uneven metal accumulation at the edge of the electrode. This can be seen in the atomic force microscopy (AFM) image shown in Figure 3.3. While this is not a major issue when measuring homopolymer films, there were concerns about how block copolymer thin films would assemble on these rough electrode edges. To mitigate any possible issues, an alternative fabrication process was developed. In this process, a negative resist was used to produce an undercut resist profile. The etching step was then avoided altogether, and electrodes were simply deposited directly on the oxide surface. Due to the undercut and lack of substrate rotation during deposition, there is no buildup of metal on the resist sidewall, and the electrode edge is smooth. All of the data taken in Chapter 4 and onwards was taken using IDEs created by this raised electrode process. These devices have produced high quality measurements of homopolymers, block copolymers, electron conducting materials, and inorganic ion conductors. This is the process recommended for all IDE studies going forward. The fabrication procedure as performed in the PNF is described in detail in the following section.

3.2.1 Raised IDE Fabrication Procedure

The goal of this process is to create an array of raised interdigitated electrodes with gradually sloped sidewalls and minimal surface roughness. Negative photoresist is used to avoid buildup of metal on the resist sidewalls during deposition. This process uses gold as the electrode material, with a thin titanium adhesion layer, but other metals (platinum, chromium) could be used with minimal changes to procedure. A simplified process schematic is shown in Figure 3.4.

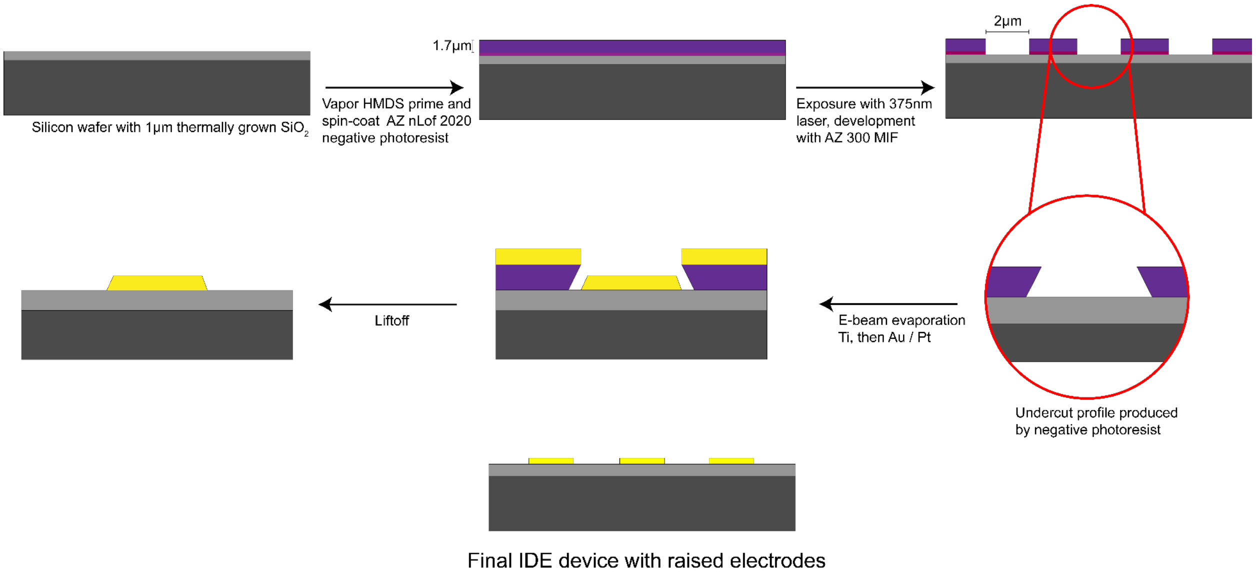

Figure 3.4 – Process flow diagram for creation of raised IDEs

1. **HMDS vapor prime.**

   Take a fresh thermal oxide (1 µm) coated Si wafer and remove any dust with a nitrogen gun. Prime the wafer for photoresist adhesion by placing it in the vacuum oven and running and HMDS (hexamethyldisilazane) vapor prime recipe.[1]

2. **Spin coat AZ nLoF 2020 photoresist.**

   Deposit around 8 µL and slowly deposit onto the wafer, taking care not to allow any bubbles to be created on the surface. Spin coat at 4000 rpm, 4000 rpm s^{-1} acceleration, for 45 s. This will result in a photoresist thickness of approximately 1.7 µm.

3. **Bake at 110 °C for 1 min.**

   The wafer is now ready for the photolithography step. Wafers prepared to this point can be kept for quite some time, as long as they stored away from UV exposure. Wafers kept in the dark can be used for lithography as long as several months in the future.

4. **Expose.**

   IDEs have been successfully patterned using both the 3C Technical GCA AutoStep 200 5x Reduction Stepper and the Heidelberg MLA150 Direct Write Lithographer tools in the PNF. The AutoStep relies on the use of a physical mask to define the pattern, which limits the flexibility of the device gemoetry that can be patterned. The exposure time is extremely short (< 1 s), though, so it can be considered an option for a very common device design that will be fabricated often. More commonly, the Heidelberg direct tool was used. This process has been optimized for that tool.

   Prepare a Heidelberg job that writes the negative image of the desired device geometry. When the negative resist is exposed, it will be crosslinked and remain insoluble during development. This can be done in the CAD software used to create the pattern file, or

---

[1] Early iterations of the IDE fab process involved depositing HMDS by spin coating followed by annealing on a hot plate. While this does produce a surface that is well-coated by photoresist, the HMDS is much less stable when deposited in this way.

it can be done directly in the Heidelberg software during job file creation. If a bounding box is drawn around the entire pattern, the Heidelberg "XOR" option will result in writing over the whole bounded area except where the pattern is drawn. Expose the pattern using the 375 nm laser with a dose of 290 mJ cm^{-2} and a focus of +1 relative to whatever dose is written on the tool. This dose and focus is chosen to ensure an undercut in the resist profile, as illustrated in Figure 3.4. If the dose is not high enough, the sidewall profile will be more vertical, and metal will adhere to the resist during deposition. This sidewall coverage results in the same sort of jagged electrode edge that was obtained with the positive photoresist process. An AFM image of electrodes created using an exposure dose of 210 mJ cm^{-2} is shown in Figure 3.5a. The rough edge characteristic of sidewall coverage during metal deposition is evident. Conversely, when a dose of 290 mJ cm^{-2} is used (Figure 3.5b), the electrode edge is smooth.

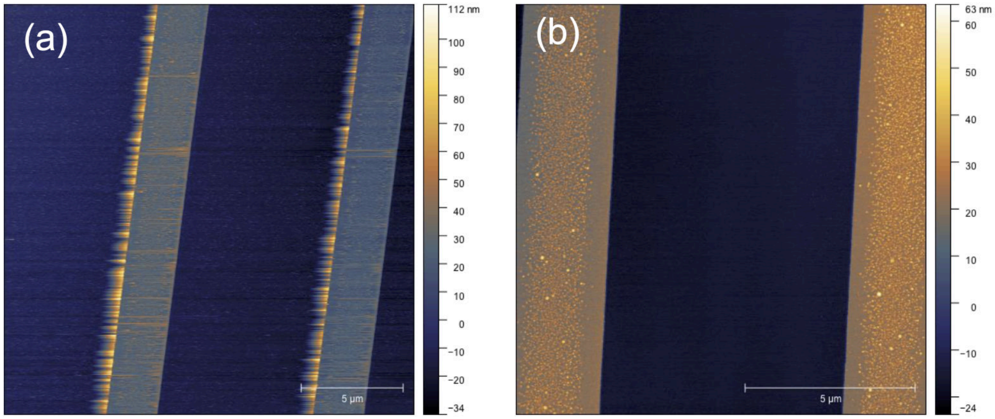

Figure 3.5 – AFM of metal electrodes prepared with an exposure dose of (a) 210 mJ/cm^{-2} and (b) 290 mJ/cm^{-2}

5. **Post exposure bake at 110 °C for 1 min.**

   This is an absolutely critical step. The post bake is necessary to fully crosslink the exposed areas and ensure that they will be insoluble in the developer.

6. **Develop in AZ MIF 300 for 1 min.**

Agitate slightly every 15 s or so while the wafer is in the developer. Stop the development by running under DI water stream for 90 s.

7. **Deposit metal electrodes.**

   All deposition for this work was done by electron-beam evaporation, though thermal evaporation or sputtering may be used as needed. Essentially any metal can be deposited here. Examples of metals that have been used include Au, Ag, Pt, Ti, and Cu. If a noble metal (Au, Ag, Pt) is desired for the final electrode material, a thin (5 nm) adhesion layer is necessary to fully bind the metal to the substrate. Ti or Cr, metals that very readily form an oxide, have very good adhesion with the SiO_2 substrate. The Au or Pt metal then adheres well to the Ti layer. Common electrodes made by this aproach consist of a 5 nm Ti adhesion layer followed by 25 - 95 nm of Au or Pt. Importantly, the substrate should not be rotated during deposition. This will result in undesirable metal deposition on the resist sidewalls.

   An important consideration for the quality of the deposited metal film is the deposition rate. Primarily this will affect the grain size of the resulting film. Different metals exhibit different relationships between deposition rate and surface roughness. For Ti, Au, and Pt, slow deposition results in smoother films. A deposition rate of 1 Å s^{-1} provides a good compromise between process speed and film roughness. Ag, conversely, benefits from faster deposition. 3 Å s^{-1} deposition produced much smoother films. Another important criteria is the chamber vacuum. The e-beam evaporation tool used requires a minimum vacuum of 1×10^{-6} torr. For many metals, especially those which readily oxidize (*e.g.* Al), reaching a vacuum of 1×10^{-8} will produce much higher quality films.

8. **Liftoff excess metal and remaining photoresist.**

   Place the wafer face-down in a dish containing NMP at 80 °C. Leave undisturbed at 80 °C for at least three hours and preferably overnight. Note that, because the photoresist is crosslinked, the NMP is not dissolving the material into solution. Rather, the entire crosslinked film is being delaminated by the NMP getting between the substrate and the resist. Ideally, this film should come off in one piece, and this can be helped by leaving it for a full 12 - 24 hours.

After the wafer has soaked in NMP for a sufficiently long to remove the vast majority of the remaining resist, remove it and spray it with NMP from a squirt bottle. Without letting the NMP dry, place it face-up in another dish of NMP at 80 °C. Sonicate for 5–15 minutes. Remove the wafer and rinse successively with NMP, acetone, and IPA, then sonicate briefly in IPA. Finally, rinse thoroughly with DI water and confirm complete liftoff under the microscope. If small amounts of resist remain between the electrodes, these can be removed by place the wafer face-up in a dish with just enough NMP to barely cover. Then take a clean room swab and gently brush the area with remaining resist. Repeat the NMP, acetone, IPA, and DI water rinsing steps. Once the liftoff is complete, perform an oxygen plasma descum on the wafer.

9. **Optional: Dice the wafer.**

   The individual IDEs can be removed from the wafer by hand using a diamond scribe or by using a dicing saw. The former is considerably faster, and was used most often. The dicing saw has a number of key advantages, though. First, the saw can produce identical size and shape IDEs, whereas the manual method produces nonuniform size. More importantly, the manual dicing method has a relatively high failure rate, and IDEs can be easily destroyed in the process. For IDEs or other similar devices fabricated on quartz must be diced using the saw, as there is no single crystal Si substrate to guide the manual cleaving.

A picture of an IDE is shown in Figure 3.6a. The large Au pads on the top and bottom of the device are the contact pads where probe tips can be connected. Each contact pad is connected to one half of the electrode array in the middle. The optical micrographs in

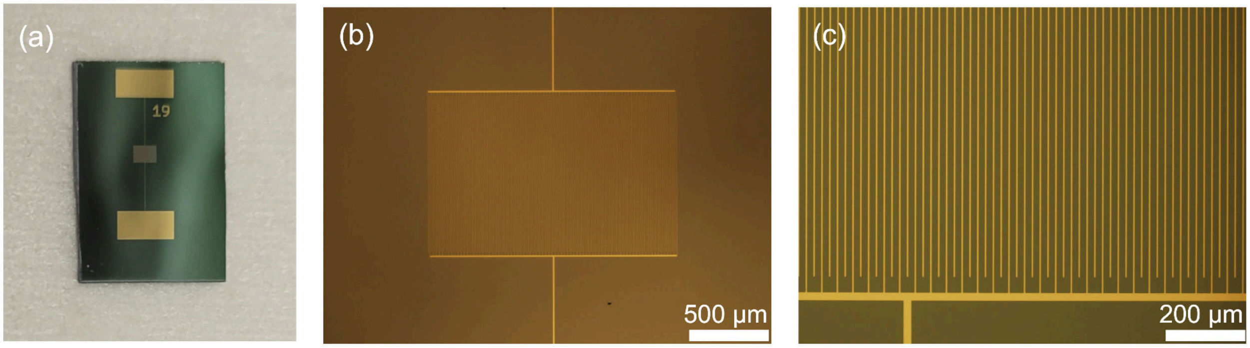

Figure 3.6 – (a) Picture of an IDE with standard geometry and optical microscope images of the IDE at (b) 4x and (c) 20x magnification

Figure 3.6b,c show the interdigitated electrode array at different magnifications. The device shown has the standard dimensions of $N = 160$ electrodes, $l = 1$ mm electrode length, $d =$ 8 μm electrode spacing, and $w = 2$ μm electrode width.

3.3 Derivation of IDE Cell Constant

Throughout this work ionic conductivity of different materials is determined using EIS of thin films spin cast on coplanar interdigitated electrodes (IDEs). This approach is unconventional, and an important prerequisite to this work was to carefully understand how the dimensions of the IDE features—the length (l), number (N), width (w) and spacing between the electrodes (d)—affects the measured impedance, as well as how that impedance data can be correctly analyzed. In this section, a theoretical prediction for how the measured resistance, as determined by EIS, should relate to the material conductivity and the IDE geometry is derived. This prediction is validated experimentally in Chapter 4.

The measured resistance (R) of a system is related to the material conductivity (σ) by some function of the measurement cell geometry—the cell constant (κ). A large body of work has been dedicated to the understanding of electric fields generated by IDEs, and how they penetrate through an overlying film.[118] Although coplanar interdigitated electrodes generate elliptic field lines which are complex to describe mathematically, the extreme dimensions in the thin film system allows for some convenient simplifying assumptions to be made. In this way, the otherwise nontrivial cell constant of the IDE system may be approximated by an equivalent parallel plate configuration. Equation 3.1 has been used both by our group previously[108,109] as well as by other groups[119–121] to relate the resistance measured by EIS of polymer thin films using IDEs to the conductivity.

$$\sigma = \frac{d}{R(N-1)lh} \tag{3.1}$$

Here N is the number of interdigitated electrodes in the array, l is the electrode length, and h is the height of the overlying polymer film. These previous works have not provided a complete derivation of this equation, however. Given the centrality of this relationship to all of the work in this thesis and the importance of validating the assumptions made in the use of Equation 3.1 to this work, a more thorough treatment of this derivation is warranted.

The cell constant, κ, of a general electrochemical system comprised of electrodes separated by a medium with conductivity, σ, and relative permittivity, ε_{R}, can be defined either in terms of the resistance or the capacitance of the cell.[122]

$$\kappa = R\sigma = \varepsilon_{\mathrm{R}}\varepsilon_0/C \tag{3.2}$$

Here, ε_0 is the vacuum permittivity. The capacitance (C) is defined as the ratio of total surface charge (Q) to the applied potential difference (φ), $C = Q/\varphi$. C for a cell of arbitrary geometry under an electric field $\vec{E}$ can be found by applying Maxwell's first equation, resulting in:

$$C = \frac{\varepsilon_{\mathrm{R}}\varepsilon_0 \oiint \vec{E}d\vec{S}}{\oint \vec{E}d\vec{L}} \tag{3.3}$$

In the case of a parallel plate cell the solutions to these integrals are trivial, and the capacitance is given by the well-known relationship:

$$C = \frac{\varepsilon_{\mathrm{R}} \varepsilon_0 A}{d} \tag{3.4}$$

where A and d are the electrode surface area and interelectrode distance, respectively. By comparing Equations 3.2 and 3.4, the resistance of a parallel plate device can be related to the conductivity by $R = d/\sigma A$.

The task of finding solutions to Equation 3.3 for a coplanar IDE geometry is considerably more complex. To do so, we first follow the derivation laid out by Gevorgian *et al.* which involves conformally mapping the complex IDE geometry to an equivalent parallel plate geometry.[123] Next, we use simplifying assumptions based on the geometry of the system to further reduce the complexity of the cell constant expression. For this we turn to the derivation of Nigon *et al.* to define a cell constant for very thin films on IDEs.[124] Lastly, we make one further simplifying assumption to arrive at the cell constant used in the text.

3.3.1 Cell constant for coplanar electrodes by conformal mapping

By recognizing the symmetric and periodic nature of the IDE, the capacitance of the system can be taken as the capacitance between two adjacent electrodes with spacing d, length l, and width w multiplied by $N - 1$ pairs of electrodes. We assume here that the difference in capacitance of the outermost electrodes is minimal given the large number of electrodes used in our IDEs ($N = 160$). Gevorgian *et al.* discusses in detail how these outer electrodes can be more accurately accounted for. We also assume the fringing effect near the base of the electrodes (< 30 µm wide) is minimal compared to the length of the electrode (1 mm long), and thus can be ignored. Furthermore, as the width of the electrodes is much greater than their thickness, the height of the electrodes can be ignored. Based on these simplifications we consider the capacitance between two half electrodes covered by a conductive film of height h, shown in Figure 3.7a.

The elliptic field lines illustrated in Figure 3.7a can be converted to an equivalent parallel

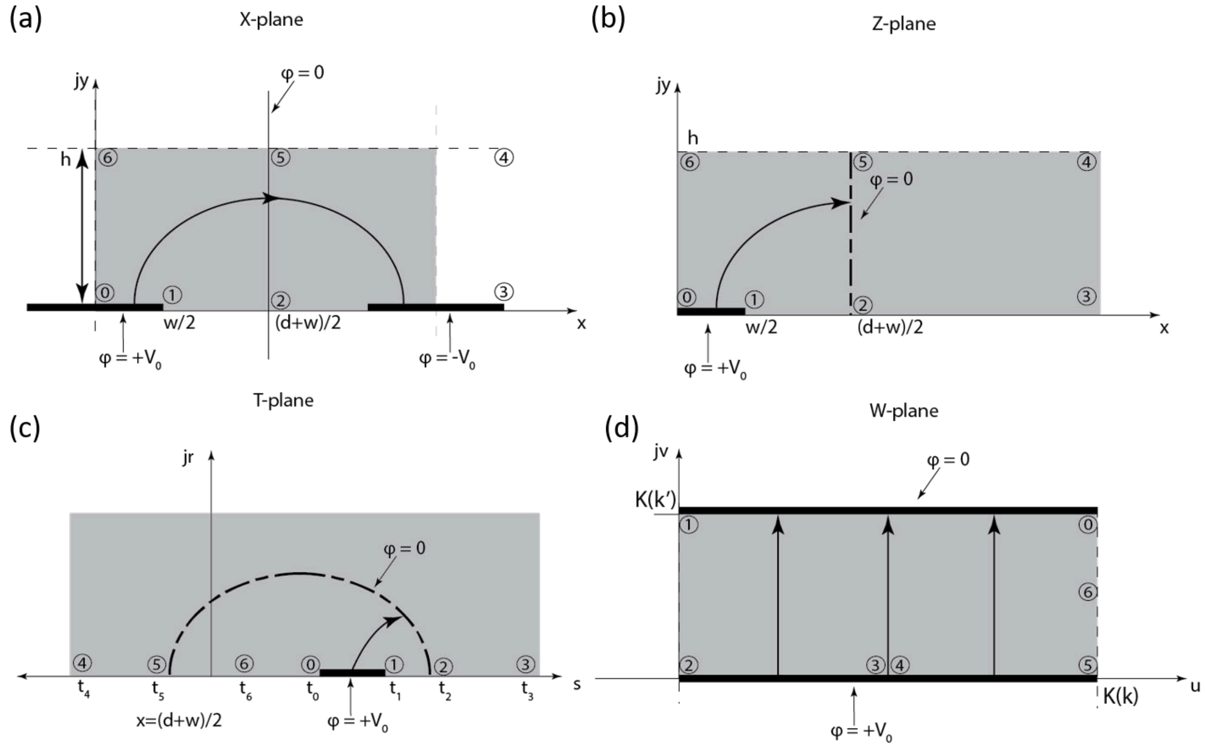

Figure 3.7 – Conformal mapping of IDE cell constant from real space to equivalent parallel plate geometry

plate geometry by a series of conformal mappings. First, the capacitance between two half electrodes with potential $+V_0$ and $-V_0$ can be found by instead finding the capacitance between one half electrode and the equipotential line at $x = (w + d)/2$, the area bounded by the polygon $\overline{2065}$. The system is symmetric about this line, and the total capacitance between the two half electrode strips can be taken as half of this simplified expression (*i.e.* two of these half capacitors in parallel). This symmetric system is depicted in Figure 3.7b, referred to as the Z-plane. As Gevorgian notes, the field lines do not change if we imagine an infinite strip of perfect metal of height h extends beyond the $\varphi = 0$ line. No mapping is required between the X-plane and Z-plane, as it is solely a reframing of the problem in the same coordinate space.

Mapping the semi-infinite strip (triangle), $\overline{3064}$ shown in Figure 3.7b rather than the rectangle $\overline{2065}$ allows us to eschew the standard Schwartz-Christoffel integral assisted mapping, and instead map this semi-infinite strip to the T-plane by:

$$t = \cosh^2\left(\frac{\pi z}{2h}\right) \tag{3.5}$$

Here, $z = x + jy$ is the coordinate in the complex Z-plane and $t = s + jr$ is the coordinate in the T-plane. The relevant T-plane vertices are given by

$$\begin{gathered} t_0 = 1, t_1 = \cosh^2\left(\frac{\pi w}{2h}\right), t_2 = \cosh^2\left(\frac{\pi(d+w)}{2h}\right), \\ t_3 = t_4 = \infty, t_5 = -\sinh^2\left(\frac{\pi(d+w)}{2h}\right), t_6 = 0 \end{gathered}$$

This mapping is conformal, meaning that the orthogonality of lines in the Z-plane at non-critical points will be preserved upon mapping to the T-plane. Equipotential lines and lines of equal flux will therefore remain perpendicular upon transformation, and the solutions obtained by this method will be analytical.

Next, the upper half plane is mapped to a rectangle in the W-plane by Schwartz-Christoffel mapping by the function:

$$w = c_1 \int_t^{t_5} \frac{dt}{\sqrt{(t-t_0)^2(t-t_1)^2(t-t_2)^2(t-t_5)^2}} + c_2 \tag{3.6}$$

Here c_1 and c_2 are constants which are found by comparing the vertices in the T-plane to their corresponding points in the W-plane. This solution is in the form of elliptic integrals:[125]

$$w = c_1 \int_0^1 \frac{d\xi}{(1-\xi^2)(1-k^2\xi^2)} + c_2 \tag{3.7}$$

The capacitance of the rectangle $\overline{2065}$, which involved elliptic electric field lines, has now been reduced to an equivalent parallel plate geometry with "surface area" $lK(k)$ and "distance" $K(k')$. Here l is the electrode length and $K(k)$ is the complete elliptic integral of the first kind. The elliptic modulus, k, is given by:

$$k = \frac{\sinh\left(\frac{\pi w}{4h}\right)}{\sinh\left(\frac{\pi(w+d)}{4h}\right)} \sqrt{\frac{\cosh^2\left(\frac{\pi(w+d)}{4h}\right) + \sinh^2\left(\frac{\pi(w+d)}{4h}\right)}{\cosh^2\left(\frac{\pi w}{4h}\right) + \sinh^2\left(\frac{\pi(w+d)}{4h}\right)}} \tag{3.8}$$

The complementary modulus, k' is given by $k' = \sqrt{1 - k^2}$.

After accounting for the capacitance between the other half electrode and the equipotential line $\overline{25}$ (and adding these capacitors in series), the capacitance between the two half electrodes—the fundamental repeat unit for the IDE capacitance—is given by:

$$C_{\text{unit}} = \frac{1}{2}\varepsilon_{\text{R}}\varepsilon_0 l \frac{K(k)}{K(k')} \tag{3.9}$$

The total IDE capacitance for an IDE with N total electrodes can be taken as the addition of $N - 1$ of these unit cells in parallel, resulting in a total capacitance of:

$$C_{\text{IDE}} = \frac{1}{2}\varepsilon_{\text{R}}\varepsilon_0 (N-1) l \frac{K(k)}{K(k')} \tag{3.10}$$

This analytical solution, first obtained by Gevorgian *et al.*, can be applied to any IDE system with sufficiently many and relatively long electrodes covered by a thin dielectric layer.[123] Other formulations of the IDE capacitance have been derived as well,[126,127] but the Gevorgian model has been shown to work well for many such systems, both theoretically and experimentally.[128,129] While this analytical solution has been derived for the system capacitance, by comparing it to Equation 3.2, a formula for the conductivity as a function of resistance can be obtained:

$$\sigma = \frac{2}{R(N-1)l} \frac{K(k')}{K(k)} \tag{3.11}$$

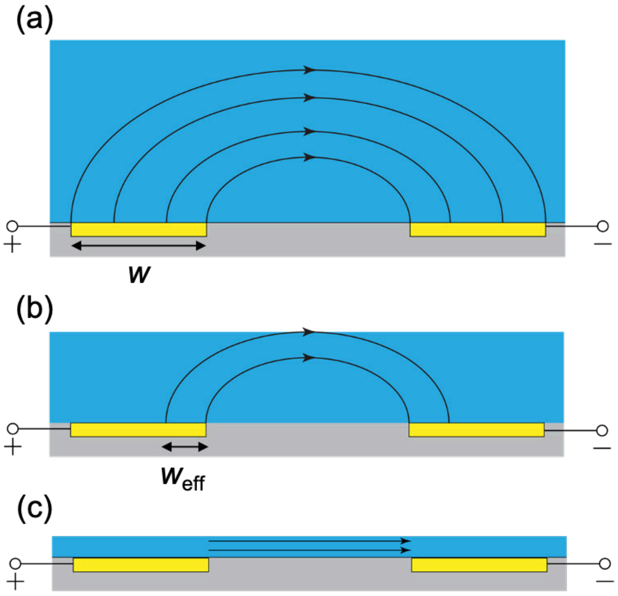

Figure 3.8 – Electric field lines produced by coplanar electrodes in the case of (a) a film with height $h > d + w$, (b) $h < d + w$, and (c) $h \ll d + w$

3.3.2 Simplification in the case of thin films

So far we have considered a generic case where the film height (h) is larger than the width and distance of the IDE. In this case, as depicted in Figure 3.8a, the electric field lines are elliptical and do not necessarily sense the full thickness of the overlying film. In the case depicted in Figure 3.8b where the film height is less than the maximum that can be sensed by the electrodes. This applies to systems in which there is an insulating dielectric capping layer, or, as in our system, air above the film. For such cases, we can follow the derivation of Nigon *et al.* to simplify the elliptic integral terms in Equations 3.10 and 3.11 to a more manageable form.[124] A more detailed derivation is provided in the Supporting Information of *ref* [124], and the interested reader is encouraged to refer there for a more in-depth understanding of this derivation. This simplification applies to IDEs coated with extremely thin films such that $d, w \gg h$ and $k \to 0$ $(k' \to 1)$, which is the case shown in Figure 3.8c. If we define $A = \exp\left(\frac{-\pi d}{4h}\right)$ and $B = \exp\left(\frac{-\pi w}{4h}\right)$, Equation 3.8 can be rewritten as:

$$k = \frac{B^{-1} - B}{(AB)^{-1} - AB} \sqrt{\frac{((AB)^{-1} + AB)^2 + ((AB)^{-1} - AB)^2}{(B^{-1} + B)^2 + ((AB)^{-1} - AB)^2}} \tag{3.12}$$

After factoring and regrouping terms, this can be rearranged to:

$$k = \sqrt{2}A \frac{1 - B^2}{1 - A^2B^2} \sqrt{\frac{1 + A^4B^4}{(1 + A^2)(1 + A^2B^4)}} \tag{3.13}$$

In the limit of increasingly thin films or large IDE geometries, $A \to 0$ as $d/h \to \infty$ and $B \to 0$ as $w/h \to \infty$ we can take a Taylor expansion around 0, resulting in:

$$k = \sqrt{2}A(1 - B^2) \left(1 - \frac{A^2}{2} + o(A^2) + o(AB)\right) \tag{3.14}$$

Here we use the Landau little-o notation to group higher order terms. As shown in *ref.* [124], stopping the Taylor series at this point still yields a very accurate result for k. Simplifying further to $k = \sqrt{2}A$ is still a reasonable assumption when w/h is large.

$K(k)$ and $K(k')$ are in turn simplified by taking a Taylor expansion of the elliptic integrals around $k = 0$:

$$K(k) = \frac{\pi}{2} \left(1 + \frac{k^2}{4} + o(k^2)\right) \tag{3.15}$$

$$K(k') = \frac{2}{\pi} \ln\left(\frac{4}{k}\right) K(k) - \left(\frac{k^2}{4} + o(k^2)\right) \tag{3.16}$$

Dividing 3.16 by 3.15 and applying the expression for the elliptic modulus in 3.14, we obtain (after some considerable algebraic rearrangement):

$$\frac{\pi}{2} \frac{K(k')}{K(k)} = \ln\left(\frac{2\sqrt{2}}{A}\right) + B^2 + o(A^2)o(B^2) + o(AB) \tag{3.17}$$

When d/h and w/h are both very large, the first order approximation should still be very good. Note that to a first order approximation the cell constant is not a function of B, and is therefore independent of w. Recalling that $A = \exp\left(\frac{-\pi d}{4h}\right)$:

$$\frac{\pi}{2}\frac{K(k')}{K(k)} = \ln\left(\frac{2\sqrt{2}}{A}\right) = \ln\left(2\sqrt{2}\right) + \frac{\pi d}{4h} = \frac{\pi}{4h}(d + \Delta d) \tag{3.18}$$

where $\Delta d = 4\ln(2\sqrt{2})h/\pi \approx 1.324h$

Combining this with the expression given in 3.11, we obtain a simplified equation for the cell constant:

$$\sigma = \frac{1}{R}\frac{d + \Delta d}{(N-1)lh} \tag{3.19}$$

This expression is valid for IDE geometries where the electrode spacing and width are large and the film is extremely thin ($d/h, w/h \to \infty$). Notably the cell constant for such configurations is independent of the electrode width.

3.3.3 *Further simplification of the Nigon model for IDE cell constant*

As discussed by Chen and coworkers, as the film height decreases, the "effective electrode width" (w_{eff}) decreases as well.[127] That is, the electrode width required to fully probe the film decreases as h decreases. As illustrated in Figure 3.8 in the limit as $h \to 0, w_{\text{eff}} \to 0$ as well. Chen predicts that the effective electrode width is a function of the film height and the electrode spacing:

$$\frac{w_{\text{eff}}}{d} = \sqrt{1 + \left(\frac{h}{d}\right)^2} - 1 \tag{3.20}$$

As shown in Figure 3.9a, the effective width of the electrodes for all relevant cell geometries are less than 10 nm, irrespective of the actual electrode width. With these length scales it is reasonable to approximate even the widest electrodes as point sources.

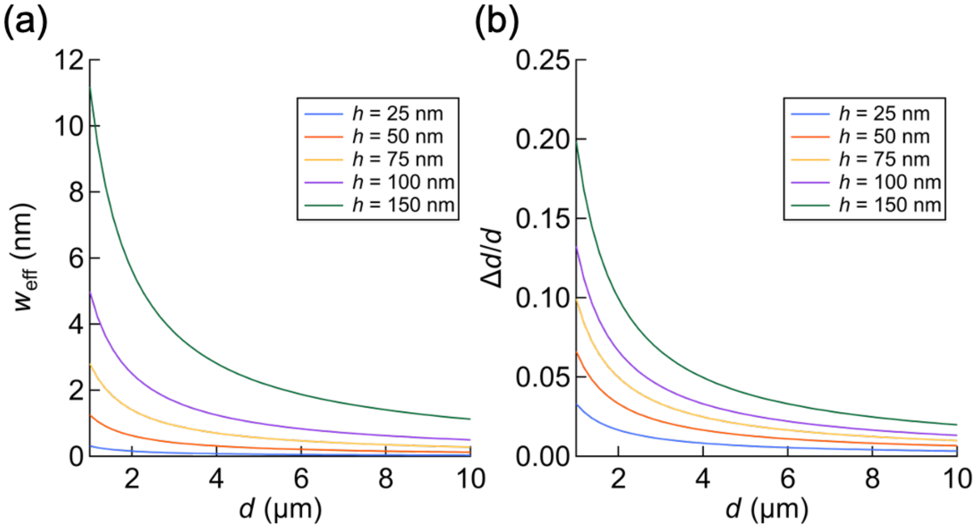

Figure 3.9 – (a) Effective electrode width and (b) error associated with neglecting the Δd in Equation 3.19 as a function of d and h

We can then make the final simplifying assumption that, because $h \ll d$, Δd will also be very small. This term can be neglected when the interelectrode distance is several orders of magnitude larger than the film height, with minimal additional error. As shown in Figure 3.9b, the error introduced by neglecting this term is less than 20% for all configurations used in this study, and rapidly approaches zero at higher d and lower h. This error is of similar or smaller magnitude than the typical uncertainities associated with film thickness estimations and repeat sample measurements. With this final simplification, we have successfully reduced the complicated relationship between IDE geometry and cell constant to the simple linear expression Equation 3.1:

$$\sigma = \frac{d}{R(N-1)lh}$$

Chapter 4

Interrogation of Electrochemical Properties of Polymer Electrolyte Thin Films†

ABSTRACT

The ability to characterize bulk and interfacial transport properties of polymer electrolytes is critical to realizing their potential applications in electrochemical energy storage devices. In this chapter, we leverage custom microfabricated interdigitated electrode array (IDEs) as a platform to probe ion transport properties of polymer electrolytes films through electrochemical impedance spectroscopy (EIS) measurements. Using poly(ethylene oxide) (PEO) blended with lithium bis(trifluoromethanesulfonyl)imide (LiTFSI) as a model dry polymer electrolyte system, we investigate how geometric parameters of the IDEs influence the quality and analysis of EIS measurements. By focusing on films on the nanometer film thickness (around 50 nm), EIS measurements revealed diffusional processes near the electrode/polymer interface that may be difficult to observe with conventional thick films. Moreover, irreversible impedance spectra were observed at elevated temperatures when using IDEs with large electrode metal fractions. These irreversible processes were eliminated through passivation of the IDE with different oxides (SiO_2, Al_2O_3, or TiO_2). Ultimately, the ionic conductivity of PEO-LiTFSI electrolytes is confidently determined when appropriate IDE geometries and equivalent circuits are used. Our work demonstrates the use of IDEs and nanothin polymer

---

†. This work was originally reported in *J. Electrochem. Soc.*, **2019**, 165, H1028

electrolytes films as a versatile platform for rapid and efficient interrogation of both bulk and interfacial electrochemical properties.

4.1 Introduction

A platform that enables rapid and efficient fundamental electrochemical studies is vital to understanding the transport of electroactive species in any material system. Interdigitated electrode arrays (IDEs) have been developed and utilized for highly sensitive electrochemical measurements of small quantities of materials. The conventional uses for IDEs have focused around sensor applications (chemical- and bio-sensor, *etc.*), ceramic solid electrolyte films, polymers, and redox cycling of electroactive species in liquid media.[120,130–133] The sensitivity of the IDE is controlled through multiple geometric design parameters: the number of interdigitating electrode "teeth" (N), the length (l) and width (w) of the electrodes, the separation distance between electrodes (d), and the height of the film under investigation (h). Other design considerations include substrate support (*e.g.*, Si/SiO_2, polyimide, etc.), electrode material (*e.g.*, Au, Pt, carbon, etc.), and the choice of coplanar or raised electrodes. Importantly, the design and fabrication of IDEs must be tailored to fit the application.[134]

The high sensitivity of IDEs enables good signal-to-noise ratio during electrochemical measurements of thin layers in the nanoscale thickness regime.[133] Thin film measurements enable characterization of bulk transport properties while also amplifying the presence of any interfacial effects that may enhance or inhibit ion transport. Understanding interfacial behavior of polymer electrolytes has critical implications on the performance of energy storage and conversion devices. In fuel cells, for example, proton transporting polymers such as Nafion form nanoscale thin coatings (4–10 nm) on electrocatalyst particles present in the porous electrodes.[120,121] Hydration and proton transport at the polymer/catalyst interface are critical to the electrochemical conversion performance.[135] As another example, conventional polymer binders (*e.g.*, PVDF) in lithium-ion battery electrodes reportedly form layers in the range of 6 nm to 24 nm depending on the mass loading of redox-active particles and electron conductive carbon black.[136] Such nanoscale film thicknesses would certainly apply to dry solid polymer electrolytes when serving as a binder and electrolyte for solid-state battery electrodes. In turn, interfacial interactions controlling ion-transport in polymer electrolyte layers near surfaces can dictate the accessible energy capacity.[136] In addition, nanoscale processes become evident through nanostructured block copolymer electrolytes and polymer nanocomposites.[108,109,137–141] Consequently, electrochemical characterization of polymer films at the nanoscale are vital going forward, and IDEs will readily facilitate such an approach.

Here we are motivated to demonstrate how IDEs in concert with electrochemical impedance spectroscopy (EIS) can be a versatile platform to probe the transport properties of ion-conducting polymer electrolytes. These polymeric materials are of continued interest for energy storage and conversion devices such as solid-state batteries, fuel cells, and supercapacitors.[142] We focus on poly(ethylene oxide) (PEO) blended with lithium bis(trifluoromethanesulfonyl)imide (LiTFSI) (PEO-LiTFSI) as a model dry polymer electrolyte system, which has long been a focus of research and development for lithium-ion batteries.[23] Electrochemical impedance spectroscopy (EIS) is a common analytical tool to probe the transport properties of polymer electrolytes. Critically, the resistive and capacitive properties of the system are intimately linked to the quality of the EIS response and to subsequent fitting to an equivalent circuit model. The vast majority of polymer conductivity studies to date have employed a parallel plate cell configuration, with the electrolyte film sandwiched and pressurized between two metal electrodes. These polymer electrolyte films are usually on the order of several microns thick.[81,143] This setup is relatively straightforward to assemble, and the resulting EIS spectra can be fit to a commonly used equivalent circuit model. From this model one can extract the film resistance and then calculate the conductivity using an easily understood cell constant ($\sigma = d/(RA)$), where R is the recorded resistance, A is the electrode surface area, and d is the distance between the electrodes. Determining an equivalent circuit of resistors and capacitors to fit EIS data must consider all processes present in the electrochemical system. Translating the utility of IDEs towards different materials systems and environments requires careful consideration of IDE design parameters and how those parameters affect the measurement response. The choice of IDE geometric parameters such as the electrode width and spacing will certainly affect such processes, and IDEs must be designed to amplify the processes of interest and minimze those that might overshadow them. Once the impedance data has been fit to an appropriate equivalent circuit, the film resistance can be obtained, which, after careful consideration of a cell constant, can be used to determine the conductivity of the material. While the cell constant of a coplanar IDE can be quite complex to derive mathematically, thin films may allow for a simplified model to be used to describe the system.

In this chapter we explore the resistive behavior of thin polymer electrolytes as observed by EIS measurement and the effect of IDE geometry on such behavior. Our approach involves testing how IDE geometric design parameters can influence the quality and analysis of EIS measurements. This approach requires careful choice of equivalent circuit model for EIS data fitting to confidently extract resistive and capacitive properties of the material. For this purpose, we choose PEO mixed with LiTFSI salt as a model dry polymer electrolyte system, as it has been extensively studied in thick films. Relying on previously reported work regarding the cell constant of an IDE as a function of system geometry, we experimentally validate the assumptions made in that analysis for thin film polymer electrolytes. We then explore the influence of the IDE design on the quality and accuracy of the EIS measurement. We examine the effect that the high electrode surface area has on both the impedance measurements and the stability of the system. We suggest guidelines for the IDE design and EIS data analysis which can help to account for additional phenomena that occur when the electrode area is high. These considerations enable us to use this method to study both bulk and thin film polymer electrolyte properties.

4.2 Results and Discussion

To interrogate the electrochemical behavior of thin film polymer electrolytes, interdigitated electrodes (IDEs) were prepared according to the first generation fabrication process described in Section 3.2. The IDE schematic is illustrated in a top-down and cross-sectional view in Figure 4.1. The different IDEs are characterized by four parameters: the number of interdigitating electrode "teeth" (N total, $N/2$ of each polarity), the overlapping length of the electrodes (l), the width of the electrodes (w), and the separation distance between electrodes (d). In order to quantitatively compare the effect of both electrode spacing and width simultaneously, another parameter, the metal fraction of the electrode (η) is introduced, defined as $\eta = w/(w + d)$. For each of the devices used, N was 160, and l was 1 mm. In this study, the width and separation distance of the electrodes vary from 1–30 µm and 1–10 µm, respectively.

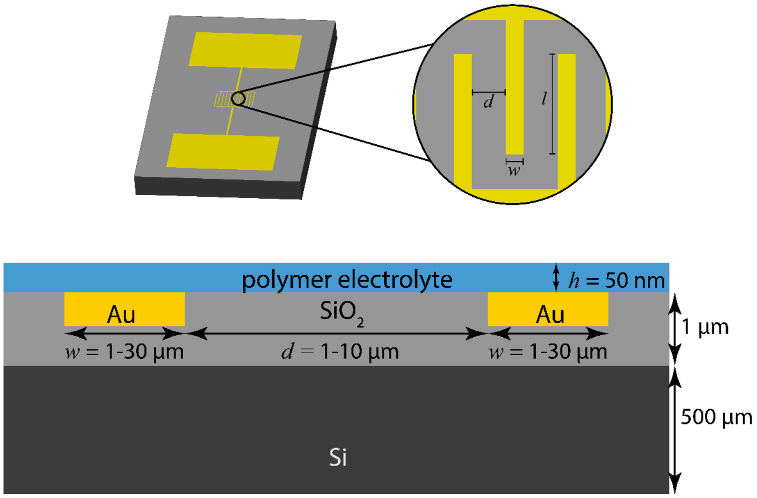

Figure 4.1 – Illustration of the IDE design and relevant dimensions from top-down view and cross-section. The dimensions that were used in this study are: l = 1 mm, d = 1–10 µm, w = 1–30 µm, h = 30–110 nm.

It is important to first demonstrate that IDEs coated with thin films of polymer electrolyte can produce high quality impedance spectra that can accurately model with an appropriate equivalent circuit. An IDE with dimensions $d = 8$ μm, $w = 2$ μm was coated with 50 nm of PEO-LiTFSI. Potentiostatic EIS measurements were then performed at different perturbation potentials, and data was fit to a Kramers-Kronig compliant circuit using the Gamry software. The reuslts of these tests are plotted in Figure 4.2. At 10 mV—a common perturbation potential for bulk polymer electrolyte studies—the data appears linear and stable, as evidenced by the reasonable Kramers-Kronig fitting (Figure 4.2a). There is, however, a fair amount of noise in the system. This type of noise can be a drawback of the IDE system. The noise can be reduced by using a higher potential amplitude. Figure 4.2b–d show the results from EIS measurements at 50 mV, 100 mV, and 200 mV, respectively. As the potential, and thus the current measured by the instrument, increases, the noise in the impedance data decreases. Across this range of potentials, the impedance is stable and linear. At higher potentials (Figure 4.2e–f) the Kramers-Kronig circuit does not accurately fit the measured data, suggesting some nonlinearities are present. For the rest of this dissertation, all measurements are made using a 100 mV potential amplitude which is well within the linear regime but is high enough to limit noisiness in the data.

4.2.1 Linear relationships between the film resistance, electrode spacing and film height

To investigate the effect of the IDE geometry on the measured impedance, we first prepared 50 nm PEO-LiTFSI films on IDEs with different spacing ($d =$ 1–10 μm) and constant electrode width ($w = 2$ μm). We performed a potentiostatic electrochemical impedance spectroscopy (EIS) measurement to determine the response of the system as the electrode spacing is varied. Figure 4.3 shows the Nyquist plots of these measurements taken at 70 °C. All impedance spectra look qualitatively similar, though the radii of the characteristic semi-

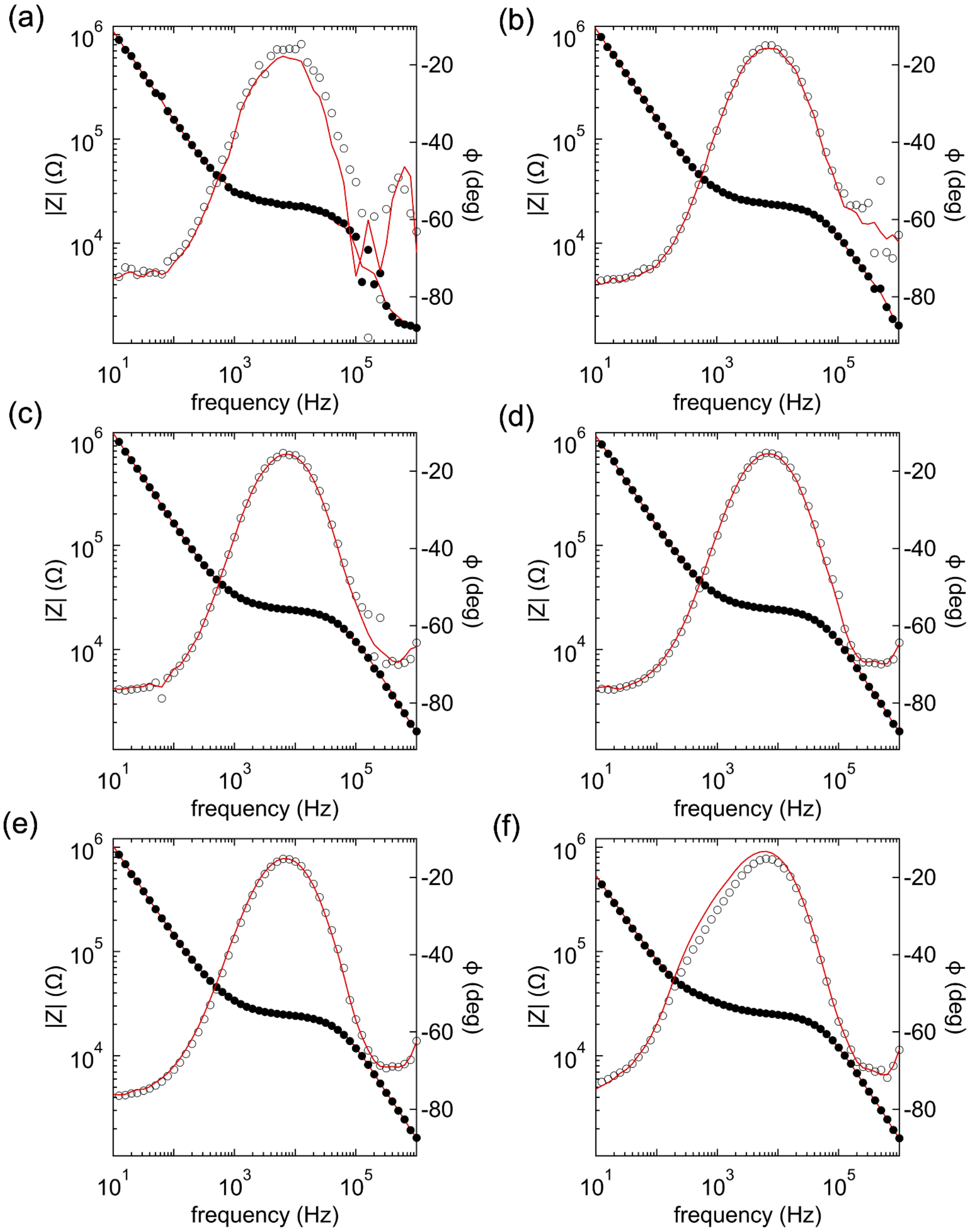

Figure 4.2 – Impedance spectra (black circles) and Kramers-Kronig fitting (red lines) of 50 nm PEO-LiTFSI film on w = 2 μm, d = 8 μm IDE produced by different perturbation potentials: (a) 10 mV, (b) 50 mV, (c) 100 mV, (d) 200 mV, (e) 300 mV, and (f) 1 V.

circle increase with increasing electrode spacing, indicating that the film resistance increases as the electrodes are moved farther apart. To further explore the relationship between the electrode spacing and the measured resistance, fitting to an equivalent circuit is required to extract the polymer electrolyte resistance from the impedance spectra.

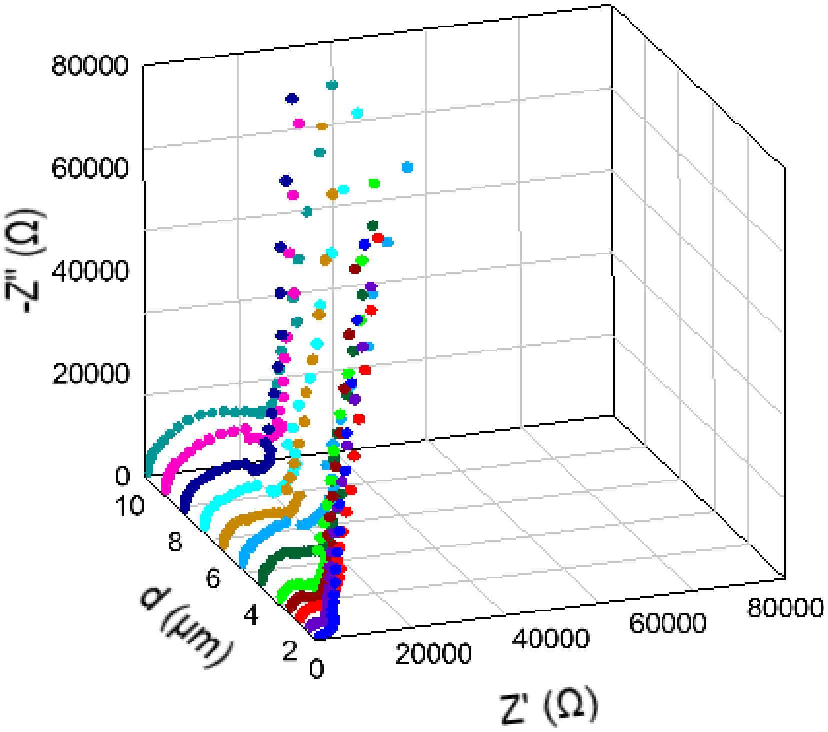

Figure 4.3 – Nyquist plots for IDEs coated with $h = 50$ nm PEO-LiTFSI at 70 °C, with increasing inter-electrode distance (d) and constant width ($w = 2$ µm)

Choosing an equivalent circuit to fit impedance data requires careful consideration of the processes present in the electrochemical system. Model 1, shown in Figure 4.4a, describes the basic elements of a polymer electrolyte-IDE system. The circuit includes a resistor (R_f) and constant phase element (CPE_f) in parallel to describe the response of the film itself at low and high frequencies, respectively. It also includes a constant phase element (CPE_{int}) in series with the film components to describe the behavior of the system near the ion-blocking electrodes. Constant phase elements were chosen to describe some of the "imperfect" capacitor-like behaviors of these systems, including complex phenomena such as the formation of the electric double layer. Model 1 contains an additional resistor (R_p) in series with these elements to account for intrinsic resistive losses caused by the experimental setup, as well as a capacitor (C_{sub}) is to account for the parasitic capacitance of the silicon oxide substrate. The equations describing the impedance of each of these elements, as well as the overall circuit, are given in the Section 4.4.4. This model is similar to that which has been used in previous studies of polymer electrolytes in bulk, and has been used by others to describe thin films on IDEs.[120,144,145]

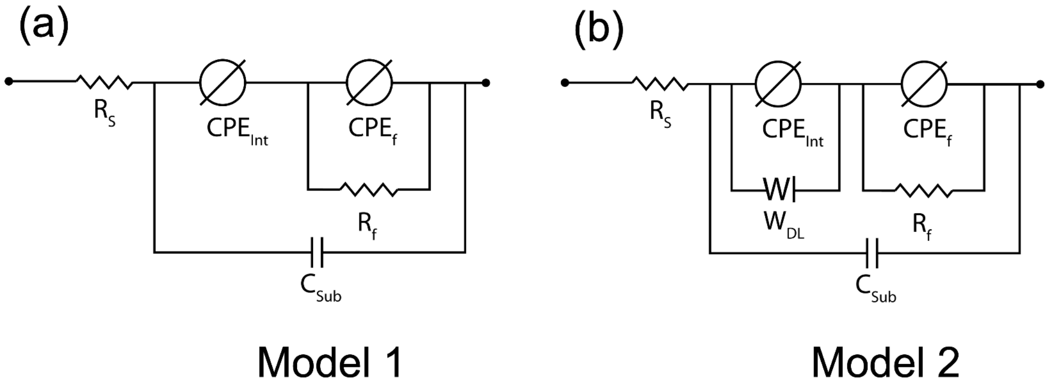

Figure 4.4 – Equivalent circuit diagrams for (a) Model 1 and (b) Model 2 used to fit EIS data. R_{f} in both circuits represents the film resistance that is used to calculate conductivity. W_{dl} represents a finite, or bounded, Warburg element (T element).

To illustrate the expected response of a polymer electrolyte system, we caluclated solutions to the equation for Model 1 as a function of frequency. Simulated impedance curves obtained from this method are shown in Figure 4.5. Three regimes are delineated in the Bode plot shown in Figure 4.5a. Regime I, in the high frequency range, is dominated by capacitive-like elements, such as the polymer film constant phase element (CPE_f). This is evident from the steady change in total impedance with frequency, and a correspondingly low phase in Figure 4.5b (close to -90°, the phase response of an ideal capacitor). Here the impedance of the film CPE is less than that of the film resistance, and the resistor is effectively bypassed. Regime II corresponds to the so-called "resistive plateau", where the magnitude of the total impedance is essentially constant with frequency. Here, the film resistance (R_{f}) is the predominant factor in the impedance response, as the film capacitor is effectively shut off and the interfacial capacitance is still relatively small. The parallel combination of the film resistance and capacitance gives rise to the characteristic semicircle seen in the Nyquist plot (Figure 4.5c). Lastly, regime III is the capacitive regime at low frequencies, where again the impedance is frequency dependent. The magnitude of the impedance increases due to the interfacial constant phase element ($\mathrm{CPE}_{\mathrm{int}}$), which models processes such as the formation of the double layer at the electrode-polymer film interface. This CPE manifests itself in the Nyquist plot as a nearly vertical line at the end of the partial semicircle (an ideal capacitor would exhibit a perfectly vertical tail).

Understanding the expected response of the system in question and how the relevant circuit elements relate to the measured spectrum allows one to quickly assess the quality of the measured data and make qualitative comparisons between different datasets. For example, observing an increase to the height of the resistative plateau as the measurement temperature is decreased provides a good initial confirmation that the expected behavior—a decrease in conductivity with decreasing temperature—is being observed. The quality of the impedance spectra also dictates how confident one can be with the equivalent circuit fitting. As the film resistance is often the parameter of interest, it is ipmerative that the resistive plateau be broad, or the semi-circle motif most be nearly complete. The breadth of the plateau is determined by the difference between the interfacial and film capacitance values, where larger differences result in a broader plateau regime. This can be described quantitatively by considering cutoff frequencies between the capacitive and resistive regimes. The cutoff frequency is commonly defined as the point at which the real and imaginary components (resistive and capacitive, respectively) of the total impedance are equal. This cutoff frequency corresponds to a phase angle of -45°. This formulation is analogous to the -3dB cutoff frequency commonly discussed in the context of a low-pass filter RC circuit. The cutoff frequencies between regimes I and II and regimes II and III are approximately $f = 1/(2\pi R_{\mathrm{f}} Q_{\mathrm{f}}) \approx 8$ kHz and $f = 1/(2\pi R_{\mathrm{f}} Q_{\mathrm{int}}) \approx 8\mathrm{Hz}$ (curve A), respectively. These are

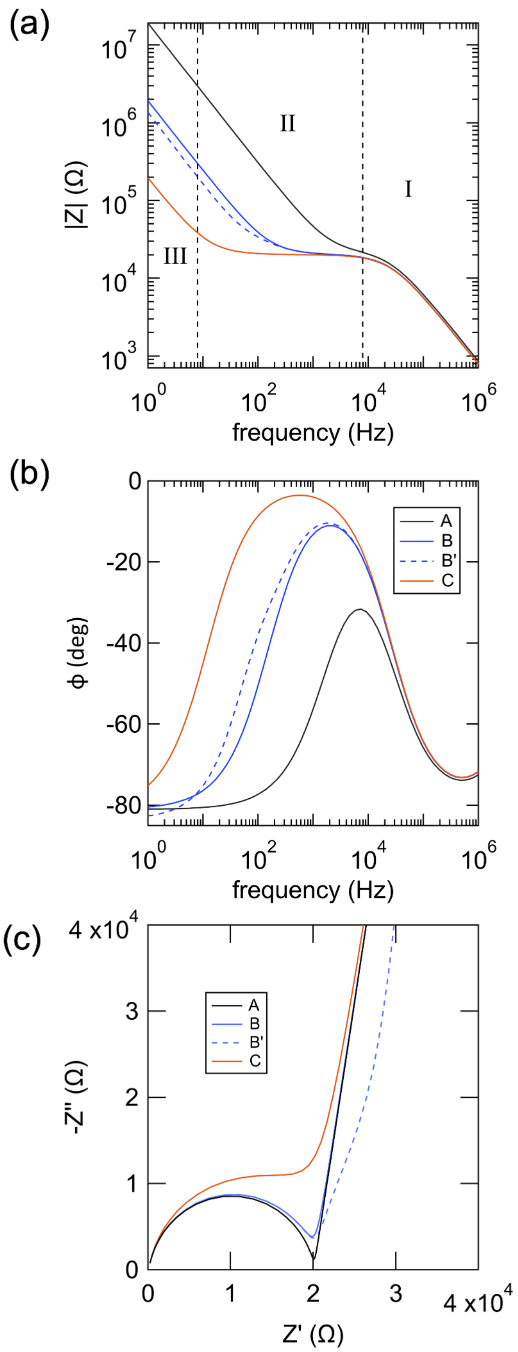

Figure 4.5 – Calculation of impedance spectra using values of $R_\mathrm{f} = 20$ kΩ, $C_\mathrm{sub} = 1$ fF, and $Q_\mathrm{f} = 1$ nF. All parameters are held fixed except for Q_int which was varied from 1000, 100, and 10 nF for A, B, and C, respectively. Curve B' shows the spectra for Model 2 using the same parameters as curve B, but including a Bounded Warburg element in parallel with $\mathrm{CPE_{int}}$ ($Q_\mathrm{W} = 2 \times 10^6$ S $\mathrm{s}^{0.5}$, $B = 6.8 \times 10^{-2}$ $\mathrm{s}^{-0.5}$).

the frequencies above which the impedances of constant phase elements $\mathrm{CPE_f}$ and $\mathrm{CPE_{int}}$ fall below that of $\mathrm{R_f}$. A more precise definition would include the exponents a_f and a_int for the constant phase elements to account for the fact that they due have some in-phase (resistive) component. However, this correction is small given that a is typically 0.8 or greater, and the qualitative understanding of what the cutoff frequencies mean does not change.

The three orders of magnitude difference in the cutoff frequency arises from the equivalent difference in the value of the capacitances used to calculate curve A (1×10^{-6} F *vs.* 1×10^{-9} F for the interface and film capcitances, respectively). As the interfacial capacitance is decreased from curve A (1×10^{-6} F) to B (1×10^{-7} F) to C (1×10^{-8} F), we see the breadth of the plateau diminishes and the maximum phase angle reached decreases. Correspondingly, the semicircle motif in the Nyquist plot becomes less complete. In practice, the difference between the capacitance values is often small, and the resistance is therefore more difficult to fit precisely. This issue can arise from poor contact between the electrode and electrolyte film, which results in an artificially small interfacial capacitance. Other factors more specific to the IDE-thin film configuration are discussed at length in later parts of this chapter.

The circuit elements in Model 1 accurately reflect the physical processes apparent in the measurement of PEO-LiTFSI on these IDEs, as indicated by the qualitative similarities between the experimental data in Figure 4.3 and the simulated impedance shown in Figure 4.5. Indeed, the fitting curve in Figure 4.6a shows that Model 1 accurately captures the impedance response of the system in the relevant high and intermediate frequency regimes, and the film resistance can be extracted with confidence. The film resistances obtained by fitting the experimental data to this equivalent circuit are plotted in Figure 4.7. There is a clear linear relationship between the interelectrode spacing and the measured resistance of the film. As discussed in the previous chapter, the cell constant for this system, given by Equation 4.1 predicts a linear relationship between electrode distance and film resistance when several appropriate assumptions are included.

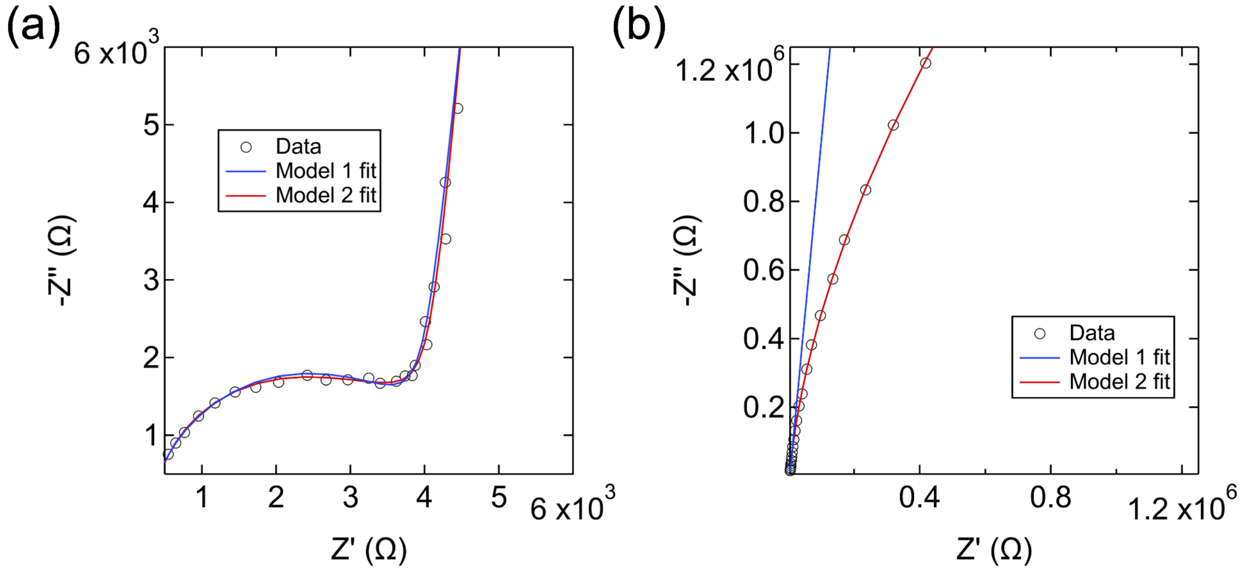

Figure 4.6 – Experimental impedance data for IDEs with $d = 2$ µm, $w = 2$ µm coated by 50 nm PEO-LiTFSI film at 70 °C, and fits to Model 1 and Model 2. The same impedance data and fits are shown in (a) and (b) at different scales.

$$\sigma = \frac{d}{R(N-1)lh} \tag{4.1}$$

It is important to note that the method of conformal mapping used to arrive at this equation assumes that the electrode teeth are sufficiently long relative to the electrode width such that fringing effects near the edges are negligible and describing the electric field distribution can be simplified to a two-dimensional problem. In all our electrode designs, the length of the electrodes is several hundred times the electrode width, and therefore this assumption is reasonable. Furthermore, the large number of teeth allows us to neglect the fringing effects near the edge of the array, as they will be negligible for most of the interdigitated electrode teeth.[118] All formulations of the IDE cell constant based on conformal mapping result in the same dependence on the number and length of teeth, and we therefore do not vary those parameters in this study. However, changing these parameters may be necessary for other material systems to ensure that the measured film resistance values are within the measurable range of the instrumentation.

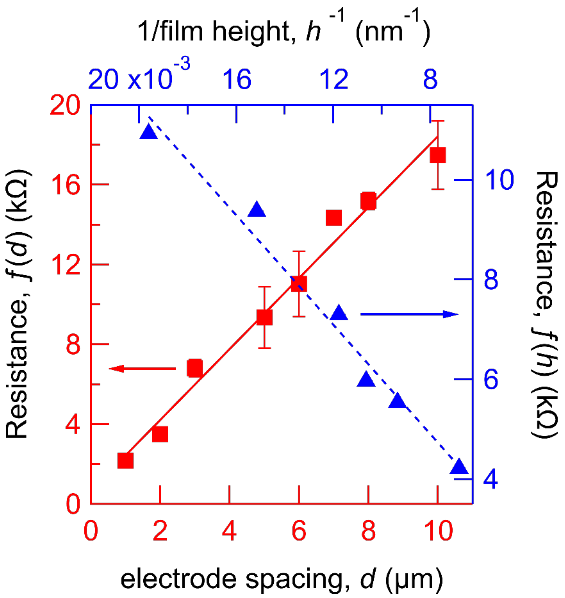

Figure 4.7 – Measured resistance values, R_f, obtained from fitting to Model 2 as a function of d (red, left axis) and h (blue, right axis)

We then spin coated films of different thickness on IDEs with constant $d = 8$ μm and $w = 2$ μm to validate the dependence of the measured resistance on film thickness. PEO-LiTFSI of varying height are cast from the same solution of polymer and salt, diluted as necessary to produce thinner films. The ratio of $[\mathrm{Li}^+]/[\mathrm{EO}]$ is kept constant for all films, and therefore the conductivity is not expected to differ. Films with heights ranging from 50 nm to 110 nm were prepared. The resistance values obtained by fitting the data to Model 1 is shown in Figure 4.7. As predicted by Equation 4.1, the relationship between R_f and h is linear for all heights tested here, and the conductivity is the same for all films thicker than 40 nm. Moreover, the calculated conductivity at 70 °C (9×10^{-4}) is similar to what has been measured in thick film studies, giving us confidence that the thin film and IDE configuration can be used to accurately determine bulk material properties.[42] 50 nm films were used for the remainder of this study.

This validation of Equation 4.1 for resistive thin film polymer electrolytes allows one to convert the measured resistance to conductivity by a simple, linear relationship. This powerful approach to measuring polymer electrolyte conductivity does, however, require careful consideration of the geometric parameters of the system. IDEs must be designed such that the necessary assumptions can be made to use Equation 4.1, chiefly that the film height be vanishingly small compared to the interelectrode distance. Moreover, it must be demonstrated that there is no dependence of the measured film resistance on the width of the electrodes (w).

4.2.2 Effect of electrode surface area on the impedance response of the system

We measured the impedance behavior of IDEs with constant spacing ($d = 2$ μm) and different electrode width ($w = 1$–5 μm) to determine the effect of the electrode width, and therefore electrode surface area, on the electrochemical response of the system. The Nyquist and Bode plots from these experiments are presented in Figure 4.8. As we expect from Equation 4.1, the Nyquist semicircle radius does not change significantly with increasing w (Figure 4.8a). However, as the width of the electrode is increased, the transition from the semicircle to the low-frequency capacitive tail becomes less sharp. This can also be visualized by the increase in the maximum phase reached in the Bode plot (Figure 4.8c) and the broadening of the resistive plateau in the total impedance (Figure 4.8b). The polymer-electrode interfacial area increases proportionally as the electrode width increases. The interfacial capacitance—equal to the product of the electrode surface area (A) with the specific capacitance of the electrode (C_0)—should therefore also increase with w. In the simulated impedance spectra shown in Figure 4.5, Q_{int} is varied to illustrate its effect on the overall shape of the impedance curves. As noted by Huggins, a large difference in the high and low frequency capacitance values will lead to a more complete semicircle in the Nyquist plot.[112] A corresponding increase in the breadth of the resistive plateau is seen in the Bode plot as the cutoff frequency between regimes II and III is shifted towards lower frequency. This is demonstrated in the simulated impedance and may explain the change in the measured impedance data in Figure 4.8.

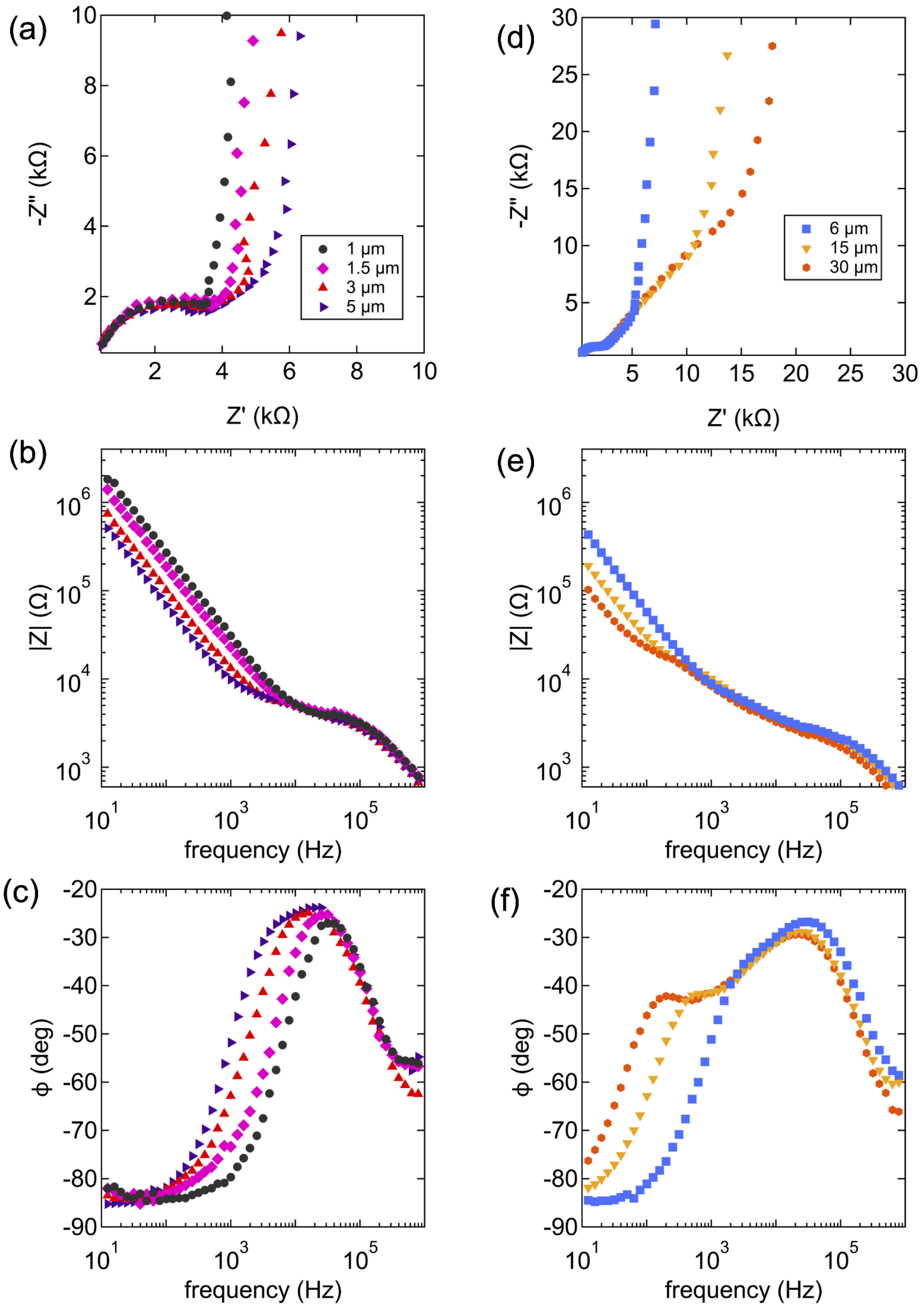

Figure 4.8 – Impedance spectra for IDEs with d = 2 µm, w = 1–30 µm coated by PEO-LiTFSI, shown by (a, d) Nyquist plots and (b, c, e, f) Bode plot, at 70 °C

A more dramatic qualitative change to the impedance curves is made even evident when the electrode width is increased further. The experimental data shown in Figure 4.8d–f demonstrates the predicted increasing resistive plateau width; however, the qualitative shape of the impedance spectra changes at higher widths. When measurements are taken on IDEs with $w > 5$ µm, it becomes apparent that the plateau region is accompanied by a secondary process not predicted by Model 1. This process is manifest in the apparent shoulder seen in the Bode phase plot in the 1–10 kHz frequency range (Figure 4.8f). The poor fitting of Model 1 to a device with $d = 2$ µm, $w = 7$ µm geometry is evident in Figure 4.9, where the transition from the high frequency semicircle to low frequency tail is not modeled well. Fitting this portion of the impedance spectra is crucial to determining the film resistance, and therefore understanding this secondary process is critical.

4.2.3 Modeling diffusional processes in thin films on IDEs

Model 1 is clearly missing the required circuit elements to capture the full impedance spectra produced by high-width IDEs. The lower frequency range, in particular, is poorly captured by this equivalent circuit. The large electrode area, relative to the thickness of the film, creates a significant interfacial region not present in bulk measurements. The low frequency behavior ($f < 1$ kHz), therefore, might be attributable to diffusional or absorptive processes that are observed in measurements of thin films or confined layers.[146,147] To describe such behavior, the Warburg element—a specific type of constant phase element—is used in equivalent circuit models to describe diffusional process and was selected as a starting point for our analysis. The Warburg element arises from the solution to the equations describing diffusion in electrochemical systems using semi-infinite boundary conditions.[147] This assumes that the electroactive species diffusing in the polymer electrolyte toward the electrode are not affected by the finite dimensions of the film, but rather experience a constant concentration of charged species in the bulk. In thin films this assumption is valid only at certain frequencies. At low enough frequencies the AC cycle is long enough for the ions to traverse distances on the order of the length scale of the system.[147] To account for the limiting dimensions of the system we replace the standard Warburg element with a finite, or bounded, Warburg element (sometimes referred to as an T-element).

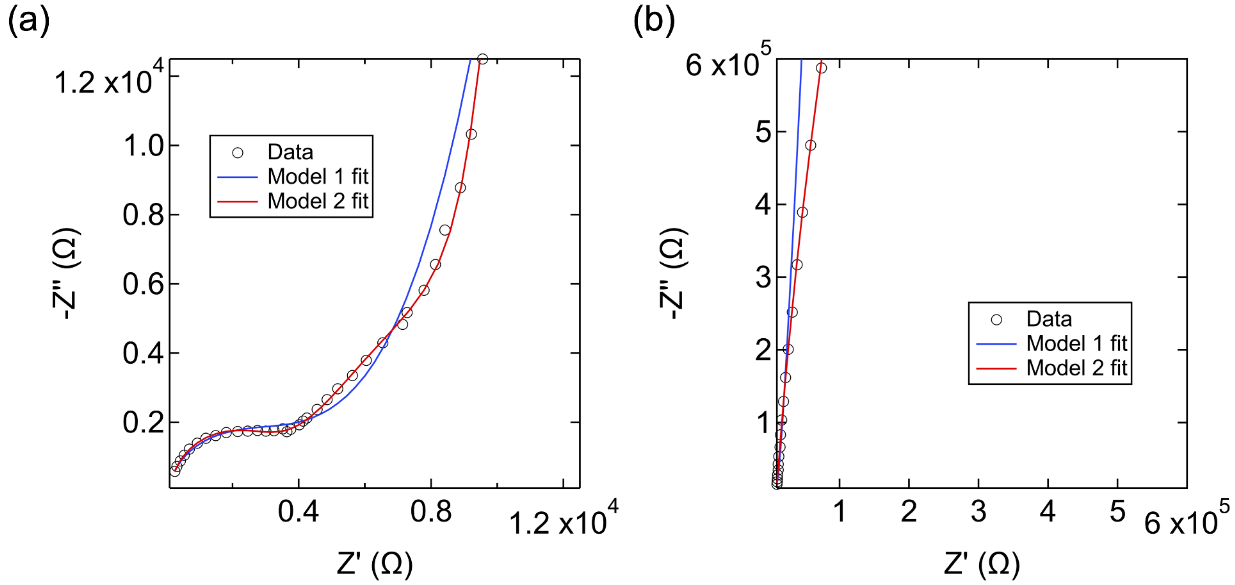

Figure 4.9 – Experimental impedance data for IDEs with $d = 2$ µm, $w = 7$ µm coated by 40 nm PEO-LiTFSI film at 70 °C, and and fits to Model 1 and Model 2. The same impedance data and fits are shown in (a) and (b) at different scales.

Model 2 (Figure 4.4b), which includes a bounded Warburg element in parallel with the interfacial CPE, accurately modeled the EIS data produced by high width electrode IDEs. As can be seen in Figure 4.9 the impedance spectra for high width devices ($w = 7$ µm) was fit well only by Model 2, even in the high frequency (low impedance) regime. As a secondary, diffusion-like process becomes more obvious in the frequency range of the resistive plateau, the deviation in the calculated film resistance by the two equivalent circuits models increases as well. Moreover, while Model 1 does accurately obtain the film resistance for low width ($w < 3$ µm) IDEs, Model 2 is necessary to fully capture the low frequency ($f < 100$ Hz) behavior of the system (Figure 4.6b). Although, it is not strictly necessary to use Model 2 to obtain conductivity values for some IDE designs, Model 2 gives a more accurate description of the total impedance spectrum and is therefore used to obtain the resistance values reported in this chapter.

The finite Warburg element has been previously used in systems involving confined geometries and blocking boundaries such as thin films and porous materiales.[147–149] At high frequencies where the AC cycle is too short for the finite dimension of the film to be relevant, the finite Warburg is identical to the standard Warburg element. At lower frequencies, where the finite expression is necessary, the response of the finite Warburg element includes an additional term, $\coth(B\sqrt{j\omega})$ where $B = \frac{\delta}{D}$. Here δ is the thickness of the film and D is the diffusion coefficient. This term considers the length scale of diffusion and the diffusion coefficient of the electroactive species. As can be seen by curve B' in Figure 4.5, the addition of a bounded Warburg can introduce a similar bend located somewhere between regimes II and III. Previous studies which have invoked this finite Warburg element have also included additional elements such as a resistor and capacitor in series with the Warburg element to model the adsorption kinetics of ionic species at the electrode interface.[145,150] The more detailed version of Model 2 which includes these elements is presented in the Supporting Information of *ref.* [134], and may be a considered a starting point for other studies of thin film electrolytes. We found, however, that the inclusion of a bounded Warburg element alone was sufficient to model these systems.

In the coplanar electrode design, the confined diffusional process could be associated with two possible length scales. First, in the case of vertical diffusion of the ions away from the electrodes, the film thickness (approx. 50 nm) is the limiting dimension. Second, the distance between the electrodes (2 µm) is the limiting dimension in the case of ions diffusing horizontally between electrodes. The frequency at which this finite diffusion begins to occur can be predicated by simple dimensional analysis, $f_{\mathrm{d}} = D/L^2$.[147] Here D is the diffusion coefficient of Li^+ or TFSI^- ions in PEO at 70 °C (1×10^{-7} cm^2 s^{-1} or 3×10^{-7} cm^2 s^{-1}, respectively), and L is the film thickness in the direction of ion transport.[151] For 2 µm and 50 nm lengths the predicated values for f_d are 2–8 Hz and 4–12 kHz, respectively. As can be seen in Figure 4.8d and Figure 4.8e, the diffusional shoulder appears in the kHz regime, implying that the diffusional process we observe occurs in the vertical direction.

Although Equation 4.1 predicts no relationship between the film resistance and the electrode width, we do observe a change in the overall impedance spectra produced by high-w devices. Large electrode area devices are accompanied by a secondary response in the resistive plateau region, which we attribute to diffusion of ionic species through the vertical direction of the film. It is clear from this that the diffusional processes—which can be described by the bounded Warburg element—are present in all our measurements. In some configurations, it is more evident in the frequency regimes of interest to resistance measurements. When the appropriate equivalent circuit is used to the model the EIS data from these high width devices, the diffusion parameters and the film resistance can still be extracted with confidence. However, in the most extreme cases, these measured resistance values appear to deviate from the predicted values.

4.2.4 Resistance values deviate from expectation at high electrode metal fraction

The measured resistance obtained independently by varying the d and w of the IDEs can be plotted together to understand the effect of varying the ratio of these two parameters. Figure 4.10 presents the measured film resistances as a function of electrode metal fraction, η ($\eta = w/(d + w)$). The resistance values predicted by Equation 4.1 are shown as a solid line for the IDEs with constant $d = 2$ µm, and a dashed line for the IDEs with constant $w = 2$ µm. There is a strong agreement between the predicted and measured values when $\eta < 0.8$. At higher metal fractions, there is a slight deviation from the predicted values, as the experimentally determined resistance is slightly lower than anticipated. However, in the low to moderate metal fraction regime, these experimental observations validate the simplifying assumptions discussed previously to justify using Equation 4.1 when $h \ll (d+w)$ in coplanar electrode devices. There are several possible explanations for the slight decrease in measured resistance on the high width IDEs.

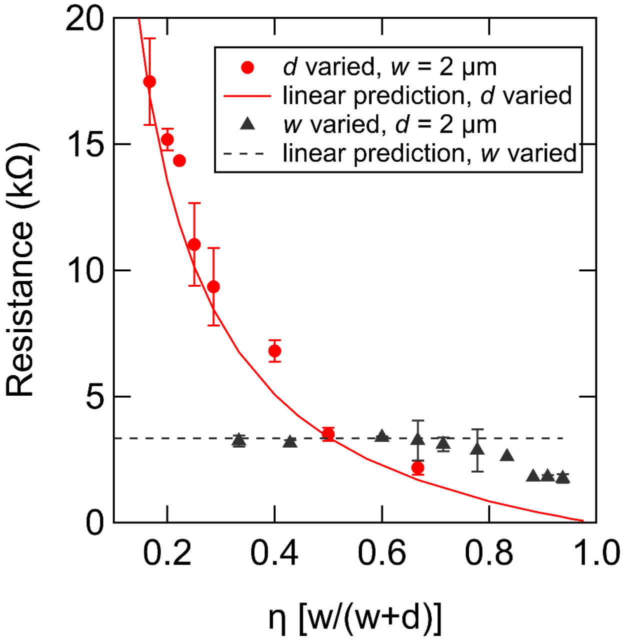

Figure 4.10 – Resistance values obtained by fitting EIS data to Model 2 versus the electrode fraction (η) at 70 °C. The solid red line represents the resistance values predicted by Equation 4.1 for increasing distance with a constant 2 µm electrode width. The dashed black line represents the predicted resistance for increasing width with a constant 2 µm spacing.

The high electrode fraction relative to the electrode spacing may bring into question the validity of the assumptions made to arrive at Equation 4.1. When thicker films ($h \geq w, d$) are measured using IDEs the measured resistance is expected to decrease as a function of electrode width. This is due to the increase in the thickness of the film that would be subject to the electric field, as these wide electrodes are able to produce longer field lines. However, this is unlikely to be the case here, as the film height is already much smaller than the maximum penetration depth of the electric field produced by the electrodes. As discussed by Chen and coworkers, the effective width of the electrodes approaches zero as the ratio of h/d approaches zero.[127] As shown in Chapter 3, the electrodes in our IDEs behave essentially as point sources, and the high electrode width should not drastically alter the electric field felt by the polymer film. We expect that in the limit of very thin films, the electric field should be nearly uniform through the material. However, these extreme electrode fraction regimes have not previously been experimentally explored, and the fringing effects on the electric field distribution caused by these wide electrodes might not be accurately portrayed by Equation 4.1.

It is also possible that the gold substrate meaningfully changes the measured resistance of these films. It is known that in thin films the substrate material strongly influences the structure and properties of the overlying polymer film.[152] Weaker interactions between the PEO electrolyte and the gold electrode (compared to interactions with the interelectrode SiO_2) might result in changes in the measured ionic conductivity. In calculating the predicted resistance shown in Figure 4.10, it is assumed that the material conductivity was the same for all films spin cast from the same solution. If, however, the actual film conductivity deviates due to the substrate-polymer electrolyte interactions, our prediction for the expected resistance would be inaccurate. More about the differences between the gold and silica interfaces are discussed in the next part of this chapter.

4.2.5 Guiding principles for selecting IDE geometry

The above experiments demonstrate that the choice of IDE geometry can significantly influence the measured impedance of the same polymer electrolyte film. Without careful consideration, impedance responses can be mistakenly attributed to the wrong elements, and incorrect values for film resistance obtained. In this work, we attempt to formulate guiding principles that will help to reduce these possible errors and to the selection of the appropriate IDE design. Equation 4.1 can reasonably be used to describe the cell constant of nano-thin films on micron-scale IDEs. However, it is strictly necessary that the spatial frequency of the IDE be much larger than the film thickness ($d + w \gg h$) to simplify the analysis of the cell constant to the linear form of Equation 4.1.

To characterize capacitive and diffusional processes, which become prominent in thin film configurations, more complex equivalent circuits are needed. This is necessary to confidently extract a film resistance from the impedance spectra. Although the EIS data appears to be fit well by Model 2 for all IDE configurations, at very high electrode fraction ($\eta > 0.8$) the measured resistance deviates considerably from the expected values predicted by Equation 4.1. At lower electrode fractions ($\eta < 0.8$) Equation 4.1 accurately predicted the measured resistance of the polymer electrolyte films. While the width of the electrodes must be large enough to thoroughly sense the entire film and produce a broad resistive plateau, the interelectrode distance must then be sufficient enough to prevent behavior owing to an excessively high electrode fraction. This in turn must be balanced by the desire to fabricate IDEs which can measure over a wide range of resistances, allowing for a single device geometry to be used to study the effects of electrolyte salt concentration, polymer chemistry or molecular weight, and system temperature, all of which change the film conductivity by several orders of magnitude.

4.2.6 Temperature dependent impedance response of thin film polymer electrolytes

One can glean information about the molecular-scale mechanisms of ion transport by observing the relationship between the film ionic conductivity and temperature. With the relationship between IDE geometry, measured resistance, and electrolyte conductivity well-understood, we measure conductivity of thin films of PEO-LiTFSI across a temperature range from 70 to 130 °C. The full temperature dependence of the ionic conductivity for PEO-LiTFSI on IDEs ($d = 8$ µm, $w = 2$ µm, $\eta = 0.2$) is presented in Figure 4.11. The heating and cooling cycles showed little hysteresis, implying that these electrolytes are thermally stable up to at least 130 °C on IDEs with low metal fraction.

Previous works have fit temperature-dependent conductivity data to a Vogel-Tammann-Fulcher (VTF) equation, $\sigma = A\exp[-E_\text{a}/(R(T - T_0))]$.[153] This model is more broadly use to describe the temperature dependence of any process that is intrinsically related to the

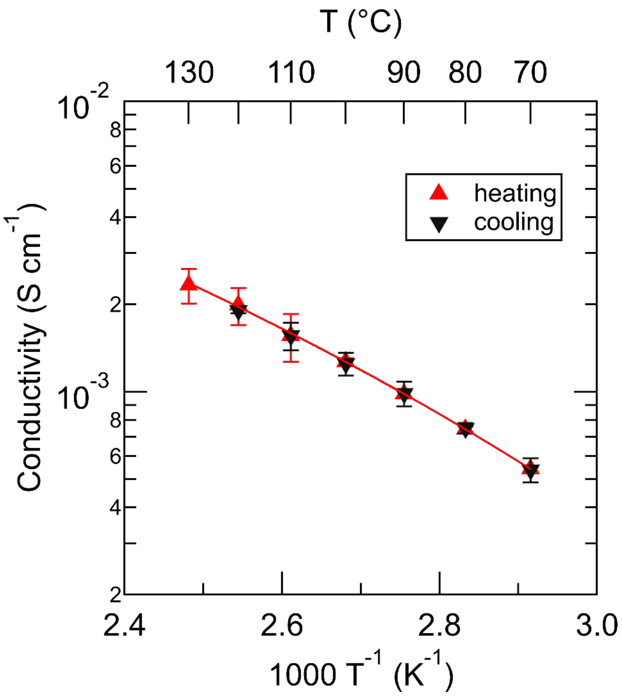

Figure 4.11 – Temperature dependence of conductivity for PEO-LiTFSI measured on top of IDE with d = 8 µm, w = 2 µm, η = 0.2. The solid red line represents the data for the heating cycle fit to the Vogel-Tammann-Fulcher equation using a least squared regression method. The obtained fitting parameters were $A = 0.150 \pm 0.038$ (S cm^{-1}), $E_\mathrm{a} = 7880 \pm 773$ (J mol^{-1}), and $T_0 = 174.4 \pm 8.9$ (K).

segmental dynamics of the polymer, such as viscosity or glass transition. The conductivity data taken from the cooling cycle are well fit by a VTF model. The fitted value for T_0 of 174 K is close to the commonly used value of $T_0 \approx T_\mathrm{g} - 50$ K ($T_\mathrm{g} \approx 223$ K for PEO-LiTFSI).[84] Moreover, the values of A and E_a (0.15 S cm^{-1} and 7880 J mol^{-1}, respectively) make sense physically and are in good accord with previously reported values.[153] The fact that the measured conductivity is well fit by this model implies that the same segmental dynamics that underpin ionic mobility in bulk samples are observed in nanothin films as well. Moreover, the values for conductivity measured here match those measured previously for the PEO-LiTFSI system.[42] Despite the dimensions of the film and large substrate interfacial area, the mechanism of ion transport is not altered drastically, and the bulk conductivity of the material can be reliably determined.

4.2.7 Thermal stability of thin polymer electrolyte films

Spin coating of polymer electrolytes from dilute solutions can produce smooth, high-quality films. However, these films can exhibit instability upon thermal treatment, causing changes in their structure due to rupture or dewetting. To investigate the thermal stability of PEO-LiTFSI films, we measured their impedance behavior before and after the thermal cycling. Figure 4.12a presents Nyquist plots of a heating cycle of IDE ($d = 2$ µm, $w = 2$ µm, $\eta = 0.5$) coated with PEO-LiTFSI. As expected, the semicircle radius decreases when the temperature is raised from 70 to 130 °C, indicating a lower resistance. When the film is cooled back to 70 °C after half an hour at 130 °C, the measured impedance is almost identical to the initial measurement. As expected, similar initial resistance is measured on an IDEs with the same spacing and higher width ($d = 2$ µm, $w = 7$ µm, $\eta = 0.78$) at 70 and 130 °C (Figure 4.12b). However, when the film is cooled back down to 70 °C, the resistance has increased significantly.

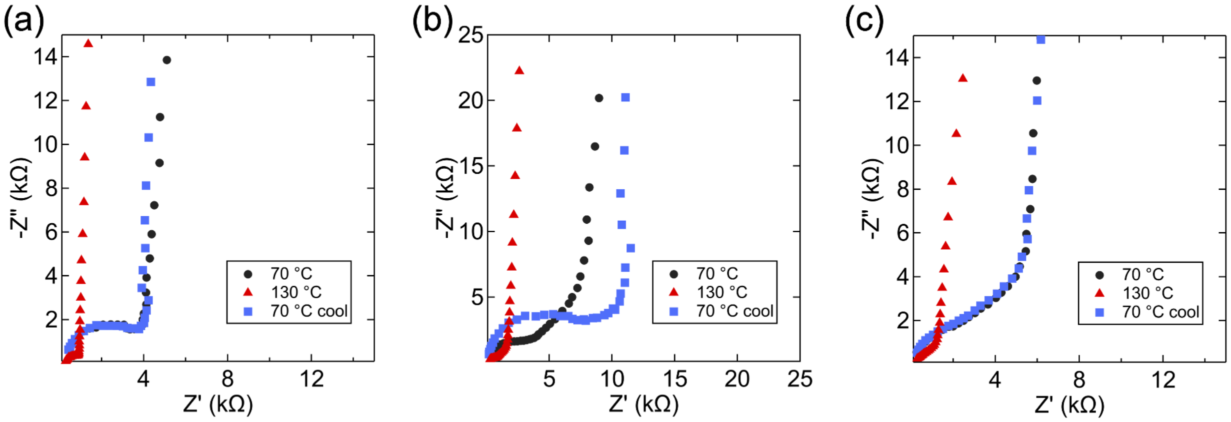

Figure 4.12 – Nyquist plots showing measurements of PEO-LiTFSI made at 70 °C, then 130 °C, and then again after cooling to 70 °C for IDEs with (a) $d = 2$ µm, $w = 2$ µm, $\eta = 0.5$ (b) $d = 2$ µm, $w = 7$ µm, $\eta = 0.78$ and (c) $d = 2$ µm, $w = 7$ µm, $\eta = 0.78$ with 1 nm of SiO_2 passivation layer

This increase in resistance at elevated temperature also exhibits a time dependence. As can be seen in Figure 4.13, EIS measurements made over the course of several half hour intervals at 130 °C show a steady increase in the total impedance of the film. This irreversible change in impedance implies that the PEO film is thermally unstable when coated on high metal fraction IDEs. Interestingly, however, Kramers-Kronig fitting of this data suggests that the measurement itself is stable (Figure 4.13b). This suggests that the instability of the thin film that results in thermal hysteresis proceeds over longer time scales than the impedance measurement itself. Although the thin film is changing slowly over time, over the roughly 1 min required for an individual impedance measurement, the system is stable.

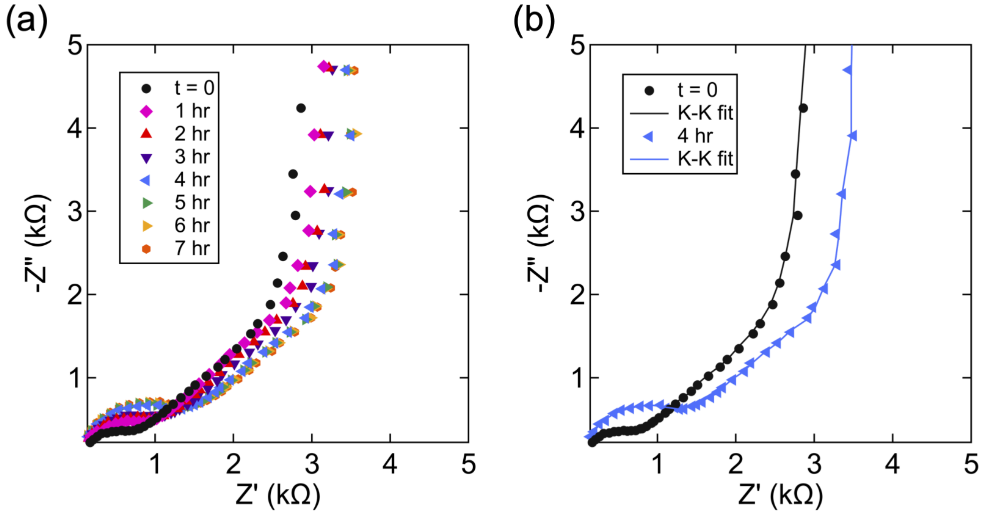

Figure 4.13 – (a) Impedance of PEO-LiTFSI on d = 2 µm, w = 7 µm, η = 0.78 IDEs over the course of several hours at 130 °C; (b) Kramers-Kronig fitting of selected data from (a)

4.2.8 Passivation of IDEs with thin dielectric layers

The observed thermal instability is evident only for high Au electrode fraction IDEs. We therefore suspect that the effect is related to the polymer-gold interface. To eliminate the influence of the Au interface, we passivated the entire IDE with 1 nm of SiO_2 by plasma-enhanced ALD. This process conformally coats the device, removing any direct contact between gold electrode and the polymer film. The temperature dependent Nyquist plots of PEO-LiTFSI films on passivated high electrode fraction IDEs (d = 2 µm, w = 7 µm, η = 0.78)—those which previously presented thermal instability—are presented in Figure 4.12c.

When the film is heated to 130 °C and cooled down back to 70 °C, no changes in the measured impedance spectra are observed. The passivation of the gold electrodes by a thin layer of SiO_2 is sufficient to stabilize the polymer film interface at elevated temperatures.

The increase in resistance after heating on high-η IDEs might be caused by dewetting of the film from the gold electrode. Previous studies have demonstrated that elevated temperature and incompatible surface energies can cause thin polymer films to dewet.[154] Even a small degree of dewetting from the surface of the IDE could result in an apparent increase in film resistance. Unlike in other reports of PEO thin films[155], we do not observe any macroscopic dewetting of the film surface above gold electrodes on unpassivated IDEs, as observed by optical and atomic force microscopy, even after heating the films to 130 °C. However, thin films might become detached only at the innermost regions of the film near the substrate, while the outermost layer of the film—that which can be observed by optical or scanning probe microscopes—remains homogeneous.[156]

It has been suggested that imperfect attachment of the film to the electrode is more pronounced on rougher substrates.[156] The roughness of the gold electrodes (root-mean-squared roughness around 1.5 nm, as measured by AFM) could induce detachment of the film from the IDE near the surface. An AFM micrograph of a gold IDE electrode and interelectrode SiO_2 is shown in Figure 4.14a. After passivating with a layer of SiO_2 by ALD, the roughness of the electrode surface is considerably lower than that of the e-beam evaporated gold (Figure 4.14b). This effect may account for the improvement in the thermal stability of the passivated devices. Nevertheless, the unambiguous change in the measured impedance implies an intimate relationship between the polymer-substrate interactions and the electrochemical response of the system.[1]

The shapes of the Nyquist plots of the electrolyte measured on a passivated IDE is

---

1. Note that these AFM images are from IDEs fabricated using the negative photoresist process described in Section 3.2.1, whereas the EIS measurements for this chapter were made using the positive photoresist process described in Section 3.2. The arguments about how and why the surface passivation inhibits film dewetting should not be affected by the choice of fabrication process, however.

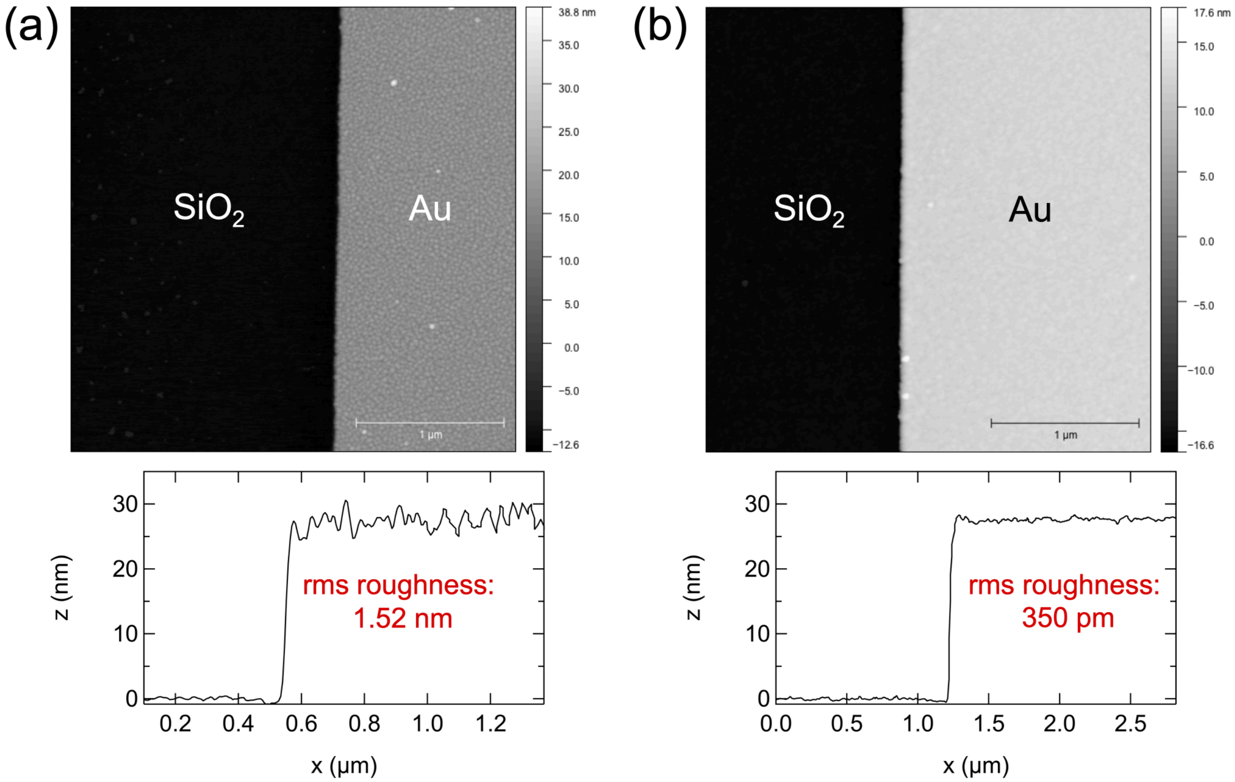

Figure 4.14 – AFM height maps of Au electrodes (a) before and (b) after passivation with 1 nm SiO_2

qualitatively similar to the unpassivated one. As can be seen from Figure 4.12c, both spectra include a partial semicircle followed by a diffusional slope, ending with a nearly vertical capacitive line. The point at which the extrapolated semicircle would cross the real axis (the film resistance) for both IDEs is identical. However, we do see a less complete semicircle in the Nyquist plot produced by the SiO_2-passivated IDEs. These changes to the impedance spectra resemble the change from curve A to curve C in Figure 4.5c, indicating an effective decrease in the effective interfacial capacitance. We expect this to be the result of decreased polarization of the interface resulting in a smaller effective electric double layer capacitance.

We measured the behavior of identical IDEs covered by PEO-LiTFSI with oxide layers of different thickness to explore the influence of the passivating layer on the impedance spectra. Figure 4.15a presents the Nyquist plots of IDEs (d = 8 µm, w = µm, η = 0.2) passivated

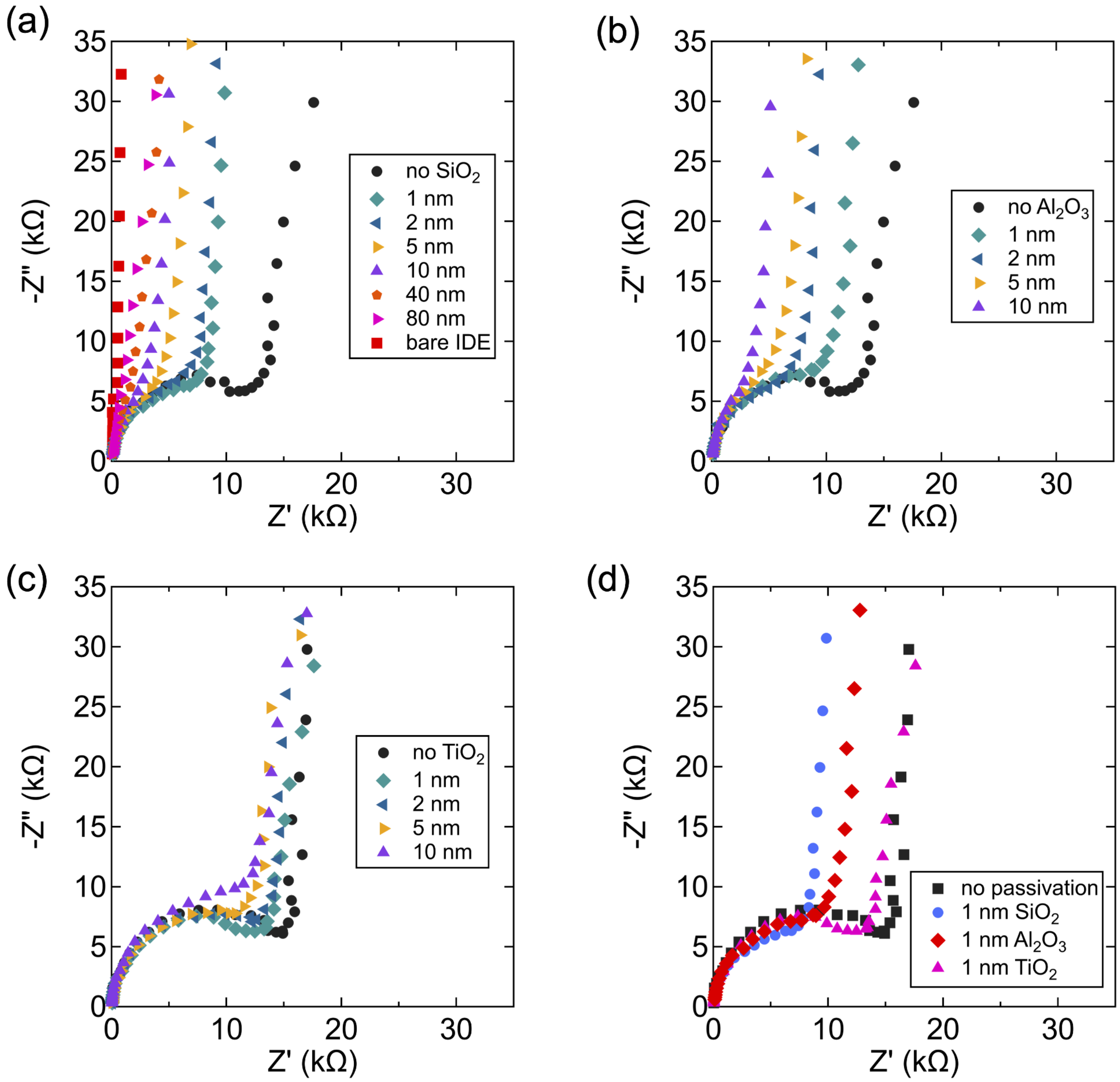

Figure 4.15 – Impedance of PEO-LiTFSI on IDEs ($d = 8$ µm, $w =$ µm, $\eta = 0.2$) passivated by different thicknesses of (a) SiO_2, (b) Al_2O_3, and (c) TiO_2; (d) comparison of IDEs passivated by 1 nm of different oxide materials

by different thicknesses of SiO_2 at 70 °C. Increasing the thickness of the dielectric leads to a reduced semicircle motif, but does not affect the radius of the extrapolated semicircle. When the passivating layer of SiO_2 exceeds 10 nm, the semicircle corresponding to the film resistance effectively disappears, and the impedance behavior approaches the purely capacitive line of the bare IDE (*i.e.* no polymer electrolyte coating). Nevertheless, we found that if the passivating layer is less than 5 nm thick, the resistance value can still be obtained by fitting to an appropriate equivalent circuit.

Although we did not change the electrode surface area or the film properties, we observed a decrease in the effective interfacial capacitance. The major contribution to the interfacial capacitance in such electrochemical systems is usually due to the formation of an electric double layer. The formation of this double layer depends on the potential difference which exist at the electrode–electrolyte interface. The introduction of a dielectric barrier between the conductive electrode and the polymer can cause a potential drop, resulting in a smaller effective double layer. This trend is confirmed by the similarity of the Nyquist plots in Figure 4.15a and the simulated curves in Figure 4.5. Lee *et al.*, reported on similar behavior of electrolyte solutions and electrodes passivated by thin Al_2O_3 layers.[157] They suggest that at thicknesses of more than 2 nm the interfacial capacitance is dominated by the passivating dielectric, not the double layer. A decrease in the interfacial capacitance was also observed when self-assembled monolayers were located between the electrode and the electrolyte solution.[158]

The aim of the aforementioned studies was to investigate the influence of the passivation layer on either faradaic reactions or the capacitive behavior of the monolayers themselves, whereas in this study, the desired measurement is the film resistance of a solid electrolyte. In this regard, increasing the dielectric thickness qualitatively alters the EIS spectra, thereby making interpretation more challenging. The interfacial capacitance decreases as the passivating layer thickness increases, and the cutoff frequency delineating regimes II and III is shifted to a higher frequency. Correspondingly, the semicircle feature is distorted, thus hampering our ability to extract meaningful parameters such as the film resistance by equivalent circuit modeling.[147] As long as the effect of the passivation layer is kept sufficiently small, however, resistance values can still be extracted from the impedance spectrum.

Passivation by other dielectric materials

It appears that the impedance quality of passivated IDEs is largely driven by a drop in interfacial capacitance, which in turn should primarily be a function of the passivation layer thickness and relative permittivity (ε_r) To explore the this, IDEs were passivated with different semiconducting materials. Nyquist plots of IDEs coated by Al_2O_3 with different thicknesses are presented in Figure 4.15b. The spectra produced are qualitatively similar to those of the SiO_2 covered IDEs. It does appear, though, that the Al_2O_3 has a less dramatic impact on the interfacial capacitance and therefore the EIS quality than SiO_2. We suggest that the higher permittivity of the Al_2O_3 layer leads to a lower voltage drop at the interface, and thus a slightly higher effective double layer formation near the electrode. Therefore, the effective interfacial capacitance is higher, and the cutoff frequency for regime III shifts to a lower value. The use of aluminum oxide rather than silicon oxide does not substantially change the measured resistance value as obtained by fitting to Model 2.

The permittivity of Al_2O_3 ($\varepsilon_\mathrm{r} \approx$ 7–9) and SiO_2 ($\varepsilon_\mathrm{r} \approx$ 3–6) are comparable, and so the observed changes are minor. To enhance any effects of changing the dielectric constant of the passivating material, we covered IDEs with high dielectric TiO_2 ($\varepsilon_\mathrm{r} \approx$ 60–100).[159] As can be seen from the Nyquist plots in Figure 4.15c, the effect of the passivating layer is much less dramatic with high permittivity TiO_2 than with either the SiO_2 or Al_2O_3. Again, as the thickness of the passivating TiO_2 is increased, the completeness of the semicircule decreases. However, even at a thickness of 10 nm, a clear semicircle region is observed and modelled accurately. Figure 4.15d shows more clearly the effect of the dielectric constant on the quality of the impedance measurements. With the same 1 nm of passivating material, the TiO_2 passivated electrodes exhibit a much more complete semicircle in the Nyquist plot—nearly as complete as the unpassivated IDE. The SiO_2 and Al_2O_3 passivated devices, however, show a greatly diminished semicircle.

Figure 4.16a demonstrates clearly that the effective interfacial capacitance increases with

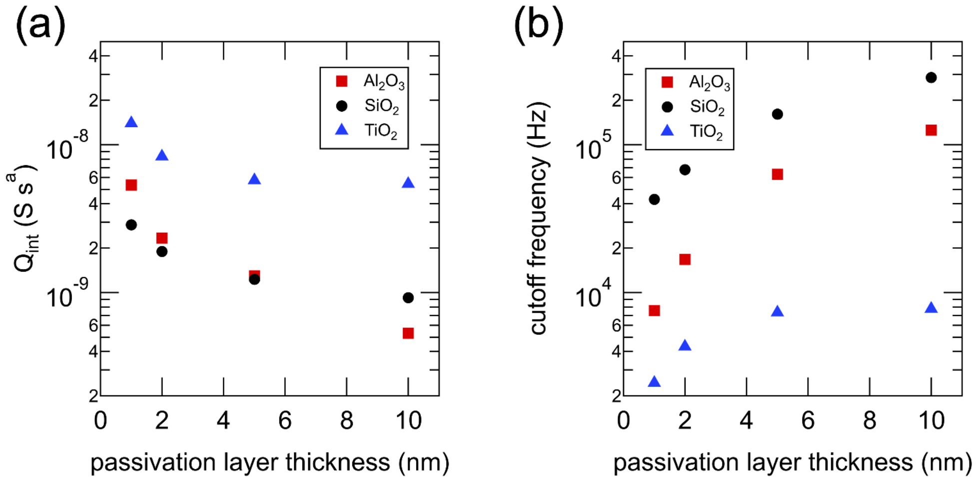

Figure 4.16 – Change in (a) Q_{int} and (b) cutoff frequency between regimes II and III as a function of passivation layer material and thickness. The cutoff frequency is taken as $1/(2\pi R_{\text{f}} Q_{\text{int}})$.

dielectric constant ($SiO_2 < Al_2O_3 \ll TiO_2$) and decreases with passivation layer thickness. This decrease in Q_{int} as the passivation layer thickness is increased corresponds to an increase in the cutoff frequency between regimes II and III (shown in Figure 4.16b). This cutoff frequency shift is a more quantitative way of considering the incompleteness of the semicircle motif in the Nyquist plots seen in Figure 4.15. Other properties of the dielectric film such as density, defects, surface chemistry and functionalization, or electron tunneling through the material could also influence the impedance response. These effects were not explored in this study, and they merit further investigation. Regardless, the observed trend implies that thin oxide layers with high dielectric constant can promote a significant enough capacitance at the dielectric-polymer interface to produce a broad frequency bandwidth from which to fit the film resistance. Most interestingly, perhaps, this allows for the possibility of using other materials with specific physical or chemical properties to be placed between the IDE surface and the electrolyte, without substantial loss of measurement quality. We predict that these dielectric interfaces will enable the study of polymer electrolytes in highly ordered films through directed assembly, and to explore the effect of various interfaces on ionic transport in these materials.

4.3 Conclusions

Here we have demonstrated a framework for investigating the electrochemical behavior of thin polymer electrolyte films. When the geometric parameters of the IDE and the dimensions of the thin films are properly accounted for, the measured ionic conductivity of PEO-LiTFSI electrolytes is comparable to previously reported literature values. However, in the process of validating the use of IDEs for studying polymer electrolyte behavior, we find that specific electrochemical responses can become prevalent with certain cell designs and experimental conditions. We show that diffusional processes near the electrode-polymer interface that may be absent or negligible in thick films become prevalent in thin film configurations. Additional circuit elements were introduced to model these processes, which became more apparent in high width IDEs. These models could also be useful for fully describing the electrochemical response of other systems with finite dimensions, including those which may exist in thick films of nanostructured materials. The interactions between polymer and substrate must also be considered in these measurements due to the high surface area to film thickness ratio. These interactions were most apparent on high metal fraction IDEs at elevated temperatures but were eliminated by passivating the devices with a thin layer of insulating oxide material. Passivation layers decreased the interfacial capacitance of the system, but this effect was less pronounced in thinner and higher permittivity dielectric layers. More importantly, the addition of an otherwise insulating layer of material between the electrodes and the polymer film did not drastically affect the ability to measure film conductivity.

These experiments validate the assumptions made in using Equation 4.1 to describe the cell constant for IDEs with different geometries. This simplified cell constant given by equation 1 makes analysis of polymer electrolytes by IDEs an attractive method. The geometric parameters of micron-scale IDEs can be readily measured by optical and atomic force microscopy to a high degree of accuracy. The ability to accurately control and measure the cell geometry by straightforward microfabrication and microscopy gives us greater confidence in our measurements and EIS analysis. In parallel plate systems, accurate measurement of the cell constant is not trivial and requires averaging of multiple experiments with a considerable degree of uncertainty. However, a single IDE may be reused multiple times, ensuring that the cell constant for each measurement is identical. In addition, measurements with different geometries of the same electrolyte provides a simple method for validating the accuracy of our measurements with minimal use of material, as a single measurement can be made with as little as 1 mg of polymer.

As demonstrated in this study, the bulk conductivity of PEO-LiTFSI can be measured in films as thin as 50 nm. The minimization of material required for such a study offers a compelling reason to use the IDE approach. Moreover, the thin film nature of these measurements will allow for the study of any interfacial effects that may enhance or inhibit ionic mobility in polymer electrolytes. Although PEO-LiTFSI is used here as a model system, this approach should be universally applicable to polymer electrolytes, both dry and humidified. By adhering to the guiding principles set forth in this study, the transport properties of any number of conducting materials may be quantified with a high degree of confidence.

While PEO-LiTFSI is used as a model system in this work, these techniques can be applied to a wide range of systems. This high throughput approach is ideally suited for rapid, high quality characterization of newly synthesized materials, and for screening potential candidate polymer electrolytes. The ability to fabricate films as thin as a few nanometers will also allow us to probe diffusional processes that occur in polymer electrolytes and how these limiting dimensions alter ion conduction in these films. Additionally, the ability to add a layer of insulating material allows for a wide range of tunable surfaces upon which to fabricate these polymer electrolytes, thus enabling us to study the effect of surface chemistry and morphology on transport phenomena in these films. This approach will provide insight into how structure, dimensionality, and molecular-scale interactions impact ion conductivity in polymer electrolytes.

4.4 Materials and Methods

4.4.1 Materials

Poly(ethylene oxide) (M_{n} = 20 kg mol^{-1}, $Đ$ = 1.1) was acquired from Polymer Source Inc, and lithium bis(trifluoromethanesulfonyl)imide (LiTFSI) (99.95%) was purchased from Sigma Aldrich. The polymer and salt were each dried overnight under vacuum at 60°C and 120°C, respectively, and subsequently stored in an argon glovebox. Acetonitrile (99.8%, anhydrous) was purchased from Sigma Aldrich. The positive photoresist (AZ MIR 703) and developer (AZ 300 MIF) were purchased from AZ Electronic Materials. Silicon wafers (4" diameter, 500 µm thick) with 1 µm of thermal SiO_2 were purchased from Pure Wafer Inc. IDEs were fabricated using positive resist according to the process described in Section 3.2.

4.4.2 Preparation of polymer electrolyte thin films

Polymer electrolyte solutions were prepared inside of an argon glovebox. First, solutions of 10 mg mL^{-1} polymer in acetonitrile and LiTFSI in acetonitrile were prepared and allowed to stir overnight. These solutions were then mixed in a 1:3.1 salt to polymer solution volume ratio to obtain solutions with the desired molar ratio of lithium cation to ether oxygen moiety ($r = [\mathrm{Li}^+]/[\mathrm{EO}]$) of 1/20. The PEO-LiTFSI salt solutions were allowed to stir overnight at room temperature.

Polymer electrolyte thin films were made by spin casting these solutions onto the IDEs. An identical film was cast onto bare, oxygen plasma cleaned silicon with native oxide from the same solution and at the same spin speed. The thickness of this witness sample was determined using ellipsometry (J.A. Woollam alpha-SE ellipsometer). It is assumed that a film cast from the same solution and at the same spin rate onto an IDE has identical thickness. This assumption was confirmed by scratching the film on an IDE and measuring the height of the film by atomic force microscopy (AFM). The film thickness determined by each of these methods differs by less than 2 nm.

4.4.3 Passivation of IDE surfaces by ALD

IDEs were passivated by different oxide materials using ALD. SiO_2 was deposited using an Ultratech/Cambridge Fiji G2 Plasma-Enhanced ALD tool, while Al_2O_3 and TiO_2 were both deposited in an Ultratech/Cambridge Savannah ALD tool. The ALD precursors used for SiO_2, Al_2O_3, and TiO_2 were SiH_4, $Al(CH_3CH_2)_3$, and $Ti(N(CH_3)_2)_4$, respectively. The aluminum and titanium oxides were produced with water as a secondary precursor, while silicon oxide is prepared with O_2 as the oxygen source.

4.4.4 Equivalent circuit model equations

The full equations used to calculate the predicted impedance spectra in Figure 4.5 are given below.

Model 1 equation:

$$Z_1 = R_\mathrm{s} + \left(j\omega C_\mathrm{s} + \left(\frac{1}{Q_\mathrm{int}(j\omega)^{a_\mathrm{int}}} + \frac{R_\mathrm{f}}{Q_\mathrm{f}(j\omega)^{a_\mathrm{f}} R_\mathrm{f}} \right)^{-1} \right)^{-1} \tag{4.2}$$

Model 2 equation:

$$Z_2 = R_\mathrm{s} + \left(j\omega C_\mathrm{s} + \left(\left(Q_\mathrm{int}(j\omega)^{a_\mathrm{int}} + \frac{Q_\mathrm{W}(j\omega)^{0.5}}{\coth\left[B(j\omega)^{0.5}\right]} \right)^{-1} + \frac{R_\mathrm{f}}{Q_\mathrm{f}(j\omega)^{a_\mathrm{f}} R_\mathrm{f}} \right)^{-1} \right)^{-1} \tag{4.3}$$

Chapter 5

Intrinsic Ion Transport Properties of Block Copolymer Electrolytes †

ABSTRACT

Knowledge of intrinsic properties is of central importance for materials design and assessing suitability for specific applications. Fundamental understanding of ion transport properties in self-assembled block copolymer electrolytes (BCEs), however, has been hindered by the difficulty in deconvoluting extrinsic factors, such as defects, from intrinsic factors, such as the presence of interfaces between the domains. In this chapter, we quantify the intrinsic ion transport properties of a model BCE system consisting of polystyrene-*block*-poly(ethylene oxide) (SEO) and lithium bis(trifluoromethanesulfonyl)imide (LiTFSI) salt using a generalizable strategy of depositing thin films on interdigitated electrodes and self-assembling fully connected parallel lamellar structures throughout the films. Comparison between conductivity in homopolymer poly(ethylene oxide) (PEO)-LiTFSI electrolytes and the analogous conducting material in SEO over a range of salt concentrations and temperatures reveals that between 20 and 50 percent of the PEO in SEO is inactive. Using mean-field theory calculations of the domain structure and monomer concentration profiles at domain interfaces—both of which vary substantially with salt concentration—the fraction of inactive PEO in the SEO, as derived from conductivity measurements, can be quantitatively reconciled with the fraction of PEO that is mixed with greater than a few volume percent of polystyrene. Despite the detrimental interfacial effects for ion transport in BCEs, at near optimum salt

---

†. This work was originally reported in *ACS Nano*, **2020**, 14, 7, 8902–8914

concentration the intrinsic conductivity of the SEO studied here (around 10^{-3} S cm^{-1} at 90 °C, $r = 0.085$) is an order of magnitude higher than values from bulk samples of similar molecular weight SEO measured by other groups (around 10^{-4} S cm^{-1} at 90 °C, $r = 0.085$). Overall, this work provides motivation and methods for pursuing improved BCE chemical design, interfacial engineering, and processing.

5.1 Introduction

The transition to solid-state electrolytes would eliminate the need for volatile, flammable organic liquid electrolytes in use today, making batteries inherently safer and more reliable.[160] One class of promising materials for this application are solid polymer electrolytes (SPE). Block copolymer electrolytes (BCEs) in which two or more blocks, self-assembled into phase-separated nanostructured morphologies, are of particular interest for this application, as they can be independently tuned to impart multiple desirable, yet orthogonal thermal, mechanical, and electrochemical properties to a single material system.[137] For example, one of the most widely studied systems, also of great practical importance, is a BCE consisting of polystyrene (PS), poly(ethylene oxide) PEO), and lithium salts such as lithium bis(trifluoromethanesulfonyl)imide (LiTFSI). The salt is solvated in the rubbery PEO, with each Li^+ ion associating with and charge stabilized by five or six ether oxygens of the PEO. Transport occurs by a hopping mechanism across solvation sites and is governed by the segmental dynamics of the PEO matrix.[20,24] Homopolymer PEO reaches application-relevant conductivities of 0.1 to 1 mS cm^{-1} above the PEO melting temperature (around 60 °C).[42,155] Unfortunately, the use of PEO homopolymer as an SPE is not practical for many battery applications due to its low mechanical stability in the amorphous state. Incorporating the PEO into a phase-separating block copolymer with, for example, PS, *i.e.* synthesizing polystyrene-*block*-poly(ethylene oxide) (SEO), and mixing with lithium salt is one approach to simultaneously achieve charge transport through an amorphous, ion-conducting phase (PEO) while maintaining good mechanical properties, owing to a glassy, insulating block (PS).[66] Consistent with this concept, SEO and other promising BCEs that form a number of different morphologies and block architectures, including those self-assembled from linear BCEs such as 1D hexagonally-packed cylindrical, 2D lamellar, and 3D gyroid networks phases have been investigated.[87,143,161–164] Various nonlinear BCEs have been developed as well, such as brush and star shape copolymers, exhibiting more complex nanostructured morphologies.[165,166] A common challenge in the investigation and development of nanostructured BCEs is that the well-defined, self-assembled morphologies typically extend over only microscopic length scales, but path-dependent properties such as conductivity are characterized over macroscopic length scales or in bulk samples through complicated, randomly oriented grains and defect structures. Extrinsic, processing-dependent properties are therefore convoluted with intrinsic, fundamental material properties which renders the development of quantitative structure-property relationships at all length-scales difficult or impossible.

Independent knowledge of extrinsic and intrinsic material properties provides complimentary information for the development of BCEs as SPEs. The intrinsic or maximum conductivity determines, for example, if a particular material has potential to meet application-specific constraints such as the requirements to serve as the electrolyte in a Li-ion battery under the ideal circumstances and broadly provides the framework to evaluate, compare, and design new and improved materials. Moreover, knowledge of intrinsic material properties in conjunction with extrinsic material properties provides the basis to assess if process development, rather than new materials synthesis, is warranted to meet those same application-specific constraints. The interplay between extrinsic and intrinsic properties, and the complexity in deconvoluting the two, is evident in the most common approach to analyzing BCE conductivity data using an effective medium theory (Equation 5.1).[78,82] This approach posits that the BCE conductivity, σ_{BCE}, should be simply related to the conductivity of the pure conducting phase, σ_{c}, and is the volume fraction of the conducting phase, ϕ_c, and a structural factor, $f_{\mathcal{T}}$.

$$\sigma_{\mathrm{BCE}} = f_{\mathcal{T}} \phi_{\mathrm{c}} \sigma_{\mathrm{c}} \tag{5.1}$$

Here, $f_{\mathcal{T}}$ is introduced to account for the hierarchical BCE assembly. Conductivity is often assumed to be unimpeded across grain boundaries, and the value of $f_{\mathcal{T}}$ is taken as a tortuosity factor. In the effective medium theory for bulk block copolymer morphologies, $f_{\mathcal{T}}$ is estimated to be 2/3 for multi-grain lamellae and 1/3 for multi-grain ion-conducting cylinders in an insulating matrix.[87] With respect to the intrinsic conductivity of the BCE, an outstanding question in the field is whether the conductivity of the conducting phase of the BCE is the same as that of an analogous homopolymer, or if the entirety the conducting component in the BCE contributes to the overall conductivity.

Despite the challenges in quantitative and independent determination of $f_{\mathcal{T}}$ and σ_{c}, several foundational concepts concerning the magnitude and impact of extrinsic and intrinsic factors on conductivity in BCEs have been reported based on characterization of bulk samples. First and foremost, extrinsic factors play the dominant role in determining the conductivity of bulk BCE samples. In the vast majority of reports, the measured ionic conductivity of BCEs in bulk samples is lower than that of equivalent homopolymer electrolytes, after taking into account the volume fraction of the insulating block in the BCEs, by an order of magnitude or more.[84,167,168] In a few reports the domains within the multi-grain structure were aligned by the application of external electric, magnetic, or shear fields, resulting in a moderate degree of anisotropy in conductivity along and orthogonal to the alignment axis, but with conductivity values that remain 10 times or more lower than expected using an equivalent homopolymer electrolyte as the benchmark.[88,89] The profound impact of grain boundaries was demonstrated in work by Irwin *et al.* who found that in ternary block copolymer-homopolymer-salt blend systems, heating the system above the order-disorder transition temperature resulted in an abrupt increase in conductivity.[169] These disordered systems still exhibited significant structure, but the lack of grain boundaries greatly enhanced the connectivity of ion conduction pathways relative to the compositionally-equivalent polycrystalline samples with long range order. Chintapalli *et al.* similarly found that samples with large, well-formed lamellar grains exhibited lower conductivity than small, poorly defined grains.[83] Under these conditions, extrinsic factors limiting conductivity associated with defects and grain boundaries completely overshadow other extrinsic factors, such as tortuosity, as well as intrinsic factors.

Characterization of bulk samples has also pointed to a central concept that the intrinsic conductivity of BCEs is impacted by the presence and nature of interfaces between nanodomains. Sharick *et al.* showed that high molecular weight polystyrene-*block*-poly(methyl methacrylate)-ionic liquid (PS-PMMA-IL) systems exhibit higher conductivity than low molecular weight samples. They attributed the difference in conductivity to a decrease in interfacial area between block copolymer domains per unit volume with increasing domain size.[92] Similarly, a study of a PS-PEO-PS triblock electrolytes, Bouchet *et al.* suggested that a constant nonconducting layer of approx. 1.6 nm explained the deviation in conductivity in the measured BCE from the prediction of Equation 5.1.[90] The authors relied, however, on several critical assumptions about the nature of tortuosity and defectivity within the material, rendering this quantitative analysis difficult to corroborate or expand to other material systems. A complete understanding for this reduction in ionic mobility near domain interfaces at a molecular level is still not entirely clear, and answering this question experimentally has been limited by the inability to study these systems in a perfectly ordered system. Using molecular dynamics simulation to model SEO electrolytes, Sethuraman *et al.* suggested that the glassy PS block reduces the dynamics of the rubbery PEO block primarily near the BCE interface.[170] Experimental studies of a series of poly(n-alkyl methacrylate)-*block*-poly(oligo oxyethylene methacrylate) copolymers by Soo *et al.* demonstrated that lower glass transition temperature (T_{g}) of the nonconducting blocks resulted in improved ion conductivity in the conducting poly(oligo oxyethylene methacrylate) (POEM) phase.[171] Additionally, the authors observed that compositionally identical random copolymers exhibit an order of magnitude lower conductivity compared to the phase-separated block copolymers, and they suggested that intimate mixing of the conducting and nonconducting moieties had a compounding effect on the overall material conductivity, beyond that of reduced segmental dynamics. In a similar vein, Kim *et al.* studied poly(styrene sulfonate)-*block*-poly(methyl butylene) (PSS-PMB) mixed with different ionic liquids and found that changes in the sharpness of the domain interfaces were directly correlated with the measured ionic conductivity.[172] However, in all of these studies the structure of the material was known only at a superficial level, and quantitative assessment of the effects of domain interfaces was not possible. Although the importance of understanding this interfacial region has been made clear, the ability to full quantify its effects have not been demonstrated.

Our group recently employed directed self-assembly (DSA) of thin film BCEs on interdigitated electrodes for quantitative top-down metrology to address the role of defects and grain boundaries as extrinsic factors in controlling ionic conductivity. This work studied perpendicularly oriented through-film lamellar structures of polystyrene-*block*-poly(2-vinylpyridine) (PS-P2VP), a block copolymer amenable to the complexities of DSA. Solvent annealing and graphoepitaxial techniques (200 nm wide trench structures patterned by electron beam lithography) were used to create either defect-rich or defect-free block copolymer structures.[110] After exposure to methyl iodide vapor and saturation with water vapor, the material was rendered ionically conductive while retaining the film structure. The ionic conductivity of the morphology with defects and grain boundaries was more than an order of magnitude lower than that of the fully connected and aligned morphology. Moreover, the ionic conductivity of the fully aligned morphology approaches but does not completely satisfy Equation 5.1 when using $f_{\tau} = 1$, which suggest other intrinsic factors are in play in limiting ion conduction. Although this work provided insight into the structure-property relationships in defect-controlled BCEs, translating the chemically specific processing steps required of DSA to other BCEs can be challenging. Therefore, a more simple and generalizable approach is needed to broadly differentiate the extrinsic and intrinsic conductive properties.

In the first part of this chapter, we describe the use of interdigitated electrodes and thin films in a generalizable approach to quantitatively measure the intrinsic conductivity of BCEs. In contrast to the methods described above, fully connected morphologies of lamellar domains between electrodes are formed by self-assembly with domains oriented parallel to the plane of the film. This new strategy aimed at characterizing intrinsic BCE properties is suitable for a broad range of material chemistries, whereas the past study was designed to study extrinsic factors and required a highly engineered materials system. In the second part of the paper, we showcase the strength of the generalized platform in elucidating the fundamental physics underlying the effects of BCE interfaces on ionic conductivity using a case study of SEO with LiTFSI. Our approach involves measurement of the intrinsic conductivity of SEO over a range of salt concentrations and temperatures. By comparing this intrinsic conductivity of the conductive phase of the SEO to an analogous PEO homopolymer electrolyte, we find a portion of the PEO in the block copolymer is "inactive" and quantify the extent of this inactive volume fraction. Numerous past studies have documented and quantified dramatic changes in SEO periodicity and interfacial width as a function of salt concentration and have demonstrated that structure can be captured using an effective Flory-Huggins interaction parameter, χ_{eff}, to characterize the interaction between PS and PEO mixed with LiTFSI. Ultimately, by invoking a two-phase model for the conductivity of PEO in the SEO, we find the that a substantial fraction of PEO near domain interfaces does not contribute to the overall conductivity of SEO and that this fraction can be quantitatively accounted for as a function of the salt concentration-dependent value of χ_{eff}. Critically, the absence of any temperature dependence on the value of effective inactive material above and below the T_g of the PS block suggest that that reduced percolation of ion solvation sites near interfaces, more so than segmental dynamics, is the primary factor in rendering the interfacial regions non-conductive. The results and conclusions described here, represent an important case study for the development of solid-state polymer electrolytes by understanding the limits of intrinsic ionic conductivity. Overall, we have established a platform that will enable accurate description of intrinsic ion transport properties in a wide range of heterogeneous nanostructured materials.

5.2 Results and Discussion

5.2.1 Measurement of intrinsic BCE conductivity in parallel assembled lamellae

To quantify the intrinsic ion transport behavior of block copolymer electrolytes (BCEs), we employ an experimental system consisting of thin films, interdigitated electrodes (IDEs), and electrochemical impedance spectroscopy (EIS). The block copolymer electrolyte we investigate is composed of polystyrene-*block*-poly(ethylene oxide) (SEO, M_n = 9-10 kg mol^{-1}) blended with lithium bis(trifluorosulfonyl)imide (LiTFSI) salt. The salt preferentially resides in the PEO blocks, rendering those domains ionically conductive. The salt concentration, r, is defined as the molar ratio of lithium ions to ethylene oxide repeat units ($r = [\mathrm{Li}^+]/[\mathrm{EO}]$). Interdigitated electrodes were custom-fabricated as described in Section 3.2.1. Briefly, electrodes were prepared by electron-beam evaporation of a 5 nm Ti adhesion layer and 25 nm Au on Si wafers with 1 µm thermal oxide using photolithography and liftoff techniques. The IDE arrays consist of 160 electrodes for which the width, w, of each electrode is 2 µm, the distance, d, between electrodes is 8 µm, and length of overlap, l, is 1 mm. We then coated the surface of the IDE with either 1–2 nm of SiO_2 by atomic layer deposition (ALD) or

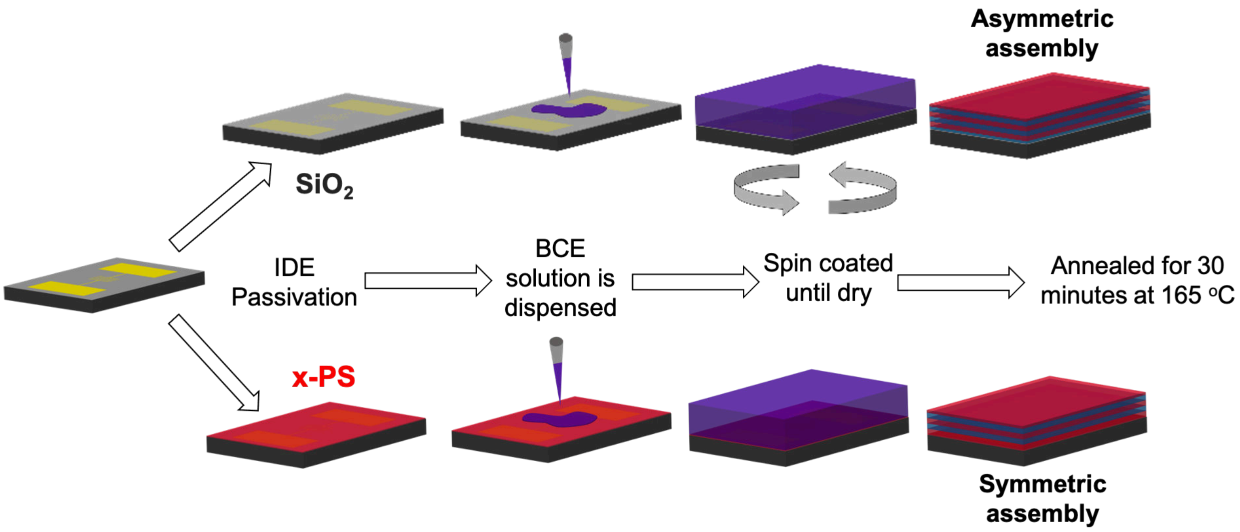

Figure 5.1 – Process flow for making symmetric and asymmetric self-assembled BCE films parallel to the passivated IDE surface

with a 4–5 nm crosslinked polystyrene mat (x-PS). These layers served three purposes: to ensure uniform surface chemistry, to induce differential and preferential wetting of the blocks of the copolymer on the IDE surface, and to inhibit dewetting phenomena. Subsequently, thin films of SEO-LiTFSI with thickness, h, less than 200 nm are deposited on the IDEs by spin coating and annealed at 165 °C for 30 min. During annealing, the SEO-LiTFSI microphase-separates into lamellar domains. As depicted in Figure 5.1, the lamellae assemble with orientation parallel to the substrate and possess long-range order and continuity. This parallel assembly is due to the preferential wetting of the substrate by one block of the copolymer and the propensity for PS to segregate to the free surface of the film owing to its lower surface energy compared to PEO.[173] By using coplanar IDEs with interelectrode spacing much larger than the film thickness ($d \gg h$), the EIS measurement probe the entire film with uniform electric field lines parallel to the plane of the polymer film.[122,128]

Smooth SEO-LiTFSI films with known and different numbers of parallel-oriented PEO-LiTFSI domains after annealing were prepared by controlling the initial film thickness and the wetting properties of the substrate. For the IDEs coated with ALD SiO$_2$, so-called

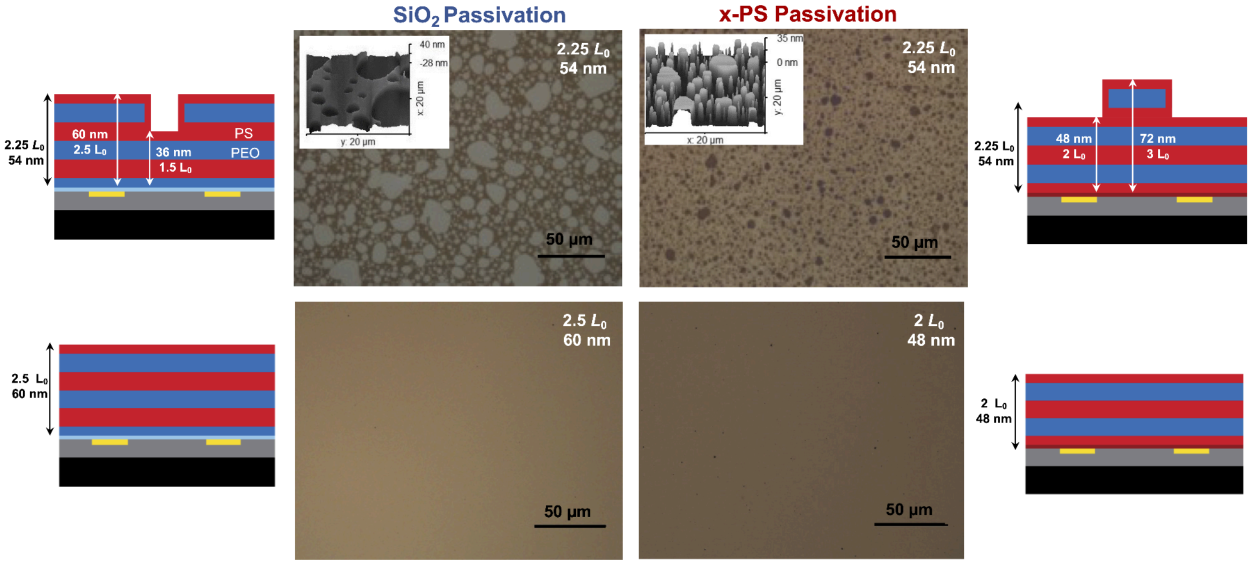

Figure 5.2 – Optical micrographs and AFM height maps of annealed SEO-LiTFSI ($r = 0.05$) films on SiO_2 and x-PS.

asymmetric wetting conditions are created such that PEO-LiTFSI preferentially wets the substrate, PS segregates to the free surface, and smooth films are formed for film thicknesses corresponding to $(n+0.5)L_0$where n is an integer.[102] For the IDEs coated with x-PS, so-called symmetric wetting conditions are created such that PS preferentially wets the substrate and segregates to the free surface, and smooth films are formed for film thicknesses corresponding to nL_0. This preferential wetting behavior is depicted schematically in Figure 5.2. The value of L_0 for SEO-LiTFSI with $r = 0.05$ was determined to be 24.0 nm by small-angle X-ray scattering (SAXS) (see Figure 5.10a). Smooth films were prepared on x-PS with thicknesses of 24 nm ($1L_0$, 1 PEO-LiTFSI domain) and 48 nm ($2L_0$, 2 PEO-LiTFSI domains), and on ALD SiO_2 with thickness of 12 nm ($0.5L_0$, 0.5 PEO-LiTFSI domains), 36 ($1.5L_0$, 1.5 PEO-LiTFSI domains), 60 ($2.5L_0$, 2.5 PEO-LiTFSI domains), 108 ($4.5L_0$, 4.5 PEO-LiTFSI domains).

Optical and atomic force micrographs confirming smooth film parallel assembly are shown in Figure 5.2 and Figure 5.3. To verify the wetting symmetry of the annealed SEO films, films of 54 nm ($2.25L_0$) were prepared on both SiO_2 and x-PS modified substrates. The optical

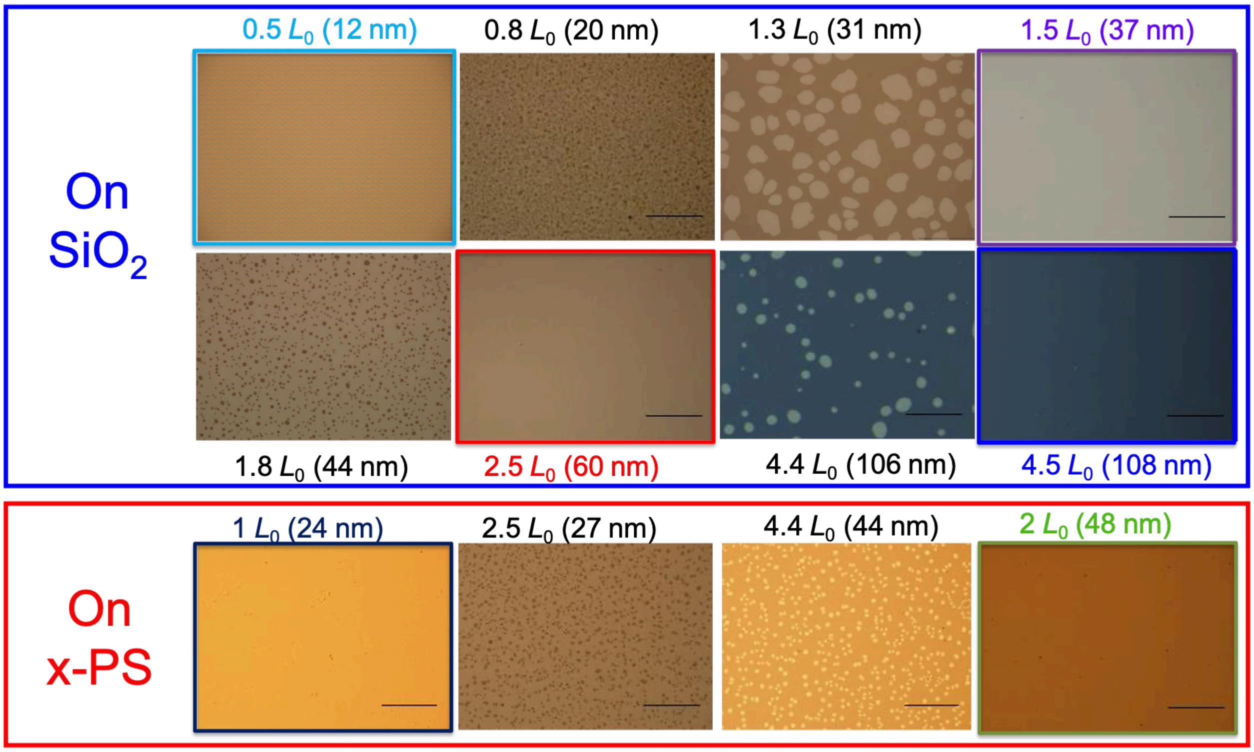

Figure 5.3 – Optical micrographs of lamellar SEO-LiTFSI ($r = 0.05$) at different thicknesses and substrates after annealing at 165 °C for 30 min. The highlighted frames are samples that were measured by EIS. The scale bar corresponds to 50 μm.

and AFM images in Figure 5.2 show the surface of these films with a terraced topography. Holes and islands each differ in height from the rest of the film by L_0 to ensure that the top surface consists entirely of PS. The height of these features was measured to be 24 nm, in good agreement with domain spacing calculated from SAXS. For the 54 nm thick film prepared on SiO_2, a majority of the film thickness is around 60 nm ($2.5L_0$), with small holes of 36 nm ($1.5L_0$). The formation of smooth features at films of 60 nm ($2.5L_0$), indicates that the wetting behavior of PS-PEO is asymmetric on SiO_2.

The optical images of films on each substrate present a mirror image of each other, indicating a difference in wetting preference between the two samples (Figure 5.3). The SiO_2 substrate exhibits a dark continuous surface with bright spots, while the film on x-PS comprises of dark spots and continuous bright phase. The AFM height map of the same samples reveals that the bright and dark spots are holes and islands, respectively. Indeed,

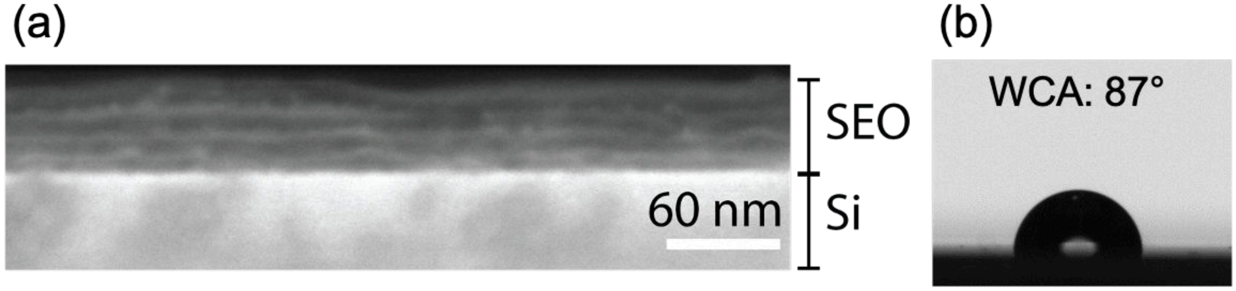

Figure 5.4 – (a) Cross-sectional SEM and (b) water contact angle of SEO parallel lamellae film

after annealing we can see a continuous layer of 48 nm ($2L_0$) and islands of 72 nm ($3L_0$), confirming the symmetric wetting behavior on the x-PS modified substrate. As can be seen from Figure 5.2 and Figure 5.3, when a film of 48 nm is spin coated and annealed on the x-PS surface there is no evidence for hole or island topology, confirming a symmetric wetting behavior.

Finally, the parallel structure can be imaged directly by taking cross-sectional SEM. A 54 nm film was spin coated and annealed on SiO_2 to create a parallel lamellar structure. To provide imaging contrast, the film was exposed to three cycles of sequential infiltration synthesis Al_2O_3 as described in *ref.* [174]. The trimethylaluminum precursor selectively interacts with the Lewis basic ether oxygens in the PEO phase, and an Al_2O_3 scaffold is formed throughout the domain, providing sharp elemental contrast under SEM. These films were then snapped in half after submerging in liquid nitrogen for 1 minute to provide a clean edge to image. A cross-sectional scanning electron micrograph of the parallel oriented lamellar domains in the SEO-LiTFSI ($r = 0.05$) films is shown in Figure 5.4a. Lastly, the preferential wetting of the free surface by PS is confirmed by water contact angle (WCA) measurement. As shown in Figure 5.4b, the WCA of the top surface of an annealed SEO-LiTFSI film is nearly 90°, the value we would expect for the hydrophobic PS block.

To investigate the ionic conduction of the parallel lamellae films as a function of thickness and wetting behavior, we preformed EIS measurements on smooth films of SEO-LiTFSI (r

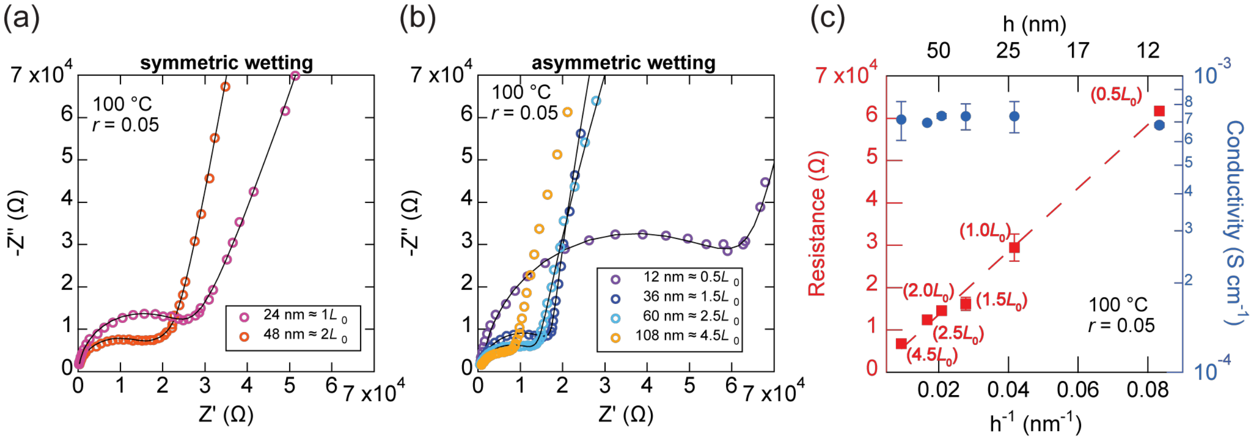

Figure 5.5 – Nyquist plots from EIS measurements of SEO-LiTFSI (r = 0.05) films with different thickness at 100 °C on (a) x-PS and (b) SiO_2 passivated IDEs. The solid lines are the curve fits to the equivalent circuit model shown shown in Figure 4.4b (Model 2). (c) Resistance and ionic conductivity as a function of film thickness at 100 °C.

= 0.05) using IDEs with x-PS or SiO_2 surfaces. Nyquist plots of smooth BCE films on x-PS coated IDEs (which elicits symmetric wetting) at 100 °C are presented in Figure 5.5a. The Nyquist curve consists of a semi-circle motif followed by a capacitive tail, characteristic of EIS measurements of polymer electrolytes with ion-blocking electrodes.[144] Because the diameter of the semicircle (or extrapolated semicircle) corresponds to the film resistance of the polymer, it is clear that the film resistance decreases as the film thickness increases from $1L_0$ to $2L_0$. Nyquist plots from measurements of smooth asymmetric SEO-LiTFSI films on IDEs coated with SiO_2 are presented in Figure 5.5b. Again, the diameter of the semicircle—and therefore the film resistance—decreases with an increase in the film thickness from $0.5L_0$ to $4.5L_0$. The decrease in the semicircle radius indicates that the EIS measurement probes the additional material the thicker films with more PEO-LiTFSI domains, *i.e.* a greater cross-sectional area of conductor is measured. This observation suggests that the alternating, non-conducting PS domains between conducting PEO-LiTFSI domains does not preclude the impedance measurement of even the uppermost domain.

To quantitatively compare the ionic conduction of the films with different thicknesses and wetting symmetry we used the equivalent circuit model described in Chapter 4 (shown in Figure 4.4b inset) to extract the film resistance, (R), from the complex impedance. Previously we demonstrated that the modeled elements in this equivalent circuit accurately represent the material properties such as the polymer electrolyte resistance.[134] The fit to this equivalent circuit of the EIS data for all of the samples are shown as the solid black lines in Figure 5.5a–b. As can be seen in Figure 5.5c, the resistance of the film increases linearly with h^{-1}, where h is the film thickness. Because we use smooth films and quantized numbers of parallel lamellae for symmetric and asymmetric assembly, h is directly proportional to both the cross-sectional area of the films and the number of conducting PEO-LiTFSI domains. Therefore, we can conclude that this linear behavior between the resistance and the film thickness confirms that each PEO-LiTFSI domain contributes equally to the measured resistance independent of wetting behavior or SEO film thickness.

We calculate the ionic conductivity using the cell constant derived in Chapter 3 which relates the measured film resistance and the conductivity:

$$\sigma = \frac{1}{R}\frac{d}{(N-1)lh} \tag{5.2}$$

The geometric IDE parameters of the system used in this study were $N = 160$ electrodes, $l = 1$ mm long electrodes, and $d = 8$ µm interelectrode spacing. Consistent with the linear trend in resistance with h^{-1} reported in Figure 5.5c, the ionic conductivity determined for all films is identical, within error, irrespective of the wetting layer or number of PEO-LiTFSI domains. Although the data above is shown only for 100 °C, the same relationship between the resistance, conductivity, and film thickness was observed across a temperature range of 80–120 °C (Figure 5.6). Notably, the conductivity measured by this methodology is an order of magnitude higher than previous reports of SEO of similar molecular weight and salt concentration.[84] This is attributable to the lack of blocking defects within the film, and we can take this conductivity to be the intrinsic conductivity of the SEO-LiTFSI system. Furthermore, as only the PEO-LiTFSI domains are assumed to contribute to the

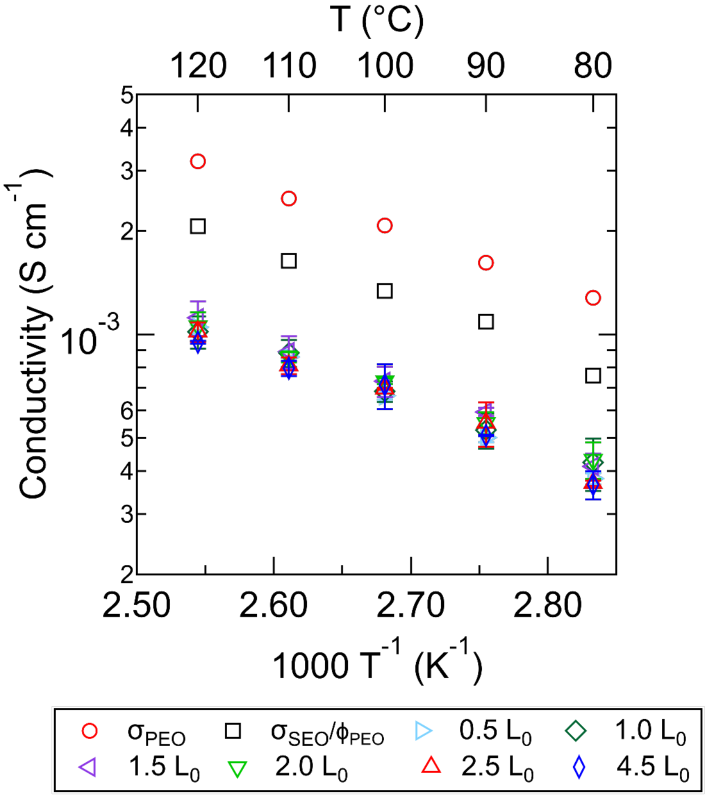

Figure 5.6 – Temperature dependent conductivity for SEO-LiTFSI (r = 0.05) at different thickness and substrate wetting

ionic conductivity, we can interpret the overall measured conductivity as that of individual PEO-LiTFSI domains.

5.2.2 Ionic conductivity in SEO films as function of salt concentration and temperature

Having established a methodology to measure the intrinsic conductivity of single-grain BCEs, we now turn our attention to these intrinsic properties being evaluated as a function of salt concentration. SEO properties that change with salt concentration include charge carrier density and the interaction parameter, χ. The latter results in variation of the lamellar period spacing and domain interface width. We measured the ionic conductivity of these well-ordered block copolymer films for SEO electrolytes at two additional LiTFSI concentrations ($r = 0.01$ and 0.085). All measurements made for these salt concentrations were of $1.5L_0$ SEO-LiTFSI films on SiO_2 coated IDEs (asymmetric wetting). The L_0 of SEO at different LiTFSI concentration was found by SAXS and are reported in Table 5.1. The SAXS profiles are presented in Figure 5.10a. The shift in the primary scattering peak to lower q values at higher r indicates that the domain spacing increases with LiTFSI concentration. As was found in previous studies of block copolymer-salt blends, this increase in domain spacing is linear with the concentration of added salt.[175,176] Ionic conductivity of these SEO films (σ_{SEO}) and homopolymer PEO-LiTFSI (σ_{PEO}) at the same salt concentrations as a function of temperature are presented in Figure 5.7. Both the BCE and homopolymer systems exhibit similar temperature-dependent conductivity behavior at all three salt concentrations. It has been reported previously that at these LiTFSI concentrations $0.01 \leq r \leq 0.085$ the ion hopping activation energies, as described by the Vogel-Tammann-Fulcher equation, for PEO and SEO electrolytes are very similar, indicating that the same mechanisms underpin ionic mobility in both studied systems.[84]

Measurements of the intrinsic transport properties allow us to directly compare between the PEO homopolymer and the SEO electrolyte. To calculate the ionic conductivity of the PEO-LiTFSI within the SEO, we divide the measured conductivity by the volume fraction of the PEO-LiTFSI domain ($\sigma_{\text{SEO}}/\phi_{\text{PEO}}$). This ϕ_{PEO} was calculated using molar volumes for the polymer and salt that were reported in previous studies, and the calculations are shown in Section 5.4.5.[177] ϕ_{PEO} was calculated to be 0.51, 0.54, 0.56 for $r = 0.01$, 0.05, and 0.085, respectively. ϕ_{PEO} increases slightly at higher salt concentrations because we assume that the LiTFSI preferentially resides in the PEO domain. The ionic conductivity of the PEO within the block copolymer, $\sigma_{\text{SEO}}/\phi_{\text{PEO}}$, is plotted along with the block copolymer and homopolymer conductivities for each salt concentration in Figure 5.7. The value of this

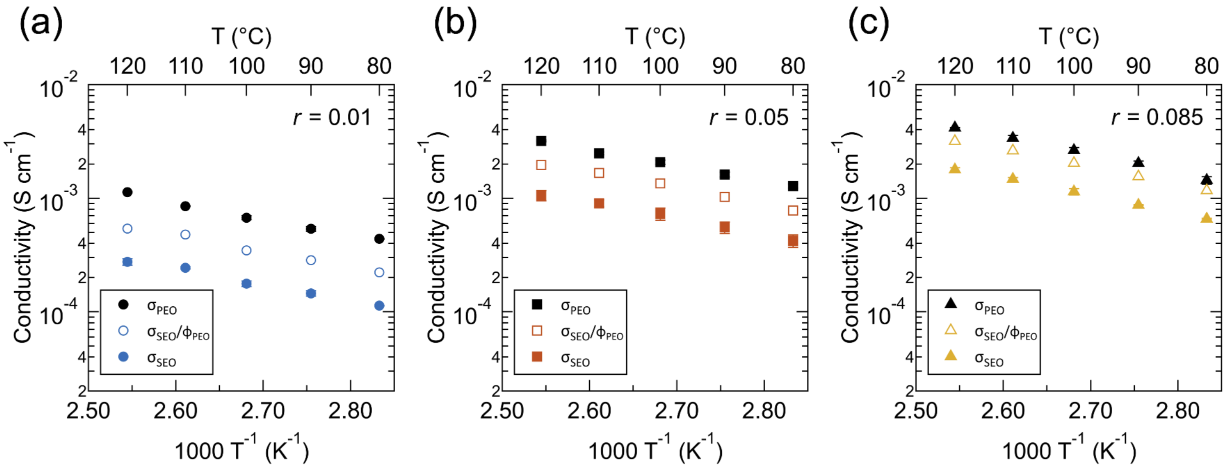

Figure 5.7 – Conductivity of PEO and SEO at (a) r = 0.01, (b) r = 0.05, and (c) r = 0.085. Open symbols represent the conductivity of the PEO within the block copolymer, *i.e.* SEO conductivity divided by the PEO volume fraction at each salt concentration. The black markers are the homopolymer PEO equivalent ionic conductivity.

volume fraction-corrected conductivity is lower than that of the homopolymer across the full range of salt concentrations. We note, however, that these values are of the same order of magnitude as the homopolymer, due to the absence of a significant number of blocking defects.

5.2.3 Intrinsic conductivity measurements reveal inactive PEO within block copolymer

To quantify the changes in conductivity of PEO-LiTFSI domain within the SEO relative to the homopolymer equivalent, we calculated the normalized conductivity, σ_{n}, where σ_{SEO}, is normalized by the homopolymer equivalent conductivity (σ_{PEO}) and the volume fraction of PEO (ϕ_{PEO}):

$$\sigma_{\mathrm{n}} = \frac{\sigma_{\mathrm{SEO}}}{f_{\tau}\phi_{\mathrm{PEO}}\sigma_{\mathrm{PEO}}} \tag{5.3}$$

Here we assume $f_\mathcal{T} = 1$ (*i.e.* no tortuosity or defects), and therefore, σ_n quantifies the intrinsic differences between the conductivity of the homopolymer PEO and the PEO within the BCE. Thus, $\sigma_\mathrm{n} = 1$ would indicate ionic conductivity equivalent to the homopolymer, $\sigma_\mathrm{n} < 1$ would indicate impediment to ionic conduction, and $\sigma_\mathrm{n} > 1$ would indicate an enhancement in ionic conduction. Normalized conductivity for each salt concentration is presented in Figure 5.8. σ_n is less than unity for all salt concentrations. The value of σ_n ranges from around 0.5 at $r = 0.01$ to around 0.8 at $r = 0.085$. Interestingly, σ_n increases significantly with salt concentration but does not exhibit any strong temperature dependence over the selected temperature range. It is important to note that in past studies using bulk samples with multi-grain morphologies, σ_n was also observed with increase in the salt concentration in SEO-LiTFSI systems.[81,84] In the analysis of bulk samples, however, changing structural factors such as grain size, defects, and estimates of tortuosity had to be considered in the interpretation of the results, thus precluding fully quantitative analysis.[83,90,167] In contrast, because we measure the intrinsic conductivity of SEO-LiTFSI as a function of r with identical structure in all samples (parallel oriented lamellae in thin films) the increase in σ_n can be unambiguously attributed to higher average conductivity of PEO-LiTFSI domains in the block copolymer at higher salt concentrations.

To understand why salt concentration may have such a strong effect on the intrinsic SEO-LiTFSI conductivity, it is instructive to return to Equation 5.1. With the well-supported assumption that the structural prefactor, $f_\mathcal{T}$, can be taken as unity, one explanation for the reduced conductivity is that all of the PEO-LiTFSI in the SEO has an inherently lower ionic conductivity with respect to the equivalent homopolymer electrolyte (*i.e.* $\sigma_\mathrm{c} < \sigma_\mathrm{PEO}$). However, this explanation is rather unlikely given the relative size of the conducting domains. PEO near the middle of domains should adopt the same melt-state conformations as the homopolymer and exhibit similar material properties. A more plausible explanation is that the volume fraction of conducting material that should be considered is less than the

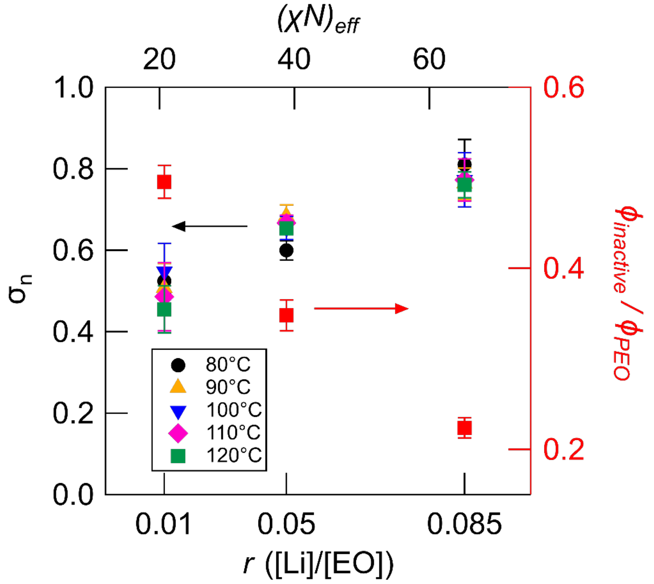

Figure 5.8 – Normalized conductivity, σ_n and the ratio of inactive PEO in the block copolymer to the total fraction of PEO, $\phi_\mathrm{inactive}/\phi_\mathrm{PEO}$ as a function of salt concentration and segregation strength

total volume fraction of PEO-LiTFSI in the system. It has been previously suggested that PEO-LiTFSI in the SEO exhibits a lower ionic mobility only locally near the polystyrene interface, while far from the interface, the PEO within the block copolymer should behave identically to the homopolymer PEO.[81,90,91,178] Here, we consider a two-layer model, in which the PEO domain is partitioned into an inactive region near the domain interface with no contribution to the conductivity, and an active region, which exhibits the same conductivity as homopolymer PEO at the same salt concentration. Using the two-layer model, we can define an "active volume fraction" (ϕ_active) of PEO within the block copolymer that contributes to the measured conductivity given by:

$$\phi_\mathrm{active} = \frac{\sigma_\mathrm{SEO}}{\sigma_\mathrm{PEO}} \tag{5.4}$$

The inactive PEO phase (ϕ_inactive) in the SEO has a corresponding volume fraction given by:

$$\phi_{\text{inactive}} = \phi_{\text{PEO}} - \phi_{\text{active}} \tag{5.5}$$

We report ϕ_{active} and ϕ_{inactive} for each salt concentration in Table 5.1, where the value of ϕ_{active} is derived from the average value of σ_{n} across the measured temperature range. We also report the fraction of PEO that is inactive relative to the total PEO volume fraction in the SEO, $\phi_{\text{inactive}}/\phi_{\text{PEO}}$ as a function of salt concentration in Figure 5.8. Nearly 50% of the PEO within the SEO is inactive at $r = 0.01$, whereas only 25% is inactive at $r = 0.085$ (Table 5.1).

The distinctive aspect of our work is the ability to precisely and quantitatively describe the extent of the active and inactive PEO regions. The idea of an inactive fraction of PEO has been suggested by others in randomly oriented SEO, but these previous works have relied on major assumptions about the tortuosity and transport across grain boundaries46 or have assumed a constant width of inactive PEO.[167] The relative magnitude of both the measured conductivity of SEO in our study and the calculated inactive volume fraction of PEO highlight the importance of measuring defect-free, single grain samples to perform any type of quantitative analysis of this interfacial region. The conductivity measured here (roughly 10^{-3} S cm^{-1} at 90 °C, $r = 0.085$) is an order of magnitude higher than values from

Table 5.1 – Calculated and Experimental Values for Block Copolymer Properties

				SST$^{\text{c,d}}$		SCFT$^{\text{c,e}}$	
r	L_0(nm)$^{\text{a}}$	$\phi_{\text{active}}{}^{\text{b,c}}$	$\phi_{\text{inactive}}{}^{\text{c,d}}$	δ(nm)$^{\text{f}}$	$\phi_{\text{PEO}}(\delta)$	δ(nm)$^{\text{f}}$	$\phi_{\text{PEO}}(\delta)$
0	18.8	–	–	–	–	–	–
0.01	21.0	0.26 ± 0.02	0.25 ± 0.02	2.63 ± 0.20	0.96 ± 0.01	2.61 ± 0.20	0.95 ± 0.01
0.05	24.0	0.35 ± 0.02	0.19 ± 0.02	2.24 ± 0.21	0.97 ± 0.01	2.25 ± 0.21	0.98 ± 0.01
0.085	26.8	0.43 ± 0.02	0.13 ± 0.01	1.66 ± 0.16	0.95 ± 0.01	1.68 ± 0.15	0.98 ± 0.01

[a] Domain spacing as determined by SAXS.

[b] $\phi_{\text{c}} = \phi_{\text{active}} + \phi_{\text{inactive}}$

[c] Average value across temperature range study; error represents standard deviation.

[d] Based on interfacial width for block copolymers in the strong segregation limit.

[e] SCFT calculations were done using the PSCF open source code.

[f] δ is the distance from center of the domain interface to edge of the inactive region.

bulk samples of similar molecular weight SEO measured by other groups (roughly 10^{-4} S cm^{-1} at 90 °C, r = 0.085).[81,84] This discrepancy is explained by the overwhelming effect that defects play in bulk, multi-grain BCE structures. The impact of these defects is significantly greater than that of the inactive PEO we find here, which at $r = 0.085$ represents less than a 25% reduction in conductivity. It would be impossible to single out this inactive interfacial phenomenon in any sample that contains significant defectivity. However, we see also that this interfacial effect can be substantial, reducing conductivity by half in the case of the $r = 0.01$ electrolyte. This highlights the possible significance of engineering the BCE interface to improve the maximum intrinsic conductivity of such systems. For example, Epps and coworkers have demonstrated one such molecular design approach by synthesizing block copolymers with a tapered interface such that the composition of the material varies gradually, rather than sharply, at the interface.[179] They have found that, in some cases, tapering can improve the conductivity relative to the nontapered block copolymer. Employing our platform to measure ionic conductivity of single-grain parallel oriented lamellar structures of interfacially engineered materials would allow one to quantitatively assess the effects of interfacial modifications and develop new design criteria to maximize the intrinsic ion conductivity of block copolymer electrolytes.

5.2.4 Intrinsic ionic conductivity is highly dependent on segregation strength between blocks

To develop quantitative ion transport-block copolymer structure relationships, the structure of the block copolymer must be fully described as a function of salt concentration. Changes to the block copolymer structure due to the addition of LiTFSI to SEO are well captured by an effective Flory-Huggins interaction parameter, χ_{eff}. For the range of r in this study, changes in salt concentration causes: 1) significant variation in the size and periodicity of the lamellae, and 2) the width, Δ, and composition profile of the interfaces between domains.[76,180] To determine χ_{eff} as a function of r, bulk samples with $r = 0.01$, 0.05, and 0.085 were prepared, and the L_0 was found from SAXS. In order to use the fixed-volume lattice model assumed in Flory-Huggins theory, the added volume of the salt to the PEO domain must also be accounted for. To do so, an effective monomer size was calculated to obtain an effective degree of polymerization, N_{eff}, which was determined based on the molar volume of LiTFSI and the salt concentration.[69] The values of L_0 and the estimated effective segregation strength, $(\chi N)_{\text{eff}}$ for the different SEO samples are presented in Table 5.1 and shown on the top axis of Figure 5.8. Over the range of salt concentrations used in this study, $(\chi N)_{\text{eff}}$ varies linearly with r (Figure 5.10b). A detailed description of the corresponding calculations are given in Section 5.4.6. We note that an important assumption in using the effective Flory Huggins parameters and effective degree of polymerization is that the PEO-LiTFSI phase is homogeneous, *i.e.* the salt is distributed uniformly throughout the PEO domain. This assumption has both experimental and computational evidence to support it, and the use of χ_{eff} to describe the phase separation behavior of salt-doped BCPs is well-established.[138,181] It is therefore reasonable to use this approximation to describe other aspects of the material which depend on χ, namely the degree of interfacial mixing, with this same treatment.

To correlate the inactive PEO region that was found by the EIS measurements to thermodynamic properties of the block copolymer, we use well-established theories in block copolymer physics to describe the compositional variation between the two domains which are separated by an extensive interfacial mixing region.[182] The composition profile of a given monomer in a diblock copolymer is described well by a hyperbolic tangent function, as in Equation 5.6 below.[64,183]

$$\phi_{\text{A}} = 0.5\left[1 + \tanh\left(2z/\Delta\right)\right] \tag{5.6}$$

Here, $\phi_{\text{A}}(z)$ is the concentration of monomer A (in this case, PEO) at a distance z from the middle of the interface. We define this interface around the midpoint between the two domains, *i.e.* $\phi_{\mathrm{A}}(0) = \phi_{\mathrm{B}}(0) = 0.5$.[184] The so-called interfacial width, which is defined by $\Delta = 1/(\frac{d\phi_{\mathrm{A}}}{dz})\Big|_z = 0$, describes how rapidly the average composition changes at the interface between the domains. For systems with larger interfacial width, the domain will be "pure" A or B (defined somewhat arbitrarily to be $\phi_{\mathrm{A}} > 0.9999$) at distances farther from the interface.[182] We take two complimentary approaches to approximate the composition profiles ($\phi_{\mathrm{PEO}}(z)$) and interfacial width (Δ) as a function of segregation strength. In the first approach, the Δ is computed using Strong Segregation Theory (SST) as described by Semenov, and then the composition profile is computed using Equation 5.6.[64] Semenov describes how the interfacial width depends on the Flory-Huggins interaction parameter, χ, and the degree of polymerization, N, and this theory has been validated experimentally.[184–186] In the second approach, we employ Self-Consistent Field Theory (SCFT) calculations using the Polymer Self-Consistent Field (PSCF) open source code developed by David Morse and collaborators.[187] These mean-field theory (MFT) calculations use the same experimentally determined values of $(\chi N)_{\mathrm{eff}}$ to determine the minimum free energy configuration of the block copolymer. The SCFT calculated composition profile can then be fit to Equation 5.6 with Δ as a fitting parameter. The details of both approaches are outlined in the Materials and Methods section of this chapter. It is important to mention that MFT calculations do not directly consider the presence of ions in the system, and therefore there is no explicit treatment of the ion distribution within the PEO phase. Nevertheless, in many polymer electrolyte studies the usage of MFT calculation closely matched experimental results.[75,97,181,188] We assume here that the salt distribution is similar for all salt concentrations studied here, and that the Li^+ concentration profile directly tracks the PEO concentration profile. These assumptions have been used to accurately describe observed behavior in several previous studies.[75,181]

Next, we quantify the spatial distribution of the inactive PEO within the SEO structure near the interface. To do so, we integrate Equation 5.6 from the point of lowest PEO concentration (the middle of the PS domain, $z = -(L_0/2)\phi_{\text{PS}}$, to a distance, δ, away from the center of the interface where the inactive portion of PEO, as determined experimentally, ends (Equation 5.7).

$$\frac{1}{L_0/2}\int_{-(L_0/2)\phi_{\text{PS}}}^{\delta} \phi_{\text{PEO}}(z)dz = \phi_{\text{inactive}} \tag{5.7}$$

Note that Equation 5.7 includes a normalization factor of $1/(L_0/2)$ that takes into account that Equation 5.6 only describes the composition profile over half a lamellar period. If the integration were performed from $-(L_0/2)\phi_{\text{PS}}$ to $(L_0/2)\phi_{\text{PEO}}$, the left-hand side of the equation would be equal to ϕ_{PEO}. The calculated composition profiles for PEO segments at the salt concentrations studied are illustrated in Figure 5.9. Figure 5.9a and Figure 5.9c show the compositional profile of PEO over a full lamellar period with L_0 and Δ as determined by SST and SCFT, respectively, and as a function of r and $(\chi N)_{\text{eff}}$. The spatial distribution of the inactive volume fraction of PEO calculated using Equation 5.7 is shown as the shaded regions beneath the curves. Figure 5.9b and Figure 5.9d depict the composition profile over half of a lamellar period, with the distance normalized by L_0. This explicitly shows how the interfacial width narrows with increasing salt concentration such that less PEO is sequestered near the interface. In the two-layer model described above, PEO-LiTFSI exhibits conductivity equal to that of the homopolymer at distances greater than δ away from the middle of the domain interface. The results of these calculation are provided in Table 5.1 for each concentration and for both mean-field models. We find that the value of δ decreases with salt concentration from around 2.4 nm at $r = 0.01$ to around 1.7 nm at $r = 0.085$.

Strong evidence to validate that this model captures the amount and spatial distribution of the inactive PEO in the SEO is derived from analysis of the predicted composition at the edge of the inactive region. We can observe that for all salt concentrations and temperatures studied here, using either SST or SCFT to describe the compositional profile, the volume fraction of PEO at the boundary of the inactive region, $\phi_{\text{PEO}}(z = \delta)$, is calculated to be

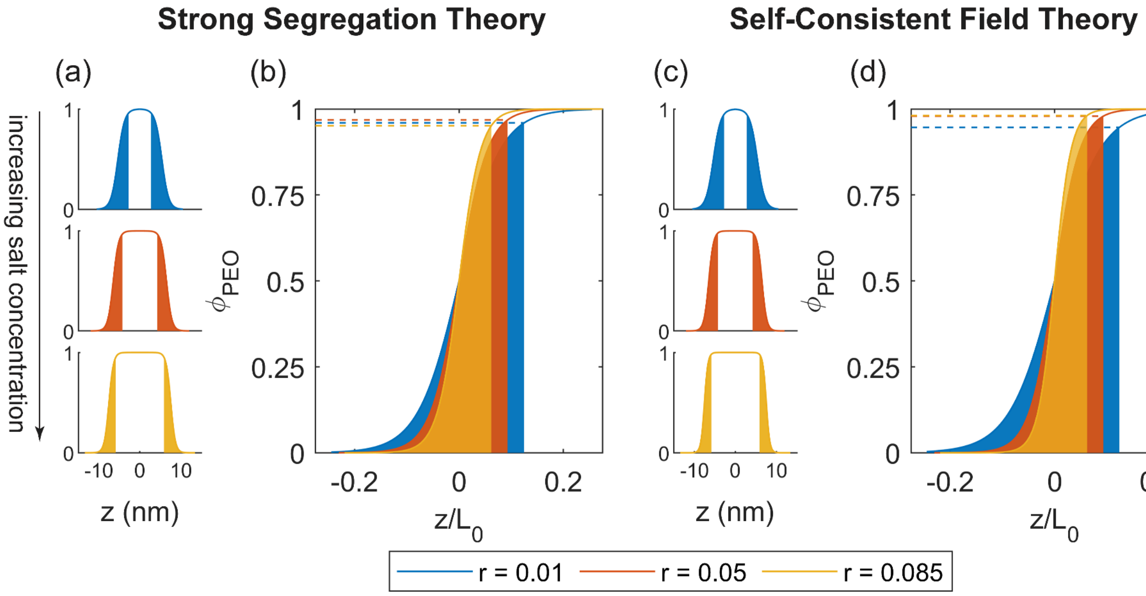

Figure 5.9 – PEO monomer concentration across one full lamellar period obtained by (a) SST and (c) SCFT at different salt concentrations. Average PEO concentration profiles from (b) SST predications and (d) SCFT calculations across a half lamellar period (from center of PS domain to center of PEO domain) with distance normalized by the domain spacing. Shaded regions correspond to the effective inactive interfacial region determined via Equation 5.7. The distance from the middle of the interface ($z = 0$) to the right edge of the shaded region is δ.

between 0.94 and 0.99. This similarity in the predicted composition across very different segregation strengths, L_0, and Δ clearly suggests that: 1) ionic conductivity in BCEs is correlated to the local composition, and 2) the inactive PEO is localized entirely to the mixed interface region and does not extend into the pure PEO phase ($\phi_{\mathrm{PEO}} > 0.9999$). It is important to note that the conductivity is likely not a step function in local PEO volume fraction, and instead likely varies smoothly with increasing PEO content. Nevertheless, even a few percent nonconducting PS in PEO appears to dramatically hinder ion transport through the PEO.

The increase in domain spacing with salt concentration clearly results in a greater fraction of "active" PEO (Figure 5.9a and Figure 5.9c). Larger domain spacing as a result of higher molecular weight has previously been reported to increase σ_{n}.[78] Sharick *et al.* found that high-MW PS-PMMA-ionic liquid systems exhibited higher normalized conductivity than lower-MW systems at the same ion concentration, and attributed this to the presence of fewer PS-PMMA interfaces per unit volume.[92] Panday *et al.* saw a similar trend in SEO-LiTFSI systems, where the highest conductivity was observed for the highest molecular weight (largest domain spacing) samples.[81] However, domain size relative to the interfacial width may not alone account for increased normalized conductivity in these systems. Previously, Kim *et al.* demonstrated that the highest normalized conductivities in PSS-PMB-IL block copolymer electrolytes were achieved when ions were confined to PSS domains with sharper interfaces.[172] Similarly, we see that after normalizing the domain profiles and predicted inactive regions by the domain size, there remains a clear change in the composition profile shape as a function of segregation strength, and the sharper domain profiles correspond to reduced inactive, non-conducting fraction of PEO. This clearly demonstrates that both the shape and size of the interface relative to the conducting domain size (both of which are functions of χ and N) dictate the maximum conductivity in a microphase separated BCE. While these ideas have been discussed in previous studies, by using our platform we were able to show the exact changes in the BCE interface solely by interpretation of the electrochemical measurements and without any structural assumptions. These findings have profound implications for the design of new BCEs with interfacial mixing representing a key design parameter when developing new materials.

5.2.5 *Intrinsic conductivity measurements provide molecular-level insight into transport*

The data and analysis presented here may shed some light on the nature of ion transport mechanisms that contribute to reduced conductivity in the mixed interfacial regions. One proposed explanation for lower ionic conductivity near domain interfaces relates to the reduction in segmental mobility of the PEO domain near the glassy polystyrene.[155,170,179]

Although segmental mobility and the composition dependent T_g of PEO intermixed with PS almost certainly increases with an increase in the volume fraction of the higher T_g PS, this does not seem to be the primary factor in affecting the measured conductivity. Over the temperature range of 80 °C to 120 °C, similar temperature dependence was observed for both homopolymer PEO and SEO samples, despite 80 °C being very near the T_g of PS in SEO. This indicates that the low mobility of the polystyrene—which increases several orders of magnitude in this temperature range—is not the predominant factor in limiting the ionic mobility within the interface.[189] Moreover, the T_g values for homopolymer PEO and in the block copolymer are very similar at the studied salt concentrations.18 Although this intermixing certainly reduces the local mobility of the few PEO units directly connected to PS chains, this likely does not explain the observed changes in conductivity. The more plausible primary mechanism to explain the reduced conductivity near domain interfaces relates to the interconnectivity of solvation sites which facilitate ionic mobility.[37–39] A study by Pesko *et al.* examined the changes in ionic conductivity of PEO derivatives with short PEO blocks separated by different lengths of aliphatic spacer blocks.[39] It was found that the dilution of the ether oxygen coordination sites by the nonpolar chains lead to a decrease in the measured ionic conductivity which could not be explained solely by changes in T_g. They suggested that the disruption of the connectivity between the PEO solvation sites greatly reduces the capacity for efficient Li^+ transport mechanism. Soo *et al.* also observed a similar dilution effect in random copolymers, which exhibited a ten-fold decrease in conductivity relative to the compositionally equivalent block copolymer.[171] For SEO-based BCEs, we propose that dilution occurs within the BCE interfaces where PEO solvation sites are diluted by intermixed PS segments. It is possible that even small fractions of PS (as few as 1–6% by volume) may significantly disrupt the solvation site network required for ionic motion.

With this experimental approach leveraging parallel assembled lamellae, we have clearly demonstrated the importance of interfacial mixing in dictating the intrinsic conductivity of

BCEs. However, we acknowledge the precise contribution of the different mechanisms to the reduced ionic conductivity in BCEs has not been delineated in the current study. In particular, we note that both methods used to determine the extent of the interfacial mixing layer rely on mean field approaches which neglect the presence and location of the ions, aside from their effect on χ_{eff}. Therefore, more experimental and computational data on the distribution and solvation environment of the ions in BCE are warranted in future studies. In addition, more finely detailed simulations that describe the molecular level interactions between ions and the polymer within this intermixed region may provide further insight. Such computational efforts will be best coupled with our experimental systems wherein the effects of tortuosity, defects, and grain boundaries are nonfactors.

5.3 Conclusions

We have presented here a robust method for measuring the intrinsic ionic transport of BCE nanostructures and precisely described the effects of BCE interfaces in controlling ionic conduction. The generalizable strategy involved depositing thin film BCE consisting of SEO and LiTFSI salt on interdigitated electrodes and self-assembling parallel fully connected lamellar structures. Measuring the ionic conductivity of the fully connected structures enables us to measure the intrinsic conductivity of SEO-LiTFSI BCEs. Normalizing the intrinsic ionic conductivity to the volume fraction of the conducting phase and the equivalent homopolymer PEO-LiTFSI electrolyte, over a range of salt concentrations and temperatures, enables the quantification of an inactive volume fraction (ϕ_{inactive}) of the PEO phase limiting ionic conduction. The temperature-averaged values of ϕ_{inactive}, which is localized at the PS-PEO interface, were 0.25, 0.19, and 0.13 for $r = 0.01$, 0.05, and 0.085, respectively. It is important to note this is the first report on the quantification of ϕ_{inactive} over a range of r and temperature that is done without the need to make any assumptions about the nature of tortuosity and defectivity within the material. Even with presence of the inactive fraction, conductivity of the SEO studied here (around 10^{-3} S cm^{-1} at 90 °C) is an order of magnitude higher than values from bulk samples (around 10^{-4} S cm^{-1}) at $r = 0.085$ at similar molecular weight. By using mean-field theory calculations, we determined the interfacial concentration profiles and quantified the physical extent of this inactive region comprising intermixed PS and PEO segments. Importantly, our analysis revealed that while intermixing may reduce segmental mobility (due to high T_{g} PS), the lack of temperature dependence in the normalized conductivity indicated reduced segmental mobility was not the predominant factor in limiting ionic transport within the interface. This suggests other factors such as the disruption of the solvation site connectivity may play a more prominent role.

While our study on thin film BCEs is fundamental by design, our work establishes the need to understand the intrinsic interfacial factors governing the limits of ionic conduction when considering application-specific needs. First, by knowing the maximum attainable intrinsic conductivity of known nanostructured materials, one can develop bulk materials processing strategies for implementation if the conductivity is sufficient for the targeted application. Second, one can alternatively take a molecular design approach to synthesize new nanostructured polymers where intrinsic interfacial factors are tuned to push the limits of the maximum attainable ionic conductivity. Third, this approach to characterizing the intrinsic and interfacial contributions to ionic transport in heterogeneous materials may be expanded to other critical components of an electrochemical system. Although polymer electrolytes are often considered in the context of macroscopic membrane separators, their presence within electrodes as charge transporting binder materials is critical to the performance of solid-state batteries. The nanoscale layers formed between electrode particles can have an outsized role on the overall performance of the system, and this experimental platform may enable understanding transport in these regions. The experimental platform developed here enables reliable, high-throughput methods for determining the maximum attainable conductivity in heterogeneous BCEs, and this approach will enable rapid screening of new materials for practical application.

5.4 Materials and Methods

5.4.1 Materials

Polystyrene-*block*-poly(ethylene oxide) (SEO, M_n = 9-10 kg mol^{-1}, $Đ$ = 1.07) and poly(ethylene oxide) (PEO, M_n = 20 kg mol^{-1}, $Đ$ = 1.07) were purchased from Polymer Source Inc. and used after vacuum drying at 50 °C for 24 hr. The x-PS (crosslinked polystyrene) was received from AZ Electronic Materials. All other chemicals—acetonitrile (99.8 %, anhydrous), toluene, and LiTFSI (lithium bis(trifluoromethanesulfonyl)imide)—were purchased form Sigma Aldrich. LiTFSI was further dried under vacuum at 100 °C for 24 hours. Polymers and LiTFSI were stored in an Ar glovebox after the drying processes. The negative photoresist (AZ nLof 2020) and developer (AZ 300 MIF) used for microfabrication of IDEs were purchased from AZ Electronic Materials. Silicon wafers (4" diameter, 500 µm thick) with 1 µm of thermal SiO_2 were purchased from Pure Wafer Inc.

5.4.2 Block copolymer characterizations

Small-angle X-ray scattering (SAXS) was performed using the SAXSLAB GANESHA instrument at the University of Chicago X-ray Facility. Silicon nitride membranes (100 nm thick, 2.25 × 2.25 mm^2 area) were fabricated in-house to serve as support for the polymer material. Polymer films, with and without salt, were cast from solution onto the silicon nitride membranes and annealed at 165 °C for 30 minutes. Primary scattering peaks, q^*, were found by peak fitting using the SAXSGUI MATLAB program developed by SAXSLAB. The block copolymer domain spacing, L_0, was taken as $2\pi/q^*$. Tapping mode atomic force microscopy (AFM) was performed using the Cypher ES AFM in the University of Chicago MRSEC Facility. AFM micrographs were analyzed using Gwyddion, and hole or island depths were captured by standard image processing techniques. The heights of these topographical features were used to verify the domain spacings measured by SAXS.

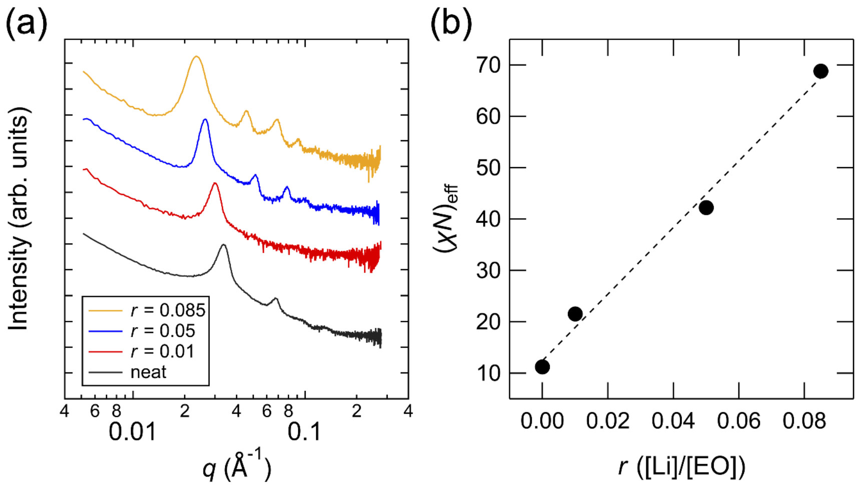

Figure 5.10 – (a) Bulk SAXS of SEO-LiTFSI at different salt concentrations used to determine L_0 and χ and (b) $(\chi N)_{\text{eff}}$ as a function of salt concentration

5.4.3 Self-assembly of SEO parallel lamellae on IDEs

SEO-LiTFSI solutions were prepared inside of an argon glovebox. First, solutions of SEO polymer in acetonitrile and LiTFSI in acetonitrile were prepared and left to stir overnight. Then, these two solutions were mixed at an appropriate ratio to obtain the desired molar ratio of lithium salt to ether oxygen ($r = [\text{Li}^+]/[\text{EO}]$). Thin films were then prepared by spin coating and thermal annealing. Interdigitated electrode (IDE) surfaces were first homogenized to ensure uniform wetting of the substrate and parallel orientation of the lamellae. For asymmetric assembly (PEO wetting of the IDE surface) we used an Ultratech/Cambridge Fiji G2 Plasma-Enhanced ALD to passivate the IDEs with thin layers of SiO_2 (around 1nm). To obtain symmetric wetting (PS wetting the IDE surface), the IDE was passivated with a thin layer of cross-linked polystyrene (x-PS). The x-PS solution was first spin coated on top of an IDE, resulting in thin layer of polystyrene (around 5 nm). Next, the IDE was annealed at 250 °C for 5 minutes to graft and crosslink the mat, and the remaining ungrafted polystyrene was removed by rinsing thoroughly with toluene (5 minute sonication three times in toluene, followed by direct rinsing with squirt bottle). The passivated IDEs were spin coated with SEO-LiTFSI solutions to achieve the desirable thickness. Thicknesses were determined by spin coating a witness sample on Si with native oxide and measuring with ellipsometry (J.A. Woollam alpha-SE ellipsometer). The SEO-LiTFSI coated IDEs were annealed on a hot plate at 165 °C for 30 minutes to drive phase separation and form an ordered parallel lamellae structure. The entire spin coating and annealing processes were done inside an Ar glovebox.

5.4.4 Ionic conductivity measurements

Polymer electrolyte films were spin cast onto IDEs fabricated according to the procedure described in Section 3.2.1. IDEs had dimensions of $N = 160$, $l = 1$ mm, $w = 2$ µm, and $d = 8$ µm. EIS measurements were performed with a potential amplitude of 100 mV over a frequency range of 1 Hz–1 MHz, and impedance spectra were fit to the equivalent circuit model shown in Figure 4.4b (Model 2). Conductivity was then taken using the cell constant derived in Section 3.3. Reported conductivity values are the average of three samples, with error bars corresponding to the standard deviation.

5.4.5 Conductive phase volume fraction calculations

The volume fraction of the PEO-LiTFSI conducting phase as a function of r was calculated using the following equation from Timachova *et al.*:[177]

$$\phi_c = \frac{\frac{M_{\mathrm{PEO}}}{\rho_{\mathrm{EO}}} + r\frac{M_{\mathrm{LiTFSI}}}{\rho_{\mathrm{LiTFSI}}}}{\frac{M_{\mathrm{EO}}}{\rho_{\mathrm{PEO}}} + r\frac{M_{\mathrm{LiTFSI}}}{\rho_{\mathrm{LiTFSI}}} + \frac{M_{\mathrm{PS}}M_{\mathrm{EO}}}{M_{\mathrm{PEO}}\rho_{\mathrm{PS}}}} \tag{5.8}$$

M_{EO}, M_{LiTFSI}, M_{PEO}, and M_{PS} refer to the molar mass of the EO repeat unit, LiTFSI salt, and M_{n} of the PEO and PS blocks with values of 44.05, 287.09, 9,000, and 10,000 g mol^{-1}, respectively. ρ_{PEO}, ρ_{PS}, ρ_{LiTFSI} are the densities of PEO, PS, and (solvated) LiTFSI with values of 1.128, 1.028, and 2.392 g cm^{-3}, respectively. The values of ϕ_c are used to calculate ϕ_{active} and ϕ_{inactive} in Table 5.1.

5.4.6 Estimation of the interfacial width by Strong Segregation Theory (SST) predications

To calculate the interfacial width, Δ, we use the following expressions proposed by Semenov[64] to adjust the Helfand[190] expression for homopolymer blends to block copolymers by two corrections:

$$\text{Helfand: } \Delta_0 = \frac{2b}{\sqrt{6}}\chi^{-0.5} \tag{5.9}$$

$$\text{Chain connectivity correction: } \Delta_1 = \Delta_0\left[1 + 0.853(\chi N)^{-\frac{1}{3}}\right] \tag{5.10}$$

$$\text{Fluctuation correction: } \Delta = \left[\Delta_1^2 + \frac{v\Delta_0}{2b^2}\ln\left(\frac{L_0}{\Delta_0}\right)\right]^{0.5} \tag{5.11}$$

Here b is the average statistical length of the polymers chains ($b_{\text{SEO}} = 6.3\text{Å}$)[191], v is the average molar volume for the BCE ($v_{\text{SEO-LiTFSI}} = 114\text{Å}^3$), N is the degree of polymerization, L_0 is the natural spacing of the BCE, and χ is the Flory-Huggins interaction parameter.

Note that in the current study we make use of an effective Flory-Huggins parameter, χ_{eff}, which accounts for the changes in χ due to the addition of LiTFSI. Additionally, the added volume of the lithium salt physically swells the system, which gives a higher effective degree of polymerization relative to the same reference volume, N_{eff}. The parameters χ_{eff} and N_{eff} can be determined by using the relationship between the change in the measured L_0 (taken from SAXS and AFM) and $(\chi N)_{\text{eff}}$.

The starting point for finding χ_{eff} is to determine the value for χ of the neat PS-PEO BCP. We use values for χ_{SEO} reported in a study by Epps and Bates:[65]

$$\chi_{\mathrm{SEO}} = \frac{29.8}{T} - 22.9 \times 10^{-3} \tag{5.12}$$

where T is the absolute annealing temperature (here, T = 165 °C). the degree of polymerization, N, was calculated by the molecular weights and densities of the PS and PEO blocks which are described above with the respect to a reference volume of 118 $\mathrm{\AA}^3$. It is well-documented that LiTFSI preferentially goes into the PEO domain and swells it. Therefore, the increase in N relates only to the PEO phase and can be calculated by:[69]

$$N_{\mathrm{eff}} = N + rv_{\mathrm{LiTFSI}} \frac{M_{\mathrm{EO}}}{M_{\mathrm{PEO}}} \tag{5.13}$$

where v_{LiTFSI} is the molar volume of LiTFSI, $M_{\mathrm{LiTFSI}}/\rho_{\mathrm{LiTFSI}}$. v_{LiTFSI} is also normalized to a reference volume of 118 $\mathrm{\AA}^3$. N is the degree of polymerization of neat (9-10k) SEO.

By knowing how N_{eff} varies with salt concentration and using L_0 data from SAXS measurements, we can use the following equation to get an effective Flory Huggins parameter:

$$\chi_{\mathrm{eff}} = \chi \left(\frac{L_0}{L_{0,r=0}} \right)^6 \left(\frac{N_{r=0}}{N_{\mathrm{eff}}} \right)^4 \tag{5.14}$$

where χ is the Flory-Huggins interaction parameter for the neat polymer which was calculated using Equation 5.12. Table 5.2 summarizes the calculated $(\chi N)_{\mathrm{eff}}$ for different salt concentrations of LiTFSI. We note that these values for χ_{eff} are in good agreement with previously reported values as a function of r.[68] These values, combined with the Equation 5.11 were then used to estimate the interfacial width as a function of salt concentration reported in Table 5.1.

Table 5.2 – Block Copolymer Values for SST Caluculations

r([Li$^+$]/[EO])	L_0 (nm)	N_{eff}	χ_{eff}	$(\chi N)_{\text{eff}}$
0	18.8	248	0.045	11.2
0.01	21.0	252	0.082	19.6
0.05	24.0	267	0.145	38.4
0.085	26.8	281	0.232	65.2

Table 5.3 – Interfacial width determined by SST and SCFT

		Δ (nm)	
r ([Li$^+$]/[EO])	$(\chi N)_{\text{eff}}$	SST	SCFT
0.01	19.6	3.31	3.63
0.05	38.4	2.62	2.33
0.085	65.2	2.23	1.70

5.4.7 Calculations of the interfacial width by self-consistent field theory (SCFT) calculations

To calculate Δ by SCFT, we used the Polymer Self-Consistent Field (PSCF) software, an open source code developed by Morse and coworkers.[187] To calculate the PEO concentration profiles we used L_0, Neff, and χ_{eff} found by SAXS measurements and Equations 5.12 and 5.13 respectively. A MATLAB script developed by the same group as part of the Broadly Accessible SCFT project was used to visualize the BCE profile. PEO monomer density profiles obtained from these SCFT calculations were fit to a hyperbolic tangent:

$$\phi_{\text{PEO}}(z) = 0.5\left[1 + \tanh\left(\frac{2z}{\Delta}\right)\right] \tag{5.15}$$

where z is the distance from the middle of the interface. Here Δ is obtained as a fitting parameter. The values of Δ from both methods are listed in Table 5.3.

Chapter 6

Effect of Wetting Symmetry on the Measured Ionic Conductivity of Cylinder-Forming Block Copolymer Electrolyte Thin Films

ABSTRACT

We have demonstrated how IDEs can be used to determine the intrinsic ionic conductivity of self-assembled single grain thin films of lamellae-forming block copolymer electrolytes (BCEs). In this chapter, we consider thin film structures where the domains are not perfectly ordered or vary spatially in three dimensions, rendering quantitative descriptions of the structure more challenging. In systems of polystyrene-*block*-poly(ethylene oxide) with lithium bis(trifluoromethanesulfonyl)imide (SEO-LiTFSI), we find that when the conductive material assembles into hexagonally packed cylinders within a nonconducting matrix, the defects arising from grain boundaries can produce orders of magnitude lower measured conductivity. This effect is overshadowed, however, if a thin (approximately 5 nm) wetting layer of conductive PEO-LiTFSI forms near the electrode surface. This wetting layer can completely dominate the EIS signal and give confounding results when compared to the top-down surface morphology. In contrast, when the conductive block forms a continuous structure—either lamellar or cylinders with the conductive block as the matrix—the measured conductivity is indifferent to the wetting layer and is determined primarily by volume

fraction of conducting material and interfacial mixing. Only in such cases where blocking defects play no role in the film conductivity can the effects of intrinsic properties on the ion transport, such as interfacial mixing, being clearly articulated.

6.1 Introduction

Block copolymer electrolytes (BCEs) are of great interest for their potential role as ion conducting membranes in a number of electrochemical energy storage devices, including fuel cells, supercapacitors, and lithium batteries.[142] These materials often consist of an ion conducting block and a mechanically rigid domain which phase separate at nanometer length scales, forming ordered nanostructures of 1D hexagonally packed cylinders, 2D lamellar sheets, or 3D percolating networks of conductive material.[67,87,88,163] Significant research effort has been put towards understanding how this nanostructure affects the transport of ions in these materials. To date, the majority of these studies have been performed on "bulk" systems, where micron thick membranes are measured in parallel plate geometries. These thick films are comprised of randomly oriented grains with impossible-to-predict ion conduction pathways, thus making quantitative correlation of structure and function difficult.[84,90,92] Recently, we have developed a platform to probe thin polymer electrolyte films with coplanar electrodes, where nanostructure can be precisely controlled or measured quantitatively by top-down microscopy.[108–110,192] We have demonstrated through the use of this platform the outsized role that defects play in the measured ionic conductivity. When a significant number of blocking defects exist between the two electrodes, the measured resistance as determined by electrochemical impedance spectroscopy (EIS) is as much as four orders of magnitude higher.[110] We have shown, however, if the block copolymer is assembled as a single grain with no blocked conduction pathways, the conductivity is of the same order of magnitude as the equivalent homopolymer ion conducting polymer.[192]

In these previous studies, the polymer structure was well-described by a two-dimensional picture which could be extended through the thickness of the film. In other words, blocking defects in the path of ion conductor can be seen from top-down images, and can be assumed to block the entire conduction pathway. Recent studies of bulk systems have demonstrated that similar outsized effects of blocked pathways can arise from selective alignment of polymer domains near the electrode surface and can dominate the overall measured conductivity. Sutton *et al.* found that thermal annealing of a gyroid-forming poly(isoprene-styrene-ethylene oxide) (ISO) material greatly reduced the conductivity of the material, despite no changes to the bulk structure of the ISO film.[164] This was attributed to the preferential formation of a polystyrene wetting layer near the surface of the stainless-steel electrode. When a PEO brush was first grafted to the electrode surface to induce preferential wetting of the ion conductive PEO domain, no decrease in conductivity was observed upon high-temperature annealing. Coote *et al.* recently showed that conductivity of a polystyrene-poly(ionic liquid) (PS-PIL) block copolymer was 20-fold in the in-plane direction of the film than in the through-plane direction.[193] This highly anisotropic conductivity could be explained by a three-layer model wherein the top and bottom of the cast film formed highly oriented lamellar layers oriented parallel to the electrodes, separated by a randomly oriented bulk. This ordered layer was the dominant factor in the observed conductivity when the electric field applied was normal to the orientation of the lamellar sheets. When the electric field was parallel to the well-aligned lamellae, the conductivity approached the theoretical value for the randomly order bulk.

Several reports have already demonstrated the importance of structural inhomogeneities near the electrode surface in the measurement of thin films as well. Paul *et al.* showed that Nafion conductivity exhibits a strong thickness dependence in the range of 4-200 nm, where thinner films showed greatly reduced ion conductivity.[121] This was attributed to the inability of these nanothin films to form the percolating water channels necessary for ion transport in perfluorinated ionomer materials. More recently, Su *et al.* showed that the pretreatment of gold electrodes with a controlled peptide sequence greatly altered the structure of ionomer films that were around 25 nm thick, resulting in a three-fold increase in the conductivity measured by EIS.[194] Furthermore, recent reports have shown that polymer dynamics and ion conduction can substantially deviate from bulk values near the surface of IDEs, dependent on the chemical composition, thermal history, and substrate preparation.[155,195] A more complete understanding of how the electrode surface functionalization affects the assembly and dynamics—and in turn, the electrochemical behavior—of polymer electrolytes is critical to developing higher performing polymer-based electrochemical devices.

In this chapter we examine the effects of electrode wetting, film structure, and surface topography on the measured in-plane ionic conductivity of thin films of different cylinder-forming polystyrene-*block*-poly(ethylene oxide) blended with lithium bis(trifluoromethanesulfonyl)imide (SEO-LiTFSI) BCEs. We find that when an ion conductive layer forms near the surface of the electrodes which differs in the number of defects from the rest of the film, the signal is dominated by this relatively small fraction of the film. If, on the other hand, this wetting layer is nonconductive, the conductivity observed by electrochemical impedance spectroscopy (EIS) is equal to that of the film far from the electrodes. In good accord with our previous findings, the blocking defects formed by randomly oriented grains of a cylinder-forming BCE shows orders of magnitude lower conductivity than the equivalent homopolymer when the conducting material is the minority block. Conversely, when the majority block of a cylinder-forming block copolymer is the conducting material, defects are not ion-blocking, and conductivity is well-predicted by volume fraction and interfacial mixing arguments as was the case in well-ordered lamellar block copolymer electrolyte films. Both film structures form continuous ion conduction pathways, and so defects are not expected to meaningfully effect ion transport. These findings inform how EIS measurements of thin film nanostructured electrolytes should be made and interpreted.

6.2 Results and Discussion

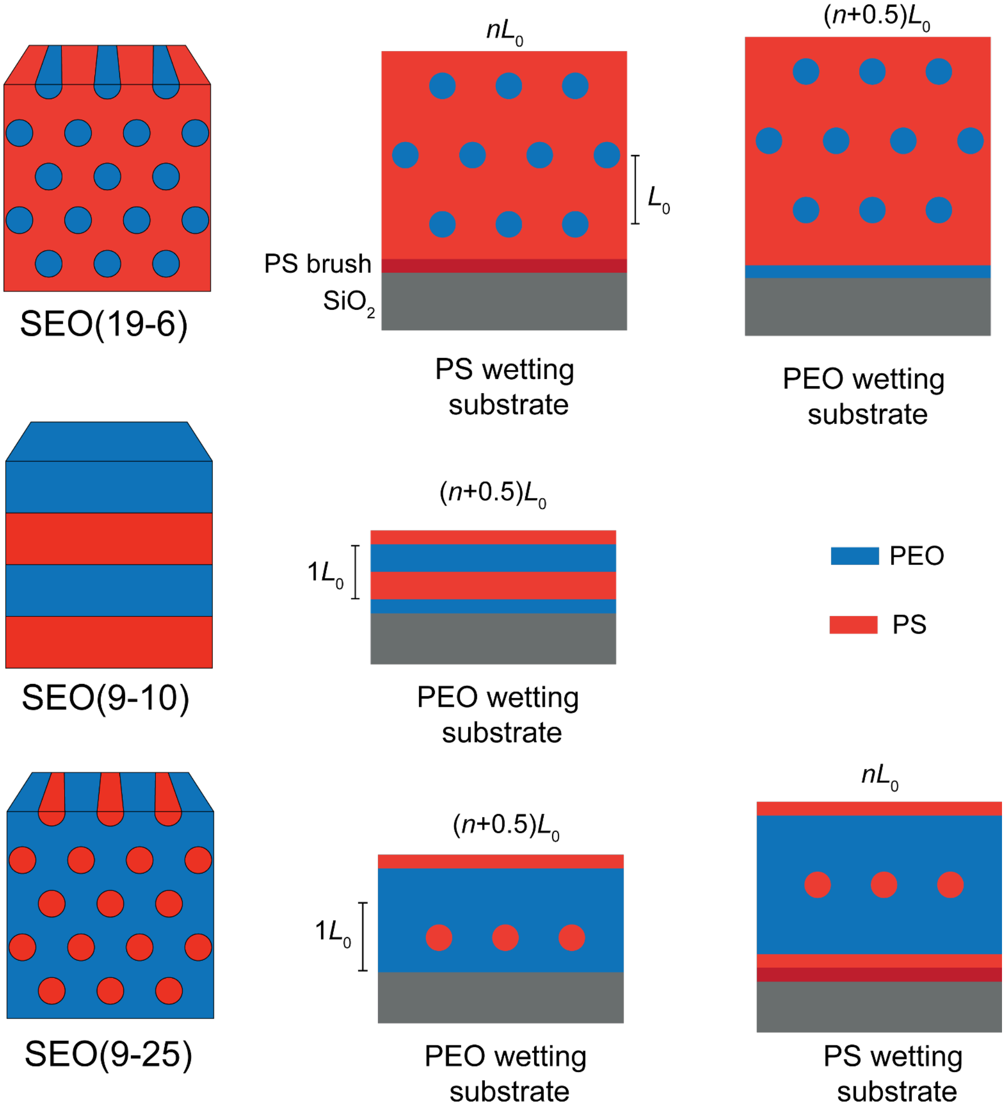

Figure 6.1 – Schematic overview of materials and structures studied in this chapter

Figure 6.1 provides a schematic overview of the materials and thin film structures studied in this work. Three SEO materials are examined in this study. Each material is referred to as SEO(x-y) where x and y refer to the M_n (in kg mol^{-1}) of the polystyrene (PS) and poly(ethylene oxide) (PEO) blocks, respectively. The materials were selected such that they form lamellae, hexagonally packed PEO cylinders in a PS matrix, or a continuous PEO phase with hexagonally packed PS cylinders depending on the volume fraction of each block, as illustrated in Figure 6.1. All characterization was done with mixtures of SEO and LiTFSI at a salt concentration of $r = 0.05 = [\mathrm{Li}^+]/[\mathrm{EO}]$. The volume fraction of the conducting PEO phase (ϕ_{PEO}) (PEO + LiTFSI) is 0.51 for the lamellae-former SEO(9-10), 0.24 for the PEO cylinder-former SEO(19-6), and 0.75 for the PS cylinder former SEO(9-25). The volume fraction calculations are performed exactly as they were in Chapter 5. The morphology and L_0 listed in Table 6.1 were determined from bulk small angle X-ray scattering (SAXS), shown in Figure 6.2. The SAXS profile for the SEO(9-25) material does not show a definitive HEX' morphology, but this morphology should be exhibited based on the volume fraction of the two blocks.

Thin films of the block copolymer materials are spin cast onto these functionalized IDEs for EIS measurements or onto functionalized Si for grazing incidence small angle X-ray scattering (GISAXS) and scanning electron microscopy (SEM) measurements. Thin film structure is controlled by spin coating films to a desired thickness on substrates with preferential wetting of one block. Generally, Si substrates or IDEs are coated with a thin, homogeneous layer of material to induce preferential wetting by either the PEO or PS domain of the BCE. A 1 nm layer of SiO_2 is deposited by atomic layer deposition (ALD) to create a hydrophilic surface to induce PEO domain wetting. A 5 nm PS brush is prepared on the IDE surface to create a hydrophobic, PS wetting substrate. In all cases the PS has lower free energy with the free surface, and it will preferentially segregate to the top of the film. By controlling the wetting behavior at both surfaces, we can orient the block copolymer domains (either

Table 6.1 – Physical properties of SEO block copolymers studied

Material	ϕ_{PEO} [a]	Morphology [a]	L_0 [a,b]
SEO(19-6)	0.24	HEX[b]	24.4 nm
SEO(9-10)	0.51	LAM[b]	24.0 nm
SEO(9-25)	0.75	HEX'[c]	32.5 nm

[a] All at $r = 0.05$

[b] Determined from SAXS of bulk samples

[c] Assumed from volume fractions

cylinders or lamellae) parallel to the substrate such that their orientation relative to the applied electric field is known.[104] The resulting ion conduction pathways should be readily probed by the electric field lines produced by the IDE, which are approximately parallel to the substrate.[134] The ability to study ion transport in thin films by this methodology has already clarified the quantitative effect of defects and interfacial mixing on ion transport in very well-ordered block copolymer films. In this study, this platform is leveraged to understand how the EIS measurements are affected by film thickness, defectivity, and film wetting symmetry in less well-ordered films and to provide a framework for understanding these more complex systems.

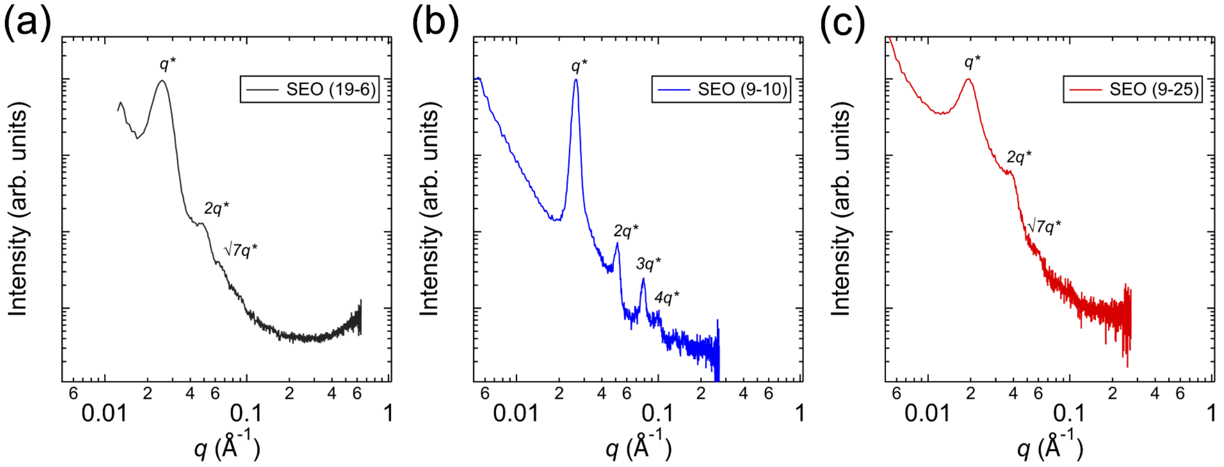

Figure 6.2 – Bulk SAXS profiles for (a) SEO(19-6), (b) SEO(9-10), and (c) SEO(9-25), all with $r = 0.05$ LiTFSI added

6.2.1 Measured impedance depends on wetting symmetry in minority-PEO BCE thin films

First, we examined the cylinder-forming SEO(19-6) material where the PEO phase is the minority component and forms hexagonally packed cylinders in a matrix of polystyrene. It has been demonstrated that parallel assembly of the cylinders can be achieved by preparing films of a thickness commensurate with multiples L_0.[196] L_0 here refers to the characteristic spacing between adjacent rows of PEO cylinders. For hexagonally packed cylinders, nearest neighbor cylinders are separated by a distance of $(2/\sqrt{3})L_0$. For symmetric wetting films, *i.e.* where both the substrate and free interface are preferentially wet by the same block, smooth films (free of topographical surface defects) with a discrete number of cylinder layers are obtained when the film thickness (h) is an integer multiple of L_0, nL_0.[197] This structure therefore consists of n layers of PEO cylinders in a matrix of polystyrene. Intermediate film thicknesses do induce these topographical features, suggesting that the parallel structure is obtained (see Figure 6.11 for SEM images).

We then verify that the structure illustrated in Figure 6.1 is obtained upon spin coating and annealing by GISAXS and SEM. The GISAXS diffraction pattern of a $3L_0$ thick film of SEO(19-6) on PS brush substrates, shown in Figure 6.3b, shows a strong peak in the q_y direction at $q_\mathrm{y} = 0.21$ nm^{-1} and higher order peaks at two and three times this value. Absence of an in-plane peak at $q_\mathrm{y} = 2\pi/L_0$ indicates there is no perpendicularly oriented cylinders in the film. The peaks are diffuse in the q_z direction, however, indicating that the parallel oriented cylinders are oriented randomly in the plane of the film. A more quantitative analysis confirming the parallel assembly is discussed in the Section 6.4.4. The parallel orientation is confirmed by the SEM image in Figure 6.3c of a $1L_0$ film on PS brush. Randomly oriented, fingerprint pattern cylinders are clearly seen. The average center-to-center spacing of these cylinders of 27.8 nm is in good agreement with the L_0 taken from bulk SAXS measurements. SEM images of thicker films on PS brush show similar features, which, combined with the GISAXS data, indicates that parallel cylinders exist throughout the thickness of the film at least up to 3 layers thick.

The electrochemical impedance of these parallel oriented cylinders is examined by assembling such films on top of interdigitated electrodes which have been surface-homogenized with either SiO_2 by ALD or by a PS brush. Figure 6.4b shows impedance spectra taken of $1L_0$ and $2L_0$ thick films of SEO(19-6), $r = 0.05$ with a PS brush coated IDE. The IDE

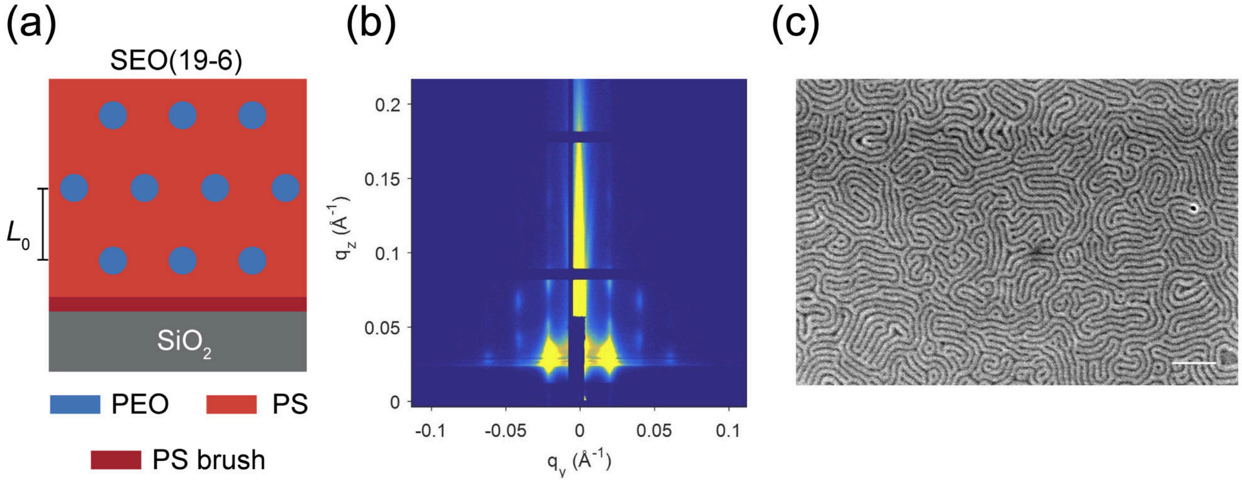

Figure 6.3 – (a) Schematic cross-section of $3L_0$ parallel oriented cylinder structure on PS brush; (b) 2D GISAXS pattern from a $3L_0$ (73 nm) thick film on PS brush; and (c) SEM image of top surface of $1L_0$ (24.2 nm) film on PS brush. The SEM scale bar is 200 nm.

geometric parameters used here are N = 480, l = 3 mm, d = 8 µm, and w = 2 µm. The additional number and length of teeth compared to what we have used previously was made necessary by the comparatively higher impedance of these films compared to other materials studied. These devices are referred to as "high surface area IDES", while all other measurements will be made with the "standard IDEs" used in previous chapters (N = 160, l = 1mm, d = 8 µm, w = 2 µm). Qualitatively, the impedance spectra look just as should be expected for a polymer electrolyte, with a semicircle motif at higher frequency (lower impedance) corresponding to the ionic resistance and film capacitance, and a low frequency capacitive tail.[112,134] Moreover, the film resistance (R), seen from the radius of the semicircle, decreases by half as the film thickness is increased from $1L_0$ and $2L_0$. This suggests that each layer of the conductive cylinders is fully probed by the impedance measurement, despite the discrete nature of the conductive medium. Impedance spectra are then fit to an equivalent circuit model as discussed in Chapter 4 (Model 2), and ionic conductivity is determined by Equation 6.1.

$$\sigma = \frac{d}{R(N-1)lh} \tag{6.1}$$

Measured conductivity for the $1L_0$ and $2L_0$ films is nearly identical across the entire temperature range of 80–130 °C, as seen in Figure 6.4c, giving us high degree of confidence in our interpretation of these measurements. This suggests that the fingerprint pattern observed from the top layer of cylinders by top-down SEM is representative of the defect structure that exists farther below the surface.

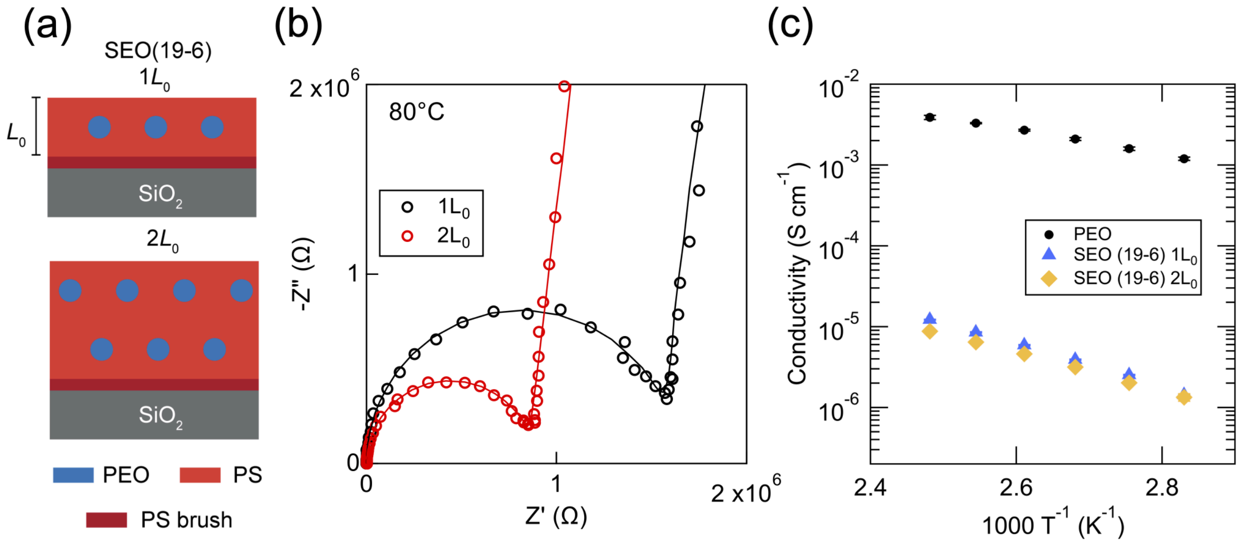

Figure 6.4 – (a) Schematic cross-section of $1L_0$ and $2L_0$ parallel oriented cylinder structure on PS brush; (b) EIS spectra of $1L_0$ and $2L_0$ thick films of SEO(19-6) at $r = 0.05$ on high surface area IDEs; and (c) temperature dependent conductivity of SEO(19-6) and PEO both at $r = 0.05$

When comparing the conductivity of these films to that of homopolymer PEO $r = 0.05$ (measured on standard IDEs), the effect of the fingerprint structure on the measured conductivity is evident (Figure 6.4c). Despite the conducting PEO being the same in both materials, the fingerprint PEO-cylinder forming material exhibits a conductivity more than two orders of magnitude lower than the homogenous PEO. While the lower volume fraction of PEO in the SEO(19-6) (25% PEO) and interfacial mixing between the PEO and PS are expected to reduce the conductivity to an extent, the ion blocking defects formed by the blocking defects constitute the majority of this reduced conductivity. Our previous work has demonstrated that such defects should be expected to dominate the measured conductivity of block copolymer electrolytes as measured by EIS.[109,110] For that reason, it is expected that we should see a lower conductivity in the cylinder-forming material than in the fingerprint lamellae structure examined in a previous study from our group due to the higher number of terminal defects in the PEO minority block.[110] Lastly, we see identical measured conductivity regardless of film thickness when the PEO cylinders are assembled on PS brushes, suggesting that this fingerprint structure produces similar defect structures throughout the film in this configuration.

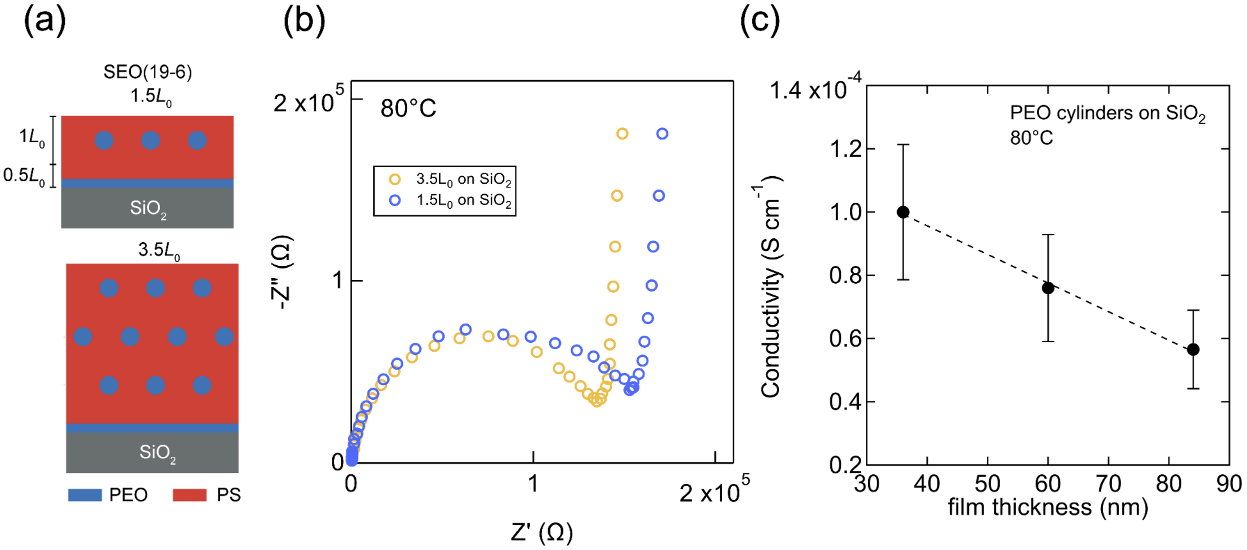

Figure 6.5 – (a) Schematic cross-section of $1.5L_0$ and $3.5L_0$ parallel oriented cylinder structure on SiO_2; (b) EIS spectra of SEO(19-6) at $r = 0.05$ on SiO_2 brush passivated IDEs; and (c) conductivity of SEO(19-6) at $r = 0.05$ on SiO_2-functionalized IDEs as a function of film thickness (dashed line shows linear fit of conductivity *vs.* thickness)

The relationship between conductivity and film thickness is considerably more complex in the case where the same PEO cylinder-forming SEO(19-6) is assembled on a PEO-wetting substrate, as illustrated in Figure 6.5. Smooth films (without surface topographical features) are achieved when the film thickness equals $(n + 0.5)L_0$. The impedance curves from SEO(19-6) films on SiO_2 passivated standard IDEs shown in Figure 6.5b are qualitatively similar to those of the same material on PS brush substrates, with the classic semicircle and capacitive tail motif. As expected, the thicker $3.5L_0$ film exhibits a lower resistance (smaller semicircle radius) than that of the $1.5L_0$ film; however, when this is normalized by the change in thickness, it is apparent that the measured conductivity decreases linearly with increasing film thickness (Figure 6.5c). This thickness-dependent conductivity can be attributed to the formation of a thin wetting layer of PEO that forms a continuous ion conduction pathway on the SiO_2 substrate. The formation of a contiguous wetting layer consisting of the minority block of a cylinder forming material when this block preferentially wets the substrate has been previously established.[197,198] This PEO wetting layer exhibits a much higher conductivity than the overlying fingerprint structure, as evidenced by the more than 10-fold higher conductivity in the $(n + 0.5)L_0$ films relative to the $1L_0$ film, as shown in Figure 6.6. However, as the $(n+0.5)L_0$ films consist of a combination of the defect fingerprint structure with a contiguous PEO wetting layer, the overall magnitude of the conductivity is dictated by the fraction of the film consisting of this high conductivity surface layer. Thicker films are comprised of increasingly more fingerprint structure with same $0.5L_0$ thick defect-free layer, and therefore exhibit a lower overall conductivity.

We can approximate the conductivity of this wetting layer to compare the relative ion transport through this and the overlying portion of the film. Note, the wetting layer cannot be produced in isolation—a $0.5L_0$ film results in a disorder state being trapped by confinement effects.[197] However, by comparing the conductivity of fingerprint structure, which can be obtained in isolation, to the total conductivity of the composite fingerprint/wetting layer structure, we can infer the magnitude of the wetting layer conductivity. Equation 6.2 below shows mathematically how this is done.

$$(n + 0.5)\sigma_{(n+0.5)L_0} = 0.5\sigma_{\mathrm{WL}} + n\sigma_{1L_0} \tag{6.2}$$

Here $\sigma_{(n+0.5)L_0}$ is the conductivity of the entire structure, σ_{WL} is the conductivity of the

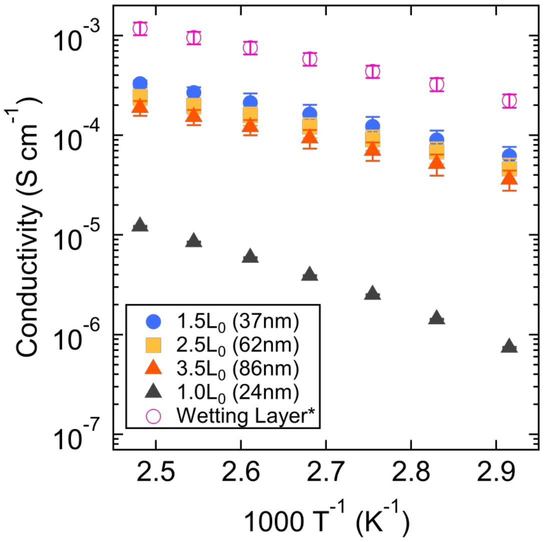

Figure 6.6 – Temperature dependent conductivity of SEO(19-6) at $r = 0.05$ for different thicknesses and on different substrate chemistries. *PEO wetting layer conductivity is calculated from Equation 6.2, with the value shown being an average of using 1.5, 2.5, and $3.5L_0$ conductivities. Error bars for the wetting layer represent one standard deviation from this average value.

wetting layer, and σ_{1L_0} is the conductivity of the fingerprint structure taken from the $1L_0$ structure on PS brush described previously.

The conductivity of the PEO wetting layer is plotted alongside the other relevant film structures in Figure 6.6. The values shown are an average of those obtained from Equation 6.2 with $n = 1$, 2, and 3, and the error bars represent one standard deviation. We see that these values exceed that of the fingerprint structure ($1L_0$ film) by more than two orders of magnitude, nearly approaching the values of homopolymer PEO after accounting for reduced volume fraction of active material. Despite representing a small fraction of the total film thickness (only 14% in the case of the $3.5L_0$ thick film), this wetting layer contributes to the majority of the measured conductivity. That is not to say that the fingerprint structure is not also sensed—the thickness dependence in the measured conductivity of these PEO wetting SEO(19-6) films shows that the overlying fingerprint structure still contributes to the total impedance of the film, but not a manner that manifests itself in a separate impedance response. However, by preparing films at different film thicknesses, we can infer the magnitude of each contribution the film structure. In this case, the cylinder-forming portion of the film has substantially lower conductivity, and its contribution the total impedance is small. However, the ability to decouple these two sections of the film allows us to be more quantitative in our analysis of the structure-function relationships of the material.

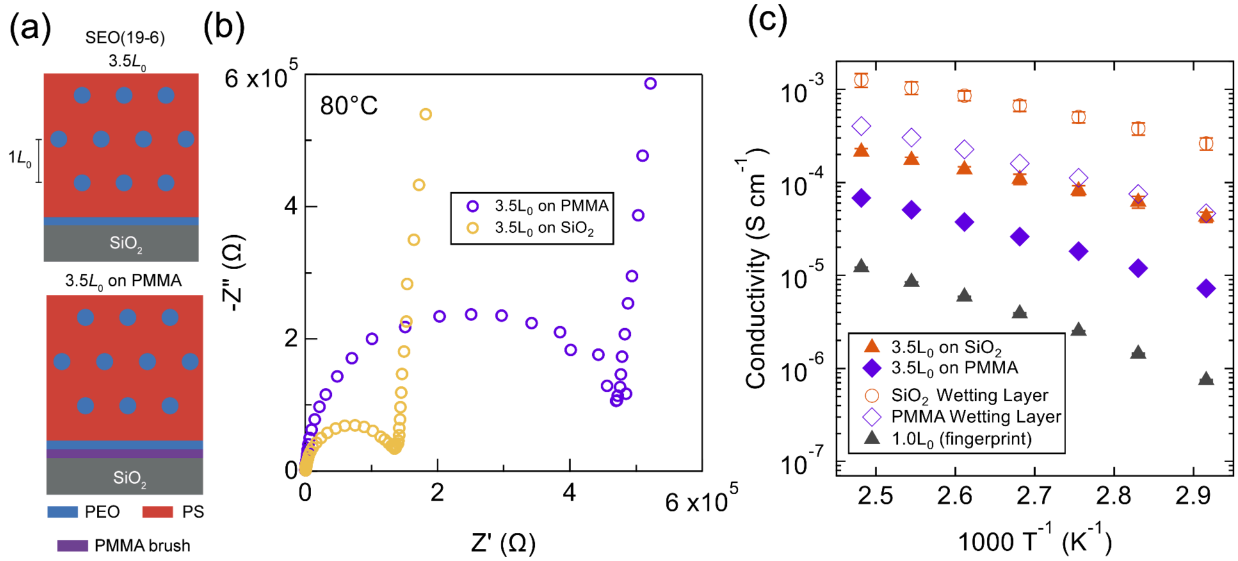

Figure 6.7 – (a) Schematic cross-section of 3.5L_0 parallel oriented cylinder structure on either SiO$_2$ or PMMA brush; (b) EIS spectra and (c) temperature dependent conductivity of SEO(19-6) at $r = 0.05$ measured on IDEs functionalized with either SiO$_2$ or PMMA brush. The conductivity of the wetting layer on SiO$_2$ and PMMA is calculated by Equation 6.2 as described above.

We attempted to eliminate this wetting layer from the EIS measurements by introducing a PEO wetting 6 nm PMMA brush. This PMMA brush layer should be miscible with the PEO but be glassy and nonconductive.[199,200] Blends of PEO and PMMA have been shown to exhibit an order of magnitude lower conductivity than PEO homopolymer electrolytes.[201,202] Moreover, in a previous study of thin films of PEO on IDEs with grafted PEO brushes, we saw a nearly 50% reduction in conductivity from the bulk value as the film thickness decreased to around 20 nm total.[155] We should therefore expect to see a substantial drop in conductivity in this roughly 10 nm total wetting layer due to decreased segmental mobility and diluted

PEO solvation sites. Figure 6b shows the impedance of $3.5L_0$ thick films of SEO(19-6) on SiO_2 and PMMA brush passivated IDEs. Although qualitatively similar in shape, the PMMA brush surface induces a significantly higher impedance. The conductivity of this film is roughly three times lower than that of the SiO_2 wetting film. We can again estimate a conductivity of this PMMA-PEO mixed wetting layer, shown in Figure 6.7c. The PEO-PMMA wetting layer conductivity is around three-fold lower than the unmixed wetting layer on the SiO_2 substrates, mostly as a result of decreased segmental mobility and PEO solvation site connectivity in the brush region.[39,179,203] However, this is still more than five times more conductive than the $1L_0$ fingerprint structure on PS brush. This result highlights a critical fact in understanding the impedance response of block copolymer electrolytes: defects represent a substantially higher impediment to ion transport than intermixing with a glassy, nonconductive material. Even in the case of a fully miscible system, such as the PEO-PMMA mixed wetting layer here, where one component is grafted to an immobile interface, the ion conduction through this layer still exceeds that of a defective fingerprint structure by more than an order of magnitude. Although this mixing and dilution of the efficient ion solvation sites of the PEO represents a significant barrier to rapid ionic transport, it is still substantially less meaningful to the overall impedance of the measured film. Understanding this fact and having knowledge of how a given block copolymer assembly near a given surface is paramount to fully characterizing the ion transport properties of the material.

6.2.2 Measured impedance is independent of wetting symmetry when conducting domains are continuous

Finally, we examine the impedance response of BCE structures where continuous ion conduction pathways exist through the entire film. This is the case of lamellae-forming SEO(9-10) that was studied extensively in Chapter 5, as well as with the SEO(9-25) material. In the case of SEO(9-25), PS forms the cylinder phase, and we expect that the conductive phase of

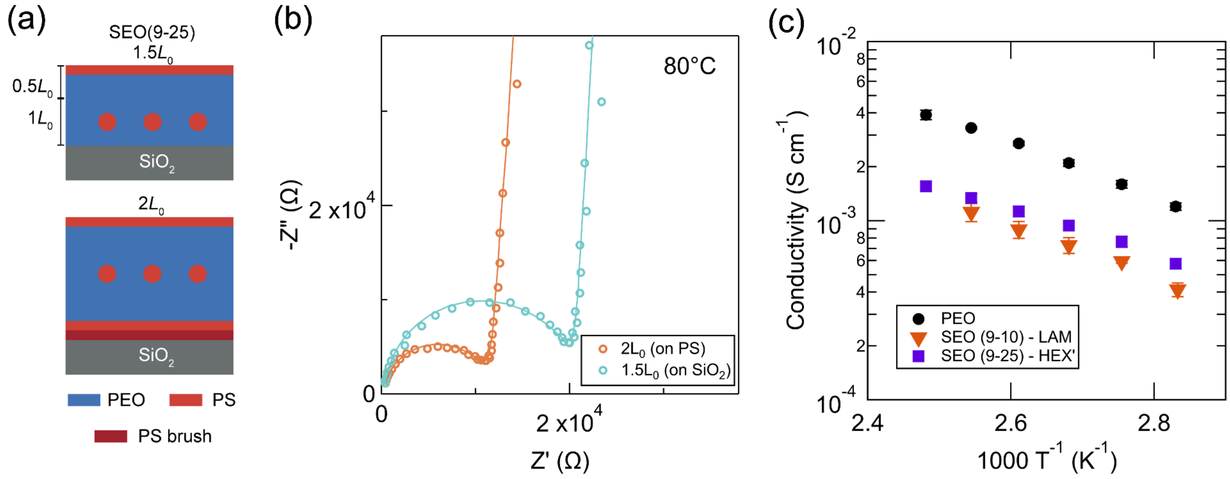

Figure 6.8 – (a) Schematic cross-section of Film of $1.5L_0$ and $2L_0$ SEO(9-25) on either SiO$_2$ or PS brush substrates; (b) EIS spectra of SEO(9-25) at $r = 0.05$ (PS cylinders) on PS brush and SiO$_2$ coated IDEs; and (c) average conductivity of SEO(9-25) $1.5L_0$ and $2L_0$ structures compared to homopolymer PEO and lamellar SEO(9-10) (thickness averaged value from Chapter 5)

the material to form a continuous network. Defects and tortuosity should therefore play a negligible role in the measured ionic conductivity. From the bulk SAXS measurements (SI), the material shows a characteristic domain spacing of $L_0 = 32.2$ nm. Top-down SEM images do not show the same fingerprint structure as seen with the SEO(19-6), however, likely due to the large volume of material above the PS cylinders and the continuous layer of PS that likely forms on the free surface (see schematics in Figure 6.8a). Regardless, we can see that films spin cast at $1.5L_0$ on SiO$_2$ or $2L_0$ on PS brushes form smooth films with no holes or islands. The EIS spectra obtained from these films is shown in Figure 6.8b. Again, the same qualitative spectrum is observed, and the resistance of the film scales linearly with the film height. The conductivity obtained from both the symmetric and antisymmetric wetting is nearly identical because unlike in the case of the PEO cylinder-forming material, the PEO wetted substrate does not introduce a substantial more interconnected ion conduction channel to the film structure. Instead, the overlying cylinder pattern in the case of SEO(9-25) already provides a continuous network for ion transport, and the presence of a non-cylinder forming wetting layer (either at the free surface or substrate interface) does not produce a qualitatively different ion transport pathway. Here, the conductivity deviates from the PEO homopolymer only by the difference in volume fraction of active material and due to interfacial mixing between the PS and PEO domains.

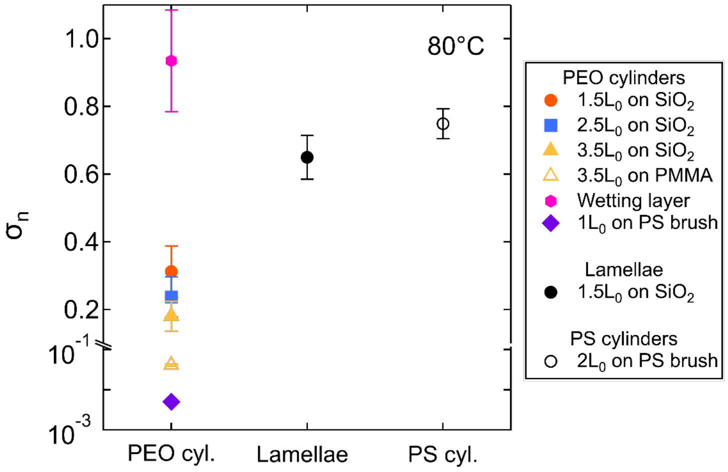

Figure 6.9 – Summary of normalized conductivities (σ_n) at 80 °C of different film structures of SEO-LiTFSI at $r = 0.05$. The conductivity was normalized by the conductive PEO volume fraction (ϕ_{PEO}) and the conductivity of equivalent PEO homopolymer at $r = 0.05$.

The preferentiality of a given block to wet the electrode surface has been shown here to have dramatic effects on the apparent conductivity of the material, and this wetting preferentiality can lead to potential misinterpretation of the structure-function relationships. For example, by top-down SEM alone, the $1.5L_0$ film on SiO_2 exhibits only the defect filled fingerprint structure. Comparing this structure to the relatively high conductivity measured by EIS of this film, one could erroneously conclude that these defects play only a minimal role in preventing ion transport in these structures. This conclusion would be in direct contrast to that of Kambe *et al.* regarding the effect of defects in perpendicularly oriented lamellar block copolymer electrolytes.[110] Moreover, one could compare the $3.5L_0$ and $1.5L_0$ films and erroneously infer that the EIS measurement was producing a lower measured conductivity due to the junction potential formed by increasing amount of nonconducting

PS between the electrodes and the uppermost layers of PEO-LiTFSI. However, by careful consideration of the full film structure, we can confidently conclude that, as was the case in the study of lamellae-forming SEO, the increasing film thickness does not in fact affect the EIS measurement. Instead, these thin film EIS measurements offer a sensitive probe of the underlying surface layer formed in these systems. From the magnitude of the conductivity of this layer relative to that of PEO homopolymer, it is clear that this wetting layer forms a fully continuous ion conduction pathway between electrodes, with little to no defects. While this structure was already known to exist in cylinder-forming linear diblock copolymers, more complex phase behavior exhibited by different chain architectures may not have such well-understood subsurface structure. In the case of new material systems with more complex surface interactions, EIS can serve as a tool to probe the through-film structure in a way that top-down microscopy cannot. Future studies may be able to use this to sensitively probe interfacial phenomena occurring in heterogenous electrochemical systems in a nondestructive way.

The effects of wetting layers, defectivity, and film thickness should only manifest in systems where the in-plane ion conduction pathways are nonuniform through the thickness of the film. Our previous study of parallel oriented lamellae demonstrated that when all ion conduction pathways are fully unhindered by defects, the presence of a $0.5L_0$-thick PEO wetting layer near the electrode surface has no meaningful effect on the overall transport in the system.[192] To clearly visualize the impact of the film structure, wetting symmetry, and morphology on the measured conductivity, we plot the conductivity of all samples measured in this study divided by ϕ_{PEO} and the conductivity of equivalent homopolymer PEO at the same r value to yield a normalized conductivity, σ_{n} (Figure 6.9).

$$\sigma_{\mathrm{n}} = \frac{\sigma_{\mathrm{BCE}}}{\phi_{\mathrm{PEO}}\sigma_{\mathrm{PEO}}} \tag{6.3}$$

The values for σ_{n} fall roughly into two bands: one where a continuous ion conduction pathway exists and ion transport is predominantly limited by interfacial mixing between the blocks, and another where conduction pathways are significantly hindered by ion-blocking defects in the film. The PS cylinder-forming SEO(9-25) clearly falls into the former category, as the film consists of a majority PEO and defects are expected to be conductive rather than ion blocking. Here, wetting preference and film height are nonfactors in the conductivity as they do not affect the proportion of film that is continuous and conductive. The case of the lamellae-forming SEO(9-10) smooth films is similar, as the ion conducting channels formed here are uninterrupted in the direction of ion transport on the IDEs, *i.e.* parallel to the substrate. A more interesting case arises in the case of the PEO cylinder-forming SEO(19-6) films. When the films are symmetrically wetting (PS on both top and bottom of the film), we probe only the conductivity of a film with a very large number of ion-blocking defects, and the normalized conductivity is less than 1% of the value of similar materials with different film structure. However, when the substrate is PEO wetting and a contiguous conduction pathway is opened up, we see a large increase in the value of σ_{n}, which approaches the value of the lamellae and PS cylinder SEO at decreasing film thicknesses. Such striking difference in the apparent conductivity by simply changing the electrode surface energy has been seen in bulk systems before. In the case of thin films, however, the film structure can be more carefully controlled or quantified, and the conductivity of this wetting layer may actually be estimated with some degree of accuracy. The magnitude of the conductivity of this layer when assembled on a PMMA brush falls somewhere in between that of the fingerprint sample and the SiO_2 passivated substrate. However, this layer of glassy, tethered PMMA intermixed with PEO is still significantly more conductive than the defect-filled top layer of the film. Moreover, this wetting layer can be probed nondestructively by these thin film EIS measurements, and this tool may be used to understand the wetting behavior of more complex block copolymer structures. Overall, measuring films of different thickness and on different surface energy substrates represents an important control study that should be performed before quantitative analysis of the conductivity of a microphase-separating material can be undertaken.

6.3 Conclusions

In this study we have clarified the relationship between block copolymer morphology, underlying wetting layers, and ionic conductivity. Building on our previous work that has focused on lamellar morphologies, we have shown that when the majority phase of a cylinder-forming block copolymer is ionically conductive, defects are non-blocking, and conductivity is on the same order of magnitude as the equivalent conductive homopolymer. In contrast, when the conductive phase comprises the minority block, defects are blocking, and the conductivity is reduced by orders of magnitude. If, however, the minority conductive phase preferentially wets the electrode surface, forming a thin, continuous wetting layer, the impedance signal is dominated by this layer. This gives rise to a thickness-dependent conductivity in these films, as thicker films contain a greater fraction of highly defective, low conductivity cylinder layers relative to the single wetting layer. By comparing the conductivity of these heterogenous structures to that of a film without a conductive wetting layer, the conductivity of this surface region can be estimated. The wetting layer conductivity was found to be similar in magnitude to the homopolymer conductivity due to the continuous nature of the conduction pathway, even when prepared on top of a glassy, nonconductive PMMA brush. This result emphasizes the stark difference in magnitude between the effects ion-blocking defects and reduced segmental dynamics or solvation site connectivity in mixed interfaces on the measured conductivity. The latter can only be analyzed quantitatively when the former is eliminated entirely and doing so requires careful consideration of the full film structure, most notably at the electrode-electrolyte interface.

These findings have implications for both the fundamental study of ion transporting materials, as well as how these materials interact with electroactive electrodes. When new nanostructured electrolyte materials are prepared and measured, it is critical that the effect of film structure is accounted for when determining the inherent conductivity of the material. Material systems where the conductive phase is the minority block may present a greater challenge in this regard as the ability to form continuous structures is highly dependent on the film thickness, electrode surface energy, and geometry of the measurement setup. Due to the wealth of research performed on block copolymer thin films on planar substrates and the wide array of measurement techniques available to probe the structure of these films (including AFM, electron microscopy, GISAXS and GIWAXS, neutron scattering, and TOF-SIMS), the IDE presents an attractive platform to make electrochemical measurements in the same configuration. Only in the coplanar cell geometry can certain surface-induced ion conduction pathways be accurately sensed and quantified. These surface dependent wetting and conducting layers will be even more important when the electrodes are redox active, and ion transport into and out of the electrode is measured along with ion transport through the electrolyte. For example, the wetting of a SEO-based electrolyte near a silicon anode is likely similar to the wetting on the SiO2 passivated IDEs used here. Understanding how each block of the copolymer preferentially interacts with the anode particle surface may be necessary to accurately describe the performance of the system as a whole. In the future, an IDE can be an enabling platform to study such interfacial systems in a controlled and systematic manner.

6.4 Materials and Methods

6.4.1 Materials

Block copolymers—SEO(9-10) (M_n = 9-10 kg mol^{-1}, $Đ$ = 1.07), SEO(19-6) (M_n = 19.5-6 kg mol^{-1}, $Đ$ = 1.07), SEO(9-25) (M_n = 9-25 kg mol^{-1}, $Đ$ = 1.12)—and homopolymer PEO (M_n = 20 kg mol^{-1}, $Đ$ = 1.10) were purchased from Polymer Source Inc. and vacuum dried at 50 $^{\mathrm{C}}$ before use. The hydroxy-terminated poly(methyl methacrylate) (PMMA) (M_{n} = 6.5 kg mol^{-1}, $Đ$ = 1.18) and hydroxy-terminated PS (M_{n} = 10 kg mol^{-1}, $Đ$ = 1.05) brush materials were purchased from Polymer Source and used as received. Lithium bis(trifluoromethanesulfonyl)imide (LiTFSI) was purchased from Sigma Aldrich and dried under vacuum at 100 °C before use. PEO, SEO, and LiTFSI were stored in an argon glovebox. Acetonitrile (99.8 %, anhydrous) and toluene were purchased from Sigma Aldrich and used as received. Silicon wafers (4" diameter, 500 µm thick) with and without 1 µm of thermal SiO_2 were purchased from Pure Wafer Inc.

6.4.2 Substrate preparation

IDEs and Si substrates were prepared in the same manner to ensure that block copolymer assembly would be identical on both. IDEs were prepared as described in Chapter 3. IDEs and Si wafers were cleaned with acetone, IPA, deionized water, and finally a reactive ion plasma descum prior to deposition of either ALD SiO_2 or polymer brush. PS or PMMA brushes were prepared by first dissolving the polymer in toluene at 1 wt%. This solution was then spin coated on a plasma cleaned Si or IDE substrate at 4000 rpm followed by annealing at 200 °C for 5 minutes in a nitrogen glovebox. The substrates were subsequently cleaned by three-fold sonication in toluene to remove ungrafted polymer.

6.4.3 Thin film fabrication

All polymer electrolyte thin films were prepared by spin casting from solutions prepared inside of an argon glovebox. Solutions of polymer in either acetonitrile or a mixture of acetonitrile and toluene were mixed with solutions of LiTFSI in acetonitrile. The solution concentration varied between 4 mg mL^{-1} and 20 mg mL^{-1} to control the film thickness. All films cast for SEM, GISAXS, or EIS measurement were spin coated inside of an argon glovebox. After spin coating, block copolymers were annealed on a hot plate inside of the glovebox at 165 °C for 1 hour (SEO(9-10) and SEO(9-25)) or 215 °C for 14 hours (SEO(19-6)). Film thickness was determined by ellipsometry using a J.A. Woollam alpha-SE ellipsometer.

6.4.4 Block copolymer characterizations

Small-angle X-ray scattering (SAXS) was performed using the SAXSLAB GANESHA instrument at the University of Chicago X-ray Facility. Silicon nitride membranes (100 nm thick, 2.25×2.25 mm^2 area) were fabricated in-house to serve as support for the polymer material. Polymer electrolyte films were cast from solution onto the silicon nitride membranes and annealed at 165 °C for 1 hour (SEO(9-10 and SEO(9-25)) or 215 °C for 14 hours (SEO(19-6)). Primary scattering peaks, q^*, were found by peak fitting using the SAXSGUI MATLAB program developed by SAXSLAB. The block copolymer domain spacing, L_0, was taken as $2\pi/q^*$.

GISAXS measurements were performed at beamline 8-ID-E of the Advanced Photon Source, Argonne National Laboratory with 10.86 keV ($\lambda = 0.11416$ nm) synchrotron radiation. Samples were enclosed and measured inside a low vacuum chamber (10^{-3} mbar) to minimize concerns about radiation damage as well as to prevent extraneous scattering from ambient air. The measurement time was chosen to be 10 s per frame. For each sample, 3 data sets were taken from 3 adjacent spots on the sample and then summed in order to enhance the signal-to-noise ratio. In our work, the samples were tilted at an angle of incidence of 0.12° with respect to the incoming beam. The scattering signal was recorded with a Pilatus 1MF pixel array detector (pixel size = 172 μm) positioned at the distance 2185 mm from the sample. Each data set was stored as a 981×1043 32-bit tiff image with 20-bit dynamic range. The GISAXS image was subjected to detector nonuniformity, detection efficiency, the polarization effect and solid-angle variation correction. All the data processing and extraction were executed using the GIXSGUI package for MATLAB.[204] Figure 6.10 shows the GISAXS scattering profile from Figure 6.3c annotated with predicted scattering peaks. The

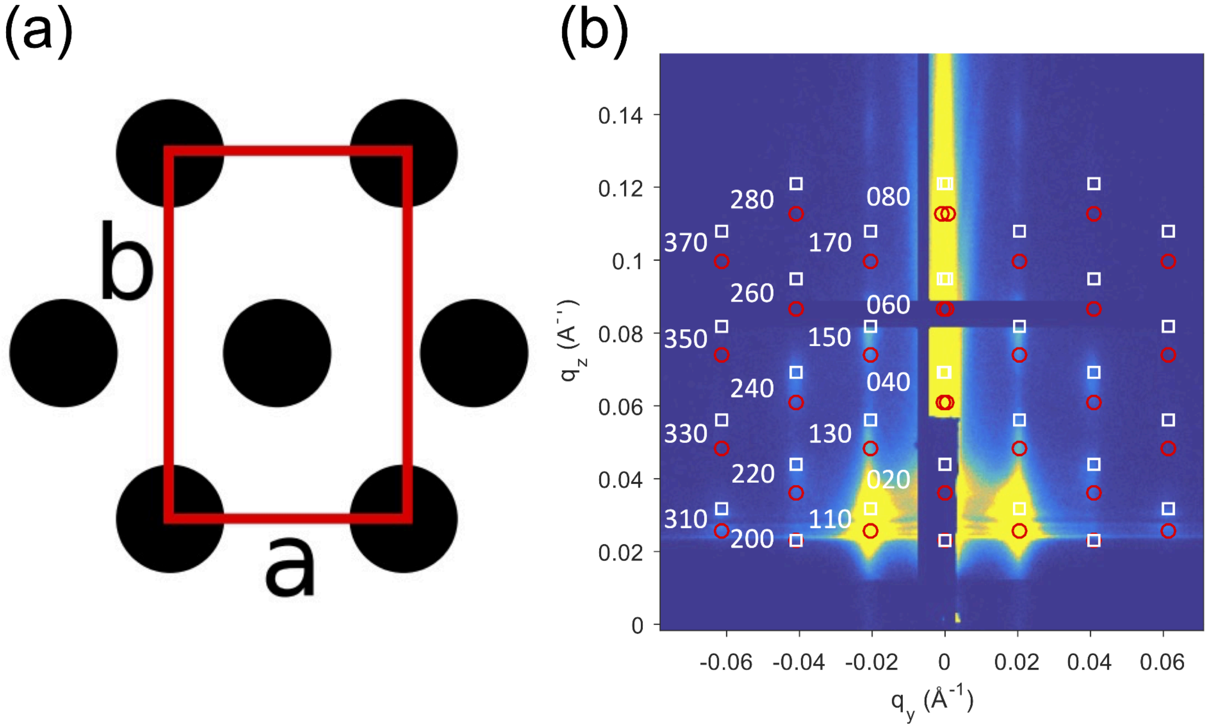

Figure 6.10 – (a) Schematic view of the sample cross-section showing a rectangular centered lattice consisting of PEO cylinders parallel to the film surface. (b) GISAXS diffraction pattern of a $3L_0$ thick film of SEO(19-6) on PS brush substrates. Red circles and white squares labeled with Miller indices are calculations using lattice parameters a, b = 30.8 and 48.0 nm (as noted in (a)) for the transmission and reflection channels, respectively.

calculated transmission and reflection peaks, assuming parallel oriented cylinders, match well with the experimental GISAXS peaks, confirming the parallel orientation of PEO cylinders.

Top-down SEM images of the BCE films were taken with the Carl Zeiss-Merlin Field Emission scanning electron microscope. The acceleration voltage was 1.25 kV with a working distance of 3 to 4 mm using an in-lens detector. The images were processed and analyzed using ImageJ. Figure 6.11 shows SEM images of SEO(19-6) on PS brush ($1.5L_0$) and SiO_2 ($1L_0$). Due to the film thickness-surface wetting combination for both samples, holes or islands form, as would be expected when parallel assembly of the cylinders is favored. The parallel assembly is evident at both thicknesses, with perpendicular assembly seen in a brief transitional region between the two film heights.

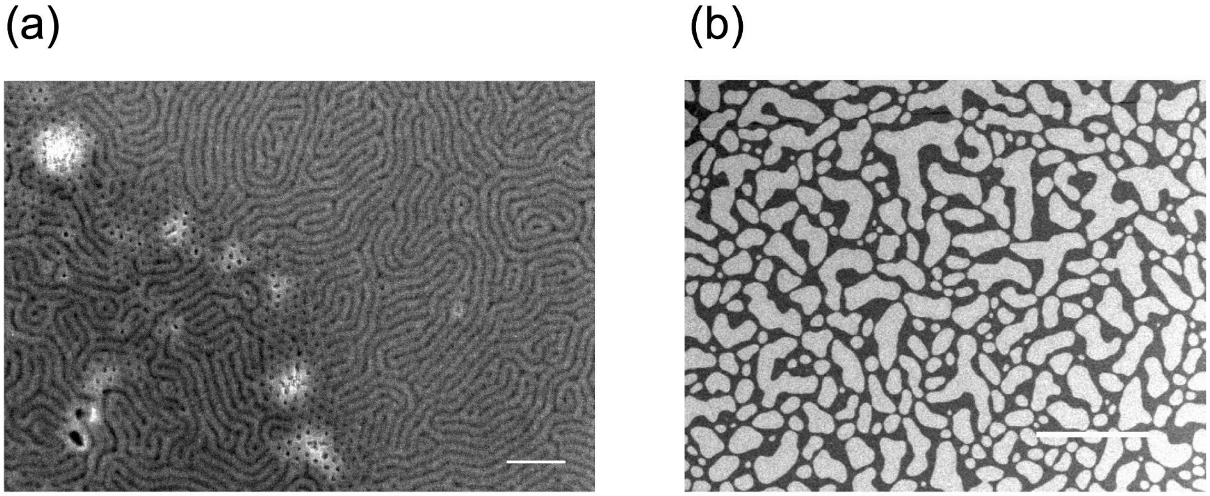

Figure 6.11 – SEM images of SEO(19-6) thin films on (a) PS brush ($1.5L_0$) and (b) SiO_2 ($1L_0$). Scale bars correspond to (a) 0.16 µm and (b) 16 µm.

6.4.5 Ionic conductivity measurements

Polymer electrolyte films were spin cast onto IDEs fabricated according to the procedure described in Section 3.2.1. IDEs used for measuring SEO(19-6) had dimensions of $N = 480$, $l = 3$ mm, $w = 2$ µm, and $d = 8$ µm. All other measurements were done using IDEs with dimensions of $N = 160$, $l = 1$ mm, $w = 2$ µm, and $d = 8$ µm. EIS measurements were performed with a potential amplitude of 100 mV over a frequency range of 1 Hz–1 MHz, and impedance spectra were fit to the equivalent circuit model shown in Figure 4.4b (Model 2). Conductivity was then taken using the cell constant derived in Section 3.3. Reported conductivity values are the average of three samples, with error bars corresponding to the standard deviation.

Chapter 7

Role of Solvation Site Segmental Dynamics on Ion Transport in Ethylene-oxide Based Side-chain Polymer Electrolytes †

ABSTRACT

Ion conducting capability is often imparted to polymeric materials through short polyether side-chains, and yet the impact of this graft polymer architecture on ion solvation and conduction has not been fully explored. In this chapter, we use a combination of impedance spectroscopy, vibrational spectroscopy, and atomistic molecular dynamics (MD) to compare the conductivity, ionic interactions, and polymer dynamics in a series of graft polyether electrolytes. We find that in poly[oligo(ethylene oxide) methyl ether methacrylate] (POEM), a widely used graft polymer electrolyte, the ionic conductivity drops more than an order of magnitude as the side-chain length is decreased from nine ethylene oxide (EO) units to three. This difference in conductivity is unexplained by differences in the calorimetric glass transition temperature (T_g), which varies only slightly with side-chain length. Through vibrational spectroscopy and MD simulations we demonstrate that both linear and graft polyethers solvate Li^+ effectively and dissociate them from large counterions, irrespective of side-chain length. Li^+ are, however, preferentially solvated by EO units far from the

---

†. This work was originally reported in *J. Mater. Chem. A*, **2021**, 9, 9937-9951

methacrylate backbone. Similarly, EO units far from the backbone show enhanced segmental dynamics, while those near the immobile methacrylate group move substantially more slowly, as quantified by bond vector autocorrelation relaxation times. This heterogeneity in both ion solvation and local segmental relaxation explains variation in ion conductivity where material-averaged properties such as T_g and number of free ions fail to do so. Importantly, the ionic conductivity is dictated primarily by the segmental mobility of the EO units which form effective solvation sites, rather than system-wide dynamics.

7.1 Introduction

In the field of lithium ion batteries, poly(ethylene oxide) (PEO) has long been the most promising candidate for use as a separator and electrolyte due to its ability to readily solvate and conduct alkali metal cations.[23] Many other materials chemistries have been considered for their potential as dry SPEs, such as polycarbonates[58,205,206] and polyesters[38,207,208], but polyethers continue to outperform these other systems in terms of ionic conductivity and remain the most widely studied class of polymer electrolytes. However, the semi-crystalline nature of PEO at ambient temperatures and resultingly low room temperature conductivity, as well as a low lithium cation transference number, and an inverse relationship between ion transport and mechanical properties have prevented homopolymer PEO from satisfying the full set of requirements to enable safe cycling of high energy density lithium metal batteries.

New directions in the field of ion conducting polymers focus on incorporating additional functionalities to the well-known ether-based electrolytes to improve on these mechanical and electrochemical shortcomings of PEO. Such materials include microphase-separating block copolymers, graft and bottlebrush polymers, and random copolymers or blends where secondary functional groups affect the phase behavior and electrochemical properties of the material.[87,178,209–211] The introduction of ethylene oxide (EO) segments as grafted side-chains on polymerizable macromonomers is a particularly attractive as this approach is accessible through a number of well-established synthetic techniques, including anionic polymerization[171], atom-transfer radical polymerization[179], and reversible-addition-fragmentation chain transfer polymerization (RAFT).[212] This method has the added benefit of reducing or eliminating room temperature crystallization of the short polyether chains. These controlled living polymerization techniques are also amenable to random or block copolymerization, which have been used successfully to incorporate additional functionalities alongside the ion conducting EO groups, such as a mechanically stabilizing group or single-ion conducting component.[213–215] The ether oxygen motif has also been incorporated into materials that are tailored for electrode binder applications due to their dynamic self-healing capability[216,217] or coupled with polythiophene groups to create dual ion-electron conducting materials.[36,218] Further improvement upon the design of these multi-functional materials, however, requires a clearer understanding of how the polymer chain architecture and composition affects the solvation and transport of ions.

Ion transport in rubbery polymer electrolytes is generally understood to require a high degree of salt dissociation, connectivity between polymer solvation sites, and fast segmental dynamics to facilitate ion transport between solvation sites. PEO forms stable complexes with alkali metal ions such as lithium through interactions with the lone pairs on the ether oxygens. This enables high degree of ionic dissociation from large, stable anions, such as the common bis(trifluoromethanesulfonyl)imide ($TFSI^-$). The low glass transition temperature (T_g) of PEO gives rise to fast segmental dynamics when completely amorphous (above roughly 50 °C), which has been shown to facilitate rapid ionic transport.[20,42] Low T_g alone, however, is not necessarily a good predictor of ionic conductivity. This fact was exemplified by a recent study of poly(trimethylene carbonate)-based polymer electrolytes, where it was demonstrated that the introduction of long alkyl side-chains lowered the glass transition temperature, but a concomitant increase in ionic conductivity was not observed.[219]

Molecular dynamics (MD) simulations indicated that, although the material overall exhibited faster dynamics when plasticizing alkyl side-chains were present, the time between ion hopping events was significantly longer. Similarly, solvation site connectivity has been explored in various systems as an additional metric to accounts for the discrepancy between trends in T_{g} and ionic conductivity.[34,37,39] Previous studies have found that in branched polyethers, the length of polymer side-chains and the spacing between them are key parameters in determining the conductivity of the system.[51,220] MD studies have sought to provide mechanistic insight into the effects of branched architecture and side-chain structure on ion transport, though a clear connection between microscopic transport phenomena and macroscopic material performance was not established.[221] Recent work by our group has demonstrated that heterogenous ion solvation and local polymer relaxation rates in graft polymers result in qualitatively different trends in ion conductivity than in linear polymer electrolytes.[22] Greater understanding of how molecular-level transport processes are affected by the graft chain architecture, chemical composition, and side-chain length are required to optimize the design and development of these systems.

In this chapter, we describe the synthesis, characterization, and computationally modeling[1] of a series of graft polyethers to examine the effects of polymer composition, chain architecture, and side-chain length on the ion solvation, average and local segmental dynamics, and transport properties of these electrolytes. We observe that the experimental ion conductivity varies by as much as an order of magnitude in POEM materials of different side-chain lengths, and this effect is not well explained by differences in T_{g} or ionic dissociation. The same trend is observed in the simulated Li-ion diffusivity. Comparing solvation site edge density from MD simulations and T_{g}-corrected experimental conductivity, we see that solvation site connectivity, as defined in previous studies, only accurately predicts conductivity or MSD at intermediate temperatures (T). We find significant deviations above

---

[1] All MD simulations were performed by Chuting Deng, a graduate student in the de Pablo group at University of Chicago. Analysis was done with help from Prof. Michael Webb from Princeton University.

and below the solvation site predicted performance at high and low values of $T - T_g$, respectively. We demonstrate that although ions are fully dissociated in all systems, Li^+ shows a strong preference for ether oxygens over carbonyl groups. Constraints on the available conformations of those ether oxygens giving rise to certain monomers having a much more significant role in solvation than others. We further see that individual EO segments relax at substantially different rates as a function of position along the side-chain. Those EO units furthest from the relatively immobile methacrylate backbone exhibit significantly faster relaxation rates than those near the backbone. This spatial variation in the segmental mobility is not captured by the T_g differences, but local EO segmental dynamics seems to be critical in producing the observed trends in ionic conductivity. Specifically, the dynamics of those EO segments which most frequently participate in the formation of solvation sites have far greater impact on the ionic conductivity than the overall segmental dynamics. Moreover, we find that making the backbone more flexible or increasing the fraction of high-mobility (far from the backbone) EO units at the same overall ether oxygen fraction both increase the ionic conductivity. These findings have broad implications for developing graft and multifunctional polymer electrolytes and provide clear design criteria for optimizing polymer architecture and chemistry for high ionic conductivity.

7.2 Results and Discussion

7.2.1 Synthesis and modeling of side-chain polyether electrolytes

To explore the effects of polymer chain architecture and composition on ion conduction and solvation in EO-based polymer electrolytes, we employ a combined experimental and computational platform involving thin film electrochemical impedance spectroscopy (EIS), Raman and Fourier transform infrared spectroscopy (FTIR), and molecular dynamics (MD) simulations. We investigate two classes of polyethers in this study: linear poly(ethylene oxide) (PEO), and a series of graft polymers based on short polyether side-chains grafted to an acrylate or methacrylate backbone. Side-chain polymers poly[(oligo (ethylene oxide)) methyl ether methacrylate] (POEM$_x$), poly[(oligo (ethylene oxide)) methyl ether acrylate] (POEA$_9$), and a random copolymer of POEM and poly(methyl methacrylate) (PMMA) were prepared by reversible addition fragmentation chain transfer polymerization (RAFT). The subscript x here refers to the number of EO repeat units in the grafted side-chain, which in this study is either 3, 5, or 9. The chemical structures of these materials are shown in Figure 7.1a. The polymerization reactions were performed at 70 °C in dimethylformamide (DMF) using azobisisobutyronitrile (AIBN) as a radical initiator and 2-cyano-2-propyl dodecyltrithiocarbonate (CPDTC) as a chain transfer agent. The reaction schemes are shown in Scheme 7.1 and Scheme 7.2. The number average molecular weight (M_n) and dispersity ($Đ$), as determined by size-exclusion chromatography (SEC), are given in Table 7.1. The polymer electrolyte systems are modeled by MD simulations using a united atom representation to characterize the equilibrium ion solvation structures and ion transport rates. Representative snapshots of the MD simulations are shown in Fig. 1b. Throughout the study, results from the simulations clarify and expand upon the experimental data and are used to help build a molecular level understanding of the effect of chain architecture and composition on polymer electrolyte ion conduction.

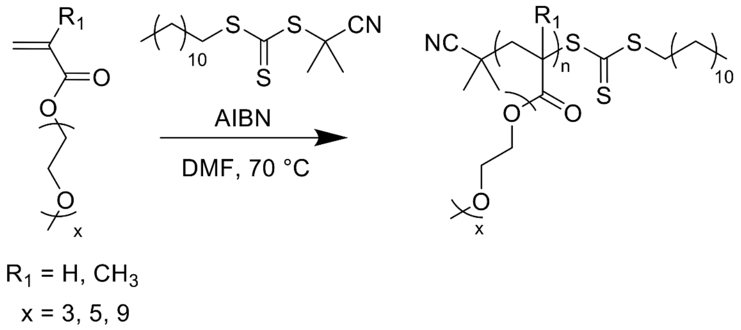

Scheme 7.1 – POEM$_x$ and POEA$_9$ synthesis reaction

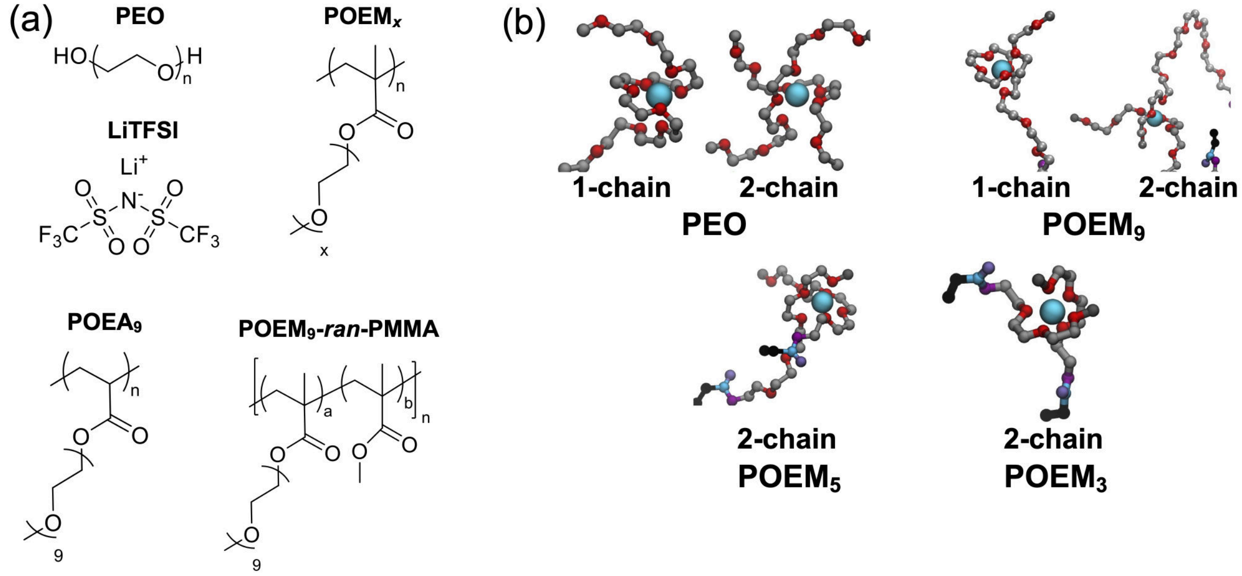

Figure 7.1 – (a) Chemical structure of polymers studied and LiTFSI salt; (b) Representative snapshots of united atom MD simulations showing common 1 and 2 chain solvation motifs in each system. Ether oxygen units are in red, Li^+ is cyan, aliphatic carbons are gray, backbone carbons are black, and methacrylate group oxygens are purple.

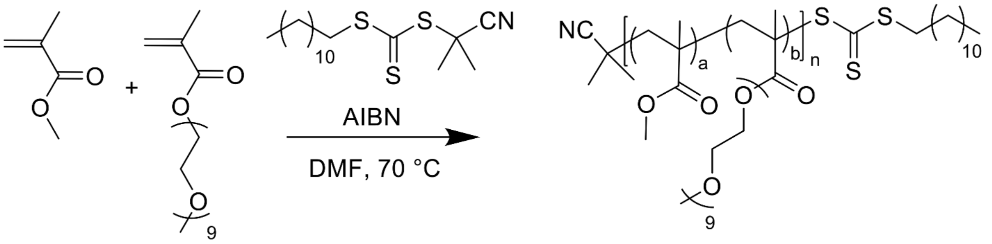

Scheme 7.2 – POEM$_9$-*ran*-PMMA synthesis reaction

7.2.2 Side-chain length—not T_g—determines ionic conductivity in graft polyethers

All of the studied polymers are rendered ionically conductive by addition of lithium bis(trifluoromethanesulfonyl)imide (LiTFSI) blended at a ratio of $r = [\mathrm{Li}^+]/[\mathrm{EO}] = 0.05$. Note that the salt concentration is held constant with respect to the ether oxygen mole fraction of the polymer (x_{EO}), and so the mass fraction of salt in the system is not the same across different polymers. We follow the approach taken by Pesko *et al.* in defining this mole fraction.[39] Briefly, this x_{EO} quantity is the ratio of ether oxygens to the total number of atoms in the repeat unit, not including hydrogen atoms. Implicit in this choice of salt loading is the assumption that only the ether oxygen units contribute to solvation and conduction, and that the methacrylate groups constitute inactive material. The choice to hold r constant, rather than total weight fraction of salt, is common in studies of nonhomogeneous polyether electrolytes,[37,179,216] and the validity of this assumption will be discussed in greater detail in the text. After blending with LiTFSI, polymer electrolyte solutions are spin cast from either acetonitrile or a mixture of acetonitrile and toluene onto interdigitated electrodes (IDEs) that are surface-passivated with 0.8 nm SiO_2 by atomic layer deposition. These IDEs are used to perform EIS measurements on polymer films of 70 – 100 nm thickness. The resulting data is fit to an equivalent circuit model and converted to conductivity by an appropriate cell constant, as described in the previous chapters.

The temperature-dependent ionic conductivity of linear PEO and the graft polymers POEM_9, POEM_5, and POEM_3, all at a salt ratio of $r = 0.05$, is shown in Figure 7.2a. The ionic conductivity in POEM_9 is lower than that of PEO by around a factor of two at all temperatures above the PEO crystalline melting point (around 50 °C). POEM_9 conductivity it is still reasonably high, however, above the commonly cited benchmark of 10^{-4} S cm^{-1} at 50 °C.[43] More interestingly though, the conductivity of POEM_x decreases by an order of magnitude or more as x decreases from 9 to 3. This trend in ionic conductivity as a function

Table 7.1 – Physical properties of linear and side-chain polymers studied

Material	M_n (g mol^{-1})	$Đ$	x_{EO}	T_g at $r = 0.05$ (°C)
PEO	20,000 [a]	1.10 [a]	0.333	-50
POEM_9	17,700 [b]	1.13 [b]	0.265	-57
POEM_5	33,400 [b]	1.29 [b]	0.227	-41
POEM_3	21,200 [b]	1.21 [b]	0.188	-31
POEA_9	11,800 [b]	1.08 [b]	0.273	-50
POEM_9-*ran*-PMMA	13,500 [b]	1.17 [b]	0.172	-37

[a] As reported by the supplier

[b] As determined from SEC-MALS in THF at 50 °C using $dn/dc = 0.073$ mL g^{-1}

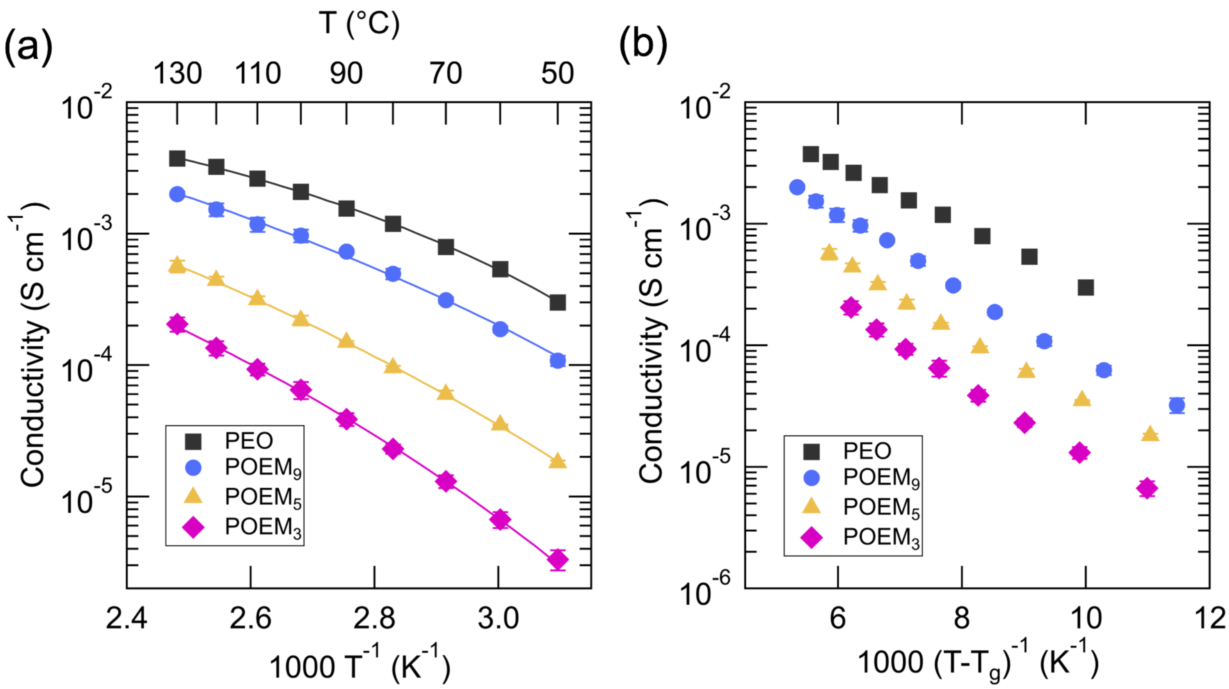

Figure 7.2 – (a) Experimentally determined temperature dependent ionic conductivity for $r = 0.05$ polymer electrolytes with solid lines representing the fits to the Vogel-Tamman-Fulcher (VTF) equation (Equation 7.1) and (b) experimental conductivity corrected by T_{g}.

of side-chain length is evident from Li$^+$ mean squared displacement (MSD) observed in the simulations (see Figure 7.3). At the end of the simulation time, Li$^+$ MSD is highest for PEO at all temperatures, and it decreases with decreasing side-chain length. Although differences in conductivity as a function of side-chain length have been observed previously in POEM and other graft polyether systems, clear mechanistic reasons for this effect have not been assigned.[220,221] Understanding why this effect arises is critical to future development of optimized polymer electrolytes based on side-chain architectures.

Ionic conductivity is commonly understood to be tied to the segmental dynamics of the polymer host.[24] Vogel-Tammann-Fulcher (VTF) behavior of ionically conductive polymers is often cited as evidence of this connection between ionic mobility and polymer relaxation times.[42,153] The conductivity of all four materials follow VTF behavior as a function of temperature, with fits to the VTF equation (Equation 7.1) drawn as solid lines in Figure 7.2a.

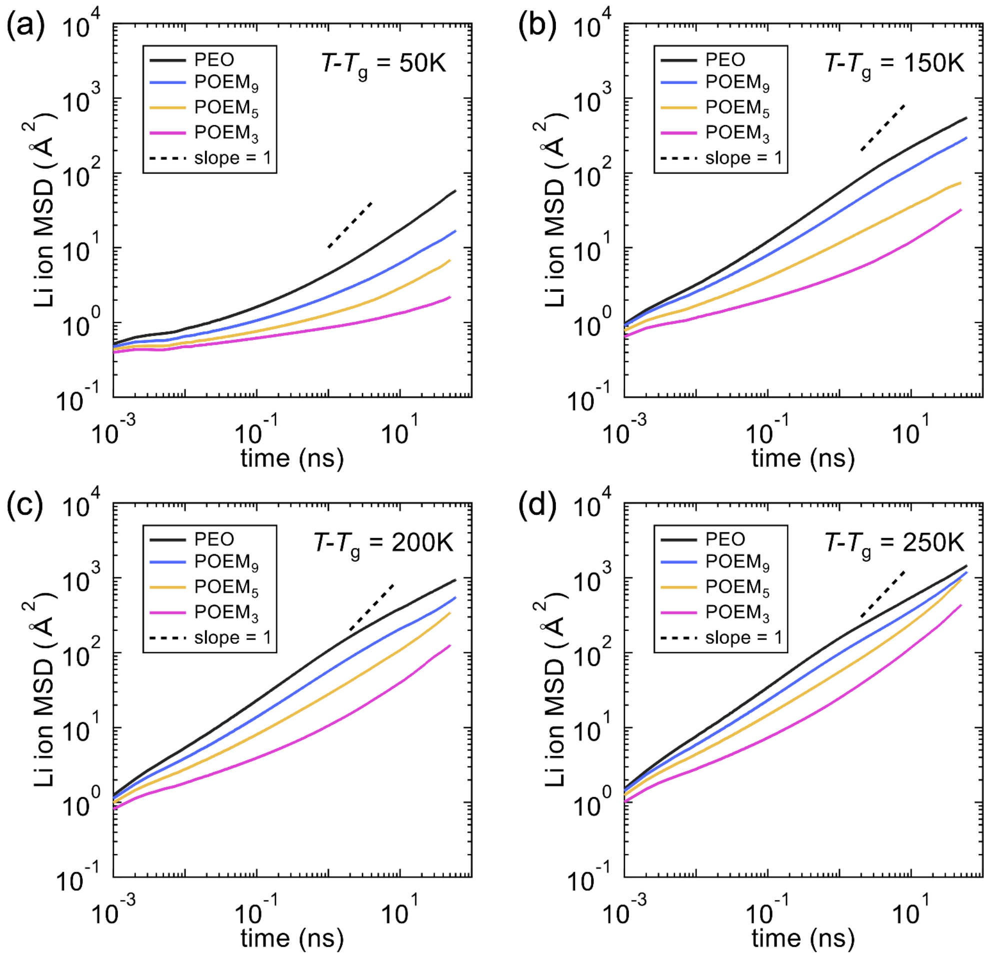

Figure 7.3 – Li$^+$ MSD data in (a) PEO, (b) POEM$_9$, (c) POEM$_5$, and (d) POEM$_3$

$$\sigma = A \exp\left[\frac{-E_\mathrm{a}}{R(T - T_0)}\right] \tag{7.1}$$

T_0 is the Vogel temperature, E_a is the pseudo-activation energy, and A is a constant prefactor. As the length of grafted side-chains is known to increase the available free volume and increase segmental mobility, it is plausible that decreased segmental dynamics in POEM$_3$ chains is responsible for the low ionic conductivity.^{222} T_g, as determined by differential scanning calorimetry (DSC), is a common proxy for describing the effects of segmental dynamics on conductivity. DSC thermograms for each polymer at $r = 0.05$ are shown in Figure 7.4, and the values for T_g are shown in Table 7.1. T_g generally increases as side-chain length decreases in POEM$_x$, which would suggest generally slower segmental dynamics and therefore lower ionic conductivity in materials with short side-chains. However, by plotting conductivity as a function of $1000/(T-T_\mathrm{g})$ (Figure 7.2b), it is clear that this difference in T_g is insufficient to explain the observed trends in conductivity. This common approach to correcting for differences in T_g suggests that if all corrected conductivity falls along the same line, differences in segmental dynamics explain all differences in conductivity, and T_g fully captures those differences in segmental dynamics.[84] Although linear PEO and graft POEM$_x$ seem to follow VTF behavior, side-chain length appears to have an additional impact on ionic mobility or that there are segmental dynamics influencing ionic mobility that are not captured by traditional T_g measurements.

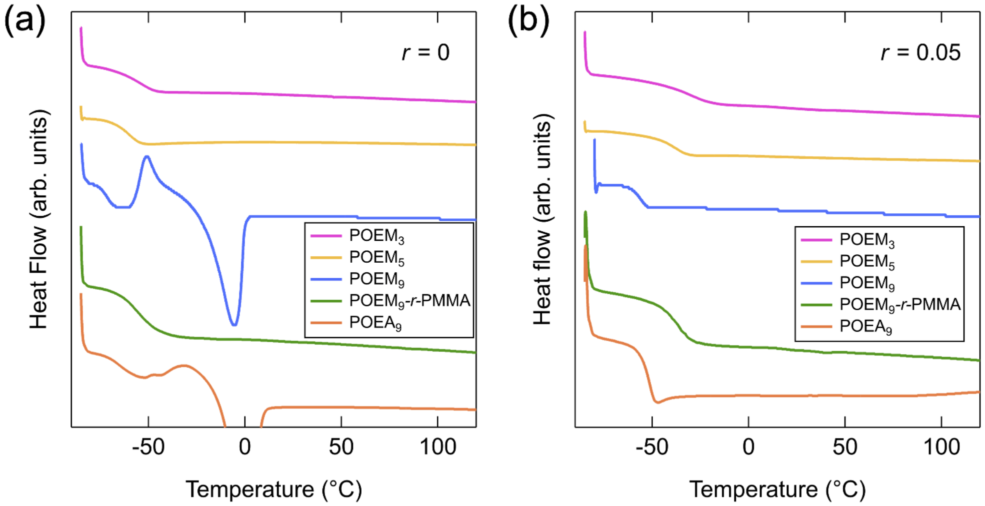

Figure 7.4 – DSC thermograms of neat and $r = 0.05$ samples. These curves represent the third heating cycle, and T_g is taken as the midpoint in the inflection in the heat flow rate.

As side-chain length effects on T_g do not provide a clear evidence that average segmental dynamics—as described by T_g—dictate the differences in ionic conductivity in graft polyethers, differences in the polymer compositions and chain architectures may instead influence the density and connectivity of solvation sites available for ion hopping. Webb and coworkers have developed a framework for quantifying the degree of solvation site connectivity based on the results of MD simulations like the ones performed here.[34,37,39] Briefly, a solvation site is defined at the centroid of a set of five or more ether oxygen atoms each within 3.7 Å of the centroid. These sites are shown as filled circles in Figure 7.5a. Solvation sites are connected by edges if the sites are within a cutoff radius of 3 Å of each other. These edges are shown as colored lines in Figure 7.5a. Note that connections between solvation sites that are farther apart than 3 Å are not shown. A more thorough explanation of the relationship between solvation site connectivity and ion transport as a function of nearest-neighbor distance can be found in previous work by Pesko *et al.*[39] Importantly, this analysis considers only ether oxygens as contributing to the formation of solvation sites. This results in an overall lower density of solvation sites and edges in POEM with lower ether oxygen mole fraction, x_{EO}, as can be seen visually in Figure 7.5a. The solvation site edge density, κ, normalized by the solvation site edge density of PEO, κ_{PEO}, is shown in Figure 7.5b for different POEM$_x$ materials. The value of $\kappa/\kappa_{\mathrm{PEO}}$ varies linearly with x_{EO}, as seen by the linear fit dashed line in Figure 7.6. In the study of a series of linear polyethers by Pesko *et al.*, $\kappa/\kappa_{\mathrm{PEO}}$ was also found to vary linearly with x_{EO} within a given family of materials.[39] The graft architecture of the polymers, moreover, does not seem to negatively influence the density of solvation sites. Nevertheless, this monotonic decrease in solvation site connectivity as a function of decreasing side-chain length does, at least qualitatively, explain the observed trend in conductivity. Solvation site density and connectivity are also found to be independent of temperature, depending solely on the ether oxygen content and polymer chain architecture, suggesting that $\kappa/\kappa_{\mathrm{PEO}}$ represents an intrinsic material property.

To quantitatively compare the calculated solvation site edge density to the experimentally determined conductivity, we introduce a normalized, temperature-reduced conductivity, σ_{nr}, similar to the scheme used by Pesko, *et al.*[39] σ_{nr} is calculated by first determining POEM conductivity at fixed values of reduced temperature, $T - T_{\mathrm{g}}$, using the VTF fits to the data described previously and then normalizing this value by differences in x_{EO} and conductivity of PEO, as shown in Equation 7.2.

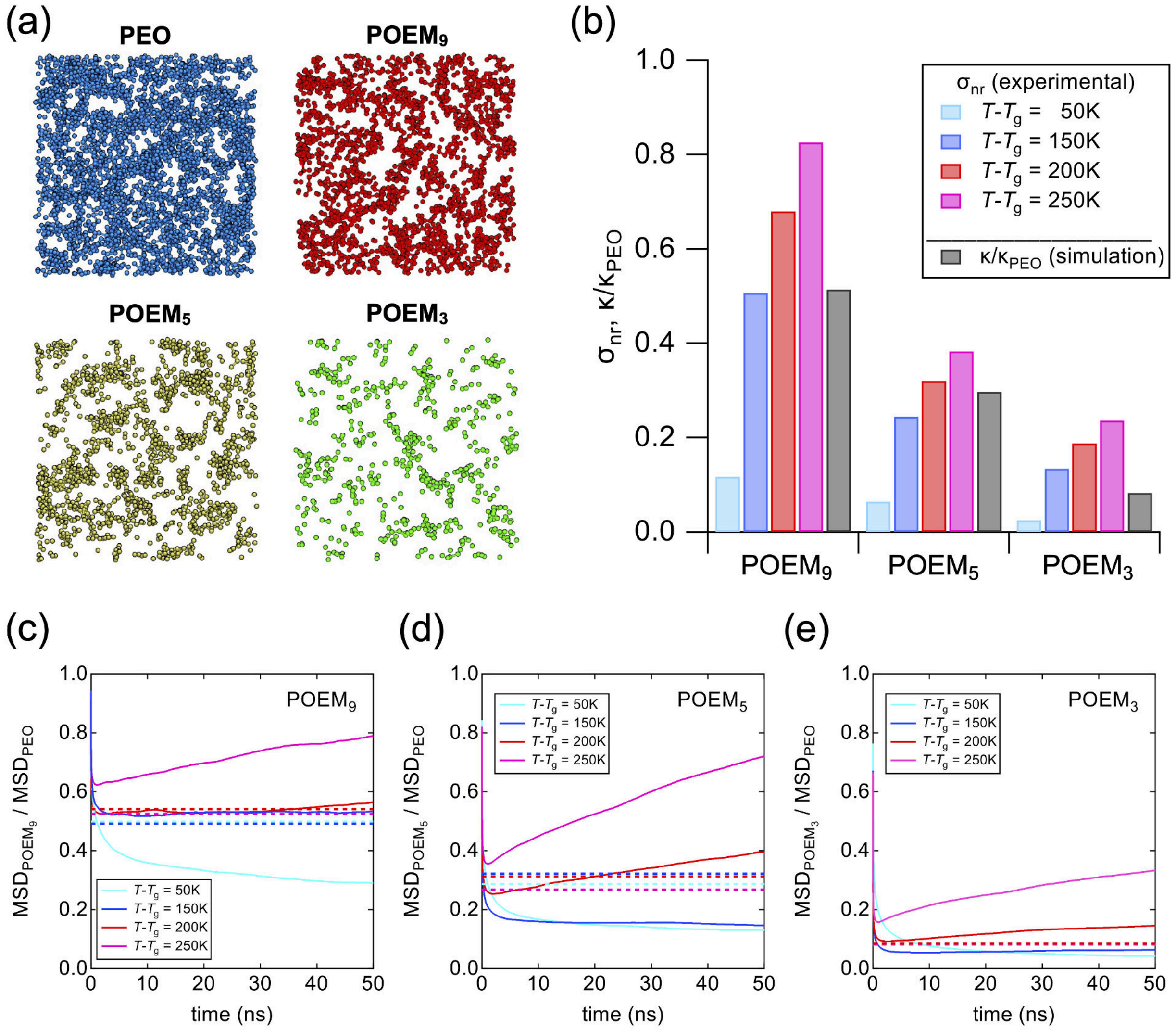

Figure 7.5 – (a) Visualization of solvation site network in PEO and POEM$_x$ from MD simulations; (b) Temperature averaged solvation site density ratio (gray) and normalized reduced conductivity (σ_{nr}, colors) at different fixed $T-T_{\mathrm{g}}$ for the three POEM$_x$ materials. Solvation site density and experimental conductivity are normalized to the value for PEO. Ratio of solvation site edge density (dashed lines) and Li$^+$ mean squared displacement (MSD, solid lines) in (c) POEM$_9$, (d) POEM$_5$, and (e) POEM$_3$ to PEO at different values of $T-T_{\mathrm{g}}$.

$$\sigma_{\mathrm{nr}} = \left(\frac{\sigma(T-T_{\mathrm{g}})}{\sigma_{\mathrm{PEO}}(T-T_{\mathrm{g}})}\right)\left(\frac{x_{\mathrm{EO,PEO}}}{x_{\mathrm{EO}}}\right) \tag{7.2}$$

Implicit in the use of this normalized conductivity are the assumptions that ionic solvation is similar in all materials being compared and that the effects of polymer segmental dynamics on ionic mobility are well captured by T_g and fits to Equation 7.1. If these assumptions are valid for a given set of materials and no other factors are expected to limit conductivity, σ_nr would represent an experimental solvation site connectivity, and it should vary with x_EO similarly to the solvation site connectivity calculated from MD simulations and be independent of temperature. As can be seen in Figure 7.5b, σ_nr increases monotonically with increasing x_EO, suggesting that solvation site connectivity does play a critical role in determining conductivity in graft polyethers. At intermediate temperatures ($T - T_\mathrm{g} = 150$ K) σ_nr is in excellent quantitative agreement with the simulated $\kappa/\kappa_\mathrm{PEO}$, suggesting that this theory fully captures the important physical properties dictating ionic conductivity. σ_nr exhibits a strong temperature dependence for all three POEM systems, however, suggesting that this parameter is not an intrinsic to the material, as was found in previous studies.[39] At temperatures above and below $T - T_\mathrm{g} = 150$ K, we see that experimental σ_nr deviates significantly from the simulated $\kappa/\kappa_\mathrm{PEO}$, by as much as a factor of 5. Specifically, at low values of $T - T_\mathrm{g}$, σ_nr is substantially lower than $\kappa/\kappa_\mathrm{PEO}$, indicating that other factors reduce ionic conductivity that are not accounted for in this normalization scheme. Conversely, at high values of $T - T_\mathrm{g}$, $\kappa/\kappa_\mathrm{PEO}$ underpredicts σ_nr, suggesting that there are factors increasing the conductivity of POEM relative to PEO. This difference is in contrast to the previous reports regarding linear polyethers where σ_nr was found to be relatively constant with temperature.[39] Note that the experimental σ_nr values presented here at high and low temperatures are extrapolated from fits to Equation 7.1, rather than experimentally measured, and they span a wider temperature range than was reported by Pesko *et al.* The low temperature values ($T - T_\mathrm{g} = 50$K) would be below the crystallization point of PEO, making experimental measurement of the ion conductivity of amorphous PEO untenable. Nevertheless, analysis of this broad temperature range provides important insight into the temperature dependent material behavior that may be missed if only a narrow range is considered.

Figure 7.5c–e shows the ratio of Li^+ mean squared displacement (MSD) from simulation

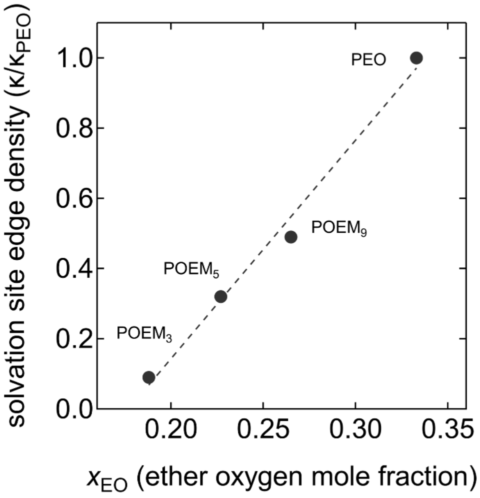

Figure 7.6 – Normalized solvation site edge density ($\kappa/\kappa_{\text{PEO}}$) as a function of ether oxygen mole fraction (x_{EO}). x_{EO} is defined as the ratio of ether oxygens in a repeat unit to the total number of atoms (not including hydrogens).

in POEM$_9$, POEM$_5$, and POEM$_3$ to Li$^+$MSD in PEO at different reduced temperatures. $\kappa/\kappa_{\text{PEO}}$ is shown as dashed lines in each system. This value is nearly invariant with temperature, showing only slight fluctuations around an average value (the temperature averaged value is shown in Figure 7.5b). Although the time scales of these simulations does not capture truly diffusive behavior, the effective diffusivity (*i.e.* the MSD rate at the end of the simulation) exhibits the same qualitative trends as was observed in the experimental system. At intermediate temperatures, the ratio of Li$^+$ MSD is close to the ratio of solvation site connectivity, whereas at high and low temperatures the MSD ratios are well above or below $\kappa/\kappa_{\text{PEO}}$, respectively. It is clear that this temperature dependent behavior is inherent to graft polyethers, and one or more of the critical assumptions made in using this model must be reconsidered or refined.

7.2.3 Chain architecture influences structure of solvation environment

Our analysis of ionic conductivity behavior thus far has relied on three critical assumptions about the solvation structure within POEM. First, we have assumed that only EO units participate in creating Li^+ solvation sites and facilitating ion transport, an assumption that is well supported by previous experimental and computational work involving similar systems.[37,206] Second, we have assumed a similar degree of ionic dissociation in all systems. Third, we have neglected any effect that the polymer chain architecture (*i.e.* linear *vs.* graft) may have on the solvation environment, using ether oxygen content as the only metric for comparing between materials. To validate these assumptions, we use MD simulations, Raman, and FTIR spectroscopy to fully characterize the solvation environment and ionic interactions in PEO and POEM.

We begin by confirming the assumption that ether oxygens are the only polymer functional groups interacting with Li^+, and solvation sites are formed exclusively from these ether oxygen atoms. From MD simulations, we can quantify the percentage of the total oxygens within the first solvation shell of a lithium ion, here defined to be within 3.25 Å radius of the central ion, belonging to a given class of oxygen atom. Figure 7.7a shows the percentage of oxygens involved in solvation that come from ether (OET), carbonyl (OKT), ester (OKE), or TFSI anion (OTFSI) groups in PEO and POEM salt blended systems. We find clear evidence that ether oxygens are the only groups involved in polymer-ion solvation for all four systems, with a very small ($< 1\%$) prevalence of ester oxygen solvation counted in the $POEM_3$ and $POEM_5$ systems. From Figure 7.7a it is clear that EO oxygens form nearly the entirety of the first solvation shell. These findings are consistent with previous reports of polymer electrolyte systems with multiple potential solvating groups, where lithium ions have been observed to be highly selective towards coordination by ether oxygens over ester or carbonate moieties.[37,206] We confirm this observation experimentally using FTIR.

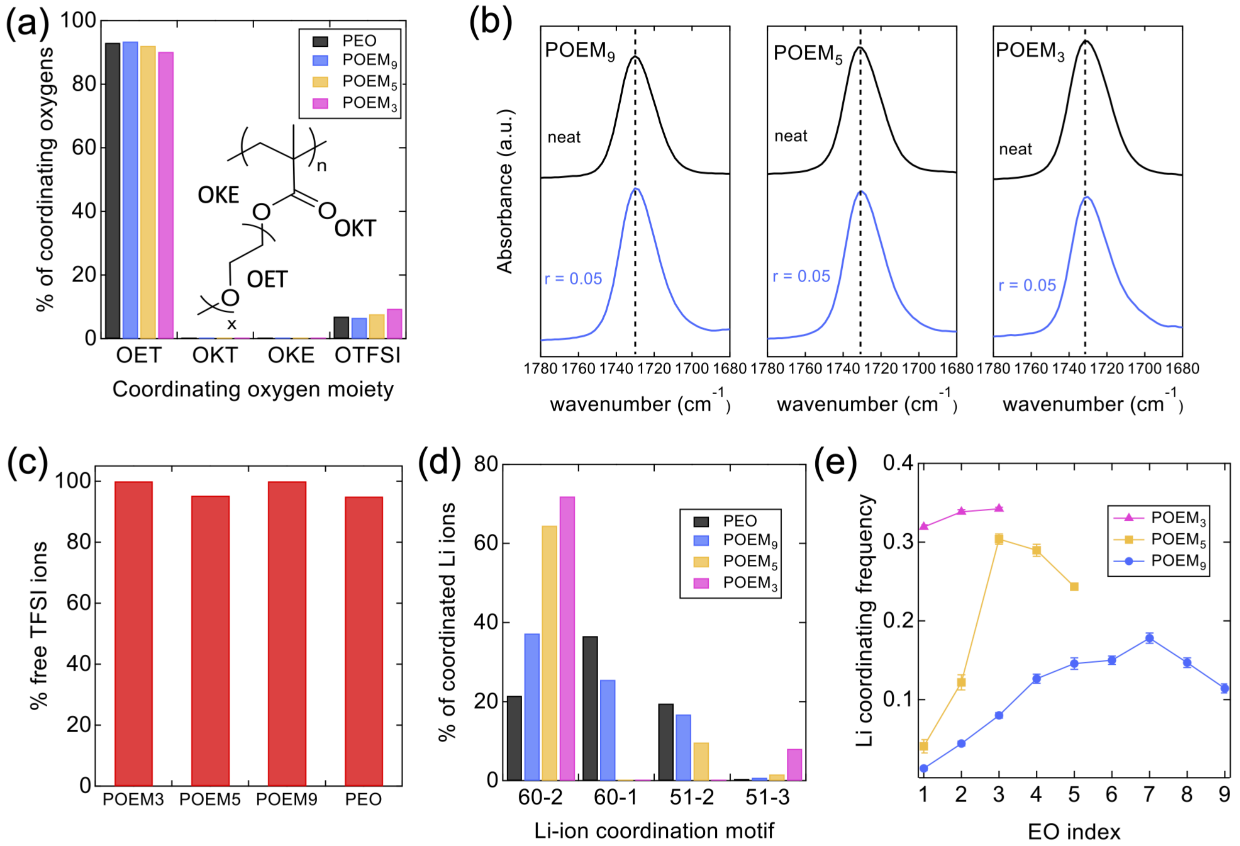

Figure 7.7 – (a) Relative percentage of solvating oxygen of each type from MD simulations (ether oxygen – OET, carbonyl oxygen – OKT, ester oxygen – OKE, TFSI- ion – OTFSI); (b) experimental FTIR spectra of the carbonyl (C=O) stretch for neat and $r = 0.05$; (c) percentage of free ions in $r = 0.05$ electrolyte systems as determined from Raman spectroscopy; (d) percent occurrence of most common solvation motifs (XY-Z refers to solvation by X ether oxygens, Y TFSI- oxygens, involving Z polymer chains plus TFSI- anions) from simulation; and (e) percent occurrence of solvation by a given ether oxygen along the POEM side-chain from simulation.

Figure 7.7b shows FTIR spectra for neat and $r = 0.05$ POEM systems in the wavenumber range 1780 – 1680 cm^{-1}. The peak at 1737 cm^{-1} in the neat samples arises from the carbonyl stretch (C=O bond), and lithium ion coordination with the methacrylate group should result in red-shifting of this peak.[223,224] The salt blended samples (blue curves in Figure 7.7b) for POEM$_9$ and POEM$_5$ show no change whatsoever from the neat samples. The $r = 0.05$ POEM$_3$ samples does exhibit a small secondary peak near 1710 cm^{-1}, suggesting that some carbonyl oxygens do interact with lithium ions. The size of the low wavenumber peak is much smaller than that of the free C=O peak at 1731 cm^{-1}, however, so the total fraction of lithium-carbonyl complexes in the systems is likely quite low.[33,225] Shifts in several of the characteristic ether side-chain peaks (C-O-C symmetric stretch at 1101 cm^{-1}, CH2 wagging at 1352 cm^{-1}) indicate that Li^+ instead coordinates with ether oxygens, though the overlap of these peaks with those of the TFSI anion make direct comparison of the neat and r = 0.05 systems difficult.[226] This is consistent with previous reports where it has been shown that in materials with both carbonate and ether functionalities, Li^+ may be preferentially coordinated with the C=O group if the ether chains contain only one or two oxygens.[205,227] Once there are at least three EO units in a chain however, the polyether chain can form a chelating structure around the lithium ion, and this solvation is favored over the C=O group association. These FTIR data are entirely consistent with the MD results, and we can confidently conclude that the vast majority of ion solvation sites are comprised of ether oxygens in all linear and graft polymers studied here. These results validate our use of constant r ($[Li^+]/[EO]$) for this study, though this strong preference for ether oxygen association may impose limitations on Li^+ conduction pathways throughout the system.

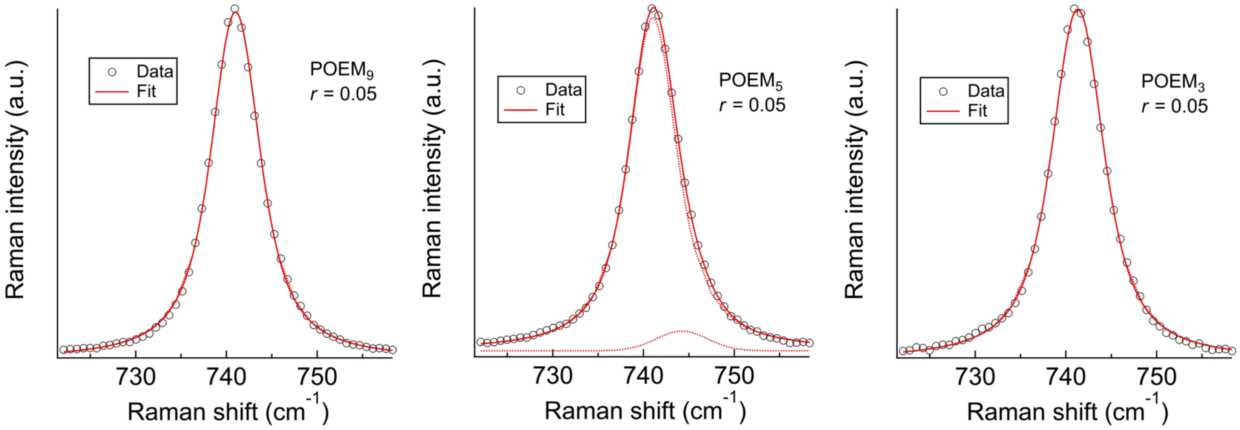

Figure 7.8 – Raman spectra and fits for $POEM_9$, $POEM_5$ and $POEM_3$ $r = 0.05$ electrolytes. Black open circles represent the raw data, dotted red lines are fits to individual peaks at 741 cm^{-1} (free TFSI) and 744 cm^{-1} (associated TFSI), and solid red lines are the combined fit. Raman data is fit to two Voigt peaks, which converge to one peak in the case of $POEM_9$ and $POEM_3$. The free ion fraction is taken from the area fraction under the 741 cm^{-1} peak.

The MD results also suggest that the prevalence of Li-TFSI complexation is low, with fewer than 10% of all solvating oxygen atoms coming from TFSI- in any given system. To experimentally confirm the absence of a large number of associated species which may reduce ionic conductivity, we use Raman spectroscopy to probe molecular vibrations of the TFSI molecule. Raman spectra for PEO and POEM $r = 0.05$ systems in the range of 720 – 760 cm^{-1} are shown in Figure 7.8. The peak in this range can be fit to a free TFSI anion peak at 741 cm^{-1} and an associated anion peak at 744 cm^{-1} to estimate a fraction of free ions in the system.[228,229] The percentage of free ions in the system is taken from the area fraction of the fitted Voigt peaks and plotted in Figure 7.7c. For all four polymer systems, the free ion content is nearly 100%, within error of the peak fitting. Although the simulations suggest that there may be a greater fraction of TFSI$^-$ in the Li$^+$ solvation shells, the Raman data suggest that these interactions are extremely weak and do not constitute ion pairs or higher order aggregates. We can assume that the ions are fully dissociated, and lithium only briefly interacts with counterions that make up a small fraction of any given solvation site. Differences in the degree of ionic dissociation is therefore not expected to be a significant contributor to the decrease in conductivity observed in short side-chain POEM.

Although the degree of solvation is quantitatively similar for all four materials, the solvation environment may be qualitatively different for each, based on the amount and configuration of ether oxygens in the system. Atomistic MD simulations allow us to further characterize these polymer electrolyte systems by the structure of individual solvation sites at the molecular level. Figure 7.7d shows the relative propensity for the four most common solvation motifs in each polymer system. Several of these most common solvation motifs are shown as simulation snapshots in Figure 7.1b. Coordination motifs are denoted by “XY-Z”, where X refers to the number of ether oxygens in the first solvation shell, Y refers to the number of TFSI molecules in the first shell, and Z is the number of polymer chains plus TFSI anions present in the solvation shell. For example, the 51-2 motif refers to coordination by five ether oxygens from a single chain and one TFSI anion. For POEM, each side-chain is considered separately, and in PEO, although it is a single long chain, we consider noncontiguous segments of the backbone to be separate chains for this purpose. We find that the most common motifs all involve either five or six ether oxygens, consistent with previous findings that this represents the most stable configurations for cation coordination.[37,230,231] However, certain motifs are inaccessible to some polymer systems, such as the 60-1 motif (six ether oxygens from a single chain). This configuration is the most likely for PEO and is also readily adopted by POEM_9, though it cannot occur in POEM_5 or POEM_3. Instead, these shorter side-chain systems exhibit a greater prevalence of the 60-2 configuration, creating the six-oxygen solvation shell from three oxygens each from two side-chains. Although Li^+ is solvated in a qualitatively similar manner across all four polymer systems studied, the local polymer conformations adopted to create those solvation shells is highly dependent on the chain architecture and conformation.

The strong preference for specific solvation motifs gives rise to heterogeneity along the side-chains of POEM, with some oxygens participating in solvation significantly more frequently than others. Figure 7.7e shows the prevalence of ionic association with specific ether oxygens in POEM as a function of distance along the side-chain. EO units are indexed from 1 being the unit closest to the methacrylate group. In POEM_3, all oxygens participate at roughly the same frequency, as there are no ways to produce the 60-2 motif (>70% of the solvation structures) without involving all three ether oxygens of a given side-chain. However, both POEM_5 and POEM_9 exhibit much higher likelihood of coordination by EO units farther from the backbone, with units 3-5 and 4-9, respectively, being significantly overrepresented in solvation. This can be understood by two combined effects. First, there are more permutations of three (or six) contiguous ether oxygens in the middle of the side-chain, and so those EO units are statistically more likely to be involved in solvation. Second, the EO units near the backbone are in very close proximity to the methacrylate group which does not participate in solvation. This limits the ability of those EO units to come close enough to EO units of another chain to form a full solvation shell. This heterogeneity in ether oxygen involvement is a direct result of the graft chain architecture, and the relative contribution of each ether oxygen to ion transport may not be equal.

7.2.4 Graft chain architecture results in heterogeneous polymer dynamics

The selective solvation by certain EO repeat units in the graft polyethers suggest that only part of the polymer chains meaningfully contribute to the measured ionic conductivity. This may explain why metrics such as T_{g} and solvation site density, which are system wide average values, do not fully capture the transport behavior. Instead, a more nuanced, local understanding of segmental dynamics and solvation is warranted. Rather than using macroscopic averages of segmental mobility by DSC, we can instead use the MD trajectories to determine the local mobility of individual ether oxygen units. Figure 7.9 shows the inverse mean relaxation time, $1/\langle\tau\rangle$, extracted from the C-O bond vector autocorrelation function (BVAF) at different $T-T_{\mathrm{g}}$ as a function of position along the polymer side-chain. Detailed explanation of this calculation are provided in the Supporting Information of *ref.* [203]. Briefly, the BVAF describes how quickly neighboring bonds decorrelate from an initial orientation. The mean relaxation time can be fit to a stretched exponential function, and $1/\langle\tau\rangle$ serves as an indicator of local segmental mobility. This analysis was introduced in a previous work led by Chuting Deng, who performed all of the simulations for this work, and the methodology is described in greater detail there.[22]

In the linear PEO system, $1/\langle\tau\rangle$ shows no dependence on ether oxygen position, as 150 kg mol^{-1} molecular weight used in the simulation is well above the chain length where chain ends ought to impact local dynamics or conductivity for most ether units.[232] In all three POEM systems, conversely, the local dynamics are strongly dependent on bond index. Those

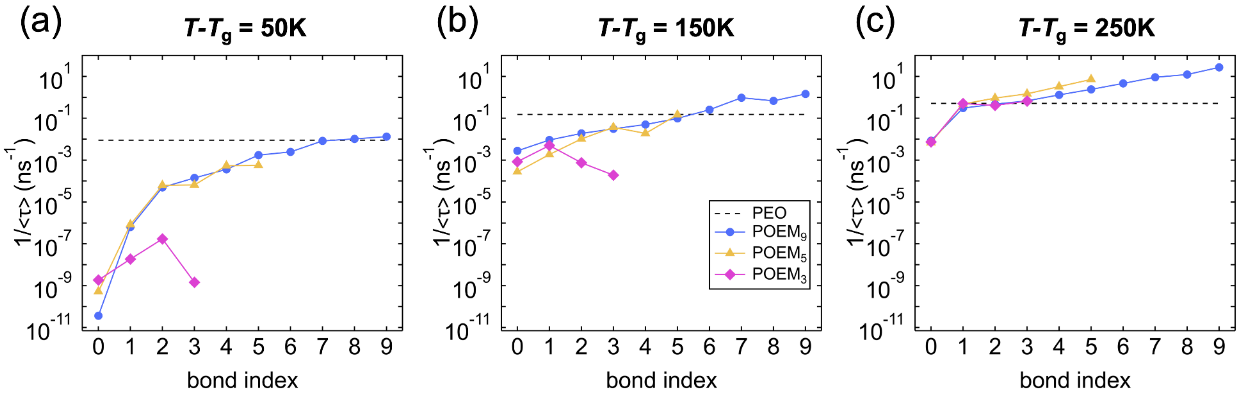

Figure 7.9 – Inverse mean relaxation time ($1/\langle\tau\rangle$) of different bonds along the polymer chains at (a) $T - T_\mathrm{g} = 50$ K, (b) $T - T_\mathrm{g} = 150$ K, and (c) $T - T_\mathrm{g} = 250$ K derived from the bond vector autocorrelation function. $1/\langle\tau\rangle$ serves here as an indicator of local segmental mobility. Index 0 is the C-C bond along polymer backbone. The other indices refer to the C-O bonds in the ether side chain with index 1 being the closest to the backbone. The solid colored lines are to guide the eye.

units closest to the polymer backbone exhibit significantly suppressed dynamics relative to PEO, while EO monomers near the side-chain end decorrelate at an equal or greater rate than PEO. This trend arises from similar competing effects that were attributed to difference in ion complexation by different EO positions. The C-C backbone carbon bond (bond index 0) exhibits between six and eight orders of magnitude slower relaxation rates than PEO, and the POEM ether units near this low mobility backbone have similarly suppressed dynamics. The POEM ether units farthest from the backbone, however, have greater free volume to sample, and exhibit faster dynamics as a result. Importantly, all of the $1/\langle\tau\rangle$ in Figure 7.9 are determined at fixed temperature above the respective T_g of each polymer. Any differences in the average mobility of ether oxygens between the different systems, therefore, are not captured by T_g, and these differences may explain the observed ionic conductivity behavior.

In addition to the clear importance of ether oxygen placement along the side-chain, the relaxation time of a given POEM EO unit relative to that of PEO is strongly dependent of temperature. In Figure 7.9a, at $T - T_\mathrm{g} = 50$ K, the mobility of the backbone and EO units near it are several orders of magnitude slower than PEO at the same relative temperature, and only EO units 7-9 in POEM9 have $1/\langle\tau\rangle$ equal to or greater than PEO. At 250 K above T_g, on the other hand, the backbone only has two orders of magnitude longer relaxation time than PEO, and essentially all ether units in the POEM systems relax as fast or faster than the linear PEO. This temperature dependence is likely due to rapidly increasing dynamics of the POEM backbone with temperature. As a reference point, the T_g of poly(methyl methacrylate), which is chemically equivalent to the POEM without the polyether side-chain, is around 100 °C compared to -50 °C for PEO. The dynamics of polymers tends to increase most rapidly at temperatures at and just above the glass transition, with relatively more modest increases in mobility with temperature at large values of $T - T_\mathrm{g}$.[233] This same effect is evident in these graft polymer systems where the lower mobility backbone sees much greater increase in local segmental dynamics than the already high mobility side-chains with the same increase in temperature.

This local heterogeneity in segmental mobility may reconcile the discrepancy between $\kappa/\kappa_\mathrm{PEO}$ and σnr discussed earlier (Figure 7.5). At intermediate $T - T_\mathrm{g}$ the average mobility of the EO units in POEM is quite similar to that of PEO, and differences in T_g accurately capture the important dynamics in the system. As a result, after normalization by $T - T_\mathrm{g}$, solvation site connectivity accurately captures the differences in conductivity as a function of POEM side-chain length. At high temperatures, many of the ether oxygens most often involved in ion complexation are more mobile than the linear PEO, and the T_g of the graft system does not adequately describe the important segmental dynamics. σ_nr therefore overpredicts the solvation site connectivity because normalization by T_g fails to account for the fast ether oxygens at the side-chain ends. This effect is more pronounced in the longer side chain materials, as there are more of these fast ether units present. In POEM$_3$ even the furthest EO unit from the backbone is still affected by the main-chain dynamics and is only marginally more mobile than PEO. In POEM$_9$, on the other hand, six of the nine side-chain oxygens exhibit faster local segmental mobility than PEO. Conversely, the dynamics of many of the most commonly solvating ether units in POEM are considerably slower than PEO at low temperatures. Here the ionic conductivity is limited by the slow dynamics of the methacrylate backbone. In this case σ_{nr} falls short of the solvation site connectivity prediction because the important dynamics in the system are slower than what is captured by the overall material conductivity. Again, the POEM$_3$ is the system most negatively impacted by the low mobility of the methacrylate backbone, whereas the highest index EO units of POEM$_9$ reach or exceed the relaxation rate of PEO. These results suggest that local segmental dynamics of the polymer side-chain are at least as important as T_{g}, ionic dissociation, and solvation site connectivity in determining ionic conductivity in graft polyethers. Both backbone flexibility and side-chain length are critical parameters in designing materials with rapid ionic transport.

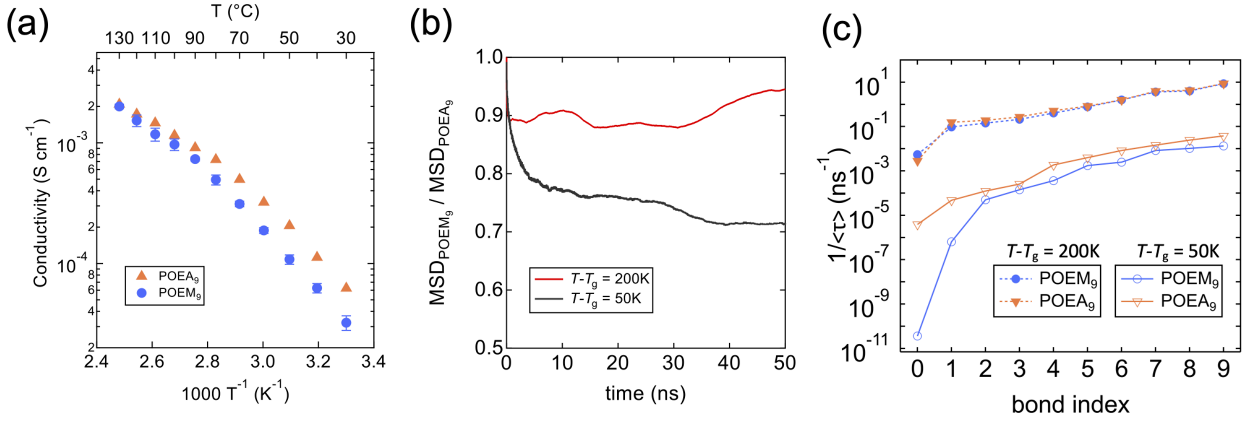

Figure 7.10 – (a) Temperature dependent conductivity (experiment), (b) Ratio of Li$^+$ MSD, and (c) inverse mean relaxation time in POEA$_9$ compared to POEM$_9$ (simulation)

To validate this model for ion transport in graft polyethers, two more materials were synthesized and characterized. POEA$_9$, the polyacrylate analogue to POEM$_9$, and a random copolymer, POEM$_9$-*ran*-PMMA, with the same x_{EO} as POEM3 were synthesized by the same RAFT polymerization as shown in Scheme 7.1 and Scheme 7.2, respectively. The experimental conductivity, Li$^+$ MSD vs time, and local BVAF decorrelation times for POEA$_9$ and POEM$_9$ at $r = 0.05$ are shown in Figure 7.10. From Figure 7.10a, we can see that the

$POEA_9$ conductivity exceeds that of $POEM_9$ at low temperatures by a factor of more than three, but the conductivity of the two systems converge above 100 °C. Although we measure the T_g of the two systems to be relatively similar (see Table 7.1), the polyacrylate backbone should be more flexible than the polymethacrylate one, as T_g of poly(methyl acrylate) is around 5 °C, well below that of polymethyl methacrylate. Previous bottle-brush copolymer systems based on POEA have been shown to exhibit higher ionic conductivity than similar systems incorporating POEM.[234] That the conductivity of these two systems converges at high temperature, however, is consistent with the hypothesis that backbone dynamics become less significant to ion transport at higher temperatures. At these elevated temperatures the difference between the relaxation times in the polyacrylate and polymethacrylate backbones is small, and the identical nature of the two side chains results in similar ionic conductivity values. These experimental observations are confirmed by MD simulations, where we find a similar temperature dependence in the ratio of Li^+ MSD in $POEA_9$ to that in $POEM_9$ (Figure 7.10b). At $T - T_g = 200$ K, the ratio of Li^+ MSD in $POEM_9$ to that of $POEA_9$ is 0.9 or greater, while at $T - T_g = 50$ K the ratio is about 0.7. Additionally, as seen in Figure 7.10c, the $POEM_9$ backbone relaxes significantly more slowly than the $POEA_9$ backbone at low temperatures, with $1/\langle\tau\rangle$ several orders of magnitude higher in the methacrylate polymer. This difference in backbone relaxation rate results in a persistently faster local relaxation rate in POEM compared to POEA at $T - T_g = 50$ K for all ether oxygens. At $T - T_g =$ 200 K, conversely, the backbone relaxation rates are identical in both systems, as are the dynamics of all ether oxygens in the two materials. Clearly, at these elevated temperatures the acrylate and methacrylate backbones both relax relatively quickly compared to the ether side-chain, and the effect of the backbone is minor in determining the material conductivity.

A $POEM_9$-*ran*-PMMA copolymer with an ether oxygen fraction similar to that of $POEM_3$ was also studied to verify the importance of side-chain length—not just x_{EO}—in determining conductivity. Figure 7.11a shows the experimental conductivity for these two

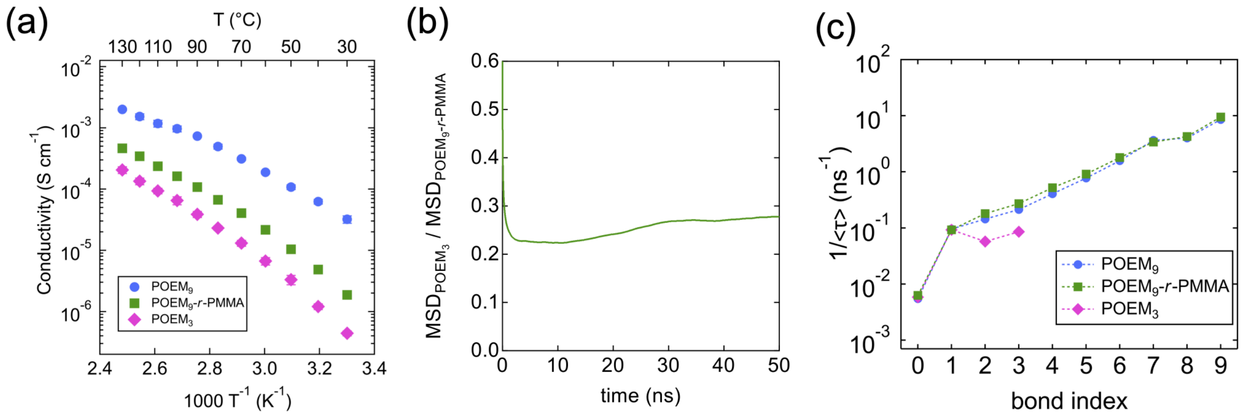

Figure 7.11 – (a) Temperature dependent conductivity (experiment), (b) Ratio of Li^+ MSD, and (c) inverse mean relaxation time in POEM_9-*ran*-PMMA compared to POEM_3 and POEM_9 (simulation)

systems. The random copolymer exhibits consistently higher ionic conductivity, by approximately three-fold, irrespective of temperature. This behavior is not explained by the modest differences in measured T_g of the two systems, nor is it captured by differences in solvation site density and connectivity, which depends primarily on x_EO. Instead, this behavior can be explained only by the outsized importance of EO units far from the backbone can have on ion transport within graft polymers. Whereas the POEM_3 consists of densely packed but extremely short side-chains, the POEM_9-*ran*-PMMA system contains a lower density of side-chains with mobile ether oxygens far from the backbone. Although the presence of randomly distributed, nonconducting PMMA units clearly disrupts the solvation network and negatively effects the material conductivity, this dilution effect is significantly less severe than the absence of any long side-chains capable of rapid segmental mobility. These findings are again confirmed by MD simulations. The ratio of Li^+ MSD of POEM_9-*ran*-PMMA to POEM_3 (Figure 7.11b) closely matches the ratio of experimentally determined conductivity (2.6-3.2 from experiment, and 2.8 at 50 ns from simulation). The local segmental mobility analysis (Figure 7.11c) similar validates this understanding of the differences between these two materials. Although the connectivity between the solvation sites should be similar between the two systems based on their similar ether oxygen content, the mobility of the

POEM_9 is relatively unperturbed by the presence of PMMA. The local mobility of the EO units furthest from the backbone remain much more flexible than those in POEM_3, and as a result are capable of facilitating more rapid ionic transport.

7.2.5 Implications for the design of polyether-based polymer electrolytes

These results underscore the critical relationship between polymer dynamics and ion transport that must be understood when measuring and analyzing new ion conducting materials, particularly those based on short side-chain ether units. We have clearly demonstrated that a single value for Tg does not account for the local heterogeneity in oxygen mobility in these side-chain systems, and it does not fully capture the relevant dynamics for producing fast ionic transport. While there are differences in the T_g of the graft polyethers examined in this study, these differences were negligible relative to the orders of magnitude different measured ionic conductivities. The observed difference in ionic conductivity was largely related to segmental dynamics, but DSC measurements failed to capture the local nature of these dynamics. The discrepancy between segmental dynamics measured by DSC and simulations highlight the importance of other experimental techniques, such as quasi-elastic neutron scattering, to probe the relevant local dynamics of these systems.[235–237] Moreover, the oxygens most likely to be involved in solvation (*i.e.* those towards the side-chain ends) were more mobile than the polymer average, giving rise to fast conduction without exhibiting a low T_g. On the other hand, materials that lack those mobile oxygens due to having only short ether side-chains were limited by the relatively low mobility backbone. Though all materials studied here exhibit a glass transition well below room temperature, it is not until around 150 K above T_g that the backbone begins to relax at a rate comparable to the ether side-chains. As a result, many of the EO units close to the backbone are prevented from effectively participating in the conduction mechanism. While side-chain mobility directly controls the conductivity, the side-chain mobility itself is largely dependent on the backbone mobility. Tailoring the connection between the side-chain and backbone to maximize flexibility offers a potential materials design opportunity to optimize the conductivity of these systems.

More generally, although low T_{g} is conventionally used as a hallmark of a potential candidate for high ionic conductivity, this may not always be a good proxy, and more detailed descriptions of segmental dynamics are necessary. As demonstrated here, such descriptions can be best captured by a combined experimental and computational approach. Local relaxation times, in addition to conventional metrics, such as ether oxygen content, T_{g}, and ionic dissociation, as well more recently introduced quantifiers, such as solvation site connectivity, must be accurately modeled in order to fully capture the ionic transport behavior of graft polyether electrolytes. Most importantly, it is the local mobility of the segments actively participating in the formation sites, not the overall dynamics of the system, that appears to be critical in limiting the ion conductivity of these materials.

Side-chain length has also been shown to be an important materials design criterion that may apply to a broad range of polyether electrolytes. In linear polyether ion conducting polymers, ether oxygen content and Tg may be used to accurately predict the conductivity of a newly prepared material. In systems where short PEO chains are connected to a polymer backbone, however, we have demonstrated that the flexibility of the main chain and its effect on the mobility of side chain ether units, as well as the length of the PEO chains have an outsized effect on the overall ionic conductivity. The role of backbone flexibility has significant implications for the development of graft copolymers based on POEM or POEA repeat units that represent an important class of potential lithium battery electrolyte membranes with a wide potential design window.[179] Even broader polymer chemistry is available in the development of bottlebrush polymer electrolytes, where the ion conducive side-chains can be incorporated by a graft-to or graft-through synthetic approach.[238–240]

With this synthetic flexibility, the choice of backbone of chemistry and side-chain linkages may be tailored to maximize ether side-chain dynamics, such as polysiloxane or polyphosphazene main chains.[241,242] Another technologically relevant system that makes use of short, periodically spaced PEO chains connected to less flexible moieties is crosslinked polyether binder materials.[243] Further investigation is warranted to explore how these ideas of local ether oxygen mobility affect conductivity in systems where ether chains are tethered at both ends, or in the case of dynamic crosslinked networks, one or both chain ends is covalently linked to a crosslinking site.21 Finally, dual ion-electron conducting polymers of interest for lithium ion battery applications often make use of ether side-chains covalently bonded to an electronically conductive conjugated backbone.[244] In these systems, the ion conductivity will likely be significantly affected by the length of ether side chain and type of covalent linkage to the rigid thiophene backbone.[36] In these systems, and in all ion conducting polymers based on nonlinear polyethers, the interplay between polymer composition and architecture, backbone rigidity, and side-chain relaxation rates will play a critical role in determining the temperature dependent conductivity behavior.

7.3 Conclusions

In this study we have clarified the relationship between side-chain length, ion solvation, segmental dynamics, and ionic conductivity in graft polyether electrolytes. Ionic conductivity of POEM$_9$ was found to be more than an order of magnitude higher than in POEM$_3$ even after correcting for differences in T_{g}. This behavior was partially explained by solvation site connectivity, but a temperature dependence in the normalized conductivity could not be reconciled by this approach. MD simulations and vibrational spectroscopy found that ions were fully dissociated in all systems, but dissolved lithium ions were found to preferentially reside in the ether side chains, rather than associating with the carbonyl groups in the methacrylate backbone. Moreover, ether units furthest from the backbone were most likely to coordinate with Li^+, suggesting that these units have an outsized effect on the formation of solvation sites and in facilitating ionic motion. Most importantly, these same ether oxygen atoms at side-chain ends exhibited much faster dynamics than those near the methacrylate backbone, and this effect explained both the trend in conductivity as a function of side-chain length as well as the temperature-dependent normalized conductivity behavior. These differences in C-O bond relaxation rates were not captured by differences in T_g, and therefore T_g alone may not be a good proxy for the relevant polymer dynamics resulting in high ionic conductivity in graft polymer electrolytes. Instead, the mobility of the EO segments that participate in solvation site formation is the most critical factor, and the dynamics of non-participating segments is secondary.

From the results presented here, several important design criteria can be proposed. First, more mobile backbone moieties can be introduced to improve the low temperature conductivity of graft polymer electrolytes. This was exemplified by comparing otherwise equivalent acrylate and methacrylate graft polyethers, where the acrylate exhibited three-fold higher conductivity at room temperature. This effect was minimal at higher temperatures, however, once the backbone dynamics approached those of the ether side-chains. Improvement to the conductivity at all temperatures was shown in a random copolymer based on long side-chains compared to that of a compositionally identical polymer with shorter side-chains. The important material parameter here was shown to be the presence of mobile oxygens at the side-chain ends, not the overall ether oxygen content. Finally, the solvation properties and segmental dynamics should be considered at a local, rather than global scale, when designing new ion conducting polymers based on short EO chains. Here, atomistic MD simulations, coupled with experimental characterizations, provided deeper insight into the important mechanisms of ion transport in these systems, and future materials design may be accelerated by taking this combined approach.

7.4 Materials and Methods

7.4.1 Materials

PEO was purchased from Polymer Source, Inc. and dried in an argon glovebox antechamber at 50 °C overnight before use. All other chemicals—acetonitrile (99.8%, anhydrous), toluene, dimethylformamide (DMF), tetrahydrofuran (THF), hexanes, diethyl ether, LiTFSI (battery grade, >99.95% trace metal basis), 2-cyano-2-propyl dodecyl trithiocarbonate (CPDTC), azobisisobutyronitrile (AIBN), and all monomers—were purchased from Sigma Aldrich. Oligo(ethylene oxide) methyl ether methacrylate (OEM$_x$, where $x = 3$, 5, or 9; $M_\mathrm{n} =$ 232, 300, or 500 g mol^{-1}), methyl methacrylate (MMA), and oligo(ethylene oxide) methyl ether acrylate (OEA$_9$, $M_\mathrm{n} = 475$ g mol^{-1}) were purified of inhibitor before use by passing through a column of basic alumina. LiTFSI was further under vacuum at 100 °C for 48 hours. Polymers and LiTFSI were stored in an argon glovebox after the drying processes. AIBN was recrystallized in ethanol before use.

Synthesis of POEM$_x$ and POEA$_9$ homopolymers

POEM$_x$ and POEA$_9$ homopolymers were prepared by RAFT polymerization according to Scheme 7.1. For the synthesis of POEM$_9$, 5 g (10 mmol) of OEM$_9$ monomer was placed in a round bottom flask along with 0.17 g (0.5 mmol) CPDTC, 8.2 mg (0.05 mmol) of AIBN, and 9.8 mL of DMF. The flask was sealed with a rubber septum and the solution sparged with dry N_2 for 30 minutes. The flask was then placed in an oil bath at 70 °C for 20 hours, after which it was quenched in an ice water bath and opened to atmosphere. The crude reaction mixture was concentrated under vacuum and then diluted with THF. This polymer was then precipitated from cold diethyl ether or a mixture of diethyl ether and hexanes. This purification process was repeated three times, or until ^{1}H-NMR spectra showed no residual monomer in the material. Purified polymer was then dried in a vacuum oven to a constant mass and then further dried under high vacuum for 24 hours before storing in an argon glovebox. The other homopolymers were prepared in a similar manner.

Synthesis of POEM$_9$-ran-PMMA random copolymer

POEM$_9$-*ran*-PMMA was synthesized according to Scheme 7.2 following the same general procedure as the homopolymer materials. 3.5 g (7 mmol) of OEM$_9$, 1.5 g (15 mmol) of MMA, 0.17 g (0.5 mmol) CPDTC, 8.2 mg (0.05 mmol) of AIBN, and 9.8 mL of DMF were combined in a round bottom flask, sealed with a rubber septum, sparged with dry N_2, and placed in a 70 °C oil bath for 20 hours. The crude solution was purified by the same process as the homopolymers. The ratio of OEM$_9$:MMA in the resulting polymer was determined by ^{1}H-NMR. The NMR spectrum and peak comparison is shown in Figure 7.12.

Polymer electrolyte solution preparation

Polymer solutions were prepared inside of an argon glovebox by dissolving polymer in either pure acetonitrile or a mixture of acetonitrile and toluene (50/50 v/v). Solutions were heated to 50 °C to help facilitate dissolution of the polymer and then were left stirring overnight. LiTFSI in acetonitrile solutions were prepared in the same manner. Polymer electrolyte solutions were prepared by blending polymer and salt solutions at an appropriate volumetric ratio to obtain a ratio of $r = 0.05 = [\text{LiTFSI}]/[\text{EO}]$.

7.4.2 Materials characterization

Size-exclusion chromatography (SEC)

Size-exclusion chromatography (SEC) measurements were conducted on a Shimadzu Prominence High Performance Liquid Chromatograph system with THF as eluent at a flow rate of 1 mL min^{-1}. Separation was achieved using two PLgel mixed-D columns (Agilent) main-

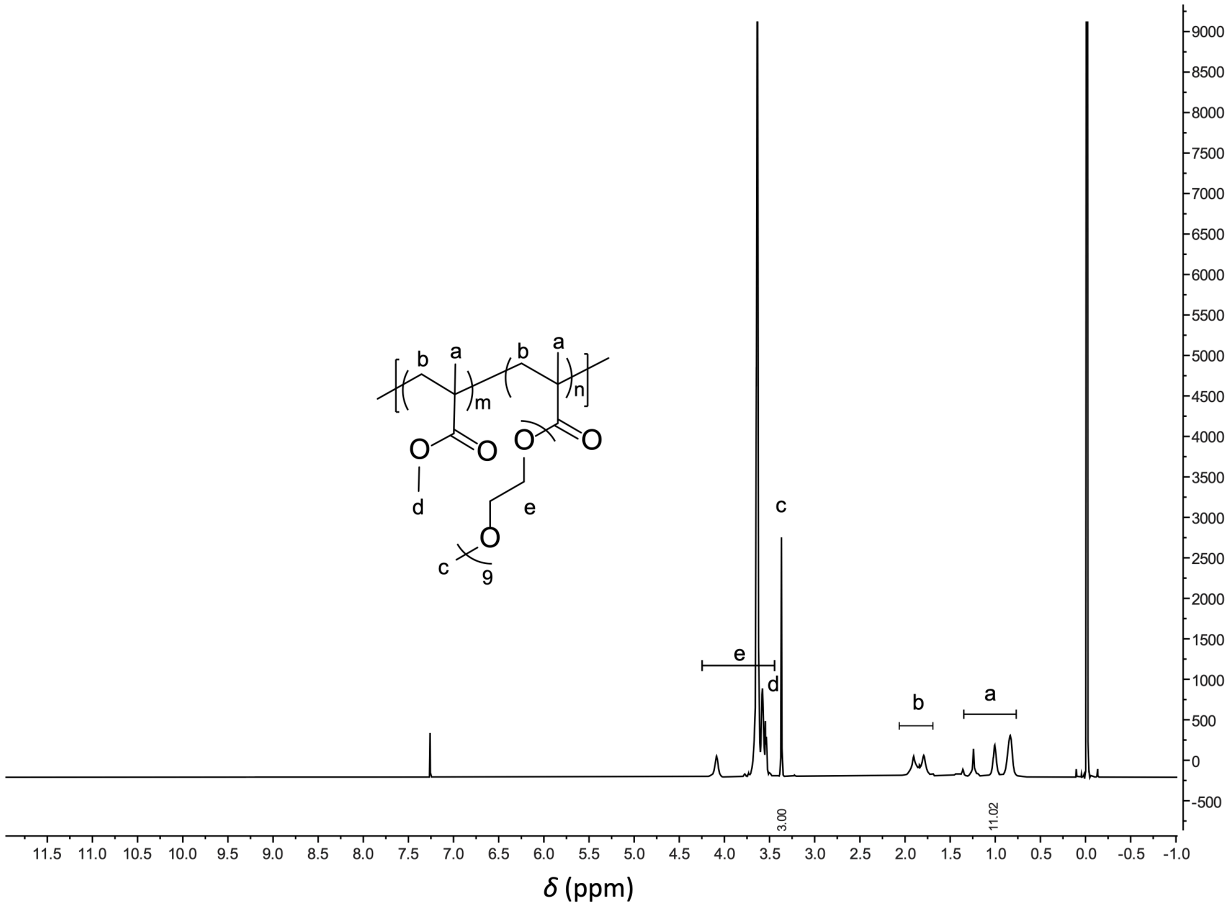

Figure 7.12 – ^{1}H-NMR spectra of POEM_x and POEA_9 in CDCl_3. The ratio of peak integrals for the ether side-chain end methyl group (c, $\delta = 3.38$ ppm) to the methacrylate backbone methyl group (a, $\delta = 0.7$ - 1.5 ppm) was used to determine the mol fraction of POEM_9 in the copolymer. $I_\text{c}/I_\text{a} = 0.273 = x_{\text{POEM}_9}$.

tained at ambient temperature. The differential refractive index signal was collected using a Wyatt Optilab T-rEX differential refractometer ($\lambda = 658$ nm). On-line multi-angle light scattering (MALS) measurement was performed using a Wyatt Dawn Heleos II light scattering detector. Weight-averaged molecular weight and dispersity were determined by MALS using the previously reported refractive index increment for POEM_9 in THF ($dn/dc = 0.073$ mL g^{-1}).[245]

Determination of copolymer composition by ^{1}H-NMR

$POEM_9$-*ran*-PMMA copolymer composition was determined by ^{1}H-NMR in $CDCl_3$. Data were acquired on a 500 MHz Bruker Avance-II+ spectrometer equipped with a ^{1}H QNP probe, using Topspin 2.1. Copolymer composition was determined by comparing the methacrylate backbone methyl group peaks (δ = 0.7 - 1.5 ppm) to the methyl ether peaks at the end of the $POEM_9$ side-chain (δ = 3.38 ppm).[246] The copolymer was determined to have a $POEM_9$ mole fraction of 0.273.

Differential scanning calorimetry

Calorimetric glass transition temperatures (T_g) of neat polymers and polymer electrolytes were determined by DSC using a TA Instruments Discovery 2500 DSC. Sample pans were prepared in the glovebox by drop casting solutions, heating at 65 °C until dry, and then repeating until 5 – 10 mg of material was in the pan. The pans were then hermetically sealed before removing from the glovebox to avoid any water adsorption before DSC measurement. Samples were conditioned at 135 °C followed by three cycles of cooling to -85 °C and heating to 135 °C at a scan rate of 10 °C/min. T_g is reported as the inflection point of the heat flow thermograms taken from the third heating curve (shown in Figure 7.4).

Fourier transform infrared spectroscopy

Samples for FTIR measurements were prepared on Au-coated Si substrates by spin coating as described in Section 2.4.1. Samples were prepared inside of a glovebox, annealed at 135 °C for 15 minutes, and sealed until immediately before measurement to minimize water absorption. Measurements were performed using a Shimadzu IRTracer-100 spectrometer using a diamond prism for attenuated total reflection (ATR) at ambient temperature from 400–4000 cm^{-1} at a resolution of 4 cm^{-1}.

Raman microscopy

Raman samples were prepared by drop casting films on Au-coated Si substrates inside of a glovebox. Films were dried and then annealed at 135 °C for 15 minutes inside of the glovebox and then sealed until measurement. Raman experiments were performed using a Horiba LabRAM HR Evolution NIR confocal Raman microscope. Raman spectra were collected with a 100x objective and a 633 nm wavelength laser.

7.4.3 Ionic conductivity measurements

Polymer electrolyte films were spin cast onto IDEs fabricated according to the procedure described in Section 3.2.1. IDEs used for measuring SEO(19-6) had dimensions of $N = 160$, $l = 1$ mm, $w = 2$ µm, and $d = 8$ µm. EIS measurements were performed with a potential amplitude of 100 mV over a frequency range of 1 Hz–1 MHz, and impedance spectra were fit to the equivalent circuit model shown in Figure 4.4b (Model 2). Conductivity was then taken using the cell constant derived in Section 3.3. Reported conductivity values are the average of three samples, with error bars corresponding to the standard deviation.

7.4.4 Molecular dynamics simulations

The simulations for this work were all performed by Chuting Deng, a graduate student in the de Pablo group at the University of Chicago. Extensive details describing the computational modeling and additional simulation results can be found in the original publication of this work.[203] Briefly, the polymers are represented by united atoms, using an adapted Trappe-UA force-field[247–249] that has been previously validated to match the density of PEO.[250] Li^+ and TFSI- ions are represented by a compatible all-atom model.[251] A cutoff radius of 12 Å is used for short range non-bonded interactions. Long range non-bonded interactions use a cutoff radius of 12 Å and are handled using the Particle-particle particle-mesh solver[252] with 10^{-4} accuracy. The simulation is conducted using the LAMMPS package.[253] The velocity-Verlet integrator with a 1 fs timestep is used. For NVT simulations, the Nose-Hoover thermostat with a damping parameter of 100 fs is used. For NPT simulations, the Nose-Hoover barostat with a damping parameter of 1000 fs is used.

Chapter 8

Solvation Site Formation and Ion Transport Mechanisms in Mixed Polarity Copolymers

ABSTRACT

Electrolytes based on mixtures of high polarity, high viscosity and low polarity, low viscosity solvents have been shown to exhibit higher ionic conductivity than electrolytes comprised of either of the constituents alone. In polymer electrolytes, however, the relationship between functional group polarity and conductivity is less well understood. In this chapter, we discuss findings from a study of copolymers consisting of highly flexible poly[oligo(ethylene oxide) methyl ether methacrylate] (POEM) and a high polarity functional group containing poly(glycerol carbonate methacrylate) (PGCMA). In copolymers of these two materials, conductivity is reduced by the addition of the glassy, yet polar, PGCMA, and no enhancement from its high polarity is observed. This is because the PGCMA groups, despite their high polarity, do not interact with lithium ions at all, as evidenced by FTIR. The transport mechanism in the copolymer is unchanged from the homopolymer POEM system, therefore, aside from effects on the segmental dynamics. Furthermore, use of a poorly dissociating lithium triflate (LiTf) does not change this trend, and the extent of ionic aggregation is not affected by the presence of PGCMA groups. Again, Li^+ interacts only with POEM and the counterion, rather than PGCMA. Finally, similar behavior is observed in a block copolymer (POEM-*block*-PGCMA), although interesting phase behavior is observed upon the addition

of salt to the material.

8.1 Introduction

Poly(ethylene oxide) (PEO), and polyethers more generally, have long been leading candidates to serve as solid polymer electrolytes (SPEs) for lithium battery applications due to their relatively fast segmental dynamics and their ability to readily solvate Li^+.[23] Use of a polyether SPE in a practical lithium battery has been hindered by several material property limitations, however. One major limitation is the relatively low ionic conductivity of PEO at room temperature compared to liquid electrolytes. In liquid electrolyte systems, high ionic conductivity is commonly achieved by blending a low viscosity solvent (such as dimethyl carbonate, DMC) with a highly polar solvent (such as ethylene carbonate, EC).[6] These blend electrolytes benefit from a combination of the high dielectric constant of the EC and the low viscosity of DMC, with the resulting ionic conductivity being higher than either of the individual solvents on their own.[254]

Inspired by the success of these small molecule blend electrolytes, recent work has attempted to translate this idea to SPEs. A coarse-grain molecular dynamics simulation study demonstrated that miscible blends of polymers with contrasting polarities may indeed exhibit a greater ionic conductivity than either homopolymer SPE.[255] This synergistic effect was attributed primarily to a greater extent of ionic dissociation in blends with a high polarity component, allowing for a greater number of free charge carriers. An experimental study of a PEO-poly(ether acetal) blend, in contrast, showed that the blend conductivity was largely identical to that of PEO homopolymer electrolyte, suggesting that the higher polarity polymer did not significantly affect the ion transport.[71] Moreover, recent work from our group demonstrated that blending PEO with a nonconductive poly(methyl methacrylate) (PMMA) has a detrimental effect on the conductivity resulting from disruption of long-range solvation site connectivity. This impact on the solvation site network will clearly be a function of the specific material chemistries of the blend material and the way that the different materials form—or do not form—solvation sites.

One class of mixed polymer electrolytes that has attracted some attention is polyether-polycarbonate materials. Both polyethers and polycarbonates are capable of solvating and conducting Li^+, although the relationship between salt concentration, segmental dynamics, and ionic conductivity is quite different in these two classes of materials.[56] Small molecule analogs consisting of mixtures of low viscosity glymes and the high polarity EC have shown a beneficial synergy, with blends showing a conductivity maximum at intermediate compositions.[256,257] Interestingly though, ions in these systems are primarily solvated by the lower polarity glyme, rather than the carbonate.[256] Nevertheless, the higher overall dielectric constant appears to have a positive contribution to the extent of ionic dissociation and, therefore, the conductivity. In systems consisting of copolymerized polyether groups and linear polycarbonate, solvation and transport may be dictated primarily by the polyether or the polycarbonate, depending on the ether chain length and polymer chain configuration.[37,205] These results suggest that the specific chemistry of the blend system may be a critical parameter in the resulting properties of the system and, macroscopic properties such the dielectric constant and glass transition temperature (T_g) may not be the only relevant criteria for polymer blend electrolytes.

To explore the design space for mixed polymer electrolyte systems more fully, a deeper understanding of the interactions between different chemical moieties and the ionic species is necessary. One relatively unexplored subset of materials that may of interest is mixed polyether-poly(cyclic carbonates). While many linear polycarbonates, such as poly(ethylene carbonate) and poly(propylene carbonate), have been studied extensively, materials containing a cyclic carbonate group are much less widely used. Given the importance of carbonate species polarity to the improved ionic conductivity seen in small molecule ether-carbonate mixtures, cyclic carbonate-containing polymers may serve as a more compelling high polarity "cosolvent" in polyether-polycarbonate mixtures. Such materials have not been widely studied, and there are open questions regarding the formation of solvation sites and the relationship between dynamics and conductivity in these systems.

In this study we synthesize and characterize random and block copolymers of poly(oligo(ethylene oxide) methyl ether methacrylate) (POEM) and poly(glycerol carbonate methacrylate) (PGCMA) to explore the ion solvation and transport behavior of polyether-poly(cyclic carbonate) mixed electrolytes. We find that conductivity is dictated almost entirely by T_g differences as the polar, glassy monomer content is varied. Ion conductivity measurements are consistent with Raman and IR experiments that demonstrate that ions are exclusively solvated by the "low polarity" POEM monomers. Both a highly dissociating lithium bis(trifluoromethanesulfonyl)imide (LiTFSI) and the weakly dissociating lithium triflate (LiTf) are similarly unaffected by presence of polar monomer groups, and difference in the conductivity of LiTFSI and LiTf systems is primarily a function of free ion fraction, as determined by Raman spectroscopy. Block copolymers of POEM and PGCMA also show exclusive solvation by the POEM phase, although the conductivity and T_g are a more complex function of composition and salt content. The neat block copolymer material shows some evidence of phase separation by SAXS and from DSC. Once salt is added however, the material is more disordered, in accord with the idea that the POEM selectively solvates the salt and becomes more polar as a result. Surprisingly, however, the conductivity is lower in the block copolymer than in a compositionally similar random copolymer, perhaps due to larger PGCMA regions impeding long range ion transport.

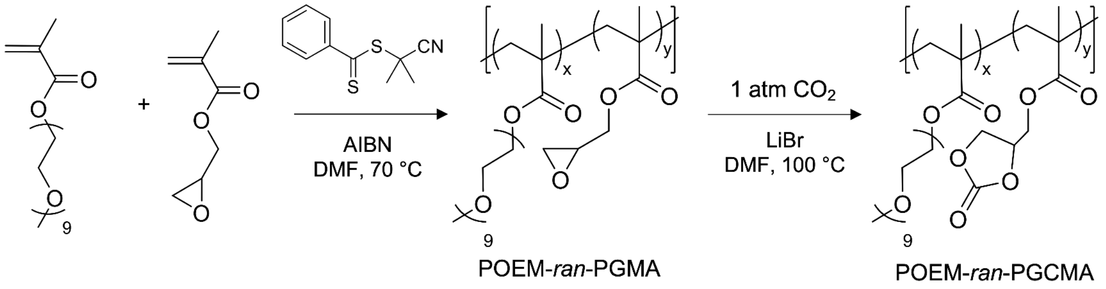

Scheme 8.1 – Synthesis of POEM-*ran*-PGMA and subsecquent functionalization to POEM-*ran*-PGCMA

8.2 Results and Discussion

8.2.1 Synthesis of mixed polarity copolymer electrolytes

To study the effects of differing monomer polarity in mixed polymer electrolyte systems on ion solvation and transport characteristics, we synthesized and characterized a series of random or block copolymers based on poly[oligo(ethylene oxide) methyl ether methacrylate] (POEM) and poly(glycerol carbonate methacrylate) (PGCMA). Note that in this chapter, all POEM has nine ethylene oxide (EO) repeat units per side-chain, so the subscript denoting the chain length is omitted for clarity. The POEM EO repeat units exhibit fast segmental dynamics, but they have comparatively lower polarity than the cyclic carbonate moieties in the PGCMA. POEM-*ran*-PGCMA is synthesized by a two-step reaction process shown in Scheme 8.1. First, OEM and glycidyl methacrylate (GMA) are copolymerized by reversible addition-fragmentation chain transfer (RAFT) polymerization using 2-cyano-2-propyl benzodithioate (CPBD) as a chain transfer agent.

A series of seven copolymers were synthesized and characterized by size-exclusion chromatography (SEC) and ^{1}H-NMR to confirm molecular weight and polymer composition. All seven materials exhibited very similar molecular weight and dispersity, around 10 kg mol^{-1} and 1.2 *Đ*, respectively (by comparison with PMMA standards, see Figure 8.1a). Figure 8.1b shows the polymer composition, as determined by NMR, plotted against the feed composi-

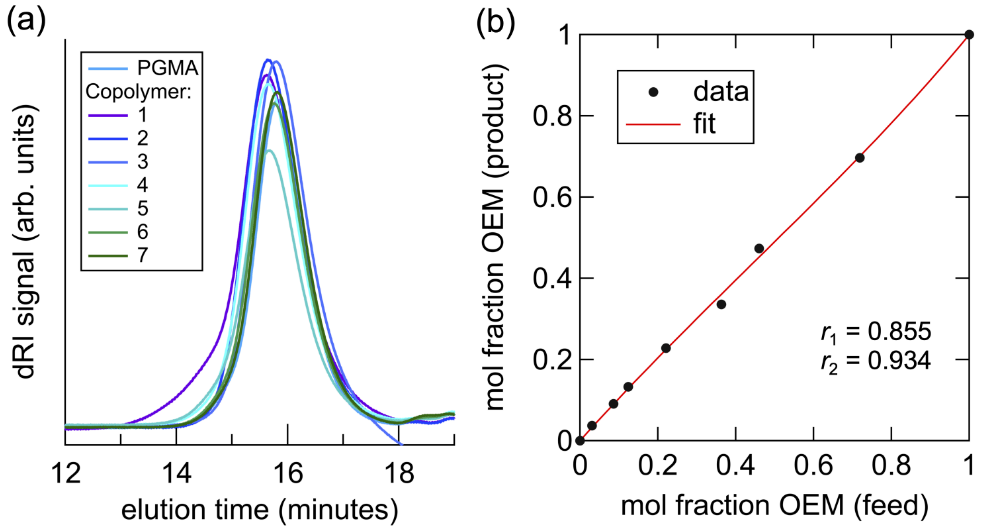

Figure 8.1 – (a) SEC traces of all POEM-*ran*-PGMA copolymers and (b) polymer mole fraction of OEM repeat units *vs.* the OEM monomer concentration in the feed. The blue line shows direct fitting to the non-linear Mayo-Lewis equation with reactivity ratios r_1 and r_2 shown. $r_1 \approx r_2 \approx 1$, so the resulting polymer chain should very close to a truly random copolymer.

tion. NMR spectra for all of the POEM-*ran*-PGMA copolymers are presented in Figure 8.12. Direct fitting to the nonlinear Mayo-Lewis equation gives reactivity ratios $r_1 = 0.855$ and $r_2 = 0.934$ (where OEM is monomer 1), indicating that the copolymers should be very close to statistical copolymers. Next, these POEM-*ran*-PGMA copolymers are converted to POEM-*ran*-PGCMA by reaction of the epoxy groups of the PGMA units with CO_2. This reaction was done according to the procedure described by Sakai *et al.* whereby the copolymer is dissolved in dimethyl formamide (DMF) along with 10 mol percent LiBr as a catalyst under 1 atm of CO_2 for 24 hours.[258] This reaction results in quantitative conversion of the epoxy group to cyclic carbonate, as observed by ^{1}H-NMR (Figure 8.13). POEM and PGMA homopolymers were also prepared by RAFT polymerization, and PGMA was converted to PGCMA in the same manner as the copolymers. It should be noted that the GMA monomer can be functionalized to GCMA and then directly polymerized, as reported previously.[259] However, the cyclic carbonate group can be susceptible to reaction with the radical chain end, resulting in branching and crosslinking that can increase both the molecular weight dispersity and T_g. The copolymer composition before and after reaction with CO_2 is shown in Table 8.1.

Table 8.1 – Composition of random copolymers before and after reaction with CO_2

Copolymer	OEM mass fraction (feed)	OEM mass fraction (product)[a]	OEM mass fraction (product, after reaction with CO_2[b]
1	0.1	0.12	0.09
2	0.25	0.26	0.21
3	0.33	0.35	0.29
4	0.5	0.51	0.44
5	0.67	0.64	0.58
6	0.75	0.76	0.71
7	0.9	0.89	0.86

[a] Determined from ^{1}H-NMR

[b] Calculated assuming 100% conversion of PGMA epoxy group

The glass transition temperature (T_g) of the POEM-*ran*-PGMCA copolymers, as well as POEM and PGCMA homopolymers, was determined using differential scanning calorimetry (DSC). DSC curves are presented in Figure 8.2a. Note that the homopolymer POEM exhibits crystallization and melting peaks, but crystallization appears to be completely eliminated by the addition of even 10% PGCMA. The T_g of each material, plotted in Figure 8.2b, is taken as the midpoint of the glass transition regime. As seen by the dashed line fit in Figure 8.2b, the midpoint T_g of POEM-*ran*-PGCMA is reasonably well described by the Fox equation, suggesting that the monomers are intimately and uniformly mixed.[260] Importantly, the ether side-chains do not exhibit a distinct T_g from the rest of the material, as can be seen in miscible blends of PEO and PMMA.[261,262] The breadth of the glass transition (ΔT_g), however, varies dramatically as a function of the copolymer composition. While the homopolymer POEM and PGCMA each exhibit only a 5–8 °C difference between the onset and end of the glass transition, this difference is nearly 60 °C in the copolymer with 58% POEM by weight. This broad range of transition temperatures in the DSC data can be interpreted as a broad range of segmental relaxation rates in the material at a fixed temperature. The implications for this broad range in dynamics for the resulting ionic conductivity will be discussed later in the text.

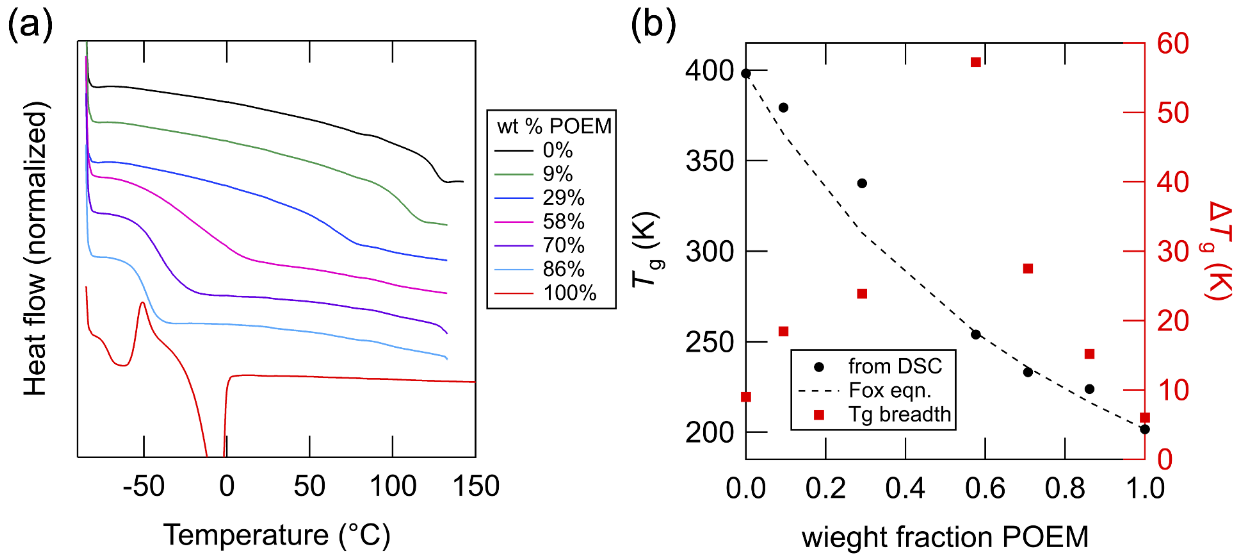

Figure 8.2 – (a) DSC curves of POEM, PGCMA, and POEM-*ran*-PGCMA copolymers and (b) T_g of PGCMA-*ran*-POEM copolymers as a function of POEM weight fraction, as determined by DSC. T_g values (left axis) are chosen from the midpoint of the transition. ΔT_g (right axis) refers to the breadth of the DSC transition, taken as the difference between endpoint temperature and the onset temperature.

8.2.2 Ionic conductivity is reduced by addition of polar, glassy PGCMA units

To study the ionic conductivity of copolymers with mixed polarity, two copolymers were selected to characterize more fully. Copolymers are referred to as OEM-GC(X-Y) where X and Y refer to the weight percent of OEM and GCMA monomers, respectively. Homopolymer POEM, OEM-GC(86-14), and OEM-GC(58-42) were blended with LiTFSI salt at a ratio of $r = [\mathrm{Li}^+]/[\mathrm{O}] = 0.05$, where [O] is the concentration of ether oxygens and carbonate groups in the system ($[\mathrm{O}] = [\mathrm{EO}]+[\mathrm{OCOO}]$). DSC traces for these electrolytes are shown in Figure 8.3, and the midpoint T_g values are reported in Table 8.2. The increase in T_g upon the addition of salt is very similar across all materials, and the trend in ΔT_g is preserved. Ionic conductivity of each electrolyte system was then determined by electrochemical impedance spectroscopy (EIS) of thin films cast on interdigitated electrodes (IDEs) as described in previous chapters. Polymer electrolytes were dissolved in a 50:50 (by volume) mixture of acetonitrile and toluene, and films of 50–100 nm were spin cast on SiO_2-coated IDEs.

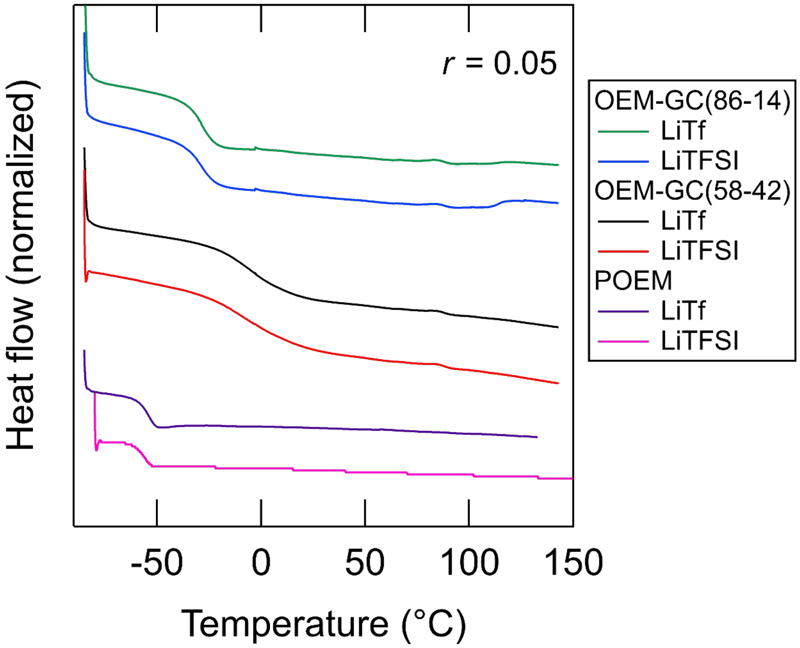

Figure 8.3 – DSC curves for POEM and selected copolymers blended with $r = 0.05$ LiTFSI or LiTf

The conductivity of POEM, OEM-GC(86-14), and OEM-GC(58-42) blended with $r = 0.05$ LiTFSI as a function of temperature is shown in Figure 8.4a. The ionic conductivity is clearly dependent on the polymer composition, with increasing carbonate content resulting in lower conductivity. To isolate any effects of the copolymer polarity, the ionic conductivity can be corrected for two factors. First, differences in T_g can be corrected for to account for differences in the segmental mobility of the materials. Second, the different polymers have different composition and, therefore, different fraction of ion solvating groups. Because we have selected to hold r constant, differences in the molar salt concentration may contribute to lower conductivity in the materials with greater carbonate content. We can account for this by introducing a solvating oxygen mole fraction, x_O, which is similar to the ether oxygen fraction that has been introduced previously.[39,203] Here, x_{O} is the number of ether oxygens plus carbonate groups divided by the total number of atoms in the average repeat unit (excluding hydrogens). Figure 8.4b shows the ionic conductivity of POEM, OEM-GC(86-14), and OEM-GC(58-42) with $r = 0.05$ normalized by the ratio of $x_{\mathrm{O,POEM}}/x_{\mathrm{O}}$ plotted as a function of $T - T_{\mathrm{g}}$. When accounting for differences in absolute salt concentration and glass transition temperature, the conductivity of all three materials collapses to a nearly identical curve.

Table 8.2 – T_{g} of polymer-salt systems studied in this chapter

		T_{g} (°C)	
Material	neat	$r = 0.05$, LiTFSI	$r = 0.05$, LiTf
POEM	-71.5	-56.6	-55.1
OEM-GC(86-14)	-49.3	-28.8	-28.8
OEM-GC(58-42)	-19.1	-6.8	-4.4
BCP(50-50)	-55.3	-29.3	-

It is clear from the results in Figure 8.4b that the addition of a highly polar monomer does not improve the ionic conductivity of these $r = 0.05$ LiTFSI containing electrolytes. In fact, the opposite is true, as materials with a greater fraction of the glassy PGCMA material exhibit a greater reduced conductivity. Interestingly, however, this difference is nearly entirely accounted for by differences in the T_{g}, as measured by DSC. This finding may appear to be in contrast to the results of our previous work regarding the effect of POEM side-chain length on conductivity.[203] There we found that differences in T_{g} produced by different side-chain lengths was modest, and did not account for the observed ionic conductivity trends. Instead, the local relaxation rate of individual EO segments was the critical parameter for describing the conductivity. Here, the side-chain length is held fixed, and a more macroscopic description of the dynamics, as is measured by DSC, is appropriate to describe the most important dynamics for determining ionic conductivity. The similar slope exhibited by each material in the $T - T_{\mathrm{g}}$ plots further indicates that the conductivity of each material is governed by similar dynamics, and the addition of PGCMA primarily has the effect of slowing the relaxation rates at a fixed temperature.

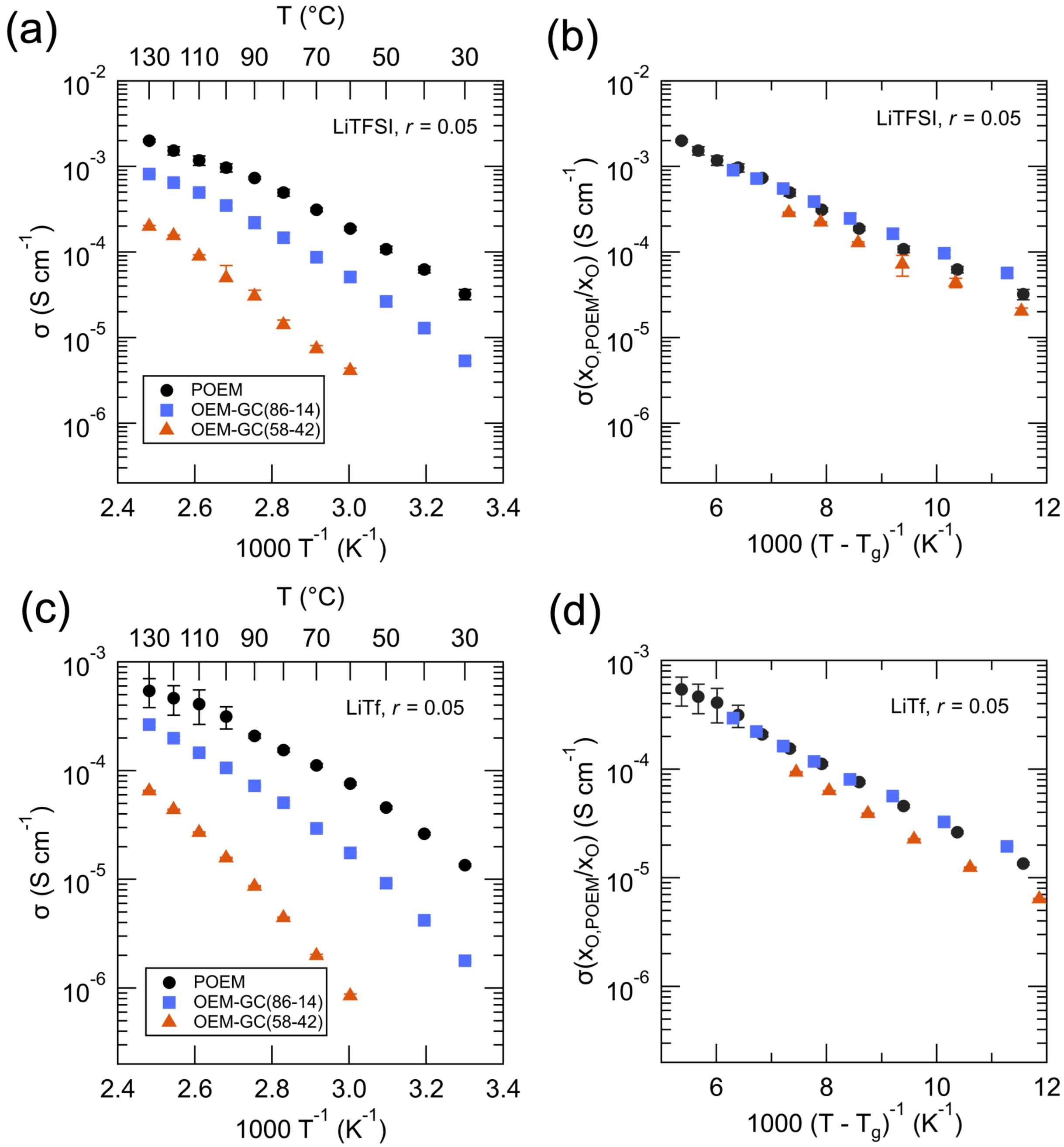

Figure 8.4 – Ionic conductivity of POEM and PGCMA-*ran*-POEM blended with (a) LiTFSI and (c) LiTf. (b,d) Ionic conductivity plotted as a function of $T - T_g$

Moreover, the difference in the breadth of relaxation rates observed in the DSC measurements appears to have little effect on the measured conductivity. Unlike in the previous study of POEM where dynamic heterogeneity along the side-chain produced meaningfully different temperature dependent conductivity behavior, here the heterogeneity in the relaxation rates probed by DSC do not seem to affect the conductivity at all. In the case of POEM with longer side-chains, Li^+ transport could occur primarily through the fastest relaxing EO units far from the glassy backbone, leading to higher-than-expected conductivity increases over shorter side-chain POEM. We expect that here the Li^+ transport again primarily occurs at the more mobile side-chain ends, though the mobility of these side-chains as a whole are depressed by the presence of the glassy PGCMA. In the case of the two copolymer systems, the fastest relaxation rates are similar, as evidenced by the similar onset of T_g. However, long range ion transport requires ions to move between solvation sites of varying mobility. The conductivity, therefore, is a function of the average mobility of each of these solvating side-chains, and the distribution of relaxation rates is unimportant.

Lastly, the density of solvation sites does not appear to be a critical factor in determining ionic conductivity of these copolymers. The density and connectivity of solvation sites has previously been demonstrated to be a major factor in limiting the ionic mobility of linear polyethers,[34,39] side-chain polyethers,[203] and polyether-polycarbonate copolymers.[37] Typically, as the mole fraction of EO units in the system decreases, the solvation site density and connectivity decreases. Here, we find that the conductivity is largely accounted for by differences in T_g and EO unit mole fraction. The second-order effect of lower solvation site density does not appear necessary to explain the conductivity. One possible explanation for this observation may be the long side-chain nature of the POEM used in these materials. In contrast to some of the previous works that have examined this phenomenon, these long (nine repeat unit) EO side-chains are each fully capable of forming highly mobile solvation sites. Although they are diluted by the presence of the nonsolvating PGCMA monomers, the distance between solvation sites may be sufficiently short that they do not substantially reduce the ion hopping rate. A recent study from our group observed that in PEO-PMMA mixed systems, disruption of the solvation site network at a length scale of 6–8 Å was most damaging to the ion transport rate. Here, the distance between adjacent POEM units separated by only a few PGCMA monomers is likely smaller than this critical length scale, and the presence of the PGCMA does not substantially alter the connectivity of the solvation sites.

8.2.3 Conductivity trends hold even with poorly dissociating salt

In mixed systems where a synergy between polymer or solvent polarity and mobility has been observed, slower mobility is offset by an increase in the salt dissociation or the number of free ions due to interactions between the high polarity group and the salt.[30,254,263] The effect of carbonate monomer concentration on conductivity in the LiTFSI electrolytes is clearly entirely a function of its effect on the T_g. This is likely explained by the highly dissociating nature of LiTFSI in polyethers. At a concentration of $r = 0.05$, LiTFSI tends to fully dissociate into free ions, as observed by Raman spectroscopy.[41] We therefore characterized another set of electrolytes consisting of POEM, OEM-GC(86-14), and OEM-GC(58-42) each blended with $r = 0.05$ lithium triflate (LiTf). LiTf is known to poorly dissociate in polyethers.[264–266] In these systems, the presence of high polarity cyclic carbonate groups should help facilitate ionic dissociation, increasing the number of mobile charge carriers and thus the conductivity. Figure 8.4c shows the conductivity of these systems as a function of temperature. We see that the conductivity monotonically decreases with carbonate content, as was the case in the LiTFSI systems. Figure 8.4d shows that after accounting for differences in T_g (reported in Table 8.2) and solvating oxygen content, the conductivity again comes close to collapsing to a single curve. We would expect that if the more polar monomer were increasing the fraction of free ions in the system, the T_g-corrected conductivity should be higher in materials with higher carbonate fraction. Instead, the conductivity is primarily a function of T_g, and the copolymer with greater carbonate content exhibits if anything a slightly lower corrected conductivity.

8.2.4 Spectroscopy shows that no Li^+ interact with carbonate groups

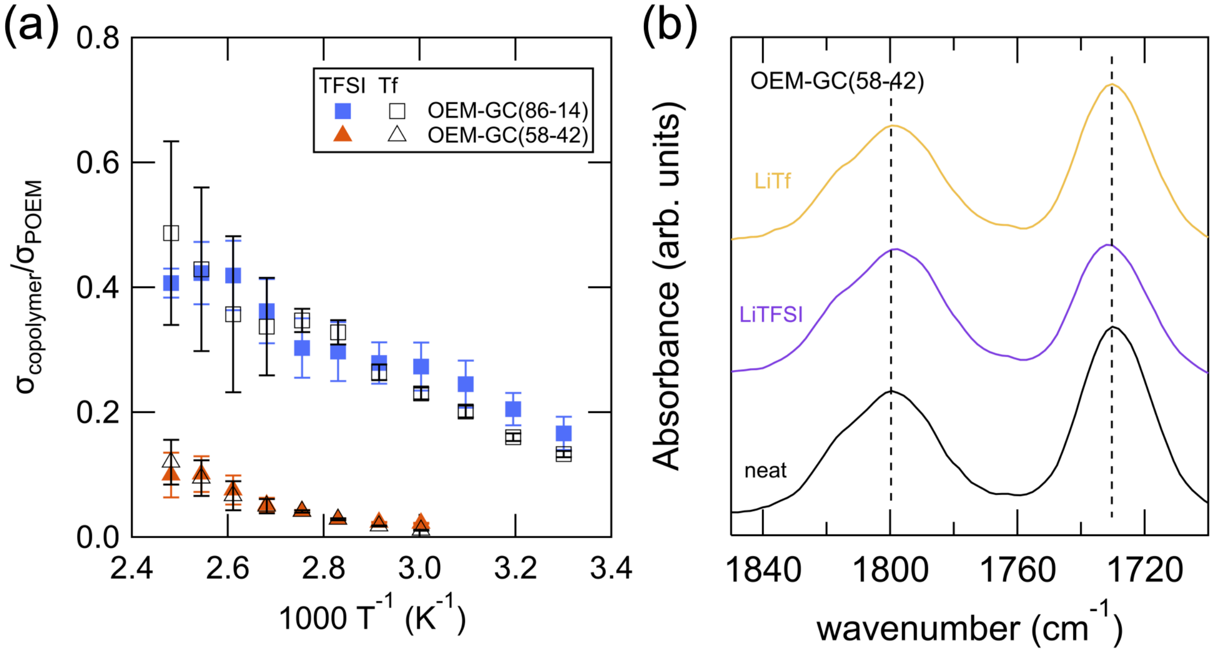

Figure 8.5 – (a) Conductivity of POEM-*ran*-PGCMA normalized by the conductivity of POEM at $r = 0.05$ with different salts as a function of temperature and (b) FTIR spectra of OEM-GC(58-42) neat (black), $r = 0.05$ LiTFSI (purple), and $r = 0.05$ LiTf (yellow)

The effect of carbonate content—or lack thereof—can be seen more directly by comparing the conductivity of the copolymer systems divided by the conductivity of POEM for each salt, shown in Figure 8.5a. This normalized conductivity shows a temperature dependence due to the differences in T_g of POEM and the two copolymers. The change of anion, however, has absolutely no effect on this ratio, indicating that there is no beneficial solvation achieved by adding PGCMA to the POEM material. Instead, the conductivity is entirely a function of differences in polymer dynamics. To understand why this is the case, we took FTIR spectra of the OEM-GC(58-42) with no salt, $r = 0.05$ LiTFSI, and $r = 0.05$ LiTf, shown in Figure 8.5b. The characteristic peaks for the cyclic carbonate group (1800 cm^{-1}) and the methacrylate ester (1731 cm^{-1}) are entirely unperturbed by the addition of either salt. If the carbonate group were interacting with Li^{+}, we should see a shoulder or a peak at lower wavenumber.[225] Instead, the FTIR spectra make clear that neither the carbonate nor the methacrylate group is involved in solvation to any degree in any of these electrolytes, and ions exclusive interact with polyether solvation sites. Moreover, the relative conductivities of the POEM and copolymer systems point to the fact the fact that there is no difference in the free ion fraction of these materials. These results suggest that neither free ion content nor conductivity in these materials is improved by introduction of highly polar PGCMA.

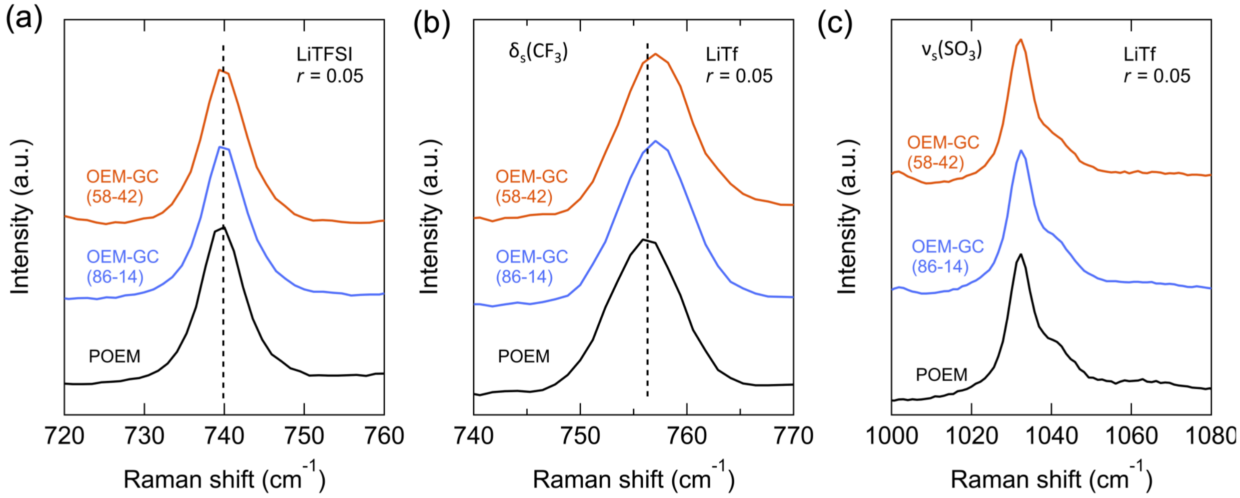

Figure 8.6 – Raman spectra of POEM, OEM-GC(86-14), and OEM-GC(58-42) blended with (a) $r = 0.05$ LiTFSI and (b,c) $r = 0.05$ LiTf

Free ion fraction can be more directly assessed by Raman spectroscopy. Figure 8.6 shows the Raman spectra for POEM, OEM-GC(86-14), and OEM-GC(58-42) with $r = 0.05$ LiTFSI or LiTf. In Figure 8.6, the spectra of the LiTFSI systems is shown in the range of 720–760 cm^{-1} where the TFSI exhibits a characteristic peak that can be used to determine the extent of interaction with Li^{+}. For all three systems, there is a narrow peak centered around 740 cm^{-1}, the location representative of free ions, *i.e.* not interacting with Li^{+} at all.[41,228,229] Ion pairs and higher order aggregates would manifest as a peak near 744 cm^{-1}.[267] For all three materials, the Raman spectra are best fit by a single Voigt function with a peak center of 740 cm^{-1}, indicating that all of the ions are fully dissociated and should contribute to the conductivity. The spectra for the LiTf systems (Figure 8.6b,c) tell a different story, however. Two characteristic wavenumber ranges can be used to estimate extent of ionic interaction in the triflate system. The 740–770 cm^{-1} corresponds to the symmetric CF_3 deformation mode while the 1000–1080 cm^{-1} range corresponds to the SO_3 symmetric stretch.[266] Free ions, ion pairs, and ionic aggregates appear at 753, 757, and 761 cm^{-1}, respectively for the $\delta_s(CF_3)$ region and at 1033, 1041, and 1051 cm^{-1}, respectively for the $\nu_s(SO_3)$ region.[266,268] Both regions show significant ion pairing and aggregation in all three materials. Furthermore, the center and shape of these peaks is not clearly dependent on the polymer composition, which indicates that the extent of dissociation is not affected by the cyclic carbonate.

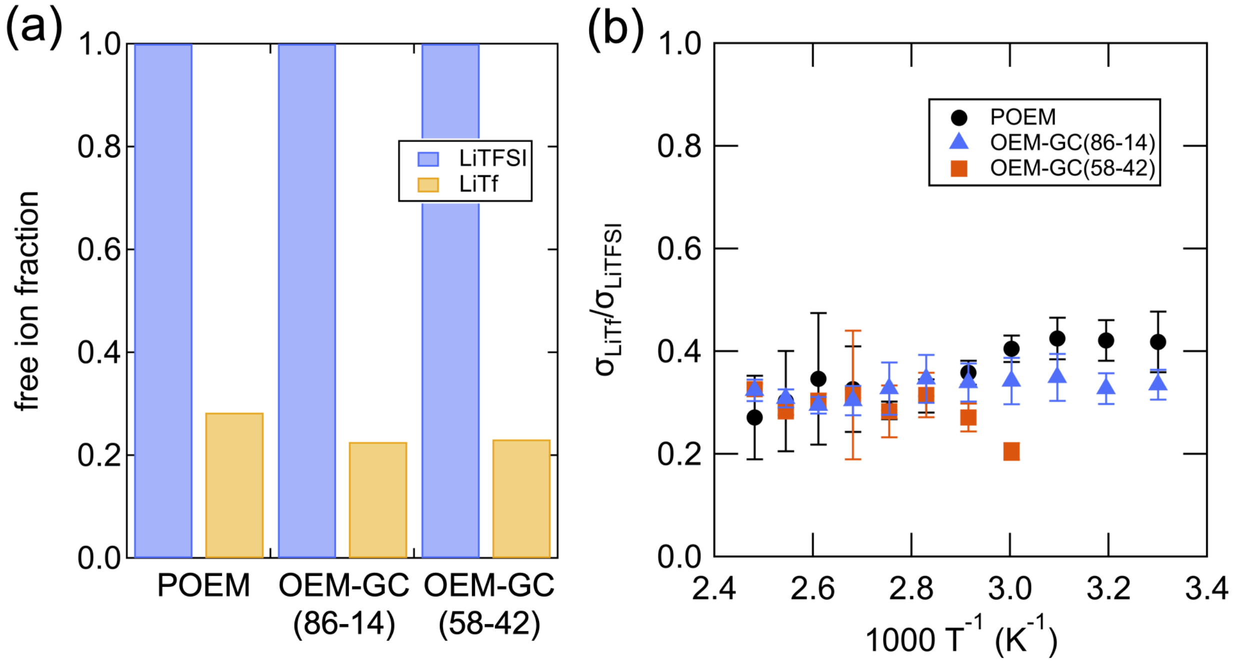

Figure 8.7 – (a) Free ion fraction, as determined from peak fitting of Raman data and (b) conductivity of the LiTf containing systems divided by the LiTFSI system with the same material as a function of temperature

The free ion fraction in the LiTf systems can be estimated by peak fitting of the $\delta_s(CF_3)$ region. The $\nu_s(SO_3)$ has also been fit in previous studies, but the presence of a small peak at approximately 1030 cm^{-1} arising from the polymer backbone makes quantitative analysis of this region more challenging. The 720–780 cm^{-1}, conversely, is completely free of polymer modes. These Raman spectra were peak fit using a linear background and three Voigt functions. By comparing the area of the 753 cm^{-1} peak to the total fit area, the free ion fraction is estimated for each polymer electrolyte system and plotted in Figure 8.7a. While the TFSI anions are fully dissociated by all three materials, only around 25% of the Tf ions are dissociated. Furthermore, there is little difference in this value across the different polymers, with POEM perhaps exhibiting a slightly higher fraction of free ions than the copolymers. Figure 8.7b shows the conductivity of LiTf containing electrolytes divided by the conductivity of the same polymer mixed with LiTFSI. The ratio of free ions in the LiTf systems to that of the LiTFSI systems closely matches the ratio of conductivities of the same systems. We expect that the change of anion should not affect the ionic mobility, especially as the T_g is very similar for each material with different salts. It is evident from this result that the primary difference in the conductivity of LiTf and LiTFSI electrolytes is the percentage of mobile, free charge carriers, and this free ion content is completely unaffected by the presence of high polarity PGCMA groups. Despite the high polarity of the cyclic carbonate group, the PGCMA behaves as completely inactive material, and only serves as a detriment to conductivity by means of increasing the T_g.

Previous studies of similar materials have shown different solvation tendencies depending on the specifics of the material chemistry. Webb *et al.* found that in a computational study of a series of polyether-polycarbonate copolymers, ether solvation was generally favorable, and if side-chain ethers were present, Li^+ was exclusively solvated by those side-chains.[37] Conversely, Morioka *et al.* showed experimentally that in a linear PEO-polycarbonate, Li^+ was actually preferentially solvated by the carbonate groups, and the salt concentration dependent conductivity and T_g were characteristic of linear poly(ethylene carbonate), not PEO.[57] In a study of POEM-*ran*-PGCMA gel polymer electrolytes (swollen with 1:1 EC:DMC solvent), ions were primarily solvated by the cyclic EC solvent, as is typical in polymer-free EC:DMC electrolytes.[269] The Li^+ that did interact with the polymer host, however, exclusively interacted with the POEM component, and not the PGCMA. Based on our previous computational and experimental results regarding solvation in POEM, it is not necessarily unexpected that the Li^+ shows a preference for the POEM phase, given the ability of each individual POEM monomer to form a fully-fledged solvation site consisting of six ether oxygens.[22,203] More surprising is the observation that the Li^+ ions show preference for interaction with the $TFSI^-$ over solvation by the carbonate group. A large fraction of the LiTf appears to exist as contact ion pairs, where the Li^+ is partially solvated by the EO side-chain but remains in close contact to the Tf^- anion, despite the availability of the highly polar PGCMA.

We can understand this finding by considering the thermodynamic driving forces governing ionic dissociation. In general, dissolution of a salt results in an unfavorable increase in enthalpy from breakup of the ion-ion interactions in the crystal (the lattice energy). This unfavorable enthalpy increase is offset by a favorable decrease in enthalpy from ion-dipole interactions between the ions and the solvent and greater entropy of the system when the salt is dissolved. In small molecule systems, an increase in the solvent polarity results in greater enthalpy decrease from ion-solvent interaction, which favors dissociation. In polymers, this should typically be the case as well, and ion dissociation should occur more readily in more polar polymers. Because free ions can act as crosslinking sites and require very specific chain conformations to form solvation sites, however, there is in fact an entropic penalty associated with a higher number of free ions.[270,271] An increase in contact ion pairs as temperature increases has been explained by this entropic driving force that is specific to polymer electrolyte systems.[270,271] This fact also possibly explains why we see the ratio of LiTf conductivity to LiTFSI conductivity decrease as temperature increases (Figure 8.7b). The poorly dissociating LiTf may exhibit a slightly increasing fraction of contact ion pairs as temperature increases, while the free ion fraction in the highly dissociated LiTFSI system remains constant. More importantly, though, it seems as though the entropic penalty arising from ion-PGCMA interaction is greater than the enthalpy gain from this strong ion-dipole interaction. The POEM chains, on the other hand, contain much less polar ether oxygens and so the ion-dipole enthalpy is smaller. However, the equilibrium configuration of the nine-repeat unit side-chain is hardly perturbed by the presence of a solvated Li^+ ion, and so the resulting entropy loss is negligible.[22] Moreover, at these relatively low salt concentrations there are sufficient POEM side-chains to form complete solvation sites with no need for crosslinking.[41,203] Ultimately, a high proportion of contact ion pairs existing entirely in the POEM phase of the material represents the lowest energy configuration for these materials, despite the high dipole moment of the PGCMA monomers.

8.2.5 Reduced conductivity in block copolymer despite some degree of phase separation

One possibility that should be considered is that preference for polyether solvation over carbonate solvation is due to the simple fact that the ether units are inherently in close proximity to one another, in contrast to the carbonate units. Each POEM monomer consists of nine ethylene oxide units convalently bonded, each of which is sufficient to form a viable Li^+ solvation site. The carbonate groups, conversely, are limited to one per PGCMA monomer, which themselves are randomly distributed along the copolymer backbone. To explore this idea further, we synthesized a block copolymer (BCP) of PGCMA and POEM. In this chain configuration, GCMA monomers will be covalently bonded mostly to other GCMA monomers, and the carbonate groups will be in much closer proximity to each other than in the random configuration. First a PGMA macroCTA was polymerized by RAFT according to Scheme 8.2. This living polymer was then purified and used as the RAFT agent for subsequent polymerization of POEM, resulting in a POEM-*block*-PGMA BCP.

This block copolymer was determined to have M_n = 18.4 kg mol^{-1}, $Đ$ = 1.29 by SEC (PMMA standards) Finally, this BCP was functionalized by the same CO_2 addition procedure described for the random copolymers to yield POEM-*block*-PGCMA (Scheme 8.3). The resulting polymer was determined to be 50 wt % POEM by ^{1}H−NMR (Figure 8.14).

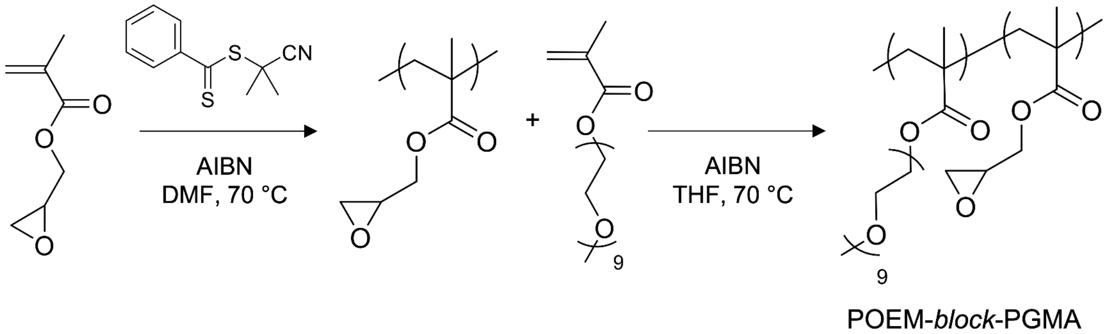

Scheme 8.2 – POEM-*block*-PGMA synthesis

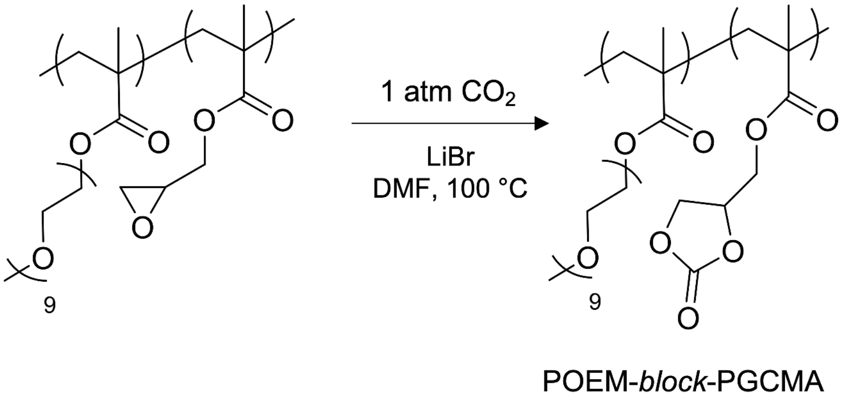

Scheme 8.3 – Functionalization of POEM-*block*-PGMA to POEM-*block*-PGCMA

DSC curves for the neat and r = 0.05 LiTFSI containing BCP are shown in Figure 8.8 and the midpoint T_g values are reported in Table 8.2. In the neat system, only one transition is evident at around -56 °C which can be attributed to the POEM block, while no signal related to the PGCMA block is clear. This does not, however, indicate that the BCP is fully disordered. Due to the similar polymer composition, the BCP can be most directly compared to the OEM-GC(58-42) copolymer. Between these materials, the BCP shows a significantly lower T_g ($>$ 30 °C difference in the neat materials), and a much more narrow glass transition breadth. Both of these results suggest that the GCMA and OEM repeat units are much less intimately mixed in the block architecture than in the random copolymer. This difference in local monomer concentration is apparent from small-angle X-ray scattering (SAXS) as well. Figure 8.9 shows SAXS data for the BCP and OEM-GC(58-42) after annealing at 150 °C. The BCP shows a clear pimary scattering peak, indicative of some degree of microphase separation, whereas the scattering profile for the random copolymer is featureless. The real spacing of the primary peak for BCP profile (around 20 nm) is where we might expect to see for a material of this molecular weight. The absence of higher order peaks, however, indicates that the polymer is not strongly phase separated. The BCP should not be thought of as fully phase separated system, though at the monomer level there is clearly a greater degree of variation in local concentration than in the random copolymer, which is uniformly mixed.

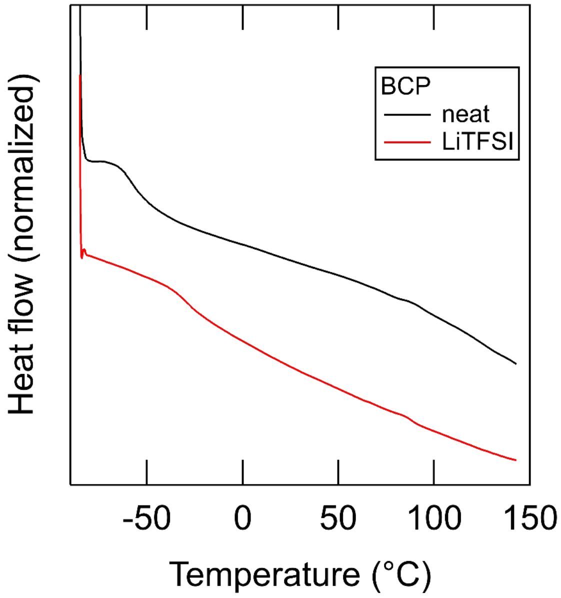

Figure 8.8 – DSC thermograms for PGCMA-*block*-POEM neat and r = 0.05 LiTFSI

The SAXS profile for the r = 0.05 LiTFSI containing BCP is also shown in Figure 8.9. Notably, the primary scattering peak appears less sharp and has shifted to higher q (lower real spacing), both of which are indications of more intimate mixing of the two blocks than in the neat system. There remains a greater degree of phase separation in the $r = 0.05$ LiTFSI BCP system than the random copolymer. The effect of the addition of salt on the compatiblity of the two blocks is also evident from the DSC data. The addition of Li^+ salt, either LiTFSI or LiTf, to the homopolymer POEM or the random copolymers has very similar effect on the Tg in all cases. However, while adding $r = 0.05$ LiTFSI to OEM-GC(58-42) raises the T_g by around 12 °C, the addition of the same amount of salt to the BCP results in a T_g increase of 26 °C. Adding salt to a polymer is well-known to increase the T_g due to an ionic crosslinking effect. In the case of the BCP, though, there is an additional effect of causing the two blocks to be more intimately mixed, resulting an even greater increase in T_g of the POEM phase.

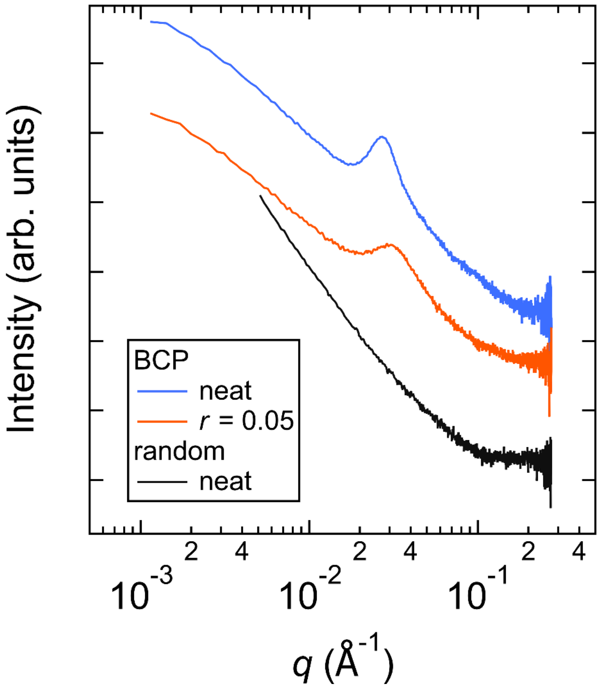

Figure 8.9 – SAXS data from neat OG(58-42), neat block copolymer, and $r = 0.05$ LiTFSI blended block copolymer

The SAXS and DSC results might suggest that the lithium salt is more uniformly distributed in the BCP than in the random copolymer, where it was completely localized to the

POEM. FTIR results for the BCP indicate otherwise, though. Figure 8.10 shows the FTIR spectra for the BCP and the OEM-GC(58-42) random copolymer. The neat spectra (Figure 8.10a) are virtually identical, indicating that the POEM does not significantly interact with the carbonate or ester moieties in either case. From Figure 8.10b and Figure 8.10c, it is clear that the addition of either LiTFSI or LiTf salt has absolutely no effect on the spectrum of either material. This result demonstrates that the lithium salt is indeed localized in the POEM phase even in the BCP. The higher local concentration of PGCMA groups clearly does not encourage Li^+ solvation by the carbonate moieties. Even in the block configuration, the entropic penalty associated with forming PGCMA, rather than POEM, solvation sites is greater than any enthalpic effects of the greater ion-dipole interaction.

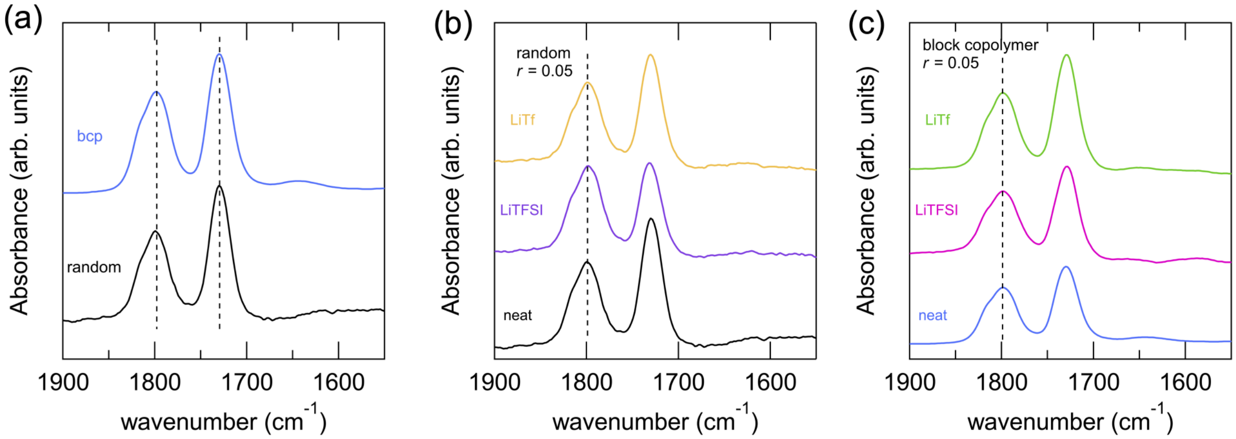

Figure 8.10 – (a) FTIR spectra of neat POEM-*ran*-PGCMA(58-42) and POEM-*block*-PGCMA(50-50) and FTIR spectra of (b) random copolymer and (c) block copolymer with $r = 0.05$ LiTFSI and LiTf

Although the polarity of PGCMA has little influence on the solvation behavior of Li^+ in the system, the polarity mismatch between the two blocks does appear to describe the phase behavior observed. The moderate degree of phase separation observed in the neat POEM-*block*-PGCMA can be understood in part because of the different polarity and dielectric constants of the two blocks.[272] As salt is added to the material, it is preferentially solvated and localized in the low polarity POEM phase. This counterintuitive fact is due to polymer-specific thermodynamic considerations and the specific chemical nature of the polyether side-chains. This localization of salt in the low polarity material, however, raises the effective dielectric constant of that phase, thereby decreasing the contrast with the high polarity, salt-free block. This is in contrast to typical amphiphilic block copolymer electrolytes such as polystyrene-*block*-PEO, where added salt resides in the polar block, causing an increase in the polarity of the high-polarity block and thereby driving further phase separation.[66,73,273] Here, the ion solvation and salt localization is driven by molecular-level and chemically specific factors, but the effects of the added salt have effects on the material phase behavior that can be explained by macroscopic phenomena such as dielectric constant.

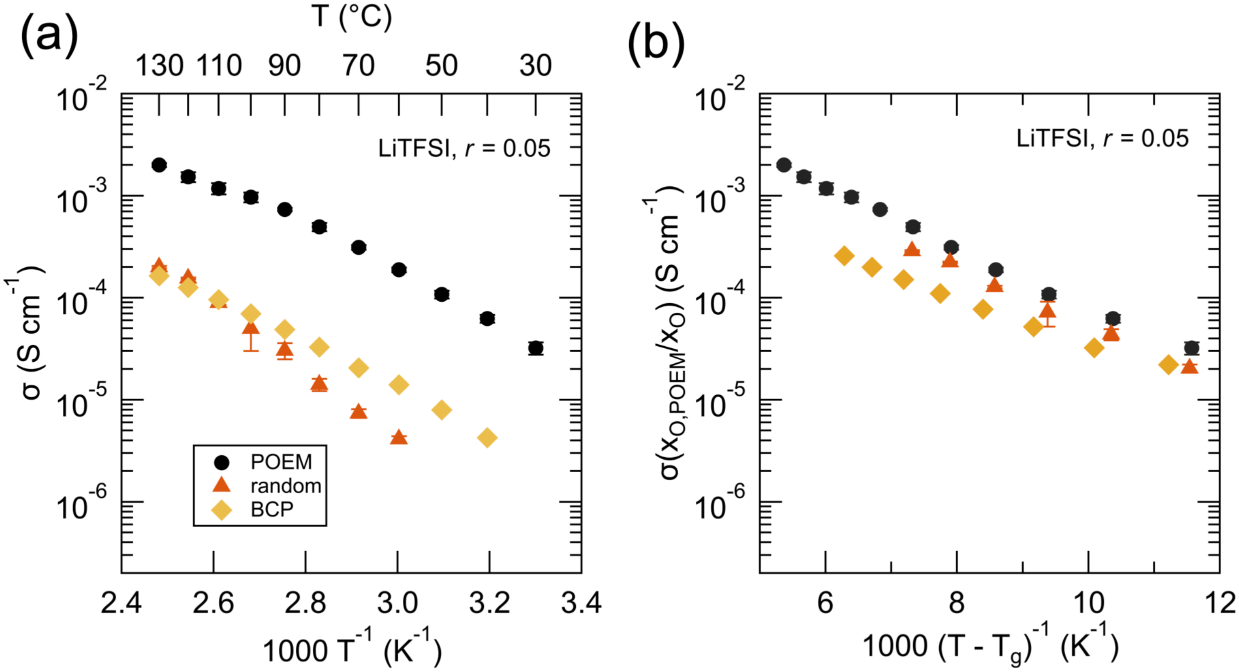

Figure 8.11 – Conductivity of POEM, OEM-GC(58-42), and BCP(50-50) as a function of (a) temperature and (b) $T - T_g$

Finally, we measured the ionic conductivity of the BCP $r = 0.05$ LiTFSI system. Figure 8.11a shows the conductivity of the BCP system after annealing at 150 °C for two hours compared to the homopolymer POEM and the OEM-GC(58-42) random copolymer system. The BCP exhibits higher conductivity than the random copolymer at low temperatures, but it has a shallower temperature dependence due to its lower T_g. At around 110 °C the conductivity of the random copolymer reaches and then exceeds that of the block copolymer. After correcting for differences in T_g (Figure 8.11b), however, the random copolymer shows a clearly higher conductivity at nearly all reduced temperatures. Moreover, while the random copolymer show very similar slope, suggesting a similar activation energy limiting the conductivity, the block copolymer exhibits a qualitatively different behavior. This may be in part a result of temperature dependent phase behavior in the block copolymer.

More surprising, though, is the fact that the more intimately mixed random copolymer exhibits a higher conductivity than the somewhat more phase separated block copolymer. This result would seem to contradict our own previous results, and those of others. We have argued previously that the greater extent of interfacial mixing present in low salt concentration block copolymer PS-PEO explains the lower normalized conductivity.[192] More recently, we have demonstrated that miscible blends of PEO/PMMA have a higher conductivity than compositionally identical PEO-PMMA block copolymers. We attributed this fact to a greater local concentration of PEO in the blends that led to greater percolation of solvation sites at the 6–8 Å length scale at which many interchain ion hopping events are expected to occur.[20] The critical difference between those studies and the present work appears to be the use of linear, rather side-chain, polyethers. In the case of linear PEO, solvation sites are formed by adjacent EO units along the backbone. Such solvation sites may be more readily disrupted for disconnected from one another by nonsolvation PS or PMMA groups than in side-chain POEM. Moreover, the intrachain hopping mechanism that is common in linear PEO may less adversely affected by the presence of nonsolvating groups than the longer range interchain hopping. This mechanism is largely absent from ion transport in the side-chain POEM systems, however.[22] The ability for ions to move via the intrachain hopping mechanism may limit the decrease in conductivity in blends of linear PEO. This apparent difference in the ion transport through mixed systems of linear *vs.* graft polyethers may have significance for the study of block copolymers, where the transport through the interfacial region likely depends on the degree of interfacial mixing.[92,172,179,192] These questions merit further investigation, especially using the type of atomistic MD simulations used recently to investigate ion hopping between solvation sites.

8.3 Conclusions

In this study we have elucidated the ion solvation and transport behavior of copolymers consisting of the side-chain polyether POEM and the cyclic polycarbonate PGCMA. Although the cyclic carbonate moiety is significantly more polar than the ether oxygens of POEM, FTIR data and conductivity results suggest that ions are exclusively solvated and transported by the POEM groups. Unlike in small molecule ether-carbonate blend electrolytes where ions are preferentially solvated by the ether groups, here we find no enhancement to the conductivity as a result of increased overall polarity of the polymer. Instead, the conductivity behavior of random copolymers of POEM and PGCMA was determined entirely by the mole fraction of EO units in the system and the average systemwide dynamics, as indicated by the midpoint T_g value. Furthermore, we demonstrated that these results were true when a poorly dissociating LiTf salt was added to the system, and Raman data confirms that the presence of highly polar carbonate moieties does not increase the extent of ionic dissociation. Rather, our results indicate that the thermodynamically favorable state consists of a high fraction of contact ion pairs of Tf^- and Li^+ partially solvated by POEM side-chains. This result likely stems from the specific entropic considerations for ion dissociation in polymeric systems. These findings indicate that the blending or otherwise mixing a highly polar component with an ether-based polymer may not be a compelling strategy to improve ionic conductivity.

Finally, the same preference for polyether solvation was found in a POEM-PGCMA block copolymer, despite high local concentration of cyclic carbonate groups available to form solvation sites. Interestingly, though, the preference for salt to reside in the lower polarity POEM phase decreases the polarity contrast with the PGCMA phase, and SAXS data indicate that the addition of salt lowers the effective Flory Huggins interaction parameter of the material. The conductivity of the block copolymer exhibited qualitatively different temperature-dependent conductivity behavior from the homopolymer and random copolymer systems, however. We suspect this has to do with the disruption of long-range percolated solvation site networks in the block copolymer due to clustering of the POEM units. The ability of the nine-EO unit side-chain to form full solvation sites is likely an important factor in the solvation site percolation threshold random copolymers. This idea can perhaps be extended to other side-chain ether polymer electrolyte systems, such as exists in the interface of phase separated POEM-based block copolymer electrolytes. The relationship between of the degree of intermixing and ion transport may be fundamentally different in side-chain, rather than linear, polyether electrolytes.

8.4 Materials and Methods

8.4.1 Materials

Acetonitrile (99.8%, anhydrous), toluene, dimethylformamide (DMF), tetrahydrofuran (THF), methanol, diethyl ether, LiTFSI (battery grade, >99.95% trace metal basis) LiTf (99.995% trace metals basis), 2-cyano-2-propyl benzodithioate (CPBD), azobisisobutyronitrile (AIBN), deuterated dimethyl sulfoxide (DMSO-d_6) and monomers were purchased from Sigma Aldrich. Oligo(ethylene oxide) methyl ether methacrylate (OEM, $M_\mathrm{n} = 500$ g mol^{-1}) and glycidyl methacrylate (GMA) were purified of inhibitor before use by passing through a column of basic alumina. LiTFSI was further under vacuum at 120 °C for 48 h. Homopolymer POEM was synthesized and purified according to the previous chapter. Polymers and salts were stored in an argon glovebox after the drying processes. AIBN was recrystallized in ethanol before use.

Synthesis of POEM-ran-PGMA copolymers

POEM-*ran*-PGMA random copolymers were synthesized by RAFT polymerization according to Scheme 8.1. Reaction mixtures consisting of 5 g total monomer, 9.1 g DMF, 55.3 mg CPBD, and 4.1 mg AIBN were stirred to combine and sparged with dry nitrogen for 20 minutes. Mass fractions of OEM in the reaction mixture and final product are listed in Table 8.1. Reactions proceeded for 7 hours at 70 °C, followed by quenching the vessel in an ice bath. Crude product was purified by evaporating DMF, redissolving in THF, and precipitating the mixture into excess hexanes. The resulting polymer was redissolved in THF and precipitated into hexanes twice more and dried overnight at 50 °C to remove remaining solvent.

Synthesis of POEM-block-PGMA block copolymers

POEM-*block*-PGMA block copolymers were synthesized by RAFT polymerization according to Scheme 8.2. First, PGMA macroCTA was prepared by RAFT polymerization of GMA. 5 g GMA, 9.3 g DMF, 55.3 mg CPBD, and 4.1 mg AIBN were stirred to combined and sparged with dry nitrogen for 20 minutes. The reaction vessel was placed in an oil bath at 70 °C for 7.5 hours, followed by quenching in an ice bath. Crude product was purified by precipitating the mixture into excess methanol. The resulting polymer was redissolved in THF and precipitated into methanol twice more and dried overnight at 50 °C to remove remaining solvent. The resulting polymer was then used as the CTA for subsequent polymerization of the POEM block. 1.5 g OEM, 1.0 g PGMA macroCTA, 2.5 mg AIBN, and 2.4 g THF were stirred to combine in a round bottom flask and sparged with dry nitrogen. The flask was placed in an oil bath at 70 °C for 6 hours before quenching in an ice bath. The crude mixture was precipitated into excess hexanes, followed by redissolution in THF and precipitation in hexanes twice more. The resulting polymer was dried at 50 °C under vacuum overnight.

Carbonization of GMA units to GCMA

GMA units were converted to cyclic carbonate GCMA units by reaction of the epoxy groups of GMA with CO_2. A similar process was used for all random and block copolymers. Polymers were dissolved in DMF (0.2 M) along with 10 mol % LiBr (relative to the GMA units) as a catalyst. CO_2 was then bubbled through the reaction mixture at 1 atm while the vessel was heated to 100 °C and kept under CO_2 atmosphere for 24 hours. After reaction, the polymer solutions were concentrated by evaporating DMF in a rotary evaporator and then precipitated into excess methanol (random copolymers 1 and 2, Table 8.1) or cold diethyl ether (block and random copolymers 3–5, Table 8.1), or dialyzed against methanol overnight (random copolymers 6 and 7, Table 8.1) to remove the catalyst. The resulting products were filtered, washed then three times using methanol or diethyl ether and finally dried under vacuum overnight at 50 °C.

Polymer electrolyte solution preparation

Polymer solutions were prepared inside of an argon glovebox by dissolving polymer in either pure acetonitrile or a mixture of acetonitrile and toluene (50/50 v/v). Solutions were heated to 50 °C to help facilitate dissolution of the polymer and then were left stirring overnight. LiTFSI in acetonitrile solutions were prepared in the same manner. Polymer electrolyte solutions were prepared by blending polymer and salt solutions at an appropriate volumetric ratio to obtain a ratio of $r = 0.05 = [\text{LiTFSI}]/[\text{EO}]$.

8.4.2 Materials characterization

Size-exclusion chromatography

Size-exclusion chromatography (SEC) measurements were conducted on a Tosoh EcoSEC system with DMF + 0.01 M LiBr as eluent at a flow rate of 1 mL min^{-1}. Separation was achieved using a Tosoh SuperAW3000 and a Tosoh SuperAW4000 column at 50 °C. Molecular weight and dispersity were determined by comparison with PMMA standards.

Determination of copolymer composition by ^{1}H-NMR

POEM-*ran*-PGMA copolymer composition and carbonization extent of reaction were determined by ^{1}H-NMR in DMSO-d_6. Data were acquired on a 400 MHz Bruker Avance III HD nanobay spectrometer equipped with a iProbe SmartProbe, using Topspin 2.1. Copolymer composition was determined by comparing the peak integrals at $\delta = 4.03$ ppm (2H, -C(O)-O-CH_2-) of $POEM_9$ units to those at $\delta = 2.80$ and 2.66 ppm (2H, -CH-O-CH_2) of the epoxy group of PGMA units. The composition of the POEM-*ran*-PGMA copolymers is reported in Table 8.1. Complete conversion of the epoxide group to cyclic carbonate was confirmed by complete disappearance of peaks at $\delta = 3.20$ ppm (1H, -CH-O-CH_2) and $\delta = 2.80$ ppm and 2.66 ppm (2H, -CH-O-CH_2) corresponding to protons in the epoxide group of PGMA units.

Differential scanning calorimetry

Calorimetric glass transition temperatures (T_g) of neat polymers and polymer electrolytes were determined by DSC using a TA Instruments Discovery 2500 DSC. Sample pans were prepared inside an argon glovebox by drop casting solutions, heating at 65 °C until dry, and repeating until 5–10 mg of material was in the pan. The pans were then hermetically sealed before removing from the glovebox to avoid any water adsorption before DSC measurement.

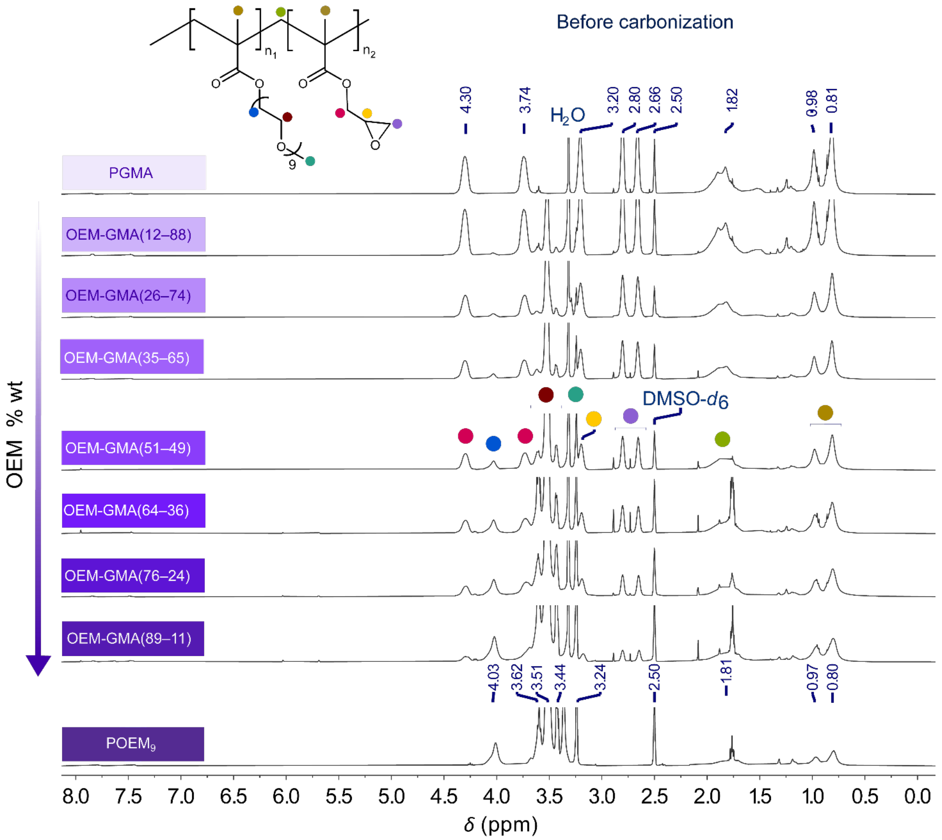

Figure 8.12 – ^{1}H-NMR spectra of POEM-*ran*-PGMA copolymers synthesized by RAFT

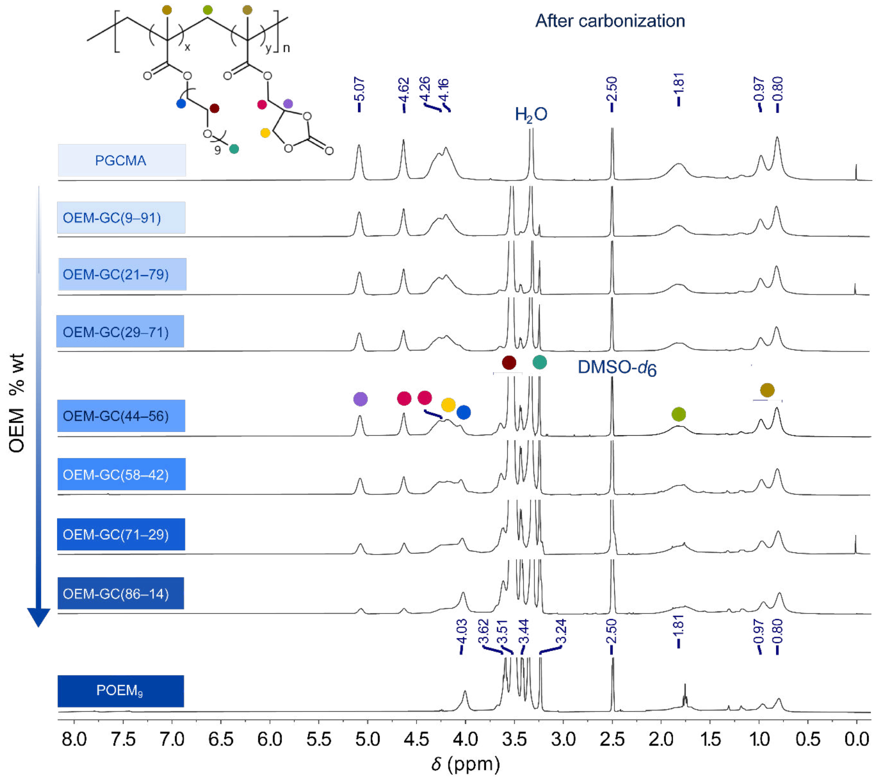

Figure 8.13 – ^{1}H-NMR spectra of POEM-*ran*-PGCMA copolymers after carbonization. Peaks corresponding to the GMA epoxide group have been completely replaced by peaks corresponding to GCMA units.

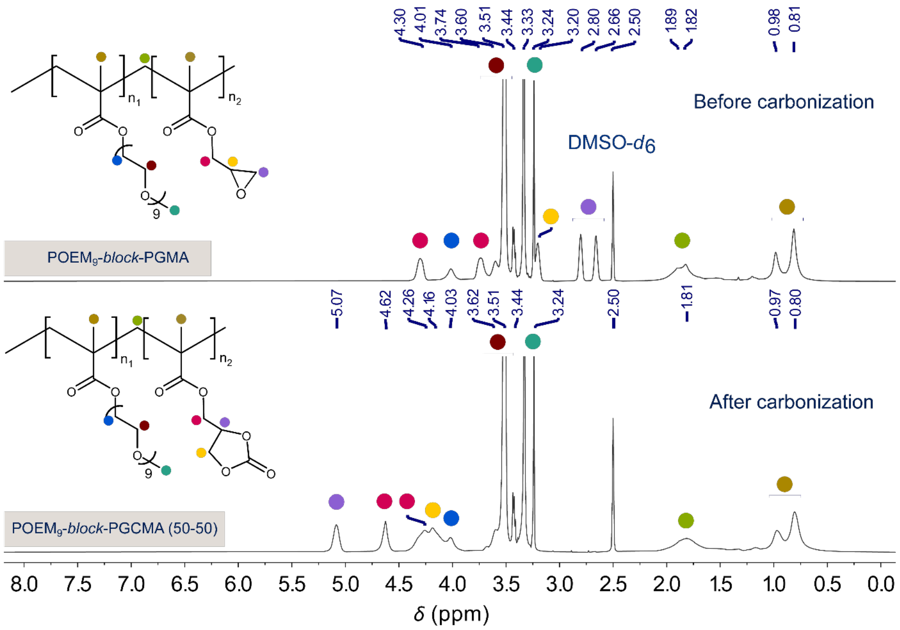

Figure 8.14 – ^{1}H-NMR spectra of POEM-*block*-PGMA and POEM-*block*-PGCMA

Samples were conditioned at 135 °C followed by three cycles of cooling to -85 °C and heating to 135 °C at a scan rate of 10 °C/min. T_{g} midpoint and breadth values were taken from the third heating curve.

Fourier transform infrared spectroscopy

Samples for Fourier transform infrared spectroscopy (FTIR) measurements were prepared on Au-coated Si substrates by spin coating as described in Section 2.4.1. Samples were prepared inside of a glovebox, annealed at 150 °C for 15 minutes, and sealed until immediately before measurement to minimize water absorption. Measurements were performed using a Shimadzu IRTracer-100 spectrometer using a germanium prism for attenuated total reflection (ATR) at ambient temperature from 400–4000 cm^{-1} at a resolution of 4 cm^{-1}.

Raman microscopy

Raman samples were prepared by drop casting films on Au-coated Si substrates inside of a glovebox. Films were dried and then annealed at 135 °C for 15 minutes inside of the glovebox and then sealed until measurement. Raman experiments were performed using a Horiba LabRAM HR Evolution NIR confocal Raman microscope. Raman spectra were collected with a 100x objective and a 633 nm wavelength laser.

8.4.3 Ionic conductivity measurements

Polymer electrolyte films were spin cast onto IDEs fabricated according to the procedure described in Section 3.2.1. IDEs used for measuring SEO(19-6) had dimensions of $N = 160$, $l = 1$ mm, $w = 2$ µm, and $d = 8$ µm. EIS measurements were performed with a potential amplitude of 100 mV over a frequency range of 1 Hz–1 MHz, and impedance spectra were fit to the equivalent circuit model shown in Figure 4.4b (Model 2). Conductivity was then taken using the cell constant derived in Section 3.3. Reported conductivity values are the average of three samples, with error bars corresponding to the standard deviation.

Chapter 9

Summary and Outlook

9.1 Dissertation Summary

The work has described new experimental methods for the study of polymer electrolyte thin films, and deeper understanding of the relationship between polymer chemistry, nanostructure, and ion transport has been developed. First, the use of interdigitated electrodes (IDEs) to measure the conductivity of polymer thin films was thoroughly investigated. In Chapter 3, a derivation for the simplified, linear form of the IDE cell constant was derived. Though this cell constant had been used previously by others, no justification for the use of this equation was provided. Here, the cell constant was derived from a general expression for the elliptic electric field lines produced by IDEs. The general IDE cell constant requires use of elliptic integrals and is a function of the IDE electrode spacing and width. A more compact form of the cell constant was derived by conformal mapping and by making simplifications about the system based on the relative length scales of the IDE geometry and thin film height. The result of this derivation was a cell constant that varies linearly with the electrode spacing and film height, but is independent of electrode width.

The validity of these simplifying assumptions was tested experimentally in Chapter 4 using a model SPE system of PEO and LiTFSI. IDEs with different dimensions were coated with polymer films of different height and used to make electrochemical impedance spectroscopy (EIS) measurements. Modeling this impedance data using equivalent circuits was discussed in depth. The film resistance taken from model fits of the EIS data varied linearly with the IDE electrode spacing and the film height, as predicted by the simplified cell constant derived in Chapter 3. The impedance data when the electrode width was varied were more complex, though. When the electrode width was relatively low (equal to or smaller than the electrode spacing), the resistance was invariant with width, as predicted. At high electrode widths, however, a secondary electrochemical phenomenon emerged in the impedance data. These speactra required inclusion of an additional model circuit element to accurately describe the full system. The secondary process was fit by a bounded Warburg element, suggesting that it was diffusional in nature with a finite boundary condition. This phenomenon was likely the result of the thin film nature of the experiment and the extreme conditions of the cell when more than half of the IDE surface consisted of gold electrode. It was hypothesized that the high electrode surface area resulted in a depletion of ions in the bulk of the film, leading to a chemical potential gradient in addition to the electrical potential applied by the electrodes. These two potentials lead to observation of both migration of the ions in phase with the applied potential (resistance) as well as counter-diffusion of ions due to concentration gradients (Warburg). With thoughtful design of the IDE geometry and film thickness, this secondary process could be eliminated, and the bulk conductivity of the SPE could be measured clearly.

As is common in the study of thin films, dewetting was also found to be an issue with these measurements. In particular, significant hysteresis in the measured impedance was observed as films were heated and cooled. This dewetting was particularly evident when IDEs with large fractions of the surface consisted of gold electrodes. Both the surface energy and roughness of the gold surface could contribute to the dewetting of a thin film. Both issues were addressed by passivation of the entire surface with a thin oxide layer deposited by atomic layer deposition. When this passivation layer is kept below roughly 2 nm, high quality impedance measurements can still be made. These results open the door to the use of a wide variety of dielectric materials to control the assembly of thin films without prohibiting the subsequent measurement of the SPE film.

Next, the use of IDEs to measure the impedance of block copolymer electrolyte (BCE) thin films was demonstrated. In Chapter 5, thin films of a lamellae-forming polystyrene-*block*-poly(ethylene oxide) (SEO) BCE were assembled on top of IDEs. By passivating the IDE surface with a material that was preferentially wet by one of the blocks, parallel assembly into a single grain was achieved. We demonstrated that in this configuration, irrespective of which block wet the substrate, conductivity was identical at all film thicknesses. This value was interpreted as the intrinsic conductivity of the material, which allowed direct comparison to the equivalent homopolymer conductivity without the obfuscation of grain boundaries and tortuosity that are present in bulk measurements. A reduction in conductivity relative to the homopolymer was found, even after eliminating all structural factors and accounting for active material volume fraction. Interestingly, the difference in conductivity between the block copolymer and homopolymer showed no temperature dependence, suggesting that the glassy nature of the PS block was not the primary reason for the reduction in ionic mobility at the interface. Instead, our results indicate that the composition of the interface, and the resulting disruption of the Li^+ solvation sites, is the primary cause for reduction in the intrinsic block copolymer conductivity. This hypothesis was supported by mean field calculations used to estimate the change in interfacial width as a function of the lithium salt concentration. This work verified and elucidated long-held hypotheses in the field of BCEs that have been experimentally inaccessible using conventional bulk measurement techniques.

In Chapter 6, the use of IDEs for measuring BCE conductivity was extended to cylinder-forming materials. Unlike in the case of lamellar BCEs, however, the measured conductivity of a minority-PEO cylinder-forming SEO electrolyte strongly depended on the wetting symmetry of the thin film as well as the film thickness. In the case where the PS block wet the IDE substrate, the film conductivity was dominated by the grain boundaries and blocking defects present in the fingerprint pattern cylinders. This type of defect structure, as well as its effect on the measured conductivity of the film, is comparable to that of a bulk BCE film.

If instead the PEO block preferentially wets the surface, a thin conductive layer forms across the IDE surface. The fingerprint pattern is still evident from the top surface using top-down scanning electron microscopy, but the measured conductivity is primarily a function of the PEO wetting layer. This fact is evident from the decrease in conductivity as the film thickness of such samples increases. The relative fraction of the film that is fully connected (defect free) decreases with increasing film thickness, resulting in a thickness dependence in the conductivity. This work highlights the importance of being able to fully characterize the film structure in order to analyze the measured conductivity quantitatively. Moreover, this work demonstrated the outsized impact that the material near the electrode may have on an electrochemical measurement, and care must be taken in ascribing properties to the bulk material and the interfacial region.

Finally, focus was shifted to understanding the fundamental ion solvation and transport behavior exhibited by nonhomogeneous SPEs. Graft polymers with polyether side-chains of varying length (POEM$_x$) were synthesized by controlled radical polymerization, characterized experimentally, and modeled computationally. Experimental conductivity of these materials increased monotonically as the side-chain length increased, despite only modest decreases in the glass transition temperature with side-chain length. Ion solvation was qualitatively similar in all materials studied as well. MD simulations showed that the relaxation rate of ethylene oxide (EO) units in the side-chain vary dramatically with the position along the side-chain. This variation in local segmental relaxation rate was attributable in part to the slow relaxation rate of the methacrylate backbone. When the methacrylate backbone unit was replaced with a more flexible acrylate group, the measured conductivity at low temperatures was markedly higher. This finding was validated by the MD simulations as well. This study demonstrated that the overall dynamics of the system do not necessarily govern the ion conductivity of the material. Instead, the local mobility of the solvation sites which most often participate in ion solvation is the relevant measure of the dynamics.

In Chapter 8, we examined the effects of adding a high polarity comonomer to the POEM electrolyte system. This idea, which has been explored previously in coarse-grained MD simulations, is inspired partly by the success of mixed solvent small molecule electrolytes. Conventional lithium-ion battery electrolytes often consist of a blend of a low polarity, low viscosity solvent (such as dimethyl carbonate) and a high polarity, high viscosity solvent (such as ethylene carbonate). The mixture of these two components exhibits a conductivity higher than either of the pure components. In the case of copolymers of POEM and a side-chain cyclic carbonate material, PGCMA, this trend was not observed. Instead, the addition of the glassy, polar PGCMA primarily had the effect of increasing the T_{g} of the system, resulting in a decrease in ionic conductivity with increasing PGCMA content. FTIR and Raman measurements showed that, despite the high polarity of the GCMA monomer, Li^+ ions exclusively interacted with the EO units of POEM. Even when a poorly dissociating salt was introduced, Li^+ only interacted with POEM and the counterion. This strong preference for solvation in the ether domains was attributed to the unfavorable loss of entropy required for the carbonate side-chains to form Li^+ solvation sites. In contrast, the equilibrium POEM chain conformations are barely perturbed by the addition of the lithium ions to the system. The relatively lower enthalpy gain due to solvation by the lower polarity component is overshadowed by the entropic penalty associated with solvation by the carbonate moieties. The importance of the entropy to the total energy of the system is a distinct feature of polymer electrolytes. This difference in the thermodynamics of small molecule and polymer electrolytes must be considered in future work regarding the relationship between polarity and ion conduction in polymers.

Throughout this dissertation, new experimental techniques and approaches for the study of polymer electrolyte thin films were demonstrated, and these methods were used to develop more complete structure-function relationships for these materials. The use of IDEs to measure both the bulk and interfacial properties of polymer electrolyte thin films was demonstrated with a range of materials. A full derivation for the cell constant of the IDE and a clear set of design criteria was established that should guide future research in this area. Moreover, this platform was used to examine ordered, nanostructured materials in a way that was previously experimentally unfeasible. We have demonstrated an approach to measuring intrinsic transport properties of block copolymer electrolytes that is universal in nature and requires only rudimentary surface modifications. Throughout this dissertation, the study of homopolymer and copolymer electrolytes clarified the importance of considering the microscopic ion solvation and transport phenomena to explain macroscopic conductivity measurement results. Several of these studies were aided by the use of vibrational spectroscopy to probe polymer-ion and ion-ion interactions, as well as atomistic molecular dynamics simulations to complement experimental results. In the case of block copolymer electrolytes, disruption of the solvation site network throughout the domain interface proved to be critical to the overall conductivity of the material. In side-chain materials, we demonstrated that the mobility of the individual solvation sites actively participating in ion solvation was the limiting factor in ionic conductivity, not the overall segmental dynamics of the material. In copolymers with varying functional group polarity, the polymer chain architecture and the specific chemistry of the monomers has a large impact on the solvation of ions, and more general, macroscopic material properties such as dielectric constant were shown to be less important. These structure-property relationships and experimental approaches should be considered as future research aims to design, synthesize, and characterize new materials for use in next generation energy storage devices.

9.2 Outlook and Future Research Directions

Polymer electrolytes remain an interesting class of materials from both a fundamental polymer physics perspective and for practical battery applications. The physics governing polymer electrolytes differs in important ways from typical small molecule electrolytes, as demonstrated by the work in this dissertation. Understanding of how the long chain nature of these materials, as well as the microphase separation of BCEs, impacts ion solvation, distribution, and transport remains incomplete. Moreover, it is likely that polymer electrolytes will be a part of an eventual commercialized lithium metal battery in one form or another. Even if SPEs are not ultimately used as bulk electrolytes, they may still find a role in next-generation batteries in the form of a cathode binder material,[274] part of a composite electrolyte,[275] or as an "artificial SEI" for passivating Li metal anodes.[276] Ongoing research in each of these areas, as well as continued research on the fundamentals of the electrochemical properties of SPEs, will benefit greatly from the methodologies described in this dissertation.

Deep understanding of how SPEs assemble and conduct ions near other solid surfaces within a battery cell will be critical to developing functional devices, and the IDE-thin film platform is an excellent way to approach these questions. Interesting demonstrations of how interaction with a solid interface affects ion transport using the IDE platform have been reported recently. Dong *et al.* showed that if PEO chains were end-grafted to the IDE surface, the measured conductivity dropped monotonically as the film thickness decreased.[155] This thickness dependence in the conductivity—which was absent in films that were not grafted to the substrate—was strong evidence that ion transport was significantly hindered in the interfacial region. The reduction in ionic conductivity was most likely due to an increase in the effective T_{g} of the material near the grafted surface, a phenomenon that has been observed previously in polymer thin films.[277] Zhao *et al.* saw a similar effect in a recent study of a series of poly(ionic liquids) (PILs).[195] Although none of the materials were grafted to the IDE surface, several of the PILs showed a decrease in conductivity as the film thickness decreased below around 50 nm. This effect was again attributed to difference in the T_{g} as the film thickness was decreased. The differences in the conductivity thickness-dependence as a function of PIL chemistry was explained well by differences in the fragility of the materials (*i.e.* the temperature sensitivity of the polymer segmental mobility near T_{g}). Both of these studies were supported by and built upon the extensive existing literature on the dynamics and behavior of polymer thin films, and they represent excellent examples of how the IDE platform is uniquely capable of probing certain interfacial phenomena.

Moreover, these studies have direct practical relevance to the study of composite polymer electrolytes, where interactions between a polymer ion conductor and a ceramic surface have been thought to play a critical role in determining ionic conductivity. The surface acidity of Al_2O_3 nanoparticles has been shown to significantly affect the measured conductivity and Li^+ transference number of PEO-based composite electrolytes due Lewis acid-base interactions between the particle surface and either ions or polymer functional groups.[278] In a study of composite electrolytes based on polyacrylonitrile and lithium lanthanum titanate (LLTO, a ceramic Li^+ conductor), Liu *et al.* found that conductivity was highest in systems with LLTO nanowires, which they attributed to a highly conductive interfacial region.[279] More recently, a study from our group investigated a hydrated ion conducting system of iodomethane-functionalized poly(2-vinylpyridine) (mP2VP) grafted to high aspect ratio cellulose nanocrystals (CNCs) and found that ionic conductivity was substantially improved in the direction along the direction of the CNCs.[280] The anisotropy in measured conductivity and the increase relative to the mP2VP homopolymer were attributed to enhanced ion transport near the polymer-CNC interface. Although clear effects due to the presence and surface functionalization of nanoparticles has been demonstrated repeatedly, these studies have relied on bulk measurements to probe nanoscale interfacial phenomena. Further work in this area would greatly benefit from the simplified, highly controlled interfacial measurements that can only be made by measuring thin electrolyte films on IDEs.

The work presented in this dissertation focused exclusively on the ionic conductivity of the solid electrolytes in question, but other critical material properties such as chemical and electrochemical stability may be investigated with the IDE system as well. Of particular importance in this area is the stability of the electrolyte in contact with the Li metal anode. Recent work has shown evidence that Li metal may be chemically reactive with PEO, especially at higher temperatures, leading to changes in the ionic conductivity.[48] Liu *et al.* investigated this phenomena further using a combination of EIS measurements using IDEs and surface characterization by FTIR and X-ray photoelectron spectroscopy (XPS), finding that the Li reduces the PEO to form alkoxides.[49] This work can be built upon in a number of ways using the thin film assembly methods described in this dissertation. For example, important questions remain about how these results will translate to a block copolymer system where one block may preferentially wet the lithium metal. Moreover, this type of study could be applied to a wide range of materials chemistries in order to find materials that may be more chemically stable when in contact with the metal anode. Understanding the self-assembly and degradation processes of polymers near Li will be critical to the use of these materials in a lithium metal battery, and the thin film platform developed here is ideally suited for such future studies.

Finally, the techniques and structure-property models developed in this dissertation can be applied to a much wider range of materials than was studied here. Several broad classes of materials that have garnered attention in recent years would be suited for the IDE platform. Studying single-ion-conducting materials—those where one of the ionic species is covalently bonded to the polymer chain while the other is free to move—could be particularly fruitful. Materials that exclusively conduct Li^+ might be better capable of stabilizing Li metal deposition during battery cycling,[281,282] and a number of single-ion-conducting polymers have been synthesized, including many that phase separate into periodic nanostructures.[163,283–286] The relationships between polymer chemistry and ion content, nanostructure, and ion transport for these materials is considerably less well understood than the more conventional polymer-salt electrolyte systems. As with the BCP-salt systems investigated in this work, the thin film platform should be uniquely capable of characterizing the intrinsic transport behavior of these materials. Furthermore, the ionic dissociation and formation of solvation sites in single-ion-conducting polymers has been explored very little, and deeper understanding in these areas is critical to rational design of these materials.

REFERENCES

(1) Yoo, H. D.; Markevich, E.; Salitra, G.; Sharon, D.; Aurbach, D. On the challenge of developing advanced technologies for electrochemical energy storage and conversion. *Materials Today* **2014**, *17*, 110–121.

(2) Li, Q.; Chen, J.; Fan, L.; Kong, X.; Lu, Y. Progress in electrolytes for rechargeable Li-based batteries and beyond. *Green Energy Environ.* **2016**, *1*, 18–42.

(3) Liu, J. et al. Pathways for practical high-energy long-cycling lithium metal batteries. *Nature Energy* **2019**, *4*, 180–186.

(4) Goodenough, J. B.; Park, K. S. The Li-ion rechargeable battery: A perspective. *Journal of the American Chemical Society* **2013**, *135*, 1167–1176.

(5) Erickson, E. M.; Ghanty, C.; Aurbach, D. New horizons for conventional lithium ion battery technology. *Journal of Physical Chemistry Letters* **2014**, *5*, 3313–3324.

(6) Xu, K. Nonaqueous liquid electrolytes for lithium-based rechargeable batteries. *Chemical Reviews* **2004**, *104*, 4303–4417.

(7) Blomgren, G. E. The development and future of lithium ion batteries. *Journal of the Electrochemical Society* **2017**, *164*, A5019–A5025.

(8) Tarascon, J.-M.; Armand, M In *Materials for Sustainable Energy*; November; Co-Published with Macmillan Publishers Ltd, UK: 2010; Vol. 414, pp 171–179.

(9) Zheng, J.; Kim, M. S.; Tu, Z.; Choudhury, S.; Tang, T.; Archer, L. A. Regulating electrodeposition morphology of lithium: towards commercially relevant secondary Li metal batteries. *Chemical Society reviews* **2020**, *49*, 2701–2750.

(10) Lin, D.; Liu, Y.; Cui, Y. Reviving the lithium metal anode for high-energy batteries. *Nature Nanotechnology* **2017**, *12*, 194–206.

(11) Frenck, L.; Sethi, G. K.; Maslyn, J. A.; Balsara, N. P. Factors That Control the Formation of Dendrites and Other Morphologies on Lithium Metal Anodes. *Frontiers in Energy Research* **2019**, *7*.

(12) Zhang, X.; Wang, A.; Liu, X.; Luo, J. Dendrites in Lithium Metal Anodes: Suppression, Regulation, and Elimination. *Accounts of Chemical Research* **2019**, *52*, 3223–3232.

(13) Wood, K. N.; Noked, M.; Dasgupta, N. P. Lithium metal anodes: Toward an improved understanding of coupled morphological, electrochemical, and mechanical behavior. *ACS Energy Letters* **2017**, *2*, 664–672.

(14) Li, L.; Basu, S.; Wang, Y.; Chen, Z.; Hundekar, P.; Wang, B.; Shi, J.; Shi, Y.; Narayanan, S.; Koratkar, N. *Self-heating-induced healing of lithium dendrites*; tech. rep. 6383; 2018.

(15) Monroe, C.; Newman, J. Dendrite Growth in Lithium/Polymer Systems. *Journal of The Electrochemical Society* **2003**, *150*, A1377.

(16) Monroe, C.; Newman, J. The Impact of Elastic Deformation on Deposition Kinetics at Lithium/Polymer Interfaces. *Journal of The Electrochemical Society* **2005**, *152*, A396–A404.

(17) Manthiram, A.; Yu, X.; Wang, S. Lithium battery chemistries enabled by solid-state electrolytes. *Nature Reviews Materials* **2017**, *2*.

(18) Han, L.; Lehmann, M. L.; Zhu, J.; Liu, T.; Zhou, Z.; Tang, X.; Heish, T. C.; Sokolov, A. P.; Cao, P.; Chen, X. C.; Saito, T. Recent Developments and Challenges in Hybrid Solid Electrolytes for Lithium-Ion Batteries. *Frontiers in Energy Research* **2020**, *8*, 1–19.

(19) Fenton, D. E.; Parker, J. M.; Wright, V. P. *Complexes of alkali metal ions with poly(ethylene oxide)*; tech. rep. 11; 1973.

(20) Borodin, O.; Smith, G. D. Mechanism of ion transport in amorphous poly(ethylene oxide)/ LiTFSI from molecular dynamics simulations. *Macromolecules* **2006**, *39*, 1620–1629.

(21) Müller-Plathe, F.; van Gunsteren, W. F. Computer simulation of a polymer electrolyte: Lithium iodide in amorphous poly(ethylene oxide). *The Journal of Chemical Physics* **1995**, *103*, 4745–4756.

(22) Deng, C.; Webb, M. A.; Bennington, P.; Sharon, D.; Nealey, P. F.; Patel, S. N.; de Pablo, J. J. Role of Molecular Architecture on Ion Transport in Ethylene oxide-Based Polymer Electrolytes. *Macromolecules* **2021**, acs.macromol.0c02424.

(23) Xue, Z.; He, D.; Xie, X. Poly(ethylene oxide)-based electrolytes for lithium-ion batteries. *Journal of Materials Chemistry A* **2015**, *3*, 19218–19253.

(24) Bresser, D.; Lyonnard, S.; Iojoiu, C.; Picard, L.; Passerini, S. Decoupling segmental relaxation and ionic conductivity for lithium-ion polymer electrolytes. *Molecular Systems Design & Engineering* **2019**, *4*, 779–792.

(25) Diddens, D.; Heuer, A. Simulation study of the lithium ion transport mechanism in ternary polymer electrolytes: The critical role of the segmental mobility. *Journal of Physical Chemistry B* **2014**, *118*, 1113–1125.

(26) Wang, Y.; Fan, F.; Agapov, A. L.; Saito, T.; Yang, J.; Yu, X.; Hong, K.; Mays, J.; Sokolov, A. P. Examination of the fundamental relation between ionic transport and segmental relaxation in polymer electrolytes. *Polymer* **2014**, *55*, 4067–4076.

(27) Adnan, S. B.; Mohamed, N. S. Conductivity and dielectric studies of Li2ZnSiO4 ceramic electrolyte synthesized via citrate sol gel method. *International Journal of Electrochemical Science* **2012**, *7*, 9844–9858.

(28) Hollingsworth, S. A.; Dror, R. O. Molecular Dynamics Simulation for All. *Neuron* **2018**, *99*, 1129–1143.

(29) Borodin, O.; Smith, G. D. Molecular Dynamics Simulations of Comb-Branched Poly (epoxide ether) -Based Polymer Electrolytes. **2007**, 1252–1258.

(30) Wheatle, B. K.; Keith, J. R.; Mogurampelly, S.; Lynd, N. A.; Ganesan, V. Influence of Dielectric Constant on Ionic Transport in Polyether-Based Electrolytes. *ACS Macro Letters* **2017**, *6*, 1362–1367.

(31) Abbott, L. J.; Lawson, J. W. Effects of Side Chain Length on Ionic Aggregation and Dynamics in Polymer Single-Ion Conductors. *Macromolecules* **2019**, *52*, 7456–7467.

(32) Seo, Y.; Shen, K. H.; Brown, J. R.; Hall, L. M. Role of Solvation on Diffusion of Ions in Diblock Copolymers: Understanding the Molecular Weight Effect through Modeling. *Journal of the American Chemical Society* **2019**, *141*, 18455–18466.

(33) Sun, B.; Mindemark, J.; Morozov, V. E.; Costa, L. T.; Bergman, M.; Johansson, P.; Fang, Y.; Furó, I.; Brandell, D. Ion transport in polycarbonate based solid polymer electrolytes: Experimental and computational investigations. *Physical Chemistry Chemical Physics* **2016**, *18*, 9504–9513.

(34) Webb, M. A.; Savoie, B. M.; Wang, Z. G.; Miller, T. F. Chemically Specific Dynamic Bond Percolation Model for Ion Transport in Polymer Electrolytes. *Macromolecules* **2015**, *48*, 7346–7358.

(35) Arges, C. G.; Li, K.; Zhang, L.; Kambe, Y.; Wu, G. P.; Lwoya, B.; Albert, J. N.; Nealey, P. F.; Kumar, R. Ionic conductivity and counterion condensation in nanoconfined polycation and polyanion brushes prepared from block copolymer templates. *Molecular Systems Design and Engineering* **2019**, *4*, 365–378.

(36) Dong, B. X.; Nowak, C.; Onorato, J. W.; Strzalka, J.; Escobedo, F. A.; Luscombe, C. K.; Nealey, P. F.; Patel, S. N. Influence of Side-Chain Chemistry on Structure and Ionic Conduction Characteristics of Polythiophene Derivatives: A Computational and Experimental Study. *Chemistry of Materials* **2019**, *31*, 1418–1429.

(37) Webb, M. A.; Jung, Y.; Pesko, D. M.; Savoie, B. M.; Yamamoto, U.; Coates, G. W.; Balsara, N. P.; Wang, Z. G.; Miller, T. F. Systematic computational and experimental investigation of lithium-ion transport mechanisms in polyester-based polymer electrolytes. *ACS Central Science* **2015**, *1*, 198–205.

(38) Pesko, D. M.; Jung, Y.; Hasan, A. L.; Webb, M. A.; Coates, G. W.; Miller, T. F.; Balsara, N. P. Effect of monomer structure on ionic conductivity in a systematic set of polyester electrolytes. *Solid State Ionics* **2016**, *289*, 118–124.

(39) Pesko, D. M.; Webb, M. A.; Jung, Y.; Zheng, Q.; Miller, T. F.; Coates, G. W.; Balsara, N. P. Universal Relationship between Conductivity and Solvation-Site Connectivity in Ether-Based Polymer Electrolytes. *Macromolecules* **2016**, *49*, 5244–5255.

(40) Ketkar, P. M.; Shen, K. H.; Hall, L. M.; Epps, T. H. Charging toward improved lithium-ion polymer electrolytes: Exploiting synergistic experimental and computational approaches to facilitate materials design. *Molecular Systems Design and Engineering* **2019**, *4*, 223–238.

(41) Sharon, D.; Bennington, P.; Webb, M. A.; Deng, C.; de Pablo, J. J.; Patel, S. N.; Nealey, P. F. Molecular Level Differences in Ionic Solvation and Transport Behavior in Ethylene Oxide-Based Homopolymer and Block Copolymer Electrolytes. *Journal of the American Chemical Society* **2021**, *143*, 3180–3190.

(42) Lascaud, S.; Perrier, M.; Vallée, A.; Besner, S.; Prud'homme, J.; Armand, M. Phase Diagrams and Conductivity Behavior of Poly(ethylene oxide)-Molten Salt Rubbery Electrolytes. *Macromolecules* **1994**, *27*, 7469–7477.

(43) Goodenough, J. B.; Kim, Y. Challenges for rechargeable Li batteries. *Chemistry of Materials* **2010**, *22*, 587–603.

(44) Barai, P.; Higa, K.; Srinivasan, V. Lithium dendrite growth mechanisms in polymer electrolytes and prevention strategies. *Physical Chemistry Chemical Physics* **2017**, *19*, 20493–20505.

(45) Stone, G. M.; Mullin, S. A.; Teran, A. A.; Hallinan, D. T.; Minor, A. M.; Hexemer, A.; Balsara, N. P. Resolution of the modulus versus adhesion dilemma in solid polymer electrolytes for rechargeable lithium metal batteries. *Journal of the Electrochemical Society* **2012**, *159*, 222–227.

(46) Xia, Y.; Fujieda, T.; Tatsumi, K.; Prosini, P. P.; Sakai, T. Thermal and electrochemical stability of cathode materials in solid polymer electrolyte. *Journal of Power Sources* **2001**, *92*, 234–243.

(47) Patel, S. N. 100th Anniversary of Macromolecular Science Viewpoint: Solid Polymer Electrolytes in Cathode Electrodes for Lithium Batteries. Current Challenges and Future Opportunities. *ACS Macro Letters* **2021**, *10*, 141–153.

(48) Galluzzo, M. D.; Halat, D. M.; Loo, W. S.; Mullin, S. A.; Reimer, J. A.; Balsara, N. P. Dissolution of Lithium Metal in Poly(ethylene oxide). *ACS Energy Letters* **2019**, *4*, 903–907.

(49) Liu, P.; Counihan, M. J.; Zhu, Y.; Connell, J. G.; Sharon, D.; Patel, S. N.; Redfern, P. C.; Zapol, P.; Markovic, N. M.; Nealey, P. F.; Curtiss, L. A.; Tepavcevic, S. Increasing Ionic Conductivity of Poly(ethylene oxide) by Reaction with Metallic Li. *Advanced Energy and Sustainability Research* **2021**, 2100142.

(50) Mindemark, J.; Lacey, M. J.; Bowden, T.; Brandell, D. Beyond PEO—Alternative host materials for Li+-conducting solid polymer electrolytes. *Progress in Polymer Science* **2018**, *81*, 114–143.

(51) Barteau, K. P.; Wolffs, M.; Lynd, N. A.; Fredrickson, G. H.; Kramer, E. J.; Hawker, C. J. Allyl Glycidyl Ether-Based Polymer Electrolytes for Room Temperature Lithium Batteries. *Macromolecules* **2013**, *46*, 8988–8994.

(52) Fragiadakis, D.; Dou, S.; Colby, R. H.; Runt, J. Molecular mobility and Li+ conduction in polyester copolymer ionomers based on poly(ethylene oxide). *Journal of Chemical Physics* **2009**, *130*, 1441.

(53) Wu, I. D.; Chang, F. C. Determination of the interaction within polyester-based solid polymer electrolyte using FTIR spectroscopy. *Polymer* **2007**, *48*, 989–996.

(54) Yang, C. R.; Perng, J. T.; Wang, Y. Y.; Wan, C. C. Conductive behaviour of lithium ions in polyacrylonitrile. *Journal of Power Sources* **1996**, *62*, 89–93.

(55) Britz, J.; Meyer, W. H.; Wegner, G. Blends of poly(meth)acrylates with 2-oxo-(1,3)dioxolane side chains and lithium salts as lithium ion conductors. *Macromolecules* **2007**, *40*, 7558–7565.

(56) Kimura, K.; Yajima, M.; Tominaga, Y. A highly-concentrated poly(ethylene carbonate)-based electrolyte for all-solid-state Li battery working at room temperature. *Electrochemistry Communications* **2016**, *66*, 46–48.

(57) Morioka, T.; Nakano, K.; Tominaga, Y. Ion-Conductive Properties of a Polymer Electrolyte Based on Ethylene Carbonate/Ethylene Oxide Random Copolymer. *Macromolecular Rapid Communications* **2017**, *38*, 1600652.

(58) Tominaga, Y. Ion-conductive polymer electrolytes based on poly(ethylene carbonate) and its derivatives. *Polymer Journal* **2017**, *49*, 291–299.

(59) Matsen, M. W.; Schick, M. Stable and unstable phases of a diblock copolymer melt. *Physical Review Letters* **1994**, *72*, 2660–2663.

(60) Bates, F. S.; Fredrickson, G. H. Block copolymers-designer soft materials. *Physics Today* **1999**, *52*, 32–38.

(61) Yang, G. W.; Wu, G. P.; Chen, X.; Xiong, S.; Arges, C. G.; Ji, S.; Nealey, P. F.; Lu, X. B.; Darensbourg, D. J.; Xu, Z. K. Directed Self-Assembly of Polystyrene-b-poly(propylene carbonate) on Chemical Patterns via Thermal Annealing for Next Generation Lithography. *Nano Letters* **2017**, *17*, 1233–1239.

(62) Gunkel, I.; Thurn-Albrecht, T. Thermodynamic and structural changes in ion-containing symmetric diblock copolymers: A small-angle X-ray scattering study. *Macromolecules* **2012**, *45*, 283–291.

(63) Leibler, L. Theory of Microphase Separation in Block Copolymers. *Macromolecules* **1980**, *13*, 1602–1617.

(64) Semenov, A. N. Theory of block copolymer interfaces in the strong segregation limit. *Macromolecules* **1993**, *26*, 6617–6621.

(65) Epps, T. H.; Bailey, T. S.; Waletzko, R.; Bates, F. S. Phase behavior and block sequence effects in lithium perchlorate-doped poly(isoprene-b-styrene-b-ethylene oxide) and poly(styrene-b-isoprene-b-ethylene oxide) triblock copolymers. *Macromolecules* **2003**, *36*, 2873–2881.

(66) Young, W. S.; Epps, T. H. Salt doping in PEO-containing block copolymers: Counterion and concentration effects. *Macromolecules* **2009**, *42*, 2672–2678.

(67) Hoarfrost, M. L.; Tyagi, M. S.; Segalman, R. A.; Reimer, J. A. Effect of confinement on proton transport mechanisms in block copolymer/ionic liquid membranes. *Macromolecules* **2012**, *45*, 3112–3120.

(68) Loo, W. S.; Galluzzo, M. D.; Li, X.; Maslyn, J. A.; Oh, H. J.; Mongcopa, K. I.; Zhu, C.; Wang, A. A.; Wang, X.; Garetz, B. A.; Balsara, N. P. Phase Behavior of Mixtures of Block Copolymers and a Lithium Salt. *J. Phys. Chem. B* **2018**, *122*, 8065–8074.

(69) Chen, X.; Zhou, C.; Chen, S. J.; Craig, G. S.; Rincon-Delgadillo, P.; Dazai, T.; Miyagi, K.; Maehashi, T.; Yamazaki, A.; Gronheid, R.; Stoykovich, M. P.; Nealey, P. F. Ionic Liquids as Additives to Polystyrene- Block-Poly(Methyl Methacrylate) Enabling Directed Self-Assembly of Patterns with Sub-10 nm Features. *ACS Applied Materials and Interfaces* **2018**, *10*, 16747–16759.

(70) Huang, J.; Tong, Z. Z.; Zhou, B.; Xu, J. T.; Fan, Z. Q. Salt-induced microphase separation in poly(ε-caprolactone)-b- poly(ethylene oxide) block copolymer. *Polymer* **2013**, *54*, 3098–3106.

(71) Gao, K. W.; Loo, W. S.; Snyder, R. L.; Abel, B. A.; Choo, Y.; Lee, A.; Teixeira, S. C. M.; Garetz, B. A.; Coates, G. W.; Balsara, N. P. Miscible Polyether/Poly(ether–acetal) Electrolyte Blends. *Macromolecules* **2020**, *53*, 5728–5739.

(72) Sing, C. E.; Zwanikken, J. W.; Olvera De La Cruz, M. Electrostatic control of block copolymer morphology. *Nature Materials* **2014**, *13*, 694–698.

(73) Chu, W.; Qin, J.; De Pablo, J. J. Ion Distribution in Microphase-Separated Copolymers with Periodic Dielectric Permittivity. *Macromolecules* **2018**, *51*, 1986–1991.

(74) Shen, K. H.; Fan, M.; Hall, L. M. Molecular Dynamics Simulations of Ion-Containing Polymers Using Generic Coarse-Grained Models. *Macromolecules* **2021**, *54*, 2031–2052.

(75) Nakamura, I.; Wang, Z. G. Salt-doped block copolymers: Ion distribution, domain spacing and effective χ parameter. *Soft Matter* **2012**, *8*, 9356–9367.

(76) Brown, J. R.; Seo, Y.; Hall, L. M. Ion Correlation Effects in Salt-Doped Block Copolymers. *Physical Review Letters* **2018**, *120*, 127801.

(77) Shen, K.-H.; Hall, L. M. Ion Conductivity and Correlations in Model Salt-Doped Polymers: Effects of Interaction Strength and Concentration. *Macromolecules* **2020**, *53*, 3655–3668.

(78) Singh, M.; Odusanya, O.; Wilmes, G. M.; Eitouni, H. B.; Gomez, E. D.; Patel, A. J.; Chen, V. L.; Park, M. J.; Fragouli, P.; Iatrou, H.; Hadjichristidis, N.; Cookson, D.; Balsara, N. P. Effect of molecular weight on the mechanical and electrical properties of block copolymer electrolytes. *Macromolecules* **2007**, *40*, 4578–4585.

(79) Teran, A. A.; Tang, M. H.; Mullin, S. A.; Balsara, N. P. Effect of molecular weight on conductivity of polymer electrolytes. *Solid State Ionics* **2011**, *203*, 18–21.

(80) Simone, P. M.; Lodge, T. P. Phase behavior and ionic conductivity of concentrated solutions of polystyrene-poly(ethylene oxide) diblock copolymers in an ionic liquid. *ACS Applied Materials and Interfaces* **2009**, *1*, 2812–2820.

(81) Panday, A.; Mullin, S.; Gomez, E. D.; Wanakule, N.; Chen, V. L.; Hexemer, A.; Pople, J.; Balsara, N. P. Effect of molecular weight and salt concentration on conductivity of block copolymer electrolytes. *Macromolecules* **2009**, *42*, 4632–4637.

(82) Sax, J.; Ottino, J. M. Modeling of transport of small molecules in polymer blends: Application of effective medium theory. *Polymer Engineering & Science* **1983**, *23*, 165–176.

(83) Chintapalli, M.; Chen, X. C.; Thelen, J. L.; Teran, A. A.; Wang, X.; Garetz, B. A.; Balsara, N. P. Effect of grain size on the ionic conductivity of a block copolymer electrolyte. *Macromolecules* **2014**, *47*, 5424–5431.

(84) Chintapalli, M.; Le, T. N.; Venkatesan, N. R.; Mackay, N. G.; Rojas, A. A.; Thelen, J. L.; Chen, X. C.; Devaux, D.; Balsara, N. P. Structure and Ionic Conductivity of Polystyrene-block-poly(ethylene oxide) Electrolytes in the High Salt Concentration Limit. *Macromolecules* **2016**, *49*, 1770–1780.

(85) Schulze, M. W.; McIntosh, L. D.; Hillmyer, M. A.; Lodge, T. P. High-modulus, high-conductivity nanostructured polymer electrolyte membranes via polymerization-induced phase separation. *Nano Letters* **2014**, *14*, 122–126.

(86) McIntosh, L. D.; Kubo, T.; Lodge, T. P. Morphology, modulus, and conductivity of a triblock terpolymer/ionic liquid electrolyte membrane. *Macromolecules* **2014**, *47*, 1090–1098.

(87) Galluzzo, M. D.; Loo, W. S.; Wang, A. A.; Walton, A.; Maslyn, J. A.; Balsara, N. P. Measurement of Three Transport Coefficients and the Thermodynamic Factor in Block Copolymer Electrolytes with Different Morphologies. *Journal of Physical Chemistry B* **2020**, *124*, 921–935.

(88) Majewski, P. W.; Gopinadhan, M.; Jang, W. S.; Lutkenhaus, J. L.; Osuji, C. O. Anisotropic ionic conductivity in block copolymer membranes by magnetic field alignment. *Journal of the American Chemical Society* **2010**, *132*, 17516–17522.

(89) Park, M. J.; Balsara, N. P. Anisotropic proton conduction in aligned block copolymer electrolyte membranes at equilibrium with humid air. *Macromolecules* **2010**, *43*, 292–298.

(90) Bouchet, R.; Phan, T. N.; Beaudoin, E.; Devaux, D.; Davidson, P.; Bertin, D.; Denoyel, R. Charge transport in nanostructured PS-PEO-PS triblock copolymer electrolytes. *Macromolecules* **2014**, *47*, 2659–2665.

(91) Beaudoin, E.; Phan, T. N. T.; Robinet, M.; Denoyel, R.; Davidson, P.; Bertin, D.; Bouchet, R. Effect of interfaces on the melting of PEO confined in triblock PS-b-PEO-b-PS copolymers. *Langmuir* **2013**, *29*, 10874–10880.

(92) Sharick, S.; Koski, J.; Riggleman, R. A.; Winey, K. I. Isolating the Effect of Molecular Weight on Ion Transport of Non-Ionic Diblock Copolymer/Ionic Liquid Mixtures. *Macromolecules* **2016**, *49*, 2245–2256.

(93) Ganesan, V.; Pyramitsyn, V.; Bertoni, C.; Shah, M. Mechanisms underlying ion transport in lamellar block copolymer membranes. *ACS Macro Letters* **2012**, *1*, 513–518.

(94) Sethuraman, V.; Mogurampelly, S.; Ganesan, V. Multiscale Simulations of Lamellar PS-PEO Block Copolymers Doped with LiPF6 Ions. *Macromolecules* **2017**, *50*, 4542–4554.

(95) Gomez, E. D.; Panday, A.; Feng, E. H.; Chen, V.; Stone, G. M.; Minor, A. M.; Kisielowski, C.; Downing, K. H.; Borodin, O.; Smith, G. D.; Balsara, N. P. Effect of ion distribution on conductivity of block copolymer electrolytes. *Nano Letters* **2009**, *9*, 1212–1216.

(96) Allen, F. I.; Watanabe, M.; Lee, Z.; Balsara, N. P.; Minor, A. M. Chemical mapping of a block copolymer electrolyte by low-loss EFTEM spectrum-imaging and principal component analysis. *Ultramicroscopy* **2011**, *111*, 239–244.

(97) Gartner, T. E.; Kubo, T.; Seo, Y.; Tansky, M.; Hall, L. M.; Sumerlin, B. S.; Epps, T. H. Domain Spacing and Composition Profile Behavior in Salt-Doped Cyclic vs Linear Block Polymer Thin Films: A Joint Experimental and Simulation Study. *Macromolecules* **2017**, *50*, 7169–7176.

(98) Ketkar, P. M.; Shen, K. H.; Fan, M.; Hall, L. M.; Epps, T. H. Quantifying the Effects of Monomer Segment Distributions on Ion Transport in Tapered Block Polymer Electrolytes. *Macromolecules* **2021**, *54*, 7590–7602.

(99) Darling, S. B. Directing the self-assembly of block copolymers. *Progress in Polymer Science (Oxford)* **2007**, *32*, 1152–1204.

(100) Hu, H.; Gopinadhan, M.; Osuji, C. O. Directed self-Assembly of block copolymers: A tutorial review of strategies for enabling nanotechnology with soft matter. *Soft Matter* **2014**, *10*, 3867–3889.

(101) Edwards, E. W.; Montague, M. F.; Solak, H. H.; Hawker, C. J.; Nealey, P. F. Precise control over molecular dimensions of block-copolymer domains using the interfacial energy of chemically nanopatterned substrates. *Advanced Materials* **2004**, *16*, 1315–1319.

(102) Albert, J. N.; Epps, T. H. Self-assembly of block copolymer thin films. *Materials Today* **2010**, *13*, 24–33.

(103) Green, P. F.; Limary, R. Block copolymer thin films: Pattern formation and phase behavior. *Advances in Colloid and Interface Science* **2001**, *94*, 53–81.

(104) Suh, H. S.; Kang, H.; Nealey, P. F.; Char, K. Thickness dependence of neutral parameter windows for perpendicularly oriented block copolymer thin films. *Macromolecules* **2010**, *43*, 4744–4751.

(105) Stoykovich, M. P.; Müller, M.; Kim, S. O.; Solak, H. H.; Edwards, E. W.; De Pablo, J. J.; Nealey, P. F. Materials Science: Directed assembly of block copolymer blends into nonregular device-oriented structures. *Science* **2005**, *308*, 1442–1446.

(106) Ouk Kim, S.; Solak, H. H.; Stoykovich, M. P.; Ferrier, N. J.; de Pablo, J. J.; Nealey, P. F. Epitaxial self-assembly of block copolymers on lithographically defined nanopatterned substrates. *Nature* **2003**, *424*, 411–414.

(107) Choi, J.; Huh, J.; Carter, K. R.; Russell, T. P. Directed Self-Assembly of Block Copolymer Thin Films Using Minimal Topographic Patterns. *ACS Nano* **2016**, *10*, 7915–7925.

(108) Arges, C. G.; Kambe, Y.; Suh, H. S.; Ocola, L. E.; Nealey, P. F. Perpendicularly Aligned, Anion Conducting Nanochannels in Block Copolymer Electrolyte Films. *Chemistry of Materials* **2016**, *28*, 1377–1389.

(109) Arges, C. G.; Kambe, Y.; Dolejsi, M.; Wu, G. P.; Segal-Pertz, T.; Ren, J.; Cao, C.; Craig, G. S.; Nealey, P. F. Interconnected ionic domains enhance conductivity in microphase separated block copolymer electrolytes. *Journal of Materials Chemistry A* **2017**, *5*, 5619–5629.

(110) Kambe, Y.; Arges, C. G.; Czaplewski, D. A.; Dolejsi, M.; Krishnan, S.; Stoykovich, M. P.; de Pablo, J. J.; Nealey, P. F. Role of Defects in Ion Transport in Block Copolymer Electrolytes. *Nano Letters* **2019**, *19*, 4684–4691.

(111) Diederichsen, K. M.; Brow, R. R.; Stoykovich, M. P. Percolating transport and the conductive scaling relationship in lamellar block copolymers under confinement. *ACS Nano* **2015**, *9*, 2465–2476.

(112) Huggins, R. A. Simple method to determine electronic and ionic components of the conductivity in mixed conductors a review. *Ionics* **2002**, *8*, 300–313.

(113) Hamley, I.; Castelletto, V. In *Soft Matter Characterization*, Borsali, R., Pecora, R., Eds.; Springer Netherlands: Dordrecht, 2008, pp 1021–1081.

(114) Ren, J.; Ocola, L. E.; Divan, R.; Czaplewski, D. A.; Segal-Peretz, T.; Xiong, S.; Kline, R. J.; Arges, C. G.; Nealey, P. F. Post-directed-self-assembly membrane fabrication for in situ analysis of block copolymer structures. *Nanotechnology* **2016**, *27*, 435303.

(115) Chiefari, J.; Chong, Y. K. B.; Ercole, F.; Krstina, J.; Jeffery, J.; Le, T. P. T.; Mayadunne, R. T. A.; Meijs, G. F.; Moad, C. L.; Moad, G.; Rizzardo, E.; Thang, S. H. Living Free-Radical Polymerization by Reversible Addition-Fragmentation Chain Transfer: The RAFT Process. *Macromolecules* **1998**, *31*, 5559–5562.

(116) Perrier, S. 50th Anniversary Perspective: RAFT Polymerization - A User Guide. *Macromolecules* **2017**, *50*, 7433–7447.

(117) Bakker, A. Contact ion pair formation and ether oxygen coordination in the polymer electrolytes M[N(CF3SO2)2]2PEOn for M = Mg, Ca, Sr and Ba. *Polymer (Guildf).* **1995**, *36*, 4371–4378.

(118) Olthuis, W.; Streekstra, W.; Bergveld, P. Theoretical and experimental determination of cell constants of planar-interdigitated electrolyte conductivity sensors. *Sensors Actuators B. Chem.* **1995**, *24*, 252–256.

(119) Wuelfing, W. P.; Murray, R. W. Electron hopping through films of arenethiolate monolayer-protected gold clusters. *J. Phys. Chem. B* **2002**, *106*, 3139–3145.

(120) Modestino, M. A.; Paul, D. K.; Dishari, S.; Petrina, S. A.; Allen, F. I.; Hickner, M. A.; Karan, K.; Segalman, R. A.; Weber, A. Z. Self-Assembly and Transport Limitations in Confined Nafion Films. *Macromolecules* **2013**, *46*, 867–873.

(121) Paul, D. K.; McCreery, R.; Karan, K. Proton Transport Property in Supported Nafion Nanothin Films by Electrochemical Impedance Spectroscopy. *Journal of the Electrochemical Society* **2014**, *161*, F1395–F1402.

(122) Olthuis, W.; Streekstra, W.; Bergveld, P. Theoretical and experimental determination of cell constants of planar-interdigitated electrolyte conductivity sensors. *Sensors and Actuators: B. Chemical* **1995**, *24*, 252–256.

(123) Gevorgian, S. S.; Martinsson, T.; Linnér, P. L.; Kollberg, E. L. CAD models for multilayered substrate interdigital capacitors. *IEEE Trans. Microw. Theory Tech.* **1996**, *44*, 896–904.

(124) Nigon, R.; Raeder, T. M.; Muralt, P. Characterization methodology for lead zirconate titanate thin films with interdigitated electrode structures. *J. Appl. Phys.* **2017**, *121*, 204101.

(125) Sun, T.; Morgan, H.; Green, N. G. Analytical solutions of ac electrokinetics in interdigitated electrode arrays: Electric field, dielectrophoretic and traveling-wave dielectrophoretic forces. *Phys. Rev. E - Stat. Nonlinear, Soft Matter Phys.* **2007**, *76*, 1–18.

(126) Igreja, R.; Dias, C. J. Analytical evaluation of the interdigital electrodes capacitance for a multi-layered structure. *Sensors Actuators, A Phys.* **2004**, *112*, 291–301.

(127) Chen, J. Z.; Darhuber, A. A.; Troian, S. M.; Wagner, S. Capacitive sensing of droplets for microfluidic devices based on thermocapillary actuation. *Lab Chip* **2004**, *4*, 473–480.

(128) Nguyen, C. H.; Nigon, R.; Raeder, T. M.; Hanke, U.; Halvorsen, E.; Muralt, P. Probing-models for interdigitated electrode systems with ferroelectric thin films. *Journal of Physics D: Applied Physics* **2018**, *51*, 175303.

(129) Chidambaram, N.; Mazzalai, A.; Balma, D.; Muralt, P. Comparison of lead Zirconate Titanate thin films for microelectromechanical energy harvester with interdigitated and parallel plate electrodes. *IEEE Trans. Ultrason. Ferroelectr. Freq. Control* **2013**, *60*, 1564–1571.

(130) Mamishev, V. A.; Sundara-Rajan, K.; Yang, F.; Du, Y.; Zahn, M. Interdigital sensors and transducers. *Proceedings of the IEEE* **2004**, *92*, 808–844.

(131) McNealy, B. E.; Jiang, J.; Hertz, J. L. A precise, reduced-parameter model of thin film electrolyte impedance. *J. Electrochem. Soc.* **2015**, *162*, F537–F546.

(132) Hong, J.; Yoon, D. S.; Kim, S. K.; Kim, T. S.; Kim, S.; Pak, E. Y.; No, K. AC frequency characteristics of coplanar impedance sensors as design parameters. *Lab on a Chip* **2005**, *5*, 270.

(133) Van Gerwen, P.; Laureys, W.; Huyberechts, G.; De Baeck, M.; Baert, K.; Suis, J.; Varlan, A.; Sansen, W.; Hermans, L.; Mertens, R. Nanoscaled interdigitated electrode arrays for biochemical sensors. *Proceedings of International Solid State Sensors and Actuators Conference (Transducers '97)* **1998**, *2*, 907–910.

(134) Sharon, D.; Bennington, P.; Liu, C.; Kambe, Y.; Dong, B. X.; Burnett, V. F.; Dolejsi, M.; Grocke, G.; Patel, S. N.; Nealey, P. F. Interrogation of electrochemical properties of polymer electrolyte thin films with interdigitated electrodes. *Journal of the Electrochemical Society* **2018**, *165*, H1028–H1039.

(135) Nagao, Y. Proton-Conductivity Enhancement in Polymer Thin Films. *Langmuir* **2017**, *33*, 12547–12558.

(136) Marks, T.; Trussler, S.; Smith, A. J.; Xiong, D.; Dahn, J. R. A Guide to Li-Ion Coin-Cell Electrode Making for Academic Researchers. *Journal of The Electrochemical Society* **2011**, *158*, A51.

(137) Young, W. S.; Kuan, W. F.; Epps, T. H. Block copolymer electrolytes for rechargeable lithium batteries. *Journal of Polymer Science, Part B: Polymer Physics* **2014**, *52*, 1–16.

(138) Gilbert, J. B.; Luo, M.; Shelton, C. K.; Rubner, M. F.; Cohen, R. E.; Epps, T. H. Determination of lithium-ion distributions in nanostructured block polymer electrolyte thin films by X-ray photoelectron spectroscopy depth profiling. *ACS Nano* **2015**, *9*, 512–520.

(139) Kambe, Y.; Arges, C. G.; Patel, S. N.; Stoykovich, M. P.; Nealey, P. F. Ion Conduction in Microphase-Separated Block Copolymer Electrolytes. *ECS Interface* **2017**.

(140) Rojas, A. A.; Inceoglu, S.; Mackay, N. G.; Thelen, J. L.; Devaux, D.; Stone, G. M.; Balsara, N. P. Effect of Lithium-Ion Concentration on Morphology and Ion Transport in Single-Ion-Conducting Block Copolymer Electrolytes. *Macromolecules* **2015**, *48*, 6589–6595.

(141) Teran, A. A.; Mullin, S. A.; Hallinan, D. T.; Balsara, N. P. Discontinuous changes in ionic conductivity of a block copolymer electrolyte through an order-disorder transition. *ACS Macro Letters* **2012**, *1*, 305–309.

(142) Hallinan, D. T.; Balsara, N. P. Polymer Electrolytes. *Annual Review of Materials Research* **2013**, *43*, 503–525.

(143) Young, W. S.; Epps, T. H. Ionic conductivities of block copolymer electrolytes with various conducting pathways: Sample preparation and processing considerations. *Macromolecules* **2012**, *45*, 4689–4697.

(144) Qian, X.; Gu, N.; Cheng, Z.; Yang, X.; Wang, E.; Dong, S. Impedance study of (PEO)10LiClO4-Al2O3 composite polymer electrolyte with blocking electrodes. *Electrochimica Acta* **2001**, *46*, 1829–1836.

(145) Marzantowicz, M.; Dygas, J. R.; Krok, F. Impedance of interface between PEO:LiTFSI polymer electrolyte and blocking electrodes. *Electrochimica Acta* **2008**, *53*, 7417–7425.

(146) Inzelt, G.; Láng, G. G. In *Electropolymerization*; Wiley-VCH Verlag GmbH & Co. KGaA: Weinheim, Germany, 2010, pp 51–76.

(147) Bisquert, J; Garcia-Belmonte, G; Fabregat-Santiago, F; Bueno, P. R. Theoretical models for ac impedance of diffusion layers exhibiting low frequency dispersion. *Journal of Electroanalytical Chemistry* **1999**, *475*, 152.

(148) Remita, E.; Boughrara, D.; Tribollet, B.; Vivier, V.; Sutter, E.; Ropital, F.; Kittel, J. Diffusion impedance in a thin-layer cell: Experimental and theoretical study on a large-disk electrode. *Journal of Physical Chemistry C* **2008**, *112*, 4626–4634.

(149) Paasch, G.; Micka, K.; Gersdore, P. Theory of the Electrochemical Impedance of. *Electrochemica Acta* **1993**, *38*, 112–120.

(150) Belyaev, B.; Drokin, N. Impedance Spectroscopy Investigation of Electrophysical Characteristics of the Electrode–Liquid Crystal Interface. *Physics of the Solid State* **2015**, *57*, 181–187.

(151) Gorecki, W; Jeannin, M; Belorizky, E; Roux, C; Armand, M Physical properties of solid polymer electrolyte PEO (LiTFSI) complexes. *Journal of Physics: Condensed Matter* **1999**, *7*, 6823.

(152) Xu, T.; Hawker, C. J.; Russell, T. P. Interfacial Interaction Dependence of Microdomain Orientation in Diblock Copolymer Thin Films. *Macromolecules* **2005**, *38*, 2802–2805.

(153) Diederichsen, K. M.; Buss, H. G.; McCloskey, B. D. The Compensation Effect in the Vogel-Tammann-Fulcher (VTF) Equation for Polymer-Based Electrolytes. *Macromolecules* **2017**, *50*, 3831–3840.

(154) Sharma, A.; Reiter, G. Instability of thin polymer films on coated substrates: Rupture, dewetting, and drop formation. *Journal of Colloid and Interface Science* **1996**, *178*, 383–399.

(155) Dong, B. X.; Bennington, P.; Kambe, Y.; Sharon, D.; Dolejsi, M.; Strzalka, J.; Burnett, V. F.; Nealey, P. F.; Patel, S. N. Nanothin film conductivity measurements reveal interfacial influence on ion transport in polymer electrolytes. *Molecular Systems Design and Engineering* **2019**, *4*, 597–608.

(156) Freger, V.; Bason, S. Characterization of ion transport in thin films using electrochemical impedance spectroscopy: I. Principles and theory. *Journal of Membrane Science* **2007**, *302*, 1–9.

(157) Lee, H.; Chang, B. Y.; Kwack, W. S.; Jo, K.; Jeong, J.; Kwon, S. H.; Yang, H. Dependence of the capacitance between an electrode and an electrolyte solution on the thickness of aluminum oxide layers deposited using atomic layer deposition. *Journal of Electroanalytical Chemistry* **2013**, *700*, 8–11.

(158) Góes, M. S.; Rahman, H.; Ryall, J.; Davis, J. J.; Bueno, P. R. A dielectric model of self-assembled monolayer interfaces by capacitive spectroscopy. *Langmuir* **2012**, *28*, 9689–9699.

(159) Kumar, B.; Mittal, P.; Negi, Y. S.; Kaushik, B. K. In 2012, pp 855–864.

(160) Miller, T. F.; Wang, Z. G.; Coates, G. W.; Balsara, N. P. Designing polymer electrolytes for safe and high capacity rechargeable lithium batteries. *Accounts of Chemical Research* **2017**, *50*, 590–593.

(161) Weber, R. L.; Ye, Y.; Schmitt, A. L.; Banik, S. M.; Elabd, Y. A.; Mahanthappa, M. K. Effect of nanoscale morphology on the conductivity of polymerized ionic liquid block copolymers. *Macromolecules* **2011**, *44*, 5727–5735.

(162) Dörr, T. S.; Pelz, A.; Zhang, P.; Kraus, T.; Winter, M.; Wiemhöfer, H.-D. An Ambient Temperature Electrolyte with Superior Lithium Ion Conductivity based on a Self-Assembled Block Copolymer. *Chemistry - A European Journal* **2018**, *24*, 8061–8065.

(163) Yan, L.; Rank, C.; Mecking, S.; Winey, K. I. Gyroid and Other Ordered Morphologies in Single-Ion Conducting Polymers and Their Impact on Ion Conductivity. *Journal of the American Chemical Society* **2020**, *142*, 857–866.

(164) Sutton, P.; Bennington, P.; Patel, S. N.; Stefik, M.; Wiesner, U. B.; Nealey, P. F.; Steiner, U.; Gunkel, I. Surface Reconstruction Limited Conductivity in Block-Copolymer Li Battery Electrolytes. *Advanced Functional Materials* **2019**, *29*, 1905977.

(165) Ping, J.; Pan, H.; Hou, P. P.; Zhang, M. Y.; Wang, X.; Wang, C.; Chen, J.; Wu, D.; Shen, Z.; Fan, X. H. Solid Polymer Electrolytes with Excellent High-Temperature Properties Based on Brush Block Copolymers Having Rigid Side Chains. *ACS Applied Materials and Interfaces* **2017**, *9*, 6130–6137.

(166) Glynos, E.; Petropoulou, P.; Mygiakis, E.; Nega, A. D.; Pan, W.; Papoutsakis, L.; Giannelis, E. P.; Sakellariou, G.; Anastasiadis, S. H. Leveraging Molecular Architecture to Design New, All-Polymer Solid Electrolytes with Simultaneous Enhancement in Modulus and Ionic Conductivity. *Macromolecules* **2018**, *51*, 2542–2550.

(167) Yuan, R.; Teran, A. A.; Gurevitch, I.; Mullin, S. A.; Wanakule, N. S.; Balsara, N. P. Ionic conductivity of low molecular weight block copolymer electrolytes. *Macromolecules* **2013**, *46*, 914–921.

(168) Timachova, K.; Watanabe, H.; Balsara, N. P. Effect of molecular weight and salt concentration on ion transport and the transference number in polymer electrolytes. *Macromolecules* **2015**, *48*, 7882–7888.

(169) Irwin, M. T.; Hickey, R. J.; Xie, S.; So, S.; Bates, F. S.; Lodge, T. P. Structure-conductivity relationships in ordered and disordered salt-doped diblock copolymer/homopolymer blends. *Macromolecules* **2016**, *49*, 6928–6939.

(170) Sethuraman, V.; Pryamitsyn, V.; Ganesan, V. Influence of molecular weight and degree of segregation on local segmental dynamics of ordered block copolymers. *Journal of Polymer Science, Part B: Polymer Physics* **2016**, *54*, 859–864.

(171) Soo, P. P.; Huang, B.; Jang, Y. I.; Chiang, Y. M.; Sadoway, D. R.; Mayes, A. M. Rubbery block copolymer electrolytes for solid-state rechargeable lithium batteries. *Journal of the Electrochemical Society* **1999**, *146*, 32–37.

(172) Kim, O.; Jo, G.; Park, Y. J.; Kim, S.; Park, M. J. Ion transport properties of self-assembled polymer electrolytes: The role of confinement and interface. *Journal of Physical Chemistry Letters* **2013**, *4*, 2111–2117.

(173) Neto, C.; James, M.; Telford, A. M. On the composition of the top layer of microphase separated thin PS-PEO films. *Macromolecules* **2009**, *42*, 4801–4808.

(174) Segal-Peretz, T.; Winterstein, J.; Doxastakis, M.; Ramírez-Hernández, A.; Biswas, M.; Ren, J.; Suh, H. S.; Darling, S. B.; Liddle, J. A.; Elam, J. W.; De Pablo, J. J.; Zaluzec, N. J.; Nealey, P. F. Characterizing the three-dimensional structure of block copolymers via sequential infiltration synthesis and scanning transmission electron tomography. *ACS Nano* **2015**, *9*, 5333–5347.

(175) Epps, T. H.; Bailey, T. S.; Pham, H. D.; Bates, F. S. Phase Behavior of Lithium Perchlorate-Doped Poly(styrene- b -isoprene- b -ethylene oxide) Triblock Copolymers. *Chemistry of Materials* **2002**, *14*, 1706–1714.

(176) Teran, A. A.; Balsara, N. P. Thermodynamics of block copolymers with and without salt. *Journal of Physical Chemistry B* **2014**, *118*, 4–17.

(177) Timachova, K.; Villaluenga, I.; Cirrincione, L.; Gobet, M.; Bhattacharya, R.; Jiang, X.; Newman, J.; Madsen, L. A.; Greenbaum, S. G.; Balsara, N. P. Anisotropic Ion Diffusion and Electrochemically Driven Transport in Nanostructured Block Copolymer Electrolytes. *Journal of Physical Chemistry B* **2018**, *122*, 1537–1544.

(178) Morris, M. A.; Sung, S. H.; Ketkar, P. M.; Dura, J. A.; Nieuwendaal, R. C.; Epps, T. H. Enhanced Conductivity via Homopolymer-Rich Pathways in Block Polymer-Blended Electrolytes. *Macromolecules* **2019**, *52*, 9682–9692.

(179) Kuan, W. F.; Remy, R.; Mackay, M. E.; Epps, T. H. Controlled ionic conductivity via tapered block polymer electrolytes. *RSC Advances* **2015**, *5*, 12597–12604.

(180) Loo, W. S.; Balsara, N. P. Organizing thermodynamic data obtained from multicomponent polymer electrolytes: Salt-containing polymer blends and block copolymers. *Journal of Polymer Science, Part B: Polymer Physics* **2019**, *57*, 1177–1187.

(181) Gartner, T. E.; Morris, M. A.; Shelton, C. K.; Dura, J. A.; Epps, T. H. Quantifying lithium salt and polymer density distributions in nanostructured ion-conducting block polymers. *Macromolecules* **2018**, *51*, 1917–1926.

(182) Matsen, M. W.; Bates, F. S. Unifying Weak- and Strong-Segregation Block Copolymer Theories. *Macromolecules* **1996**, *29*, 1091–1098.

(183) Lifschitz, M.; Freed, K. F.; Tang, H. Hyperbolic tangent variational approximation for interfacial profiles of binary polymer blends. *The Journal of Chemical Physics* **1995**, *103*, 3767–3781.

(184) Anastasiadis, S. H.; Russell, T. P.; Satija, S. K.; Majkrzak, C. F. The morphology of symmetric diblock copolymers as revealed by neutron reflectivity. *The Journal of Chemical Physics* **1990**, *92*, 5677–5691.

(185) Sunday, D. F.; Maher, M. J.; Hannon, A. F.; Liman, C. D.; Tein, S.; Blachut, G.; Asano, Y.; Ellison, C. J.; Willson, C. G.; Kline, R. J. Characterizing the Interface Scaling of High χ Block Copolymers near the Order-Disorder Transition. *Macromolecules* **2018**, *51*, 173–180.

(186) Anastasiadis, S. H.; Retsos, H.; Toprakcioglu, C.; Menelle, A.; Hadziioannou, G. On the Interfacial Width in Triblock versus Diblock Copolymers: A Neutron Reflectivity Investigation. *Macromolecules* **1998**, *31*, 6600–6604.

(187) Arora, A.; Qin, J.; Morse, D. C.; Delaney, K. T.; Fredrickson, G. H.; Bates, F. S.; Dorfman, K. D. Broadly Accessible Self-Consistent Field Theory for Block Polymer Materials Discovery. *Macromolecules* **2016**, *49*, 4675–4690.

(188) Seo, Y.; Brown, J. R.; Hall, L. M. Effect of Tapering on Morphology and Interfacial Behavior of Diblock Copolymers from Molecular Dynamics Simulations. *Macromolecules* **2015**, *48*, 4974–4982.

(189) O'Connell, P. A.; McKenna, G. B. Arrhenius-type temperature dependence of the segmental relaxation below Tg. *Journal of Chemical Physics* **1999**, *110*, 11054–11060.

(190) Helfand, E.; Tagami, Y. Theory of the interface between immiscible polymers. *J. Polym. Sci. Part B Polym. Lett.* **1971**, *9*, 741–746.

(191) Fetters, L. J.; Lohse, D. J.; Richter, D.; Witten, T. A.; Zirkel, A. Connection between Polymer Molecular Weight, Density, Chain Dimensions, and Melt Viscoelastic Properties. *Macromolecules* **1994**, *27*, 4639–4647.

(192) Sharon, D.; Bennington, P.; Dolejsi, M.; Webb, M. A.; Dong, B. X.; de Pablo, J. J.; Nealey, P. F.; Patel, S. N. Intrinsic Ion Transport Properties of Block Copolymer Electrolytes. *ACS Nano* **2020**, acsnano.0c03713.

(193) Coote, J. P.; Kinsey, T.; Street, D. P.; Kilbey, S. M.; Sangoro, J. R.; Stein, G. E. Surface-Induced Ordering Depresses Through-Film Ionic Conductivity in Lamellar Block Copolymer Electrolytes. *ACS Macro Letters* **2020**, *9*, 565–570.

(194) Su, Z.; Kole, S.; Harden, L. C.; Palakkal, V. M.; Kim, C.; Nair, G.; Arges, C. G.; Renner, J. N. Peptide-Modified Electrode Surfaces for Promoting Anion Exchange Ionomer Microphase Separation and Ionic Conductivity. *ACS Materials Letters* **2019**, *1*, 467–475.

(195) Zhao, Q.; Bennington, P.; Nealey, P. F.; Patel, S. N.; Evans, C. M. Ion Specific, Thin Film Confinement Effects on Conductivity in Polymerized Ionic Liquids. *Macromolecules* **2021**, *54*, 10520–10528.

(196) Sundrani, D.; Darling, S. B.; Sibener, S. J. Hierarchical assembly and compliance of aligned nanoscale polymer cylinders in confinement. *Langmuir* **2004**, *20*, 5091–5099.

(197) Knoll, A.; Horvat, A.; Lyakhova, K. S.; Krausch, G.; Sevink, G. J.; Zvelindovsky, V. A.; Magerle, R. Phase behavior in thin films of cylinder-forming block copolymers. *Physical Review Letters* **2002**, *89*, 355011–355014.

(198) Zhang, X.; Berry, B. C.; Yager, K. G.; Kim, S.; Jones, R. L.; Satija, S.; Pickel, D. L.; Douglas, J. F.; Karim, A. Surface morphology diagram for cylinder-forming block copolymer thin films. *ACS Nano* **2008**, *2*, 2331–2341.

(199) Ito, H.; Russell, T. P.; Wignall, G. D. Interactions in mixtures of poly(ethylene oxide) and poly(methyl methacrylate). *Macromolecules* **1987**, *20*, 2213–2220.

(200) Ghelichi, M.; Qazvini, N. T.; Jafari, S. H.; Khonakdar, H. A.; Farajollahi, Y.; Scheffler, C. Conformational, thermal, and ionic conductivity behavior of PEO in PEO/PMMA miscible blend: Investigating the effect of lithium salt. *Journal of Applied Polymer Science* **2013**, *129*, 1868–1874.

(201) Jeddi, K.; Qazvini, N. T.; Jafari, S. H.; Khonakdar, H. A. Enhanced ionic conductivity in peo/pmma glassy miscible blends: Role of nano-confinement of minority component chains. *Journal of Polymer Science, Part B: Polymer Physics* **2010**, *48*, 2065–2071.

(202) Liang, B.; Tang, S.; Jiang, Q.; Chen, C.; Chen, X.; Li, S.; Yan, X. Preparation and characterization of PEO-PMMA polymer composite electrolytes doped with nano-Al_2O_3. *Electrochimica Acta* **2015**, *169*, 334–341.

(203) Bennington, P.; Deng, C.; Sharon, D.; Webb, M. A.; de Pablo, J. J.; Nealey, P. F.; Patel, S. N. Role of solvation site segmental dynamics on ion transport in ethylene-oxide based side-chain polymer electrolytes. *Journal of Materials Chemistry A* **2021**, 9937–9951.

(204) Jiang, Z. GIXSGUI: A MATLAB toolbox for grazing-incidence X-ray scattering data visualization and reduction, and indexing of buried three-dimensional periodic nanostructured films. *Journal of Applied Crystallography* **2015**, *48*, 917–926.

(205) Morioka, T.; Ota, K.; Tominaga, Y. Effect of oxyethylene side chains on ion-conductive properties of polycarbonate-based electrolytes. *Polymer* **2016**, *84*, 21–26.

(206) Tillmann, S. D.; Isken, P.; Lex-Balducci, A. Gel polymer electrolyte for lithium-ion batteries comprising cyclic carbonate moieties. *Journal of Power Sources* **2014**, *271*, 239–244.

(207) Mindemark, J.; Sun, B.; Törmä, E.; Brandell, D. High-performance solid polymer electrolytes for lithium batteries operational at ambient temperature. *Journal of Power Sources* **2015**, *298*, 166–170.

(208) Uno, T.; Kawaguchi, S.; Kubo, M.; Itoh, T. Ionic conductivity and thermal property of solid hybrid polymer electrolyte composed of oligo(ethylene oxide) unit and butyrolactone unit. *Journal of Power Sources* **2008**, *178*, 716–722.

(209) Jo, G.; Jeon, H.; Park, M. J. Synthesis of polymer electrolytes based on poly(ethylene oxide) and an anion-stabilizing hard polymer for enhancing conductivity and cation transport. *ACS Macro Letters* **2015**, *4*, 225–230.

(210) Li, S.; Jiang, K.; Wang, J.; Zuo, C.; Jo, Y. H.; He, D.; Xie, X.; Xue, Z. Molecular Brush with Dense PEG Side Chains: Design of a Well-Defined Polymer Electrolyte for Lithium-Ion Batteries. *Macromolecules* **2019**, *52*, 7234–7243.

(211) Geng, Z.; Schauser, N. S.; Lee, J.; Schmeller, R. P.; Barbon, S. M.; Segalman, R. A.; Lynd, N. A.; Hawker, C. J. Role of Side-Chain Architecture in Poly(ethylene oxide)-Based Copolymers. *Macromolecules* **2020**, *53*, 4960–4967.

(212) Shim, J.; Bates, F. S.; Lodge, T. P. Superlattice by charged block copolymer self-assembly. *Nature Communications* **2019**, *10*, 2108.

(213) Ryu, S. W.; Trapa, P. E.; Olugebefola, S. C.; Gonzalez-Leon, J. A.; Sadoway, D. R.; Mayes, A. M. Effect of counter ion placement on conductivity in single-ion conducting block copolymer electrolytes. *Journal of the Electrochemical Society* **2005**, *152*, A158.

(214) Elmore, C. T.; Seidler, M. E.; Ford, H. O.; Merrill, L. C.; Upadhyay, S. P.; Schneider, W. F.; Schaefer, J. L. Ion transport in solvent-free, crosslinked, single-ion conducting polymer electrolytes for post-lithium ion batteries. *Batteries* **2018**, *4*, 28.

(215) Porcarelli, L.; Shaplov, A. S.; Salsamendi, M.; Nair, J. R.; Vygodskii, Y. S.; Mecerreyes, D.; Gerbaldi, C. Single-Ion Block Copoly(ionic liquid)s as Electrolytes for All-Solid State Lithium Batteries. *ACS Applied Materials and Interfaces* **2016**, *8*, 10350–10359.

(216) Kato, R.; Mirmira, P.; Sookezian, A.; Grocke, G. L.; Patel, S. N.; Rowan, S. J. Ion-Conducting Dynamic Solid Polymer Electrolyte Adhesives. *ACS Macro Letters* **2020**, *9*, 500–506.

(217) Jing, B. B.; Evans, C. M. Catalyst-Free Dynamic Networks for Recyclable, Self-Healing Solid Polymer Electrolytes. *Journal of the American Chemical Society* **2019**, *141*, 18932–18937.

(218) Nielsen, C. B.; Giovannitti, A.; Sbircea, D. T.; Bandiello, E.; Niazi, M. R.; Hanifi, D. A.; Sessolo, M.; Amassian, A.; Malliaras, G. G.; Rivnay, J.; McCulloch, I. Molecular Design of Semiconducting Polymers for High-Performance Organic Electrochemical Transistors. *Journal of the American Chemical Society* **2016**, *138*, 10252–10259.

(219) Ebadi, M.; Eriksson, T.; Mandal, P.; Costa, L. T.; Araujo, C. M.; Mindemark, J.; Brandell, D. Restricted Ion Transport by Plasticizing Side Chains in Polycarbonate-Based Solid Electrolytes. *Macromolecules* **2020**, *53*, 764–774.

(220) Rolland, J.; Brassinne, J.; Bourgeois, J. P.; Poggi, E.; Vlad, A.; Gohy, J. F. Chemically anchored liquid-PEO based block copolymer electrolytes for solid-state lithium-ion batteries. *Journal of Materials Chemistry A* **2014**, *2*, 11839–11846.

(221) Karo, J.; Brandell, D. A Molecular Dynamics study of the influence of side-chain length and spacing on lithium mobility in non-crystalline LiPF6·PEOx; x=10 and 30. *Solid State Ionics* **2009**, *180*, 1272–1284.

(222) Reimschuessel, H. K. on the Glass Transition Temperature of Comblike Polymers: Effects of Side Chain Length and Backbone Chain Structure. *J Polym Sci Polym Chem Ed* **1979**, *17*, 2447–2457.

(223) Zaheer, M.; Xu, H.; Wang, B.; Li, L.; Deng, Y. An In Situ Polymerized Comb-Like PLA/PEG-based Solid Polymer Electrolyte for Lithium Metal Batteries. *Journal of The Electrochemical Society* **2020**, *167*, 070504.

(224) Selvasekarapandian, S.; Baskaran, R.; Kamishima, O.; Kawamura, J.; Hattori, T. Laser Raman and FTIR studies on Li+ interaction in PVAc–LiClO4 polymer electrolytes. *Spectrochimica Acta Part A: Molecular and Biomolecular Spectroscopy* **2006**, *65*, 1234–1240.

(225) Kimura, K.; Motomatsu, J.; Tominaga, Y. Correlation between Solvation Structure and Ion-Conductive Behavior of Concentrated Poly(ethylene carbonate)-Based Electrolytes. *Journal of Physical Chemistry C* **2016**, *120*, 12385–12391.

(226) Sim, L. H.; Gan, S. N.; Chan, C. H.; Yahya, R. ATR-FTIR studies on ion interaction of lithium perchlorate in polyacrylate/poly(ethylene oxide) blends. *Spectrochimica Acta - Part A: Molecular and Biomolecular Spectroscopy* **2010**, *76*, 287–292.

(227) Mindemark, J.; Imholt, L.; Montero, J.; Brandell, D. Allyl ethers as combined plasticizing and crosslinkable side groups in polycarbonate-based polymer electrolytes for solid-state Li batteries. *Journal of Polymer Science, Part A: Polymer Chemistry* **2016**, *54*, 2128–2135.

(228) Grondin, J; Servant, L; Rey, I; Lassegues, J. C. Infrared and Raman study of the PEO-LiTFSI polymer electrolyte. *Electrochimica Acta* **1998**, *43*, 1505–1510.

(229) Brouillette, D.; Irish, D. E.; Taylor, N. J.; Perron, G.; Odziemkowski, M.; Desnoyers, J. E. Stable solvates in solution of lithium bis(trifluoromethylsulfone)imide in glymes and other aprotic solvents: Phase diagrams, crystallography and Raman spectroscopy. *Physical Chemistry Chemical Physics* **2002**, *4*, 6063–6071.

(230) Molinari, N.; Mailoa, J. P.; Kozinsky, B. Effect of Salt Concentration on Ion Clustering and Transport in Polymer Solid Electrolytes: A Molecular Dynamics Study of PEO-LiTFSI. *Chemistry of Materials* **2018**, *30*, 6298–6306.

(231) Mao, G.; Saboungi, M. L.; Price, D. L.; Armand, M. B.; Howells, W. S. *Structure of liquid PEO-LiTFSI electrolyte*; tech. rep. 24; 2000.

(232) Devaux, D.; Bouchet, R.; Glé, D.; Denoyel, R. Mechanism of ion transport in PEO/LiTFSI complexes: Effect of temperature, molecular weight and end groups. *Solid State Ionics* **2012**, *227*, 119–127.

(233) Plazek, D. J.; O'Rourke, V. M. Viscoelastic behavior of low molecular weight polystyrene. *Journal of Polymer Science Part A-2: Polymer Physics* **1971**, *9*, 209–243.

(234) Hu, Q.; Caputo, A.; Sadoway, D. R. Solid-state graft copolymer electrolytes for lithium battery applications. *Journal of visualized experiments : JoVE* **2013**, 4–6.

(235) Mongcopa, K. I. S.; Gribble, D. A.; Loo, W. S.; Tyagi, M.; Mullin, S. A.; Balsara, N. P. Segmental Dynamics Measured by Quasi-Elastic Neutron Scattering and Ion Transport in Chemically Distinct Polymer Electrolytes. *Macromolecules* **2020**, *53*, 2406–2411.

(236) Mongcopa, K. I. S.; Tyagi, M.; Mailoa, J. P.; Samsonidze, G.; Kozinsky, B.; Mullin, S. A.; Gribble, D. A.; Watanabe, H.; Balsara, N. P. Relationship between Segmental Dynamics Measured by Quasi-Elastic Neutron Scattering and Conductivity in Polymer Electrolytes. *ACS Macro Letters* **2018**, *7*, 504–508.

(237) Loo, W. S.; Faraone, A.; Grundy, L. S.; Gao, K. W.; Balsara, N. P. Polymer Dynamics in Block Copolymer Electrolytes Detected by Neutron Spin Echo. *ACS Macro Letters* **2020**, *9*, 639–645.

(238) Bates, C. M.; Chang, A. B.; Momčilović, N.; Jones, S. C.; Grubbs, R. H. ABA Triblock Brush Polymers: Synthesis, Self-Assembly, Conductivity, and Rheological Properties. *Macromolecules* **2015**, *48*, 4967–4973.

(239) Shibuya, Y.; Tatara, R.; Jiang, Y.; Shao-Horn, Y.; Johnson, J. A. Brush-First ROMP of poly(ethylene oxide) macromonomers of varied length: impact of polymer architecture on thermal behavior and Li+ conductivity. *Journal of Polymer Science, Part A: Polymer Chemistry* **2019**, *57*, 448–455.

(240) Guo, M.; Zhang, M.; He, D.; Hu, J.; Wang, X.; Gong, C.; Xie, X.; Xue, Z. Comb-like solid polymer electrolyte based on polyethylene glycol-grafted sulfonated polyether ether ketone. *Electrochimica Acta* **2017**, *255*, 396–404.

(241) Allcock, H. R.; Austin, P. E.; Neenan, T. X.; Sisko, J. T.; Blonsky, P. M.; Shriver, D. F. Polyphosphazenes with Etheric Side Groups: Prospective Biomedical and Solid Electrolyte Polymers. *Macromolecules* **1986**, *19*, 1508–1512.

(242) Zhang, X.; Daigle, J.-C.; Zaghib, K. Comprehensive Review of Polymer Architecture for All-Solid-State Lithium Rechargeable Batteries. *Materials* **2020**, *13*, 2488.

(243) Sutton, P.; Airoldi, M.; Porcarelli, L.; Olmedo-Martínez, J. L.; Mugemana, C.; Bruns, N.; Mecerreyes, D.; Steiner, U.; Gunkel, I. Tuning the properties of a UV-polymerized, cross-linked solid polymer electrolyte for lithium batteries. *Polymers* **2020**, *12*, DOI: `10.3390/polym12030595`.

(244) Onorato, J. W.; Luscombe, C. K. Morphological effects on polymeric mixed ionic/electronic conductors. *Molecular Systems Design and Engineering* **2019**, *4*, 310–324.

(245) Hussain, H.; Mya, K. Y.; He, C. Self-assembly of brush-like poly[poly(ethylene glycol) methyl ether methacrylate] synthesized via aqueous atom transfer radical polymerization. *Langmuir* **2008**, *24*, 13279–13286.

(246) Kim, D.-G.; Kang, H.; Han, S.; Lee, J.-C. The increase of antifouling properties of ultrafiltration membrane coated by star-shaped polymers. *Journal of Materials Chemistry* **2012**, *22*, 8654.

(247) Martin, M. G.; Siepmann, J. I. Transferable potentials for phase equilibria. 1. United-atom description of n-alkanes. *Journal of Physical Chemistry B* **1998**, *102*, 2569–2577.

(248) Stubbs, J. M.; Potoff, J. J.; Siepmann, J. I. Transferable Potentials for Phase Equilibria. 6. United-Atom Description for Ethers, Glycols, Ketones, and Aldehydes. *The Journal of Physical Chemistry B* **2004**, *108*, 17596–17605.

(249) Maerzke, K. A.; Schultz, N. E.; Ross, R. B.; Siepmann, J. I. TraPPE-UA Force Field for Acrylates and Monte Carlo Simulations for Their Mixtures with Alkanes and Alcohols. *The Journal of Physical Chemistry B* **2009**, *113*, 6415–6425.

(250) Wick, C. D.; Theodorou, D. N. Connectivity-Altering Monte Carlo Simulations of the End Group Effects on Volumetric Properties for Poly(ethylene oxide). **2004**, 7026–7033.

(251) Lopes, N. C.; Pascal, B. Molecular Force Field for Ionic Liquids Composed of Triflate or Bistriflylimide Anions. *Journal of Chemical Physics B* **2004**, *108*, 16893–16898.

(252) Brown, W. M.; Kohlmeyer, A.; Plimpton, S. J.; Tharrington, A. N. Implementing molecular dynamics on hybrid high performance computers – Particle–particle particle-mesh. *Computer Physics Communications* **2012**, *183*, 449–459.

(253) Plimpton, S. Fast Parallel Algorithms for Short-Range Molecular Dynamics. *Journal of Computational Physics* **1995**, *117*, 1–19.

(254) Dahbi, M.; Ghamouss, F.; Tran-Van, F.; Lemordant, D.; Anouti, M. Comparative study of EC/DMC LiTFSI and LiPF6 electrolytes for electrochemical storage. *Journal of Power Sources* **2011**, *196*, 9743–9750.

(255) Wheatle, B. K.; Lynd, N. A.; Ganesan, V. Effect of Host Incompatibility and Polarity Contrast on Ion Transport in Ternary Polymer-Polymer-Salt Blend Electrolytes. *Macromolecules* **2020**, *53*, 875–884.

(256) Tobishima, S.; Morimoto, H.; Aoki, M.; Saito, Y.; Inose, T.; Fukumoto, T.; Kuryu, T. Glyme-based nonaqueous electrolytes for rechargeable lithium cells. *Electrochimica Acta* **2004**, *49*, 979–987.

(257) Geoffroy, I.; Willmann, P.; Mesfar, K.; Carré, B.; Lemordant, D. Electrolytic characteristics of ethylene carbonate-diglyme-based electrolytes for lithium batteries. *Electrochimica Acta* **2000**, *45*, 2019–2027.

(258) Sakai, T.; Kihara, N.; Endo, T. Polymer Reaction of Epoxide and Carbon Dioxide. Incorporation of Carbon Dioxide into Epoxide Polymers. *Macromolecules* **1995**, *28*, 4701–4706.

(259) Camara, F.; Caillol, S.; Boutevin, B. Free radical polymerization study of glycerin carbonate methacrylate for the synthesis of cyclic carbonate functionalized polymers. *European Polymer Journal* **2014**, *61*, 133–144.

(260) Schneider, H. A. Meaning of the glass temperature of random copolymers and miscible polymer blends. *Journal of Thermal Analysis and Calorimetry* **1999**, *56*, 983–989.

(261) Lodge, T. P.; McLeish, T. C. Self-concentrations and effective glass transition temperatures in polymer blends. *Macromolecules* **2000**, *33*, 5278–5284.

(262) Lodge, T. P.; Wood, E. R.; Haley, J. C. Two calorimetric glass transitions do not necessarily indicate immiscibility: The case of PEO/PMMA. *Journal of Polymer Science, Part B: Polymer Physics* **2006**, *44*, 756–763.

(263) Wheatle, B. K.; Lynd, N. A.; Ganesan, V. Effect of Polymer Polarity on Ion Transport: A Competition between Ion Aggregation and Polymer Segmental Dynamics. *ACS Macro Letters* **2018**, *7*, 1149–1154.

(264) Torell, L. M.; Jacobsson, P.; Petersen, G. A Raman study of ion solvation and association in polymer electrolytes. *Polymers for Advanced Technologies* **1993**, *4*, 152–163.

(265) Huang, W.; Frech, R. Raman spectra of PPO-salt complexes: Mixed cations and mixed anions. *Solid State Ionics* **1992**, *53-56*, 1095–1101.

(266) Huang, W.; Frech, R. Dependence of ionic association on polymer chain length in poly(ethylene oxide)-lithium triflate complexes. *Polymer* **1994**, *35*, 235–242.

(267) Aguilera, L.; Xiong, S.; Scheers, J.; Matic, A. A structural study of LiTFSI-tetraglyme mixtures: From diluted solutions to solvated ionic liquids. *Journal of Molecular Liquids* **2015**, *210*, 238–242.

(268) York, S.; Frech, R.; Snow, A.; Glatzhofer, D. A comparative vibrational spectroscopic study of lithium triflate and sodium triflate in linear poly(ethylenimine). *Electrochimica Acta* **2001**, *46*, 1533–1537.

(269) Tillmann, S. D.; Isken, P.; Lex-Balducci, A. Lithium Coordination in Cyclic-Carbonate-Based Gel Polymer Electrolyte. *The Journal of Physical Chemistry C* **2015**, *119*, 14873–14878.

(270) Johnston, S Spectroscopic studies of triflate ion association in polymer gel electrolytes and their constituents. *Solid State Ionics* **1996**, *90*, 39–48.

(271) Schantz, S. On the ion association at low salt concentrations in polymer electrolytes; a Raman study of NaCF3SO3 and LiClO4 dissolved in polypropylene oxide. *The Journal of Chemical Physics* **1991**, *94*, 6296–6306.

(272) Kumar, R.; Sumpter, B. G.; Muthukumar, M. Enhanced phase segregation induced by dipolar interactions in polymer blends. *Macromolecules* **2014**, *47*, 6491–6502.

(273) Loo, W. S.; Galluzzo, M. D.; Li, X.; Maslyn, J. A.; Oh, H. J.; Mongcopa, K. I.; Zhu, C.; Wang, A. A.; Wang, X.; Garetz, B. A.; Balsara, N. P. Phase Behavior of Mixtures of Block Copolymers and a Lithium Salt. *The Journal of Physical Chemistry B* **2018**, *122*, 8065–8074.

(274) Kwon, T. W.; Choi, J. W.; Coskun, A. The emerging era of supramolecular polymeric binders in silicon anodes. *Chem. Soc. Rev.* **2018**, *47*, 2145–2164.

(275) Chen, L.; Li, Y.; Li, S. P.; Fan, L. Z.; Nan, C. W.; Goodenough, J. B. PEO/garnet composite electrolytes for solid-state lithium batteries: From “ceramic-in-polymer” to “polymer-in-ceramic”. *Nano Energy* **2018**, *46*, 176–184.

(276) Delaporte, N.; Wang, Y.; Zaghib, K. Pre-treatments of Lithium Foil Surface for Improving the Cycling Life of Li Metal Batteries. *Front. Mater.* **2019**, *6*.

(277) Tate, R. S.; Fryer, D. S.; Paqualini, S.; Montague, M. F.; De Pablo, J. J.; Nealey, P. F. Extraordinary elevation of the glass transition temperature of thin polymer films grafted to silicon oxide substrates. *J. Chem. Phys.* **2001**, *115*, 9982–9990.

(278) Croce, F.; Persi, L. L.; Scrosati, B.; Serraino-Fiory, F.; Plichta, E.; Hendrickson, M. A. Role of the ceramic fillers in enhancing the transport properties of composite polymer electrolytes. *Electrochimica Acta* **2001**, *46*, 2457–2461.

(279) Liu, W.; Liu, N.; Sun, J.; Hsu, P. C.; Li, Y.; Lee, H. W.; Cui, Y. Ionic Conductivity Enhancement of Polymer Electrolytes with Ceramic Nanowire Fillers. *Nano Letters* **2015**, *15*, 2740–2745.

(280) Lettow, J. H.; Kaplan, R. Y.; Nealey, P. F.; Rowan, S. J. Enhanced Ion Conductivity through Hydrated, Polyelectrolyte-Grafted Cellulose Nanocrystal Films. *Macromolecules* **2021**, *54*, 6925–6936.

(281) Tikekar, M. D.; Archer, L. A.; Koch, D. L. Stability Analysis of Electrodeposition across a Structured Electrolyte with Immobilized Anions. *Journal of The Electrochemical Society* **2014**, *161*, A847–A855.

(282) Tikekar, M. D.; Choudhury, S.; Tu, Z.; Archer, L. A. Design principles for electrolytes and interfaces for stable lithium-metal batteries. *Nature Energy* **2016**, *1*, 1–7.

(283) Inceoglu, S.; Rojas, A. A.; Devaux, D.; Chen, X. C.; Stone, G. M.; Balsara, N. P. Morphology-conductivity relationship of single-ion-conducting block copolymer electrolytes for lithium batteries. *ACS Macro Letters* **2014**, *3*, 510–514.

(284) Jo, G.; Kim, O.; Kim, H.; Hyeok Choi, U.; Lee, S. B.; Jeong Park, M. End-functionalized block copolymer electrolytes: Effect of segregation strength on ion transport efficiency. *Polymer Journal* **2016**, *48*, 465–472.

(285) Li, Z.; Yao, Q.; Zhang, Q.; Zhao, Y.; Gao, D.; Li, S.; Xu, S. Creating ionic channels in single-ion conducting solid polymer electrolyte by manipulating phase separation structure. *Journal of Materials Chemistry A* **2018**, *6*, 24848–24859.

(286) Rolland, J.; Poggi, E.; Vlad, A.; Gohy, J. F. Single-ion diblock copolymers for solid-state polymer electrolytes. *Polymer* **2015**, *68*, 344–352.